

Diss. ETH No. 23333

# **Pulse-Sequence Design in Solid-State NMR Using Floquet Theory**

A thesis submitted to attain the degree of

DOCTOR OF SCIENCES of ETH ZURICH  
(Dr. sc. ETH Zurich)

presented by

KONG OOI TAN

MSc in Physics, Imperial College London

born on 9th July 1987  
citizen of Malaysia

accepted on the recommendation of

Prof. Dr. Matthias Ernst, examiner  
Prof. Dr. Gunnar Jeschke, co-examiner

2016



I would like to dedicate this thesis to my loving parents ...





# Contents

<b>Contents</b>	<b>v</b>
<b>List of Figures</b>	<b>ix</b>
<b>List of Tables</b>	<b>xiii</b>
<b>Abbreviations</b>	<b>xvi</b>
<b>Abstract</b>	<b>xviii</b>
<b>Zusammenfassung</b>	<b>xx</b>
<b>1 Introduction</b>	<b>1</b>
1.1 Biomolecular Solid-State NMR . . . . .	1
1.2 Basic NMR Theory . . . . .	2
1.3 Hamiltonians in Solid-State NMR . . . . .	4
1.3.1 Zeeman Hamiltonian . . . . .	5
1.3.2 Chemical-Shift Hamiltonian . . . . .	6
1.3.3 Dipolar-Coupling Hamiltonian . . . . .	7
1.3.4 Scalar $J$ -Coupling Hamiltonian . . . . .	9
1.3.5 The RF Hamiltonian . . . . .	10
1.4 Magic Angle Spinning . . . . .	11
1.4.1 Euler Angles and Wigner Rotations . . . . .	11
1.4.2 Averaging of Anisotropic Interaction by MAS . . . . .	13
1.4.3 Static Powder Spectra and Spinning Sidebands . . . . .	14
1.5 Adiabatic Experiment . . . . .	15
<b>2 Theory of Time-Dependent Hamiltonians</b>	<b>17</b>
2.1 Introduction . . . . .	17

---

2.2	Modulation of the Spin Tensors by RF Irradiations . . . . .	18
2.2.1	Fourier Series of Time-Dependent Hamiltonians . . . . .	18
2.2.2	Interaction-Frame Representation . . . . .	19
2.3	Modulation of the Spatial Tensors by MAS . . . . .	22
2.4	Average Hamiltonian Theory . . . . .	22
2.5	Floquet Theory . . . . .	25
2.5.1	Floquet Hamiltonian . . . . .	27
2.5.2	Operator-Based Floquet Theory . . . . .	28
2.5.3	Effective Hamiltonian . . . . .	28
2.5.4	Characteristic Frequencies . . . . .	30
2.6	Recoupling and Decoupling Sequences . . . . .	31
<b>3</b>	<b>Symmetry-Based Sequences for Scalar <math>J</math>-Coupling Experiments</b>	<b>33</b>
3.1	Introduction to $CN_n^V$ and $RN_n^V$ Sequences . . . . .	34
3.1.1	Space-Spin Selection Rules . . . . .	35
3.1.2	Resonance Conditions and Effective Hamiltonians . . . . .	36
3.2	Interference between TOBSY C9 and Decoupling . . . . .	40
3.2.1	Floquet Theory and Effective Hamiltonian . . . . .	41
3.2.2	Simulations and Experimental Results . . . . .	45
3.2.3	Conclusions . . . . .	48
3.2.4	Further Discussions . . . . .	50
3.3	Low-Power TOBSY Sequences at Fast MAS . . . . .	54
3.3.1	Experimental Results on Glycine . . . . .	56
3.3.2	Comparing DREAM and TOBSY on Ubiquitin . . . . .	57
3.3.3	Conclusions . . . . .	58
<b>4</b>	<b>Asynchronous Symmetry-Based Homonuclear Dipolar Recoupling Sequence</b>	<b>61</b>
4.1	Introduction . . . . .	61
4.2	Resonance Conditions and Effective Hamiltonians . . . . .	64
4.2.1	First-Order Effective Hamiltonian . . . . .	68
4.2.2	Second-Order Effective Hamiltonian . . . . .	69
4.2.3	Higher-Order Space-Spin Selection Rules . . . . .	74
4.3	Details of Numerical Simulations and Experiments . . . . .	77
4.4	Results and Discussions . . . . .	78
4.5	Conclusions for Asynchronous C7 . . . . .	81

---

<b>5</b>	<b>Broad-Band DREAM Recoupling Sequence</b>	<b>83</b>
5.1	Introduction . . . . .	83
5.2	Theory . . . . .	84
5.3	Computational and Experimental Methods . . . . .	89
5.4	Results and Discussions for XiX <sup>CW</sup> DREAM . . . . .	90
5.5	DQ Recoupling without CW field: XiX DREAM . . . . .	95
5.5.1	Theory . . . . .	95
5.5.2	Adiabatic Sweep via $v_m$ and Pseudo CW Field . . . . .	98
5.5.3	Conclusions . . . . .	100
<b>6</b>	<b>A Generalized Theoretical Framework for the Description of Spin Decoupling</b>	<b>101</b>
6.1	Introduction . . . . .	101
6.2	Theory . . . . .	104
6.2.1	General Floquet Description of Decoupling Sequences . . . . .	104
6.2.2	Low-Power Amplitude-Modulated XiX Sequences . . . . .	109
6.2.3	Verification of Offset-Dependent Effective Nutation Frequency and Fourier Coefficients . . . . .	111
6.3	Understanding Low-Power Decoupling Sequences . . . . .	112
6.3.1	Materials and Methods . . . . .	112
6.3.2	Decoupling Efficiency of AM-XiX and SC-AM-XiX . . . . .	113
6.3.3	Using Homonuclear Recoupling Conditions for Better Decoupling . . . . .	116
6.3.4	Offset Effects on Decoupling Efficiency . . . . .	118
6.3.5	Conclusions for AM-XiX and SC-AM-XiX . . . . .	120
6.4	Understanding High-Power Decoupling Sequences . . . . .	120
6.4.1	Comparing Basic, Supercycled and Adiabatic TPPM . . . . .	120
6.4.2	Easier Optimization of SPINAL-64 . . . . .	124
6.4.3	Elucidating Finite-Pulse Effect in Adiabatic SW-TPPM . . . . .	127
6.5	Conclusions . . . . .	132
<b>7</b>	<b>Outlook and Conclusions</b>	<b>133</b>
	<b>Appendix A</b>	<b>135</b>
A.1	Important Formulae . . . . .	135
A.1.1	Definition of Spin-Tensor Operators . . . . .	135
A.1.2	Definition of Zero- and Double-Quantum Hamiltonian . . . . .	136
A.1.3	Wigner Rotation Matrix Elements . . . . .	137
A.2	Determination of Effective Field Direction and Flip Angle using Quaternions	137

---

A.3 Spin System Details of Glycine Ethylester . . . . .	139
A.3.1 Additional Discussions for TOBSY . . . . .	140
A.3.2 SC-C9 TOBSY with XiX . . . . .	140
A.3.3 Impacts of Crystallites Selection and RF Inhomogeneity . . . . .	141
<b>Bibliography</b>	<b>143</b>
<b>Acknowledgements</b>	<b>159</b>
<b>Curriculum Vitae</b>	<b>162</b>
<b>Publications</b>	<b>163</b>

# List of Figures

1.1	CSA powder spectrum under static condition . . . . .	7
1.2	Schematic drawing of dipolar interaction . . . . .	9
1.3	Graphical representation of the Euler rotations . . . . .	12
1.4	Static and MAS spectra of powdered $^{13}\text{C}$ -glycine . . . . .	14
1.5	Schematic diagram of adiabatic and sudden experiments . . . . .	16
2.1	Schematic diagram of the origin of time-dependent Hamiltonians . . . . .	18
2.2	Schematic representation of AHT . . . . .	23
2.3	Matrix representations of the ladder operator $\hat{F}_1, \hat{F}_{-2}$ and number operator $\hat{F}_z$	26
2.4	Schematic diagram of the construction of the operator-based Floquet theory	27
2.5	Schematic drawing of the XiX <sup>cw</sup> and the symmetry-based C7 <sub>2</sub> <sup>1</sup> sequence . .	31
3.1	Schematic diagrams of $CN_n^V$ and $RN_n^V$ Sequences. . . . .	34
3.2	Schematic drawings of (a) POST element and (b) a composite $\pi$ pulse. . .	35
3.3	Space-spin selection diagrams for (a) C7 <sub>2</sub> <sup>1</sup> and (b) R26 <sub>4</sub> <sup>11</sup> . . . . .	36
3.4	Fourier coefficients $a_{\ell,s}^{(k)}$ for C9 <sub>6</sub> <sup>1</sup> . . . . .	39
3.5	The interference effect between decoupling and C sequence. . . . .	40
3.6	Pulse sequence of TOBSY C9 with decoupling . . . . .	41
3.7	Calculated scaling factor of recoupled dipolar coupling during TOBSY C9	44
3.8	Simulated interference effect between TOBSY C9 and decoupling . . . . .	46
3.9	Experimental interference effect between TOBSY C9 and CW decoupling .	47
3.10	Experimental interference effect between TOBSY C9 and XiX decoupling .	49
3.11	Experimental 1D plot of C9 transfer efficiency against rf amplitude $\nu_{11}$ . . .	50
3.12	2D MLF spectra acquired using TOBSY C9 sequence with decoupling . . .	51
3.13	Experimental data of supercycled TOBSY sequence with CW decoupling .	52
3.14	Interference analysis of supercycled TOBSY sequence with CW decoupling	53
3.15	Spin diffusion during TOBSY with different decoupling schemes . . . . .	55
3.16	Experimental C9 <sub>39</sub> <sup>1</sup> on glycine ethyl ester at 400 MHz . . . . .	56

3.17	1D spectra of $C9_{39}^1$ on glycine at 400 MHz . . . . .	57
3.18	TOBSY $C9_{48}^1$ transfer on protonated ubiquitin at $\nu_r = 55.5$ kHz . . . . .	59
3.19	TOBSY $C9_{48}^1$ transfer on deuterated ubiquitin at $\nu_r = 111.1$ kHz . . . . .	60
4.1	Pulse sequence for asynchronous $C7_2^1$ . . . . .	63
4.2	Fourier coefficients for rank-one $a_{1,s}^{(k,\ell)}$ of $C7_2^1$ . . . . .	65
4.3	Fourier coefficients for rank-two $a_{2,s}^{(k,\ell)}$ of $C7_2^1$ . . . . .	66
4.4	Fourier coefficients for the chemical-shift $a_{1,\text{eff}}^{(0,0)}$ and DQ term $ a_{2,-2}^{(2,2)} $ of $C7_2^1$ . . . . .	70
4.5	The size of the CSA cross-terms $\omega_{\text{CSA}}^{(\text{eff})}$ of $C7_2^1$ . . . . .	72
4.6	Evolution using second-order effective Hamiltonians of $C7_2^1$ . . . . .	73
4.7	Number of $\text{CSA} \otimes \text{CSA}$ cross-terms based on second-order selection rules . . . . .	76
4.8	2D simulations and experimental data of various asynchronous $C7_2^1$ scheme . . . . .	79
4.9	1D Experimental data of synchronous and asynchronous $C7_2^1$ . . . . .	80
5.1	Pulse sequence of $\text{XiX}^{\text{cw}}$ DREAM . . . . .	85
5.2	First and second moment of $\text{XiX}^{\text{cw}}$ DREAM against $\omega_1^{(\text{XiX})}/\omega_m$ . . . . .	89
5.3	Performance of $\text{XiX}^{\text{cw}}$ DREAM against carrier frequency . . . . .	91
5.4	2D experimental data of $\text{XiX}^{\text{cw}}$ DREAM on MLF . . . . .	92
5.5	2D experimental data of $\text{XiX}^{\text{cw}}$ DREAM on ubiquitin . . . . .	94
5.6	Fourier coefficients of $\text{XiX}$ pulses . . . . .	97
5.7	Simulated 1D comparison of different DQ recouplings schemes . . . . .	98
5.8	Simulated adiabatic sweep by $\nu_m$ or pseudo CW field . . . . .	99
5.9	Experimental 1D data of different adiabatic DQ recoupling sequences . . . . .	100
6.1	Schematic diagram of a generalized theoretical framework for decoupling . . . . .	104
6.2	Verification of effective nutation frequency with offset $\nu_{\text{eff}}(\nu_{\text{off}})$ . . . . .	113
6.3	Efficiency of AM-XiX and SC-AM-XiX in compensating dipolar and CSA cross terms . . . . .	114
6.4	Self-decoupling mechanism promoted by DQ recoupling in AM-XiX . . . . .	117
6.5	Offset effects on AM-XiX and SC-AM-XiX . . . . .	119
6.6	Schematic diagrams of TPPM-based decoupling sequences . . . . .	121
6.7	Decoupling performance of basic TPPM . . . . .	122
6.8	Comparison of decoupling performance among variants of TPPM . . . . .	123
6.9	Experimental data of SPINAL-64 with fixed phase $\phi + \alpha$ . . . . .	124
6.10	Comparison of decoupling performance with effective field of SPINAL . . . . .	125
6.11	Calculated dipolar and CSA cross terms using SPINAL . . . . .	126
6.12	Fourier coefficients of SW-TPPM . . . . .	128

---

6.13	Decoupling performance of SW-TPPM in compensating CSA cross terms . . . . .	129
6.14	Decoupling performance of SW-TPPM in compensating dipolar cross terms . . . . .	130
6.15	Simulated peak intensity of SW <sub>f</sub> -TPPM with different interactions . . . . .	131
7.1	Numerical optimizations of Fourier coefficients for efficient decoupling . . . . .	134
A.1	Experimental data of supercycled TOBSY sequence with XiX decoupling . . . . .	140
A.2	RF inhomogeneity of 1.3 mm probe after different CP steps . . . . .	141
A.3	Dependence of TOBSY C <sub>9</sub> <sup>1</sup> <sub>39</sub> transfer on CH dipolar coupling . . . . .	142





# List of Tables

2.1	Characteristic frequencies of pulse sequences . . . . .	31
5.1	Experimental details of DREAM and XiX <sup>cw</sup> DREAM . . . . .	90
6.1	Definition of parameters used for AM-XiX and SC-AM-XiX decoupling. . .	110
A.1	Rank $\ell = 2$ reduced Wigner matrix elements. . . . .	137
A.2	Details of spin system in PAS of a four-spin glycine ethylester at 500 MHz. .	139



# Abbreviations

1D	One Dimensional
2D	Two Dimensional
AHT	Average Hamiltonian Theory
CP	Cross Polarization
CSA	Chemical Shift Anisotropy
CW	Continuous Wave
DQ	Double Quantum
DREAM	Dipolar Recoupling Enhanced by Amplitude Modulation
EPR	Electron Paramagnetic Resonance
FID	Free Induction Decay
GAMMA	General Approach to Magnetic Resonance Mathematical Analysis
HORROR	Homonuclear Rotary Resonance
LAB	Laboratory axis system
MAS	Magic Angle Spinning
MLF	Methionine-Leucine-phenylalanine
NMR	Nuclear Magnetic Resonance
PAIN	Proton-Assisted Insensitive Nuclei
PAR	Proton-Assisted Recoupling
PAS	Principle Axis System
POST	Permutationally Offset STabilized
PDSD	Proton Driven Spin Diffusion
rf	radio-frequency
RESORT	REsonant Second-Order Transfer
SPINAL	Small Phase Incremental Alternation
TOBSY	ThroUgh-Bond correlation SpectroscopY
TPPM	Two Pulse Phase Modulation
SW <sub>f</sub> -TPPM	Frequency Swept Two Pulse Phase Modulation
XiX	X inverse X

AM-XiX	Amplitude Modulated X inverse X
SC-AM-XiX	Super Cycled Amplitude Modulated X inverse X
XiX <sup>CW</sup>	X inverse X Continuous Wave
ZQ	Zero Quantum

## Abstract

Most solid-state samples have broad static NMR spectra that are sometimes unresolvable due to anisotropic interactions like chemical-shift anisotropy and dipolar couplings. These interactions can be averaged out by magic-angle spinning (MAS) and decoupling techniques to obtain high-resolution spectra needed for structure determination. However, such interactions also contain rich structural information and have to be reintroduced back during selected time periods. This is achieved via strategic interference between rf irradiation and MAS, which prevents the averaging of the anisotropic interaction. The theoretical analysis of the spin dynamics can be complicated at times if the spin system is modulated by multiple frequencies. The time-dependent Hamiltonians can be analyzed using Floquet theory, to determine the effective Hamiltonians. The design of efficient decoupling and recoupling sequences in solid-state NMR are the main objectives of this thesis.

An introduction to the Hamiltonians involved in solid-state NMR, along with the effect of MAS will be discussed in Chapter 1. Then, an introduction to time-dependent Hamiltonians followed by the determination of effective Hamiltonians using Floquet theory will be addressed in Chapter 2. The design of efficient homonuclear polarization-transfer experiments via scalar  $J$  coupling will be demonstrated in Chapter 3. This can be achieved by using rotor-synchronized symmetry-based sequences C sequences at either moderate (25 – 40 kHz) or fast ( $> 50$  kHz) MAS frequencies. In the moderate MAS regime, heteronuclear decoupling is often needed for efficient polarization transfer. However, careful optimization is required to avoid interference between the mixing and decoupling sequence. A systematic study of the interference effect is established here and it will be shown that the implementation of XiX decoupling is preferred over CW irradiation due to lower rf requirement and better hardware control in the timing of the pulses. The usage of decoupling is however not needed anymore in the regime of fast MAS as the heteronuclear dipolar couplings are sufficiently well averaged by the C sequence itself. Despite that, the existing TOBSY sequences employ an rf field that is often several times higher than the MAS frequency, making them less attractive for biological applications. Hence, several low-power TOBSY sequences operating at fast MAS scheme are proposed and examined.

In principle, homonuclear polarization-transfer can also be mediated via dipolar cou-

pling. Nevertheless, it was shown that the transfer efficiency is reduced by the higher-ordered terms in the rotor-synchronized  $C7_2^1$  sequence. This issue is shown to be circumvented by exploiting non-rotor synchronized conditions, which generate an effective Hamiltonians that suppresses the undesired terms efficiently. The theoretical treatment and analysis of the asynchronous conditions are discussed in Chapter 4. Apart from the symmetry-based sequences, DREAM, a spin-locking sequence, is also a popular choice for dipolar-recoupling experiment because it is an adiabatic sequence, i.e. it has a theoretical transfer limit that is approaching 100%. Nonetheless, the sequence becomes selective if the chemical-shift difference of the resonances is large relative to the MAS speed. Thus, a more broad-banded version of the DREAM sequence ( $XiX^{CW}$  DREAM) is demonstrated in Chapter 5 to compensate offset more efficiently.

Besides designing efficient polarization-transfer sequences, the sensitivity of experiments can also be improved by obtaining high-resolution spectra with robust decoupling sequences. Nonetheless, the theoretical analysis of the decoupling sequences is often complicated as it involves cumbersome calculations of higher-order effective Hamiltonians. A unified framework for the theory of heteronuclear decoupling for any arbitrary decoupling sequences is proposed in Chapter 6. It will be shown that the details of a decoupling sequence are encoded in the generalized effective Hamiltonians using Fourier coefficients, which can be computed to compare the performance of decoupling sequences without the details of a spin system. An outlook and conclusions will be discussed in Chapter 7.

## Zusammenfassung

Anisotrope Wechselwirkungen, wie die dipolare Wechselwirkung oder die Anisotropie der chemischen Verschiebung, führen dazu, dass die Signale in den NMR-Spektren von Feststoffen typischerweise stark verbreitert sind. Um die für die Strukturaufklärung benötigten hochaufgelösten Spektren zu erhalten, müssen diese orientierungsabhängigen Wechselwirkungen durch Probenrotation um den magischen Winkel (MAS) und Entkopplungstechniken ausgemittelt werden. Jedoch gehen dadurch auch wertvolle strukturelle Informationen verloren. Durch Anwendung von Radiofrequenzpulsen, die während bestimmter Zeiten während des Experiments eingestrahlt werden, werden Interferenzen mit den Modulationen durch die Probenrotation ausgenutzt und eine Ausmittlung von bestimmten Wechselwirkungen verhindert. Floquet Theorie eignet sich für die Beschreibung der Spindynamik unter komplexen NMR Experimenten in denen der Hamiltonoperator durch mehrere Frequenzen moduliert ist. In diesem Fall kann ein effektiver Hamiltonoperator berechnet werden. Ziel dieser Arbeit ist die Entwicklung von effizienten Sequenzen zur Entkopplung ("Decoupling") und Wiedereinkopplung ("Recoupling") von Wechselwirkungen in der Festkörper-NMR-Spektroskopie.

In Kapitel 1 wird eine Einführung in die theoretischen Grundlagen der Festkörper-NMR-Spektroskopie gegeben. Die Struktur der relevanten Hamiltonoperatoren sowie die Konsequenzen von MAS werden diskutiert. Im Folgenden wird die Behandlung von zeitabhängigen Hamiltonoperatoren mittels Floquet Theorie beschrieben. In Kapitel 3 wird die Entwicklung von effizienten homonuklearen Polarisationstransferexperimenten auf Grundlage der  $J$ -Kopplung demonstriert. Hierbei kommen rotorsynchronisierte symmetriebasierte C-Sequenzen beim moderaten (25 – 40 kHz) oder schnellen ( $> 50$  kHz) MAS zum Einsatz. Im Regime von moderater Probenrotation ist heteronukleare Entkopplung oft die Voraussetzung für effizienten Transfer. Um destruktive Interferenz zwischen der Radiofrequenzfeldern auf den unterschiedlichen Kanälen zu vermeiden, ist in der Regel eine genaue Optimierung der Entkopplung notwendig. In einer systematischen Studie werden diese Interferenzen charakterisiert. Es wird gezeigt, dass die Verwendung einer XiX-Entkopplung der konventionellen CW-Entkopplung vorzuziehen ist, da schwächere Radiofrequenzfelder benötigt werden und die zeitliche Abfolge der Pulse besser durch die Hardware kontrol-

liert werden kann. Im Fall von schneller Probenrotation werden die heteronuklearen dipolaren Wechselwirkungen wesentlich besser durch die C-Sequenz selbst ausgemittelt und auf zusätzliche Protonenentkopplung kann daher verzichtet werden. Jedoch benötigen die verwendeten TOBSY-Sequenzen ein Radiofrequenzfeld, das ein Vielfaches der MAS Frequenz ist, weshalb sie wenig attraktiv für biologische Anwendungen sind. Daher werden mehrere TOBSY-Experimente mit niedrigen Radiofrequenzfeldern für die Anwendung bei schnellem MAS entwickelt und ihre Eigenschaften untersucht.

Homonuklearer Polarisationstransfer kann auch über die dipolare Wechselwirkung stattfinden. Es konnte allerdings gezeigt werden, dass die Transfereffizienz durch Terme höherer Ordnung im rotorsynchronisierten  $C7\frac{1}{2}$ -Experiment deutlich reduziert werden kann. Diese Problematik kann jedoch unter Ausnutzung von nicht rotorsynchronisierten Resoanzbedingungen umgangen werden. In diesem Fall wird ein effektiver Hamiltonoperator erzeugt, in dem die Fehlerterme effizient unterdrückt sind. Die theoretische Beschreibung und Analyse der asynchronen Bedingungen wird in Kapitel 4 diskutiert. Neben symmetriebasierten Sequenzen finden auch Spin-Lock Experimente, wie DREAM, häufig Anwendung in der Festkörper NMR Spektroskopie. Der grosse Vorteil dieses Experiments ist seine adiabatische Natur, weshalb die theoretische Transfereffizienz bis zu 100% betragen kann. Ist die chemische Verschiebungsdifferenz allerdings grösser als die MAS Frequenz, wird die zunehmende Selektivität des Experiments zum Nachteil. Wie in Kapitel 5 gezeigt, kann in diesem Fall mit einer breitbandigeren Variante dieses Experiments ( $XiX^{CW}$  DREAM) eine Verbesserung erzielt werden.

Ausser durch die Entwicklung von effizienten Polarisationstransferexperimenten kann die Empfindlichkeit der Experimente auch durch eine Verbesserung der Auflösung der Spektren mit robusteren Entkopplungssequenzen erreicht werden. Jedoch ist die theoretische Beschreibung von Entkopplungsexperimenten komplex, da meist Terme höherer Ordnung aufwändig berechnet werden müssen. In Kapitel 6 wird eine vereinheitlichte Theorie heteronuklearer Entkopplungsexperimente vorgestellt. Es wird gezeigt, dass die Eigenschaften der Entkopplung in einem generalisierten Hamiltonoperator durch Fourier-Koeffizienten gegeben sind. Diese können ohne die Kenntnis des exakten Spinsystems berechnet werden und zum Vergleich der Effizienzen verschiedener Sequenzen herangezogen werden.

Eine Zusammenfassung der vorliegenden Arbeit sowie ein Ausblick befinden sich in Kapitel 7.



# Chapter 1

## Introduction

### 1.1 Biomolecular Solid-State NMR

NMR is a useful tool to study polymers, inorganic materials and especially biological molecules. NMR has been a successful method to determine the structures of proteins because it provides atomic-resolution structures compared to other spectroscopic methods. As of July 2015, more than 11000 structures deposited in the Protein Data Bank (PDB) were determined by NMR, most of which are solution-state NMR. There are, however, some biological macromolecules like membrane proteins and amyloid fibrils that are insoluble and do not form high-quality crystals, a prerequisite for structure determination using X-ray crystallography. In this situation, solid-state NMR spectroscopy can be employed to study the powdered micro crystals or fibrils. Structure determination of biological molecules with solid-state NMR is a multi-step process. Firstly, sequential resonance assignment [1–3] has to be performed to correlate each NMR frequency with the nuclear spin of each amino acid in the primary sequence. Then, the secondary structures are determined by performing the secondary shift analysis [4, 5]. Alternatively, using the backbone torsion angles predicted from the chemical shifts with software like TALOS+[6], the secondary structure can be determined with the aid of Ramachandran plots. Then, one of the most important steps is to obtain structural or distance restraints, both intra- and inter-molecular via dipolar-based correlation experiments. Finally, the information is then used for the calculations of protein structure with programmes that search for the minimal target functions. Some examples of the programmes are Xplor-NIH [7], which is based on Monte Carlo methods and conventional gradient-based minimization, and simulated-annealing based CYANA [8]. Some successful examples of biological molecules studied using solid-state NMR include the HET-s, amyloid  $\beta$ -peptide ( $A\beta$ ) fibrils, human islet amyloid polypeptide (hIAPP), and membrane protein CXCR1 [9–12].

## 1.2 Basic NMR Theory

In principle, both classical and quantum mechanics are used to describe the spin dynamics and certain phenomena in NMR. The approaches of both theories are not the same, and there are some advantages and disadvantages for each of them. Quantum mechanics are exact and precise, but the theory can be cumbersome and the discussion is usually limited to small spin systems. The classical theory can be used to treat larger spin systems, but it is usually phenomenological and not exact. For instance, quantum mechanics can be used to explain the NMR spectra in the strong coupling limit but is limited for describing spin diffusion [13] in a large spin system due to the size of the memory of a computer. While the spin temperature approach in thermodynamics and rate (differential) equations are classical theories that can be used to explain the spin-diffusion process but are unable to explain the echo phenomenon [14]. Hence, different theoretical approaches are taken, depending on the nature of the context. A brief introduction to the quantum mechanical approach will be given here as it is an important tool in designing recoupling or decoupling sequences. This includes density operator, time-dependent and time-independent Hamiltonian, spin-interaction Hamiltonians etc.

### Density Operator

In the quantum-mechanical description of NMR, the state of a spin system can be described by using the density operator formalism. This is because a spin ensemble is usually considered in NMR rather than an individual spin. Therefore, the density operator formalism provides a good statistical description to the weakly interacting identical spin packets. The formal definition of a density operator is given by

$$\hat{\rho} = |\psi\rangle\langle\psi| = \sum_{i,j} c_i c_j^* |\phi_i\rangle\langle\phi_j| \quad (1.1)$$

with the expectation value of a particular operation  $\hat{A}$  over the spin ensemble formulated as

$$\begin{aligned} \langle\hat{A}\rangle &= \sum_{i,j} c_i c_j^* \langle\phi_j|\hat{A}|\phi_i\rangle \\ &= \sum_{i,j} c_i c_j^* \langle\phi_i|\hat{\rho}|\phi_j\rangle\langle\phi_j|\hat{A}|\phi_i\rangle \\ &= \sum_{i,j} c_i c_j^* \langle\phi_i|\hat{\rho}\hat{A}|\phi_i\rangle \\ &= \text{tr}\{\hat{\rho}\hat{A}\} \end{aligned} \quad (1.2)$$

### Signal Intensity and Equilibrium Density Operator

The amount of signal intensity or sensitivity of an NMR experiment can be described by the equilibrium density operator  $\hat{\sigma}_0$  of a spin ensemble. When a sample is in thermal equilibrium with the environment, the occupancy probability for the energy eigenstates in  $\hat{\sigma}_0$  is determined by the Boltzmann's distribution:

$$\hat{\sigma}_0 = \frac{\exp(-\hbar\hat{\mathcal{H}}_z/k_B T)}{\text{Tr}\{\exp(-\hbar\hat{\mathcal{H}}_z/k_B T)\}} \quad (1.3)$$

$$\approx \frac{\hat{1}}{\text{Tr}\{\hat{1}\}} - \frac{-\hbar\hat{\mathcal{H}}_z}{k_B T \text{Tr}\{\hat{1}\}} \quad (1.4)$$

$$\text{where } \hat{\mathcal{H}}_z = -\gamma\hat{I}_z B_0 \quad (1.5)$$

where the high temperature approximation ( $\hbar\gamma B_0 \ll k_B T$ ) is made to simplify Eq. (1.3). Note that the denominator in Eq. (1.3) is just a normalization factor in statistical thermodynamics. The amount of NMR signal can be calculated by taking the population difference between the spin-up  $|\alpha\rangle$  ( $(\hat{\sigma}_0)_{11}$ ) and the spin-down  $|\beta\rangle$  ( $(\hat{\sigma}_0)_{22}$ ) states. It can be calculated using Eq. (1.6) that only  $6 \times 10^{-5}$  of the spin ensemble contributes<sup>1</sup> to the NMR signal for proton at temperature  $T = 303$  K in a 18.8 T magnet.

$$(\hat{\sigma}_0)_{11} - (\hat{\sigma}_0)_{22} = \hbar\gamma B_0 / k_B T \quad (1.6)$$

### Time Evolution of the Density Operator

If the density operator commutes with the Hamiltonian  $\hat{\mathcal{H}}$ , the density operator remains stationary and it does not evolve with time. Conversely, the density operator evolves into other states if they do not commute. The master equation that dictates the dynamics of the density operator is given by the Liouville-von Neumann equation<sup>2</sup> (Eq. (1.7)):

$$\frac{d}{dt}\hat{\rho} = -i[\hat{\mathcal{H}}, \hat{\rho}(t)] \quad (1.7)$$

which has a simple analytical solution if the Hamiltonian  $\hat{\mathcal{H}}$  is time-independent:

$$\hat{\rho}(t) = e^{-i\hat{\mathcal{H}}t}\hat{\rho}(0)e^{i\hat{\mathcal{H}}t} \quad (1.8)$$

<sup>1</sup>One can see that NMR is actually an insensitive technique.

<sup>2</sup>Note that  $\hbar$  is omitted because the Hamiltonian  $\hat{\mathcal{H}}$  is always expressed in angular frequency.

The quest of solving the Liouville-von Neumann equation is actually the same as solving the Schrödinger equation [15]. Moreover, note that the identity operator  $\hat{I}$  in Eq. (1.5) is often neglected as it is scalar (a rank-zero tensor) and does not evolve under any Hamiltonian, leading to a traceless density operator. It is only important to consider the full density operator in cases when the polarization is high or special circumstances in relaxation theory.

### Single Particle and Spin Ensemble

One has to bear in mind that the physics of a single-particle system is different from that of a spin ensemble. The confusion arises because of the adoption of simple matrix representation like Pauli or equivalent representation for operator  $\hat{S}_x$ ,  $\hat{S}_y$ , or  $\hat{S}_z$  in describing the spin system in both scenarios. In principle, for a many-body system, one would have to adopt a rank- $n$  spin tensor or a  $2^n$ -th dimensional matrix representation. This is however cumbersome and unnecessary as the individual spin packets are identical and assumed to be non-interacting with other spin packets, i.e. the off-diagonal elements in the giant matrix representation are zero. Hence, it is possible to block diagonalize the giant matrix and sufficient to use the simple Pauli matrices along with density operator to describe the entire spin ensemble. Another confusion among students learning NMR theory is that it was known that the act of measurement causes the spin state to collapse to the eigenstate of the measurement operator, i.e. the FID can not be recorded continuously, and quadrature detection is not possible. The flaw lies in the fact that the previous statement is only applicable to the case of single particle, while we are dealing with a spin ensemble in NMR.

## 1.3 Hamiltonians in Solid-State NMR

It is common in solid-state NMR that the Hamiltonians  $\hat{\mathcal{H}}$  (Eq. (1.9)) that characterize the interactions are described by using spherical tensor notation. The space part  $A_\ell^{(i)}$  contains the information of interaction strength and its orientation dependence, whereas the spin part  $\hat{J}$  comprises the quantum mechanical part of the Hamiltonian  $\hat{\mathcal{H}}$ . This notation has the advantage that each tensor is manipulated independently, i.e. the spatial and spin parts are modulated by the physical rotation (MAS) and rf irradiation respectively.

$$\begin{aligned}
\mathcal{H} &= \sum_i \sum_{\ell=0}^2 \vec{A}_\ell^{(i)} \cdot \hat{\mathcal{J}}_\ell^{(i)} \\
&= \sum_i \sum_{\ell=0}^2 \sum_{q=-\ell}^{\ell} (-1)^q A_{\ell,q}^{(i)} \cdot \hat{\mathcal{J}}_{\ell,-q}^{(i)}
\end{aligned} \tag{1.9}$$

where the sum iterates over all interactions with index  $i$  and rank  $\ell$  with sub components  $q$ . Note that the sum of the rank components ( $q$  and  $-q$ ) is 0 since the Hamiltonian is a scalar quantity, and thus invariant with respect to frame transformation. A list of spherical spin tensors can be found in A.1.1. Only Hamiltonians that are relevant in solid-state NMR will be discussed in this section, that includes the Zeeman Hamiltonian, chemical-shift interaction, dipolar coupling,  $J$  coupling, and rf Hamiltonians. Other interactions that might be important in other context of solid-state NMR include quadrupolar coupling for spin  $I \geq 1$ , hyperfine coupling or pseudo-contact shift if unpaired electrons are present.

### 1.3.1 Zeeman Hamiltonian

When an NMR-active nuclei is subjected to an external magnetic field  $B_0$ , it precesses either clockwise or anti-clockwise with respect to the field depending on the sign of the gyromagnetic ratio, to attain the most stable configuration. The potential energy of such configuration is given by the Zeeman Hamiltonian. The Zeeman Hamiltonian is the most important interaction in NMR as it accounts for the sensitivity of the experiment and responsible for the precession of the nuclear spins, i.e. the FID. The Zeeman Hamiltonian under a magnetic field of  $\vec{B}_0 = B_0 \hat{z}$  is defined as

$$\hat{\mathcal{H}}_z^{(k)} = -\gamma_k \vec{B}_0 \cdot \vec{I}_k = \omega_0^{(k)} \hat{I}_{kz} \tag{1.10}$$

where  $\gamma_k$  is the gyromagnetic ratio of spin  $k$ , and  $\omega_0$  is known as the Larmor frequency. A classical analogy of the Zeeman Hamiltonian can be appreciated by considering a magnetic moment  $\mu$  subjected to an external magnetic field  $B_0$ . The magnetic moment experiences a torque, which then aligns itself so that the potential energy  $E = -\mu \cdot B_0$  is minimum. In quantum mechanics, the magnetic moment can be expressed as  $\vec{\mu} = \gamma \vec{I}$ . Once the Zeeman Hamiltonian is known for a spin system, one can determine the eigenstates and calculate the energy difference between the eigenstates, which is proportional to the amount of signal according to Boltzmann theorem if the high-field approximation is valid.

### 1.3.2 Chemical-Shift Hamiltonian

In practical NMR experiments, a bare nucleus is never measured. The nucleus is surrounded by electrons that circulate around the nucleus, giving rise to a local induced  $\vec{B}_{\text{ind}}$  field at the nucleus in addition to the external  $\vec{B}_0$  field. Classically, this can be inferred from the Ampère's or Biot-Savart law, which states that moving charges induce a magnetic field. The orientation and magnitude of this local  $\vec{B}_{\text{ind}}$  field depend on the electronic charge distribution and this distribution can be non-uniform. The energy is given by  $E = -\vec{\mu} \cdot \vec{B}_{\text{ind}}$  with  $\vec{\mu} = \gamma \vec{I}$ . In addition, the induced field  $\vec{B}_{\text{ind}} = \chi \vec{B}_0$  is approximately proportional to the  $\vec{B}_0$  field with the magnetic susceptibility  $\chi$ . The quantum mechanics counterpart of magnetic susceptibility is given by the chemical-shift tensor  $\sigma^{(k)}$ , which is used to construct the chemical-shift Hamiltonian as follows:

$$\begin{aligned} \hat{\mathcal{H}}_{\text{cs}}^{(k)} &= -\gamma_k \vec{B}_{\text{ind}}^{(k)} \cdot \vec{I}_k \\ &= -\gamma_k \cdot \sigma^{(k)} \vec{B}_0 \cdot \vec{I}_k \\ &\approx \sigma_{\text{zz}}^{(k)} \omega_0^{(k)} \hat{I}_{kz} \end{aligned} \quad (1.11)$$

where only the  $\mathbf{z}$  component is considered in the last step due to the high-field approximation in the Zeeman rotating frame. The matrix elements in  $\sigma^{(k)}$  are typically in the order of  $10^{-4}$  to  $10^{-6}$  for non-ferromagnetic substances, and expressed in terms of ppm (parts per million). The tensor  $\sigma^{(k)}(\alpha, \beta, \gamma)$  can be in general anisotropic or orientation-dependent. This results in a broad CSA spectrum with a heterogeneous line width that scales linearly with the magnetic field  $B_0$  for a static powdered sample (Fig. 1.1). A narrow spectrum can be recovered by performing MAS (Sec. 1.4), which averages out the anisotropic interaction.

The chemical-shift tensor  $\sigma$  can be expressed in the Cartesian coordinate system as  $\sigma_{\text{xx}}$ ,  $\sigma_{\text{yy}}$ , and  $\sigma_{\text{zz}}$  in the principal-axis frame, where all off-diagonal elements vanish. Alternatively, they can also be rewritten in the form of isotropic  $\sigma_{\text{iso}}$ , anisotropic  $\delta$ , and asymmetry  $\eta$  components (Eq. (1.12)). This representation is chosen because the description is more compact and convenient for the spherical coordinate system.

$$\begin{aligned} \text{Isotropy} \quad \sigma_{\text{iso}} &= \frac{\sigma_{\text{xx}} + \sigma_{\text{yy}} + \sigma_{\text{zz}}}{3} \\ \text{Anisotropy} \quad \delta &= \sigma_{\text{zz}} - \sigma_{\text{iso}} \\ \text{Asymmetry} \quad \eta &= \frac{\sigma_{\text{yy}} - \sigma_{\text{xx}}}{\delta} \end{aligned} \quad (1.12)$$

Note that different conventions are adopted in literature, and we use the convention [16] that  $|\sigma_{\text{zz}} - \sigma_{\text{iso}}| \geq |\sigma_{\text{xx}} - \sigma_{\text{iso}}| \geq |\sigma_{\text{yy}} - \sigma_{\text{iso}}|$ , so that  $\eta$  is always positive and smaller than 1

while  $\delta$  can be either positive or negative.

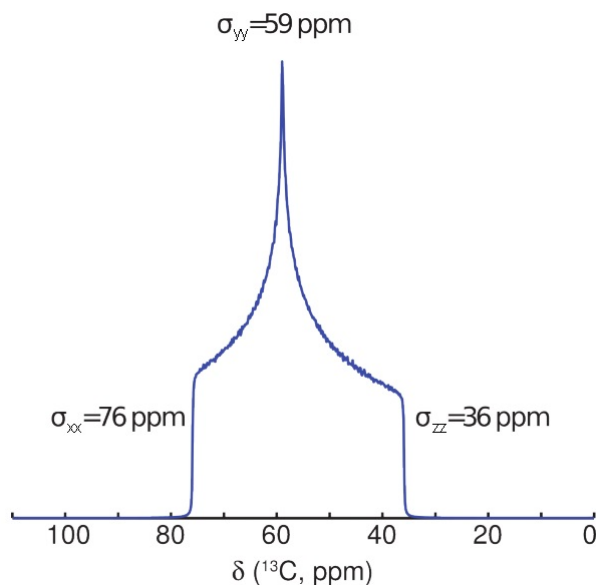


**Figure 1.1** Simulated CSA powder spectrum of a  $^{13}\text{C}$  resonance under static condition. Figure taken from *Ernst et al.* [17].

### 1.3.3 Dipolar-Coupling Hamiltonian

The dipole-dipole interaction is an interaction in which one spin experiences an additional local field (apart from the external  $B_0$  field) of a nearby spin or a magnetic dipole. The interaction between two spins is analogous to the situation in which two magnets are brought close to each other and they could either attract or repel depending on the orientations. The interaction is important in NMR spectroscopy because the interaction strength depends on the distance, i.e.  $\propto r_{kn}^{-3}$  (Eq. (1.19)). Hence, it is often used to extract structural information. This is manifested directly in the dipolar recoupling experiments like REDOR [18] in solid-state NMR and nuclear Overhauser effect (NOE) [19] in solution-state NMR.

A brief derivation of the dipolar-coupling Hamiltonian will be shown here. In classical physics, the magnetic dipole energy can be derived by considering the scalar potential  $\phi^3$  (Eq. (1.13)) of a magnetic dipole at a distance  $r$  that is sufficiently far away and seeing the dipole as a point source:

$$\phi = \frac{\vec{\mu} \cdot \vec{r}}{4\pi|\vec{r}|^3} \quad (1.13)$$

<sup>3</sup>This expression is analogous to the electric potential of an electric dipole, i.e.  $\phi^{(E)} = \frac{\vec{p} \cdot \vec{r}}{\epsilon_0 4\pi|\vec{r}|^3}$  where  $\vec{p} = q\vec{d}$  is the electric dipole moment and  $\epsilon_0$  is the permittivity of free space.

where  $\vec{\mu}$  is the dipole moment, and the local  $\vec{B}_1$  field due to dipole 1 (Fig. 1.2a) is given by

$$\begin{aligned}\vec{B}_1 &= -\mu_0 \nabla \phi \\ &= \frac{\mu_0}{4\pi} \left( \frac{3\vec{r}(\vec{\mu}_1 \cdot \vec{r})}{|\vec{r}|^5} - \frac{\vec{\mu}_1}{|\vec{r}|^3} \right)\end{aligned}\quad (1.14)$$

and the magnetic potential energy (Sec. 1.3.1) of a magnetic moment  $\mu_k$  is given by  $E = -\mu_k \cdot B$ . So, the magnetic potential energy<sup>4</sup>  $E_{21}$  of spin 2 due to presence of the local  $\vec{B}_1$  field by dipole 1 is given by

$$\begin{aligned}E_{21} &= \vec{\mu}_2 \cdot \vec{B}_1 \\ &= \frac{\mu_0}{4\pi} \left( \frac{3(\vec{\mu}_2 \cdot \vec{r})(\vec{\mu}_1 \cdot \vec{r})}{|\vec{r}|^5} - \frac{\vec{\mu}_2 \cdot \vec{\mu}_1}{|\vec{r}|^3} \right).\end{aligned}\quad (1.15)$$

Then, the dipolar-coupling Hamiltonian can be constructed by promoting the magnetic moment to the operator form  $\vec{\mu} = \gamma \vec{I}$  and one obtains

$$\hat{\mathcal{H}}_D^{(k,n)} = -\frac{\mu_0}{4\pi} \frac{\gamma_k \gamma_n \hbar}{r_{kn}^3} \left( \frac{3(\vec{I}_k \cdot \vec{r}_{kn}) \cdot (\vec{I}_n \cdot \vec{r}_{kn})}{r_{kn}^2} - (\vec{I}_k \cdot \vec{I}_n) \right) \quad (1.16)$$

$$= \vec{I}_k \mathbf{D}^{(k,n)} \vec{I}_n \quad (1.17)$$

where  $\mathbf{D}$  is the symmetric and traceless dipolar tensor with a matrix form of

$$\mathbf{D}^{(k,n)} = -2 \frac{\mu_0}{4\pi} \frac{\gamma_k \gamma_n \hbar}{r_{kn}^3} \begin{pmatrix} -1/2 & 0 & 0 \\ 0 & -1/2 & 0 \\ 0 & 0 & -1 \end{pmatrix} \quad (1.18)$$

in the principal-axis system. The general dipolar Hamiltonian defined in Eq. (1.17) can be further simplified in the case of high-field approximation, i.e. retaining only secular terms with the following forms depending on whether the coupled spin pair is homonuclear or heteronuclear.

$$\hat{\mathcal{H}}_D^{(k,n)} = \begin{cases} -\frac{\mu_0}{4\pi} \frac{\gamma_k \gamma_n \hbar}{r_{kn}^3} \frac{3 \cos^2 \theta - 1}{2} \left( 3 \hat{I}_{kz} \hat{I}_{nz} - \vec{I}_k \cdot \vec{I}_n \right) & \text{for homonuclear} \\ -\frac{\mu_0}{4\pi} \frac{\gamma_k \gamma_n \hbar}{r_{kn}^3} \frac{3 \cos^2 \theta - 1}{2} 2 \hat{I}_{kz} \hat{I}_{nz} & \text{for heteronuclear,} \end{cases} \quad (1.19)$$

where  $\theta$  is the angle between the static  $B_0$  field and the internuclear vector  $\vec{r}_{kn}$  (Fig. 1.2).

---

<sup>4</sup>Note that  $E_{12} = E_{21}$ .



There exists a particular alignment that when  $\theta = 54.7^\circ$ , the local field is perpendicular or has zero contribution along the  $B_0$  field. This special alignment ( $\theta = 54.7^\circ$ ) is called the magic angle. This is an important feature for the MAS experiment (Sec. 1.4). Note that the transverse term vanishes in the heteronuclear spin system (Eq. (1.19)) because the size of the dipolar coupling is smaller than the difference in Larmor frequencies.

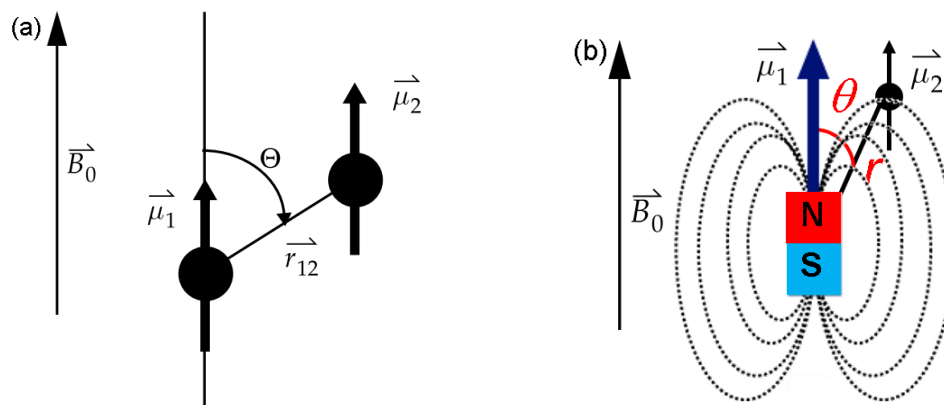


**Figure 1.2** Schematic drawing of the dipolar interaction between two magnetic dipoles. Figure taken from *Ernst et al.* [17].

### 1.3.4 Scalar $J$ -Coupling Hamiltonian

The spins can interact through space directly via dipolar coupling, or indirectly via the shared electrons in a chemical bond, known as  $J$  coupling. The strength of the coupling depends on the probability of finding electrons at the position of the nucleus ( $r = 0$ ), also called Fermi-contact interaction<sup>5</sup>. Hence, experiments employing  $J$  coupling are also known as through-bond experiments. The Hamiltonian for the scalar  $J$ -coupling is given by

$$\hat{\mathcal{H}}_J^{(k,n)} = \vec{\hat{I}}_k \mathbf{J}^{(k,n)} \vec{\hat{I}}_n \quad (1.20)$$

where the  $\mathbf{J}$  tensor is comprised of an isotropic component and an anisotropic component. Most literature considers only the isotropic component because the spin form of the anisotropic part is identical to that of a dipolar-coupling tensor and they are indistinguishable. For light nuclei considered in this thesis, the coupling is isotropic in nature, and, therefore, remains unaffected by the fast tumbling motions in solution-state NMR. Similar to the dipolar interaction, only the secular terms from the general equation (Eq. (1.20)) are retained under the high-field approximation.

$$\hat{\mathcal{H}}_J^{(k,n)} = \begin{cases} 2\pi J_{\text{iso}}^{(k,n)} \vec{\hat{I}}_k \cdot \vec{\hat{I}}_n & \text{for homonuclear,} \\ 2\pi J_{\text{iso}}^{(k,n)} \hat{I}_{kz} \cdot \hat{S}_{nz} & \text{for heteronuclear.} \end{cases} \quad (1.21)$$

<sup>5</sup>It also contributes to the hyperfine interaction in EPR.

### 1.3.5 The RF Hamiltonian

In principle, the spin magnetization can be manipulated by using rf pulses with a frequency that is matched to the Larmor frequency, regardless of the amplitude of the magnetic  $B_1$  component. This is an important aspect of NMR because it allows small-amplitude (in the mT range) pulses to be employed under the presence of large static  $B_0$  (several T) field. Obviously, it is easier to manipulate the spins by switching the small  $B_1$  rather than the large  $B_0$  field. In modern hardware design of spectrometers and NMR probes, a single-coil configuration is used to generate a linearly polarized electromagnetic wave instead of a circularly polarized EM wave (two orthogonal coils would be needed). Consequently, half of the amplitude in the counter-rotating component with respect to the Larmor precession is wasted. So, the full laboratory Hamiltonian for linearly-polarized time-dependent electromagnetic waves irradiating in the  $\hat{x}$  direction is given by

$$\begin{aligned}\hat{\mathcal{H}}_{\text{lab}}(t) &= \hat{\mathcal{H}}_{\text{rf}}(t) + \hat{\mathcal{H}}_z \\ &= 2\omega_1 \cos(\omega_{\text{rf}}t)\hat{I}_x + \omega_0\hat{I}_z\end{aligned}\quad (1.22)$$

and after the interaction-frame transformation with respect to the Zeeman Hamiltonian

$$\begin{aligned}\hat{\mathcal{H}}_{\text{rot}}(t) &= e^{-i\omega_{\text{rf}}\hat{I}_z} \hat{\mathcal{H}}_{\text{lab}} e^{i\omega_{\text{rf}}\hat{I}_z} - \omega_{\text{rf}}\hat{I}_z \\ &= (\omega_0 - \omega_{\text{rf}})\hat{I}_z + \omega_1\hat{I}_x + \omega_1 \cos[(\omega_0 + \omega_{\text{rf}})t]\hat{I}_x + \omega_1 \sin[(\omega_0 + \omega_{\text{rf}})t]\hat{I}_y \\ &\approx \omega_1\hat{I}_x \quad \text{if } \omega_{\text{rf}} = \omega_0 \gg \omega_1.\end{aligned}\quad (1.23)$$

where the first term in Eq. (1.23) vanishes if the frequency is matched perfectly disregarding offset, i.e.  $\omega_{\text{rf}} = \omega_0$ . Consequently, the large dominant Zeeman term is now removed in the rf rotating frame. Moreover, the last two terms, which are time-dependent, are neglected since they are oscillating with twice the Larmor frequency and the averaged value (0 for the cos and sin functions) is taken in this frame. Nevertheless, the fast oscillating components can give rise to the Bloch-Siegert shift [20] if the rf carrier frequency is closed to the observed resonances, i.e. the magnitude scales inversely proportional to the resonance offset.

### Rabi Oscillation and Nutations

The spin states can change from one eigenstate to another as long as the frequency  $\nu$  is matched, i.e. the difference in energy eigenvalues given by  $E = h\nu$  is satisfied, regardless of the intensity (amplitude) of the electromagnetic wave. This effect is exemplified in the case of the excitation of NMR resonances, which can take place if the carrier frequency of the rf pulse matches the Larmor frequency, regardless of the rf amplitude. Nevertheless, the amplitude of the electromagnetic wave affects the rate of transition between the two eigenstates, and hence the name Rabi or nutation frequency with a unit of Hz is used to describe the amplitude. A precise mathematical treatment of this situation is known as Rabi oscillation. An alternate view of this scenario is that when the amplitude of the wave increases, so does the number of photon absorbed per unit time. So, spin-up and spin-down states are exchanging more rapidly and hence resulted in shorter Rabi cycle, or similarly shorter excitation/inversion pulse in NMR.

## 1.4 Magic Angle Spinning

Although the anisotropic interactions provide rich information about the spin environment of the nuclei, they also render broad line width of the resonances. Hence, magic-angle spinning setups are routinely used in standard solid-state NMR experiments to obtain high-resolution spectra [21, 22]. The basic principle of MAS can be understood by first considering how the spatial part of the Hamiltonians (Eq. (1.9)) becomes time-dependent in the laboratory frame during physical rotations, which can be treated using Euler angles and Wigner rotations.

### 1.4.1 Euler Angles and Wigner Rotations

The rotation matrices along the principal axes  $x, y$ , and  $z$  in a Cartesian coordinate system is given by  $R_{x,y,z}$  (Eq. (1.24)). However, a general rotation  $R$  around an arbitrary axis can not be represented by using these simple matrices directly. A tilted-frame transformation has to be used here.

$$R_x = \begin{bmatrix} 1 & 0 & 0 \\ 0 & \cos \theta & -\sin \theta \\ 0 & \sin \theta & \cos \theta \end{bmatrix} \quad R_y = \begin{bmatrix} \cos \theta & 0 & \sin \theta \\ 0 & 1 & 0 \\ -\sin \theta & 0 & \cos \theta \end{bmatrix} \quad R_z = \begin{bmatrix} \cos \theta & -\sin \theta & 0 \\ \sin \theta & \cos \theta & 0 \\ 0 & 0 & 1 \end{bmatrix} \quad (1.24)$$

In the tilted-frame transformation, the effective axis of rotation is aligned along the principal axes in the new frame. Then, the net rotation matrix  $\mathbf{R}(\alpha, \beta, \gamma)$  can be constructed from three successive rotations, i.e.

$$\mathcal{T}_{x',y',z'} = \mathbf{R}(\alpha, \beta, \gamma) \mathcal{T}_{x,y,z} \quad (1.25)$$

$$\text{where } \mathbf{R}(\alpha, \beta, \gamma) = R_{z''}(\gamma)R_{y'}(\beta)R_z(\alpha). \quad (1.26)$$

This is the basis of Euler rotations and note that the solution is not unique and we adapt the convention that the first rotation is  $\alpha$  around  $z$  axis, followed by  $\beta$  around the new  $y'$  axis, and finally  $\gamma$  around the new  $z''$  axis (Fig. 1.3).

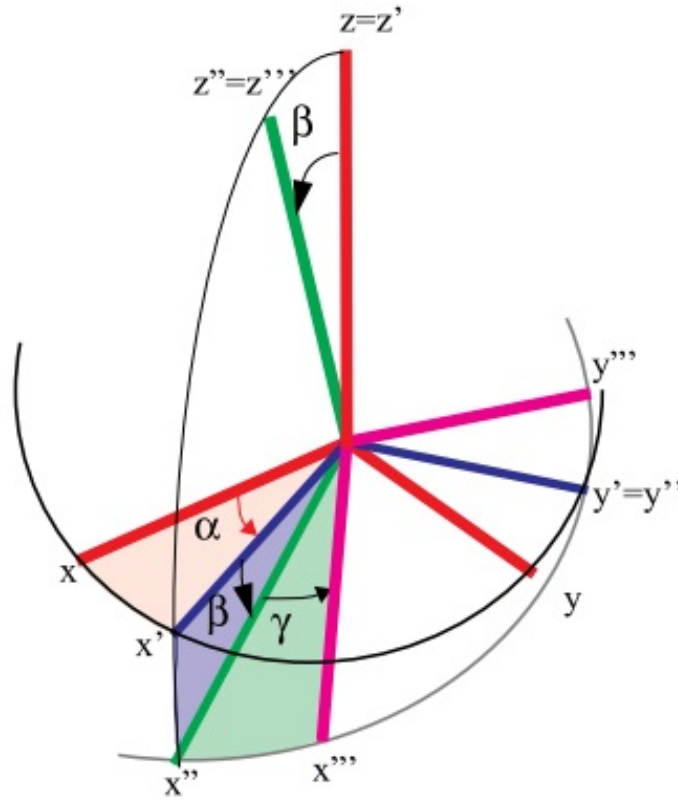


**Figure 1.3** Graphical representation of the Euler rotation matrix  $R_{z''}(\gamma)R_{y'}(\beta)R_z(\alpha)$  (Eq. (1.26)). Figure taken from *Ernst et al.* [17].

Alternatively, the rotations can also be treated according to the symmetries of the spherical-tensor components:

$$\mathcal{T}_{lm}^{(\text{new})} = \sum_{m'=-l}^{+l} \mathcal{D}_{m',m}^l(\alpha, \beta, \gamma) \mathcal{T}_{lm'}^{(\text{old})} \quad (1.27)$$

$$= \sum_{m'=-l}^{+l} e^{-i\alpha m'} d_{m',m}^l(\beta) e^{-i\gamma m} \mathcal{T}_{lm'}^{(\text{old})} \quad (1.28)$$

and for the inverse-frame transformation:

$$\mathcal{F}_{\ell m'}^{(\text{old})} = \sum_{m=-\ell}^{+\ell} \mathcal{D}_{m,m'}^{\ell}(-\gamma, -\beta, -\alpha) \mathcal{F}_{\ell m}^{(\text{new})} \quad (1.29)$$

where  $d_{m'm}^{\ell}$  is known as the reduced Wigner matrix elements, and the expression is defined explicitly in A.1.3.

## 1.4.2 Averaging of Anisotropic Interaction by MAS

In order to analyze the effect of MAS on the Hamiltonian, especially the anisotropic interactions, one must first perform the frame transformation of the interaction into the lab frame, using the Wigner rotations:

$$A_{\ell m''}^{(\text{lab})} = \sum_{m'=-\ell}^{+\ell} \mathcal{D}_{m',m''}^{\ell}(-\omega_{\text{r}}t, -\theta_{\text{r}}, 0) \sum_{m=-\ell}^{+\ell} \mathcal{D}_{m,m'}^{\ell}(\alpha, \beta, \gamma) \rho_{\ell m}^{(\text{PAS})} \quad (1.30)$$

$$= \sum_{m'=-\ell}^{+\ell} \mathcal{D}_{m',m''}^{\ell}(-\omega_{\text{r}}t, -\theta_{\text{r}}, 0) A_{\ell m'}^{(\text{rot})} \quad (1.31)$$

where  $\omega_{\text{r}}$  is the MAS frequency. In principle, one can assign  $m'' = 0$  if the high-field approximation (see Eq. (1.9)) is taken to obtain

$$A_{\ell 0}^{(\text{lab})} = \sum_{m'=-\ell}^{+\ell} e^{-im'\omega_{\text{r}}t} d_{m',0}^{\ell}(-\theta_{\text{r}}) A_{\ell m'}^{(\text{rot})}. \quad (1.32)$$

It can be inferred from the exponential term in Eq. (1.32) that the  $m' = \pm 1, \pm 2$  terms vanish if the FID is sampled at multiples of the rotor period<sup>6</sup>. Note that the time-independent component ( $m' = 0$ ) is scaled by  $d_{00}^2 = \frac{3\cos^2\theta_{\text{m}}-1}{2}$ , which will be 0 if the following condition is satisfied:

$$\theta_{\text{m}} = \cos^{-1}(1/\sqrt{3}) \approx 54.7^{\circ}. \quad (1.33)$$

The angle  $\theta_{\text{m}}$  is known as the magic angle. A more detailed analysis of the effect of MAS in the solid-state NMR is presented in Sec. 2.3.

---

<sup>6</sup>Failure to perform rotor-synchronized sampling will lead to spinning sidebands for slow MAS frequency if the MAS frequency is smaller than the size of the interaction.

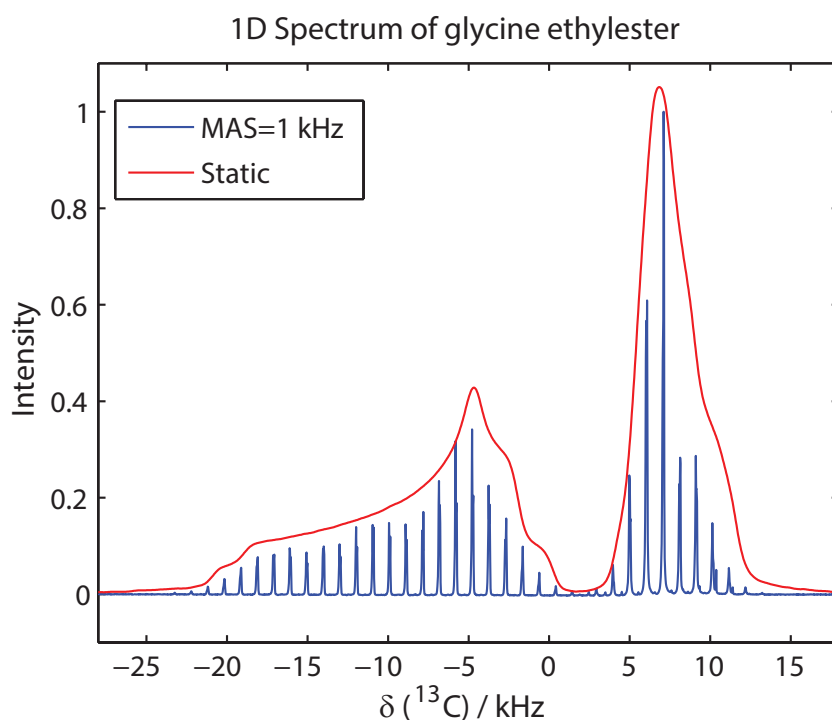


**Figure 1.4** Static (red) and MAS at  $\nu_r = 1$  kHz (blue) spectra of  $^{13}\text{C}$ -glycine ethylester measured in a 500 MHz magnet. The two spectra are normalized such that the maximum intensities are the same.

### 1.4.3 Static Powder Spectra and Spinning Sidebands

Powdered samples are often investigated in solid-state NMR as high-quality single crystals are not always obtainable, especially for insoluble biological molecules like fibrils and membrane proteins. Hence, in a powdered spectrum, the random orientations of microcrystallites have resulted in a superposition of spectra with resonances at different frequencies. Figure 1.4 shows the static powdered spectrum (red) of glycine ethylester where the resonances are broadened by CSA and dipolar couplings. The carbonyl resonance is broader as the anisotropy  $\delta_{\text{CSA}}$  is larger than that of  $\text{C}\alpha$ . The same sample measured under MAS condition is shown as an overlay (blue). A higher-resolution spectrum with spinning sidebands separated by  $\nu_r = 1$  kHz is observed. The CSA sidebands occur because all crystallites return to the original position after every rotor period, i.e. the evolution due to the CSA component is refocused. Thus, the net FID appears like a signal convolved with a Shah function. According to the convolution theorem, the resulting spectrum appears like a static spectrum multiplied by a frequency comb function separated by  $\nu_r = 1$  kHz. In principle, a higher MAS frequency would result in weaker spinning sidebands, thereby increasing the signal to noise ratio of the central peak. Note that there is some loss in the signal intensity during MAS condition because the sidebands of individual crystallites do not have the same phase [23]. All sidebands are "in phase" only in the case of a powdered spectrum.

## 1.5 Adiabatic Experiment

If an effective Hamiltonian contains an orientation-dependent spin interaction, spin packets from each crystallite will evolve at different rates, and the same final spin state can not be reached by all crystallites simultaneously. This effect accounts for the fact that the theoretical maximum amount of polarization transfer in recoupling experiment like CP is only  $\sim 73\%$  [24, 25]. In principle, a theoretical maximum of approaching  $\sim 100\%$  can be achieved using adiabatic experiments, where spin states are changing quasistatically along the slowly changing effective Hamiltonian, and end up in an eigenstate of the final Hamiltonian. Hence, most crystallites will reach the same final state simultaneously and obtain near  $\sim 100\%$  transfer efficiency. This is in contrast to the diabatic/sudden experiment in which the effective Hamiltonian remains time-independent, and the eigenstates are evolving within the defined subspace. An example of an adiabatic experiment is the design of an inversion pulse to rotate the spin state from  $\hat{I}_z$  to  $-\hat{I}_z$  (Fig. 1.5). Let us consider a time-dependent Hamiltonian  $\hat{\mathcal{H}}(t)$  with an offset  $\chi(t)$  and rf field  $|d_{\text{eff}}|$ :

$$\hat{\mathcal{H}}(t) = \chi(t)\hat{I}_z + |d_{\text{eff}}|\hat{I}_x \quad (1.34)$$

where the time-dependent Hamiltonian  $\hat{\mathcal{H}}(t)$  should be varied while fulfilling the following conditions:

$$\hat{\mathcal{H}}(0) = \chi_i\hat{I}_z \quad (1.35)$$

$$\hat{\mathcal{H}}(T/2) = |d_{\text{eff}}|\hat{I}_x \quad (1.36)$$

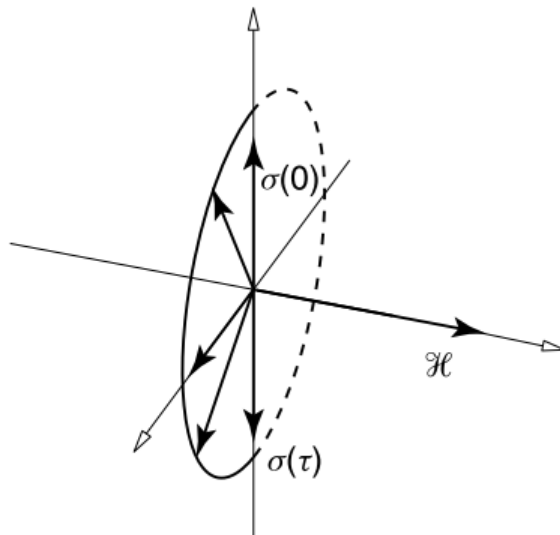
$$\hat{\mathcal{H}}(T) = \chi_f\hat{I}_z \quad (1.37)$$

to ensure that the density operator  $\sigma(T)$  is along the same direction as defined by  $\hat{\mathcal{H}}(T)$ . In general,  $\hat{\mathcal{H}}(t)$  can be varied using different mathematical expressions, but it is important that the adiabaticity  $a(t)$  has to be at least 5 so that the experiment remains adiabatic (Eq. (1.38)). In general, a truly adiabatic experiment would require infinitely long time, but this is unrealistic as it is limited by relaxation effects. A detailed description of the theory and applications of adiabatic experiments are discussed in literature [26, 27].

$$a(t) = \frac{\sqrt{\chi^2(t) + |d_{\text{eff}}|^2}}{|d\Theta(t)/dt|} \gg 1 \quad (1.38)$$

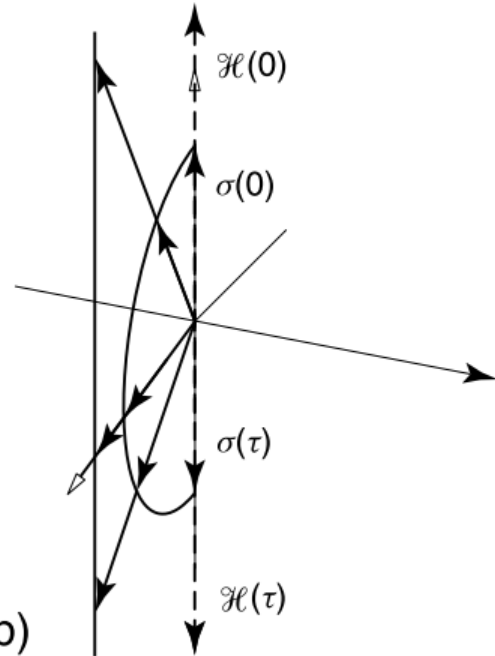
$$\text{where } \Theta(t) = \arctan(|d_{\text{eff}}|/\chi(t)) \quad (1.39)$$

“Sudden”:  
rotation of  $\sigma$  around  $\mathcal{H}$



(a)

“Adiabatic”:  
“dragging” of  $\sigma$  with  $\mathcal{H}$



(b)

**Figure 1.5** Rotation of density operator  $\sigma$  from  $\hat{I}_z$  to  $-\hat{I}_z$  under a (a) diabatic or (b) adiabatic experiment. Figure taken from *Ernst et al.* [17].

### Classical Thermodynamics and Quantum Adiabatic Theorem

Adiabatic conditions in classical thermodynamics refer to situation in which there is no heat  $Q$  gain or loss during the process, and it usually demands an infinitely slow process. Adiabatic experiment in quantum mechanics, however, has no direct relation with respect to heat exchange. Perhaps a closer analogy would have been the quasistatic process.

### Berry Phase

Berry phase is a geometrical phase acquired over the course of a cycle, when a system is subjected to an adiabatic process. The relevance of the Berry phase has been discussed in the literature [28, 29]. The implication is limited in the applications of NMR, as most adiabatic pulse sequences involve only an adiabatic half passage, i.e. are not cyclic in nature.



# Chapter 2

## Theory of Time-Dependent Hamiltonians

### 2.1 Introduction

In the static case, where the Hamiltonian  $\hat{\mathcal{H}}$  is time independent (Eq. (2.1)), the dynamics of the spin operator can be determined analytically. It is however non-trivial to treat the case when the Hamiltonians becomes time-dependent  $\hat{\mathcal{H}}(t)$ . This happens when the energy of a system is being perturbed continuously, i.e. by rf irradiation (Sec. 2.2) or physical spinning of the sample in the MAS experiment (Sec. 2.3).

$$\begin{aligned}\hat{\mathcal{H}} &= \sum_i \sum_{\ell=0}^2 \sum_{q=-\ell}^{\ell} (-1)^q A_{\ell,q}^{(i)} \cdot \hat{\mathcal{J}}_{\ell,-q}^{(i)} \\ \hat{\mathcal{H}}(t) &= \sum_i \sum_{\ell=0}^2 \sum_{q=-\ell}^{\ell} (-1)^q \underbrace{A_{\ell,q}^{(i)}(t)}_{\text{MAS}} \cdot \underbrace{\hat{\mathcal{J}}_{\ell,-q}^{(i)}(t)}_{\text{rf irradiation}}\end{aligned}\quad (2.1)$$

When the Hamiltonian changes with respect to time, the eigenvalues of the eigenfunctions change too. Moreover, the analytical solution (Eq. 1.8) to the evolution of density operator  $\hat{\rho}(t)$ , derived from the Liouville-von Neumann equation (Eq. 1.7), is applicable only if the Hamiltonian  $\hat{\mathcal{H}}$  does not have explicit time dependence. In this chapter the theoretical treatments to obtain the effective time-independent Hamiltonians during the energy perturbations will be discussed, thereby enabling the evolutions of the density operator to be determined. The quest of finding time-independent Hamiltonians is essentially similar to solving the time-independent Schrödinger equation. It is the main topic in this thesis, to determine the time-independent effective Hamiltonian that eventually governs the spin dynamics of the density operator. This is essential in designing pulse sequences, so that desired effective Hamiltonians that are robust to experimental uncertainties are obtained. Two

theoretical treatments will be discussed in this chapter, namely average Hamiltonian Theory (AHT) [30, 31] and Floquet theory [32–35].

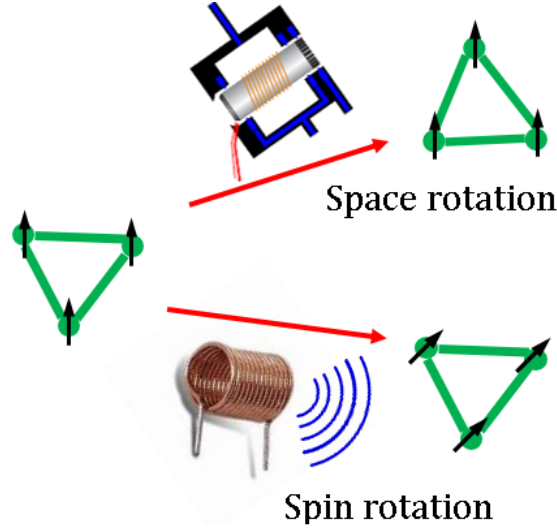


**Figure 2.1** Schematic diagram of the origin of time-dependent Hamiltonian  $\hat{\mathcal{H}}(t)$  due to physical rotations (MAS) and/or spin rotations (rf irradiation). Part of the figure is taken from *Ernst* [36].

## 2.2 Modulation of the Spin Tensors by RF Irradiations

### 2.2.1 Fourier Series of Time-Dependent Hamiltonians

If the perturbation to the Hamiltonian is periodic in nature (Eq. (2.3)), the time-dependent Hamiltonian can be expressed in a form of Fourier series (Eq. (2.2))

$$\hat{\mathcal{H}}(t) = \sum_{n=-\infty}^{\infty} \hat{\mathcal{H}}^{(n)} \cdot e^{in\omega_c t} \quad (2.2)$$

$$\text{for } \hat{\mathcal{H}}(t) = \hat{\mathcal{H}}(t + \tau_c) \quad (2.3)$$

where the cycle time  $\tau_c$  is given by  $2\pi/\omega_c$ ,  $\hat{\mathcal{H}}^{(n)}$  are the time-independent Fourier coefficients of the Hamiltonian and are not Hermitian, i.e.  $\hat{\mathcal{H}}^{(n)} \neq \hat{\mathcal{H}}^{(n)\dagger}$ , but satisfy

$$\hat{\mathcal{H}}^{(n)} = \hat{\mathcal{H}}^{(-n)\dagger} \quad (2.4)$$

so that the full Hamiltonian  $\hat{\mathcal{H}}(t)$  is Hermitian at all times  $t$ . In principle, the Hamiltonian can gain multiple time dependencies that are not necessarily commensurate, for instance

$$\hat{\mathcal{H}}(t) = \sum_{n=-\infty}^{\infty} \sum_{k=-\infty}^{\infty} \sum_{\ell=-\infty}^{\infty} \hat{\mathcal{H}}^{(n,k,\ell)} \cdot e^{in\omega_c t} \cdot e^{ik\omega_b t} \cdot e^{i\ell\omega_a t} \quad (2.5)$$

where  $\omega_a$ ,  $\omega_b$ , and  $\omega_c$  represent the characteristic frequencies with arbitrary values. In the context of this thesis, these frequencies are typically MAS frequency, modulation frequency of a multiple pulses sequence, and the effective nutation frequency (*vide infra*).

### 2.2.2 Interaction-Frame Representation

The dynamics of the spin density operator can be determined analytically if it is governed by a Hamiltonian  $\hat{\mathcal{H}}$  that commutes with itself at all times, i.e. all terms share a common set of eigenfunctions. It is a common situation in NMR that the terms in the Hamiltonian do not commute, e.g. rf irradiation that results in  $\hat{S}_x$  operator, which does not commute with the dominant Zeeman  $\hat{S}_z$  term. In this situation, one can either diagonalize the Hamiltonians by finding a new set of eigenstates, or perform an interaction-frame transformation to reduce the number of terms. It is non-trivial to diagonalize the Hamiltonians analytically and the corresponding solutions often have complicated expressions and hence yield less physical insights. Whereas interaction-frame transformation is easier to be computed and the solutions are often more intuitive, and hence this method is preferred. Firstly, the density operators in the lab  $\hat{\rho}(t)$  and rotating  $\hat{\rho}'(t)$  frame are given in Eq. (2.6).

$$\begin{aligned}\hat{\rho}'(t) &= \hat{U}_1^{-1}(t)\hat{\rho}(t)\hat{U}_1(t) \\ \hat{\rho}(t) &= \hat{U}_1(t)\hat{\rho}'(t)\hat{U}_1^{-1}(t)\end{aligned}\quad (2.6)$$

where  $\hat{U}_1$  symbolizes the propagator for the dominant Hamiltonian  $\hat{\mathcal{H}}_1$ .

$$\hat{U}_1(t) = \hat{T}\exp\left(-i\int_0^t dt_1 \hat{\mathcal{H}}_1(t_1)\right)\quad (2.7)$$

where  $\hat{T}$  is the Dyson time-ordering operator [37], which acts on the Hamiltonians in the following way

$$\hat{T}\{\hat{\mathcal{H}}(t_1)\hat{\mathcal{H}}(t_2)\} = \begin{cases} \hat{\mathcal{H}}(t_1)\hat{\mathcal{H}}(t_2) & \text{if } t_1 > t_2 \\ \hat{\mathcal{H}}(t_2)\hat{\mathcal{H}}(t_1) & \text{if } t_1 < t_2 \end{cases}\quad (2.8)$$

to ensure that the earlier Hamiltonian acts on the density operator before the later Hamiltonian, analogical to the time discrete case (Eq. (2.16)). Then, by substituting Eq. (2.6) into

Eq. (1.8), one obtains

$$\begin{aligned}
\frac{d}{dt}(\hat{U}_1 \hat{\rho}' \hat{U}_1^{-1}) &= -i[\hat{\mathcal{H}} \hat{U}_1 \hat{\rho}' \hat{U}_1^{-1} - \hat{U}_1 \hat{\rho}' \hat{U}_1^{-1} \hat{\mathcal{H}}] \\
-i\hat{\mathcal{H}}_1 \hat{U}_1 \hat{\rho}' \hat{U}_1^{-1} + \hat{U}_1 \frac{d}{dt} \hat{\rho}' \hat{U}_1^{-1} + i\hat{U}_1 \hat{\rho}' \hat{\mathcal{H}}_1 \hat{U}_1^{-1} &= -i[\hat{\mathcal{H}} \hat{U}_1 \hat{\rho}' \hat{U}_1^{-1} - \hat{U}_1 \hat{\rho}' \hat{U}_1^{-1} \hat{\mathcal{H}}] \\
\hat{U}_1 \frac{d}{dt} \hat{\rho}' \hat{U}_1^{-1} &= -i[\hat{\mathcal{H}} \hat{U}_1 \hat{\rho}' \hat{U}_1^{-1} - \hat{U}_1 \hat{\rho}' \hat{U}_1^{-1} \hat{\mathcal{H}} - (\hat{\mathcal{H}}_1 \hat{U}_1 \hat{\rho}' \hat{U}_1^{-1} - \hat{U}_1 \hat{\rho}' \hat{\mathcal{H}}_1 \hat{U}_1^{-1})] \\
\frac{d}{dt} \hat{\rho}' &= -i[\hat{U}_1^{-1} \hat{\mathcal{H}} \hat{U}_1 \hat{\rho}' - \hat{\rho}' \hat{U}_1^{-1} \hat{\mathcal{H}} \hat{U}_1 - (\hat{\mathcal{H}}_1 \hat{\rho}' - \hat{\rho}' \hat{\mathcal{H}}_1)] \\
\frac{d}{dt} \hat{\rho}' &= -i[\hat{\mathcal{H}}' - \hat{\mathcal{H}}_1, \hat{\rho}'] \\
\frac{d}{dt} \hat{\rho}' &= -i[\hat{\mathcal{H}}_0', \hat{\rho}'] \tag{2.9}
\end{aligned}$$

where  $\hat{\mathcal{H}}'$  represents the full Hamiltonian in the interaction frame and  $\hat{\mathcal{H}}_0' = \hat{\mathcal{H}}' - \hat{\mathcal{H}}_1$  is the non-dominant part of the full Hamiltonian in the interaction frame, i.e. a new effective Hamiltonian that governs the spin dynamics of the spin operator in the rotating frame. Note the similarity between the Liouville-von Neumann equation in the lab frame (Eq. (1.7)) and in the rotating frame (Eq. (2.9)).

$$\hat{\mathcal{H}}'(t) = \hat{U}_1^{-1}(t) \hat{\mathcal{H}}(t) \hat{U}_1(t) \tag{2.10}$$

### A Classical Interpretation of Interaction-Frame Transformation

A classical analogy of the interaction-frame transformation in quantum mechanics is the earth rotating-frame [38], which we are familiar with. Imagine a scenario where an astronaut in the space (lab-frame) is measuring the speed of a train that is travelling at a speed of 100 km/h on earth. The astronaut would have measured the speed to be  $\sim 1774$  km/h, as the tangential speed of earth is  $\sim 1674$  km/h. It is actually much easier if the astronaut had imagined himself rotating at the same velocity as the earth and taken the measurement, and neglect the large tangential speed (dominant Hamiltonian  $\hat{\mathcal{H}}_1$ ) in his calculations, i.e. a rotating-frame transformation.

### Applicability of Interaction-Frame Transformation

The dominant Hamiltonian  $\hat{\mathcal{H}}_1$  usually has eigenvalues and eigenfunctions that can be solved exactly, and they comprise the propagator  $\hat{U}_1(t)$  in the operators  $\hat{A}'(t)$  and state functions  $|\psi'(t)\rangle$  or density operators  $\rho'(t)$  (Eq. (2.11)). This has an advantage that the non-

dominant part  $\hat{\mathcal{H}}_0$  can be analyzed separately from the full Hamiltonian  $\hat{\mathcal{H}} = \hat{\mathcal{H}}_0 + \hat{\mathcal{H}}_1$ .

$$\begin{aligned} |\psi'(t)\rangle &= \hat{U}_1^{-1}(t)|\psi(t)\rangle \\ \rho'(t) &= \hat{U}_1^{-1}(t)\rho(t)\hat{U}_1(t) \\ \hat{A}'(t) &= \hat{U}_1^{-1}(t)\hat{A}(t)\hat{U}_1(t) \end{aligned} \quad (2.11)$$

$$\text{where } \hat{U}_1(t) = \hat{T} \exp\left(-i \int_0^t dt_1 \hat{\mathcal{H}}_1(t_1)\right) \quad (2.12)$$

In order to simplify the calculations further, especially in the treatment of AHT, it is important that the dominant Hamiltonian is cyclic, i.e.  $\hat{\mathcal{H}}_1 = \hat{\mathcal{H}}_1(t + \tau_c)$ , and hence  $\hat{U}_1(t) = \hat{1}$  (Eq. (2.12)). Hence, the operators and the density operators in both interaction and lab frames are the same, i.e.  $\hat{\mathcal{H}}_0'(t) = \hat{\mathcal{H}}_0(t)$  and  $\rho'(t) = \rho(t)$  (Eq. (2.11)). An important issue when applying interaction-frame transformation is the choice of the dominant  $\hat{\mathcal{H}}_1$  and non-dominant  $\hat{\mathcal{H}}_0$  Hamiltonian.  $\hat{\mathcal{H}}_0$  usually differs from  $\hat{\mathcal{H}}_1$  by orders of magnitude. If the size of the Hamiltonians are comparable, care has to be taken when making approximations in the interaction frame. For instance, non-secular parts of hyperfine interaction are not negligible in the nuclear Zeeman interaction frame if the sizes of both interactions are comparable.

### Schrödinger, Heisenberg, and Dirac Representation

In principle, the time-evolution operator can act either on the state functions  $|\psi\rangle$  or operator  $|\hat{\mathcal{H}}\rangle$ . In the Schrödinger representation, the state functions evolves with respect to the time-independent operator. In the Heisenberg representation, the operators are allowed to evolve in time while the state vectors remain time-independent. Nevertheless, in most cases in NMR, the calculations are performed in the Dirac or interaction picture, where both state functions and operators are acted by the unitary propagator  $\hat{U}_1(t)$ , which is usually set so that  $\hat{U}_1(t_c) = \hat{1}$ .

## 2.3 Modulation of the Spatial Tensors by MAS

The effect of MAS on the Hamiltonian has already been discussed in Sec. 1.4.1, and if the results (Eq. (1.31)) are substituted into Eq. (2.2):

$$\begin{aligned}
\hat{\mathcal{H}}(t) &= \sum_{n=-\ell}^{\ell} \hat{\mathcal{H}}^{(n)} e^{-in\omega_r t} \\
&= \sum_{n=-\ell}^{\ell} d_{n,0}^{\ell}(-\theta_r) A_{\ell n}^{(\text{rot})}(\alpha, \beta, \gamma) e^{-in\omega_r t} \cdot \hat{\mathcal{J}}_{\ell,0} \\
&= \sum_n \sum_{n'} d_{n,0}^{\ell}(-\theta_r) e^{-in'\alpha} d_{n',n}^{\ell}(\beta) e^{-in'\gamma} \rho_{\ell n'}^{(\text{PAS})} e^{-in\omega_r t} \cdot \hat{\mathcal{J}}_{\ell,0} \\
&= \sum_n \omega^{(n)} \hat{\mathcal{J}}_{\ell,0} e^{-in\omega_r t}
\end{aligned} \tag{2.13}$$

where  $\omega^{(n)}$  is the spatial tensor component of a spin interaction under MAS.

$$\omega^{(n)} = \sum_{n'} d_{n,0}^{\ell}(-\theta_r) e^{-in'\alpha} d_{n',n}^{\ell}(\beta) e^{-in'\gamma} \rho_{\ell n'}^{(\text{PAS})}. \tag{2.14}$$

The integer  $n$  is summed from  $-2$  to  $2$  because it is rank  $\ell = 2$ . In addition,  $\alpha$ ,  $\beta$ , and  $\gamma$  (Eq. (1.31)) are the Euler rotation angles from the PAS frame to the rotor axis, and  $\rho_{\ell m}^{(\text{PAS})}$  are the spatial spherical tensors defined in the PAS frame (Eq. (2.15)).

$$\begin{aligned}
\rho_{0,0} &= -\sqrt{3}\sigma_{\text{iso}} \\
\rho_{2,0} &= \sqrt{3/2}\delta \\
\rho_{2,\pm 2} &= -1/2(\delta\eta)
\end{aligned} \tag{2.15}$$

where  $\sigma_{\text{iso}}$ ,  $\delta$ , and  $\eta$  are the isotropic, anisotropic, and asymmetry components respectively (Eq. (1.12)). Note that the asymmetry  $\eta$  is zero<sup>1</sup> in the case of dipolar coupling. Further discussions of the effect of MAS on solid-state NMR can be found in the literature [23].

## 2.4 Average Hamiltonian Theory

A time-independent Hamiltonian  $\hat{\mathcal{H}}$  can be obtained by computing the average of different time-dependent Hamiltonians  $\hat{\mathcal{H}}(t)$  over the course of a period  $\tau_c$ . For instance, if different rf schemes are applied at different time periods (Fig. 2.2), the effect on the chemical-shift

<sup>1</sup> The asymmetry can be set to be non-zero if motions or dynamics are considered [39].



**Figure 2.2** Schematic representation of the replacement of a time-dependent Hamiltonian  $\hat{\mathcal{H}}(t)$  by an average Hamiltonian  $\hat{\mathcal{H}}$ .

term  $\hat{S}_z$  can be determined by performing an interaction-frame transformation (Eq. (2.10))

$$\hat{S}'_z(t_1, t_2) = e^{i\hat{\mathcal{H}}_1 t_1} e^{i\hat{\mathcal{H}}_2 t_2} \hat{S}_z e^{-i\hat{\mathcal{H}}_2 t_2} e^{-i\hat{\mathcal{H}}_1 t_1} \quad (2.16)$$

$$= \hat{U}_{\text{eff}}(t_c) \hat{S}_z \hat{U}_{\text{eff}}^{-1}(t_c) \quad (2.17)$$

$$= e^{i\hat{\mathcal{H}} t_c} \hat{S}_z e^{-i\hat{\mathcal{H}} t_c} \quad (2.18)$$

where the  $\hat{\mathcal{H}}_1$  and  $\hat{\mathcal{H}}_2$  are time-independent over the period  $t_1$  and  $t_2$ . Depending on the details and number of terms in the Hamiltonians  $\hat{\mathcal{H}}_1$  and  $\hat{\mathcal{H}}_2$ , the calculation (Eq. (2.16)) can be cumbersome if more propagators are taken into account. Therefore, instead of analyzing the effect of each propagator individually, the product of the propagators can be replaced by a single effective propagator  $\hat{U}_{\text{eff}}(t_c)$  (Eq. (2.17)) that is characterized by an average Hamiltonian  $\hat{\mathcal{H}}(t_c)$  over the total period  $t_c = t_1 + t_2$  [30, 31]. However, one has to be aware that the Hamiltonian must be periodic with a cycle time  $t_c$ , i.e. it is not applicable, for instance, in adiabatic sequences. Moreover, the analytical treatment requires a stroboscopic observation, i.e. the analytical result is only valid for detection every  $t_c^2$ .

In general, one has to invoke the Baker-Campbell-Hausdorff (BCH) relation (Eq. (2.19)) to calculate the product of the two propagators or determine  $\hat{\mathcal{H}}(t_c)$ .

$$\exp(i\hat{\mathcal{H}} t_c) = \exp(i\hat{\mathcal{H}}_1 t_1) \exp(i\hat{\mathcal{H}}_2 t_2) = \exp\left( i(\hat{\mathcal{H}}_1 t_1 + \hat{\mathcal{H}}_2 t_2) - \frac{1}{2} [\hat{\mathcal{H}}_1 t_1, \hat{\mathcal{H}}_2 t_2] - \frac{i}{12} [\hat{\mathcal{H}}_1 t_1, [\hat{\mathcal{H}}_1 t_1, \hat{\mathcal{H}}_2 t_2]] + \dots \right) \quad (2.19)$$

The average Hamiltonian  $\hat{\mathcal{H}}(t_c)$  is given by the first term in Eq. (2.19) if both  $\hat{\mathcal{H}}_1$  and  $\hat{\mathcal{H}}_2$  commute. Otherwise, one has to truncate the expansion series up to certain orders depending on the details required by an experiment. The series expansion in the exponent

<sup>2</sup>If the evolution time for a specific interaction  $t \gg t_c$ , the error from non-stroboscopic observation may be negligible.

can be rearranged according to the number of commutator involved, and  $\hat{\mathcal{H}}$  is now given by

$$\hat{\mathcal{H}} = \hat{\mathcal{H}}^{(1)} + \hat{\mathcal{H}}^{(2)} + \hat{\mathcal{H}}^{(3)} + \dots \quad (2.20)$$

where the explicit definitions of the first two orders of average Hamiltonians  $\hat{\mathcal{H}}^{(1)}$  and  $\hat{\mathcal{H}}^{(2)}$  are given in the following form to ensure that each order of the Hamiltonians is Hermitian and they are generalized for an arbitrary number of time periods.

$$\begin{aligned} \hat{\mathcal{H}}^{(1)} &= \frac{1}{t_c} \sum_{k=1}^n \hat{\mathcal{H}}_k t_k \\ \hat{\mathcal{H}}^{(2)} &= \frac{-i}{2t_c} \sum_{k>m}^n [\hat{\mathcal{H}}_k t_k, \hat{\mathcal{H}}_m t_m] \end{aligned} \quad (2.21)$$

or in a generalized continuously time-dependent form called Magnus expansion

$$\begin{aligned} \overline{\mathcal{H}}^{(1)} &= \frac{1}{t_c} \int_0^{t_c} dt_1 \hat{\mathcal{H}}(t_1) \\ \overline{\mathcal{H}}^{(2)} &= \frac{-i}{2t_c} \int_0^{t_c} dt_2 \int_0^{t_2} dt_1 [\hat{\mathcal{H}}(t_2), \hat{\mathcal{H}}(t_1)]. \end{aligned} \quad (2.22)$$

Note that the first-order average Hamiltonian  $\hat{\mathcal{H}}^{(1)}$  does not have explicit dependence on the time  $t_c$ , but the second-order  $\hat{\mathcal{H}}^{(2)}$  depends linearly on  $t_c$ . This is one of the reasons that the coherent averaging by MAS in solid-state NMR is more efficient at higher MAS frequencies (short rotor period  $t_r$ ). In general, higher order of effective Hamiltonians are smaller and the series converges due to the relation  $\hat{\mathcal{H}}^{(n)}(t_c^{(n-1)})$ . A second implication that can be inferred from the Eq. (2.22) is that all even orders of effective Hamiltonians vanish if the Hamiltonian is symmetric with respect to a certain cycle time  $t_c$ , i.e.

$$\hat{\mathcal{H}}(t) = \hat{\mathcal{H}}(t_c - t) \quad \text{for } 0 \leq t \leq t_c. \quad (2.23)$$

It was discussed earlier that the AHT treatment requires stroboscopic measurement, i.e. setting the dwell time to a multiple of cycle time  $t_c$ . This requirement can be difficult to be fulfilled if the Hamiltonians involve several time dependencies with frequencies that are not commensurate. Hence, Floquet theory can be a viable option in circumventing this issue.



### Piecewise Constant Hamiltonian

In principle, any time-dependent Hamiltonians  $\hat{\mathcal{H}}(t)$  can be expressed as a product of  $n$  piecewise constant Hamiltonians over a period of  $t/n$  as long as  $n$  is sufficiently large, i.e. the period  $t_i$  is so short that the Hamiltonian can be assumed to remain unchanged ( $t_i \ll \hat{\mathcal{H}}_1$ ). This is known as the piecewise constant Hamiltonians, and it is manifested in Eq. (2.16). This is analogous to performing integration by determining the area under an analytical function, i.e. the numerical integration is more accurate if smaller steps in the domain are taken. This has important implications in the numerical simulations of the quantum-mechanical problem.

## 2.5 Floquet Theory

Other than treating time-dependent Hamiltonians using AHT, a viable alternative is Floquet theory [32–35, 40]. As discussed in the earlier section (Sec. 2.4), the shortcoming of AHT is that the description is limited to a multiple of cycle time. This is sufficient if the Hamiltonian is only characterized by a single frequency. In solid-state NMR, the Hamiltonians often involve several time dependencies that are not necessarily an integer multiple of each other, i.e. multiple-pulse decoupling sequences are rarely rotor synchronized. This issue is circumvented in the spirit of Floquet theory. The time-dependent Hamiltonians  $\hat{\mathcal{H}}(t)$  are being treated in an infinite-dimensional Floquet space which is comprised of a spin Hilbert space and one or more Fourier spaces, i.e. the bases  $\Psi^{(\text{Floquet})}$  that span a Floquet space is given by

$$\Psi^{(\text{Floquet})} = \Psi^{(\text{Hilbert})} \otimes \Psi^{(\text{Fourier})} \quad (2.24)$$

$$= \{|\psi_1\rangle, |\psi_2\rangle, \dots, |\psi_N\rangle\} \otimes \{|-\infty\rangle, \dots, |-1\rangle, |0\rangle, |1\rangle, |2\rangle, \dots, |\infty\rangle\} \quad (2.25)$$

where  $\Psi^{(\text{Hilbert})}$  is the set of basis vectors that span a  $N$ -dimensional Hilbert spin space, which is also used in AHT. The Fourier space is an infinite-dimensional space with basis vectors  $\Psi^{(\text{Fourier})}$  that are characterized by integer quantum numbers (Eq. (2.25)) with some useful operators like ladder operators  $\hat{F}_m$  which occupy the  $m$ -side diagonal in their matrix representation form (Fig. 2.3)

$$\hat{F}_m |n\rangle = |m+n\rangle \quad (2.26)$$

and  $\hat{F}_0$  is the identity operator in the Fourier space. Another useful operator is the number operator  $\hat{F}_z$  which contains non-zero diagonal elements in its matrix representation

$$\hat{F}_z |n\rangle = n |n\rangle. \quad (2.27)$$

Furthermore, the operators obey the following relations

$$\begin{aligned} \hat{F}_m \hat{F}_n &= \hat{F}_{m+n} \\ [\hat{F}_m, \hat{F}_n] &= 0 \\ [\hat{F}_z, \hat{F}_m] &= m \hat{F}_m. \end{aligned} \quad (2.28)$$

These operators are useful in constructing Floquet Hamiltonians (*vide infra*).

$$\hat{F}_1 = \begin{pmatrix} \dots & | +2 \rangle & | +1 \rangle & | 0 \rangle & | -1 \rangle & | -2 \rangle & \dots \\ \vdots & & & & & & \\ & 0 & 1 & 0 & 0 & 0 & \\ & 0 & 0 & 1 & 0 & 0 & \\ & 0 & 0 & 0 & 1 & 0 & \\ & 0 & 0 & 0 & 0 & 1 & \\ & 0 & 0 & 0 & 0 & 0 & \\ & & & & & & \ddots \end{pmatrix} \begin{matrix} \vdots \\ | +2 \rangle \\ | +1 \rangle \\ | 0 \rangle \\ | -1 \rangle \\ | -2 \rangle \\ \vdots \end{matrix} \quad \hat{F}_{-2} = \begin{pmatrix} \dots & | +2 \rangle & | +1 \rangle & | 0 \rangle & | -1 \rangle & | -2 \rangle & \dots \\ \vdots & & & & & & \\ & 0 & 0 & 0 & 0 & 0 & \\ & 0 & 0 & 0 & 0 & 0 & \\ & 1 & 0 & 0 & 0 & 0 & \\ & 0 & 1 & 0 & 0 & 0 & \\ & 0 & 0 & 1 & 0 & 0 & \\ & & & & & & \ddots \end{pmatrix} \begin{matrix} \vdots \\ | +2 \rangle \\ | +1 \rangle \\ | 0 \rangle \\ | -1 \rangle \\ | -2 \rangle \\ \vdots \end{matrix}$$

$$\hat{F}_z = \begin{pmatrix} \dots & | +2 \rangle & | +1 \rangle & | 0 \rangle & | -1 \rangle & | -2 \rangle & \dots \\ \vdots & & & & & & \\ & +2 & 0 & 0 & 0 & 0 & \\ & 0 & +1 & 0 & 0 & 0 & \\ & 0 & 0 & 0 & 0 & 0 & \\ & 0 & 0 & 0 & -1 & 0 & \\ & 0 & 0 & 0 & 0 & -2 & \\ & & & & & & \ddots \end{pmatrix} \begin{matrix} \vdots \\ | +2 \rangle \\ | +1 \rangle \\ | 0 \rangle \\ | -1 \rangle \\ | -2 \rangle \\ \vdots \end{matrix}$$

**Figure 2.3** Matrix representations of the ladder operator  $\hat{F}_1, \hat{F}_{-2}$  and number operator  $\hat{F}_z$ . Figure taken from *Scholz et al.* [33].

### 2.5.1 Floquet Hamiltonian

A Floquet Hamiltonian  $\hat{\mathcal{H}}_F$  can be constructed by promoting a time-dependent Hamiltonian  $\hat{\mathcal{H}}(t)$  (Fig. 2.4)

$$\hat{\mathcal{H}}(t) = \sum_{n=-\infty}^{\infty} \hat{\mathcal{H}}^{(n)} \cdot e^{in\omega_m t} \quad (2.29)$$

into the form of

$$\hat{\mathcal{H}}_F = \hat{\mathcal{H}}_F^{(1)} + \hat{\mathcal{H}}_F^{(0)} \quad (2.30)$$

$$= \sum_{n=-\infty}^{\infty} \hat{F}_n \otimes \hat{\mathcal{H}}^{(n)} + \omega_m \cdot \hat{F}_z \otimes \hat{1}^{(s)} \quad (2.31)$$

where  $\hat{1}^{(s)}$  is the identity operator in the Hilbert spin space. Note that the additional term  $\omega_m \cdot \hat{F}_z$  is analogous to the fictitious Coriolis force experienced in an interaction-frame transformation.

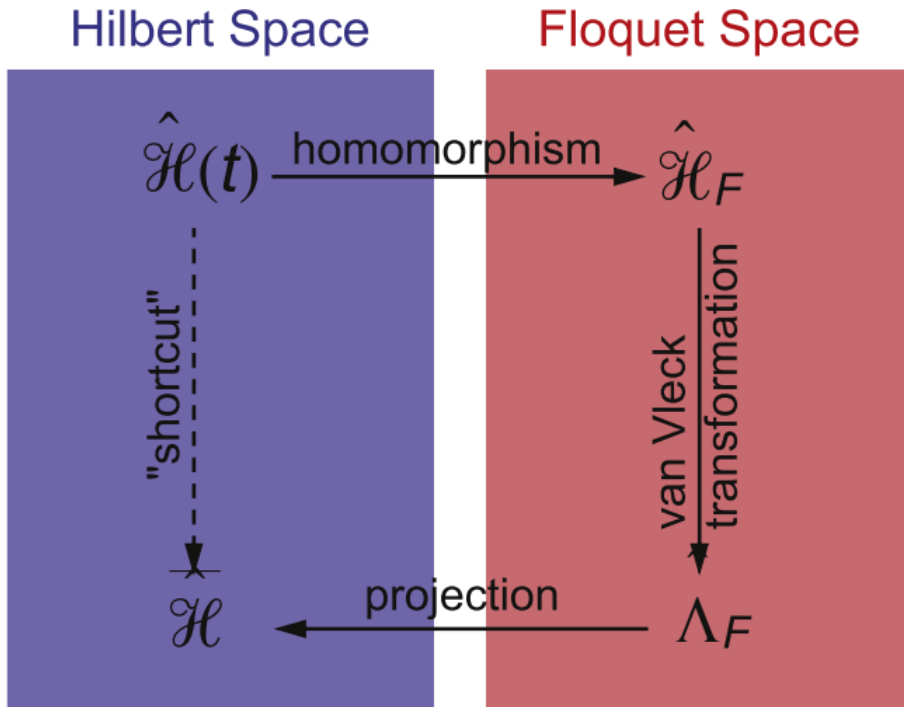


**Figure 2.4** Schematic diagram of the construction of the operator-based Floquet theory. Figure taken from *Scholz et al.* [33].

### 2.5.2 Operator-Based Floquet Theory

Once the Floquet Hamiltonians are constructed, there are several methods to proceed with the determination of the spin dynamics. The first method involves the evolution of the density operator followed by observation using detection operators defined in the Floquet space. This method has the advantage that the theory is exact and it can describe side bands and degeneracies resulting from the close energy levels between the Fourier-space and spin-space resonance conditions. Nevertheless, the calculations yield limited physical insight and are often limited to simple spin systems due to large matrices.

The second approach is to use the van-Vleck transformation [41, 42] to obtain approximately block-diagonalized Floquet Hamiltonians  $\Lambda_F$  without the need to know the detailed knowledge of the Hilbert spin space. One of the shortcomings of this approach is that the resonance condition arising from the frequency matching between the characteristic frequencies and the spin interactions in the Hilbert space can not be seen directly, i.e. additional interaction-frame transformation with respect to spin interactions must be dealt with externally. Nevertheless, this operator-based description is sufficient if the characteristic frequencies are well separated. Finally, the Floquet Hamiltonians  $\Lambda_F$  can be projected back to the Hilbert space to obtain effective Hamiltonians that are similar to AHT. The derivation of the effective Hamiltonian  $\hat{\mathcal{H}}_{\text{eff}}$  can be found in the reference [33], and the final result will be presented here and can be used as a 'shortcut' directly from  $\hat{\mathcal{H}}(t)$  (Fig. 2.4).

### 2.5.3 Effective Hamiltonian

For a time-dependent Hamiltonian  $\hat{\mathcal{H}}(t)$  that is for example, modulated by two characteristic frequencies  $\omega_r$  and  $\omega_m$ :

$$\hat{\mathcal{H}}(t) = \sum_{n=-\infty}^{\infty} \sum_{k=-\infty}^{\infty} \hat{\mathcal{H}}^{(n,k)} \cdot e^{in\omega_r t} \cdot e^{ik\omega_m t}. \quad (2.32)$$

The effective Hamiltonian is given by

$$\hat{\mathcal{H}} = \hat{\mathcal{H}}^{(1)} + \hat{\mathcal{H}}^{(2)} + \dots \quad (2.33)$$

in which the first order effective Hamiltonian  $\hat{\mathcal{H}}^{(1)}$  is comprised of the sum of all possible resonant  $\hat{\mathcal{H}}^{(n_0, k_0)}$  and non-resonant terms  $\hat{\mathcal{H}}^{(0,0)}$  (Eq. (2.34)).

$$\hat{\mathcal{H}}^{(1)} = \hat{\mathcal{H}}^{(0,0)} + \sum_{(n_0, k_0)} \hat{\mathcal{H}}^{(n_0, k_0)} \quad (2.34)$$

where  $n_0$  and  $k_0$  are integers that satisfy the resonance condition (Eq. (2.35)).

$$n_0\omega_r + k_0\omega_m = 0 \quad (2.35)$$

Similarly, the second-order effective Hamiltonians  $\hat{\mathcal{H}}_{(2)}$  are defined as follows

$$\hat{\mathcal{H}}^{(2)} = \hat{\mathcal{H}}_{(2)}^{(0,0)} + \sum_{(n_0,k_0)} \hat{\mathcal{H}}_{(2)}^{(n_0,k_0)} \quad (2.36)$$

$$\hat{\mathcal{H}}_{(2)}^{(n_0,k_0)} = -\frac{1}{2} \sum_{\nu,\kappa} \frac{[\hat{\mathcal{H}}^{(n_0-\nu,k_0-\kappa)}, \hat{\mathcal{H}}^{(\nu,\kappa)}]}{\nu\omega_r + \kappa\omega_m} \quad (2.37)$$

where  $\nu$  and  $\kappa$  can be any integer numbers as long as  $\nu\omega_r + \kappa\omega_m \neq 0$  to ensure that the denominator of Eq. (2.37) does not become  $\infty$ .

### Trimodal Floquet Theory

In principle, the resonance conditions and effective Hamiltonians can be easily extended to any arbitrary number of characteristic frequencies. For instance, for a time-dependent Hamiltonian  $\hat{\mathcal{H}}(t)$  with three characteristic frequencies  $\omega_r$ ,  $\omega_m$ , and  $\omega_{\text{eff}}$

$$\hat{\mathcal{H}}(t) = \sum_{n=-\infty}^{\infty} \sum_{k=-\infty}^{\infty} \sum_{\ell=-\infty}^{\infty} \hat{\mathcal{H}}^{(n,k,\ell)} \cdot e^{in\omega_r t} \cdot e^{ik\omega_m t} \cdot e^{i\ell\omega_{\text{eff}} t} \quad (2.38)$$

The first order effective Hamiltonian is given by  $\hat{\mathcal{H}}_{(1)}$

$$\hat{\mathcal{H}}^{(1)} = \hat{\mathcal{H}}^{(0,0,0)} + \sum_{(n_0,k_0,\ell_0)} \hat{\mathcal{H}}^{(n_0,k_0,\ell_0)} \quad (2.39)$$

where  $n_0$ ,  $k_0$ , and  $\ell_0$  are integers that satisfy the resonance condition

$$n_0\omega_r + k_0\omega_m + \ell_0\omega_{\text{eff}} = 0 \quad (2.40)$$

while for the second-order effective Hamiltonian  $\hat{\mathcal{H}}_{(2)}$

$$\hat{\mathcal{H}}^{(2)} = \hat{\mathcal{H}}_{(2)}^{(0,0,0)} + \sum_{(n_0,k_0,\ell_0)} \hat{\mathcal{H}}_{(2)}^{(n_0,k_0,\ell_0)} \quad (2.41)$$

$$\hat{\mathcal{H}}_{(2)}^{(n_0,k_0,\ell_0)} = -\frac{1}{2} \sum_{\nu,\kappa,\lambda} \frac{[\hat{\mathcal{H}}^{(n_0-\nu,k_0-\kappa,\ell_0-\lambda)}, \hat{\mathcal{H}}^{(\nu,\kappa,\lambda)}]}{\nu\omega_r + \kappa\omega_m + \lambda\omega_{\text{eff}}} \quad (2.42)$$

with  $\nu$ ,  $\kappa$ , and  $\lambda$  being any integer numbers fulfilling

$$\nu\omega_r + \kappa\omega_m + \lambda\omega_{\text{eff}} \neq 0 \quad (2.43)$$

to ensure that Eq. (2.42) does not become  $\infty$ .

### Extra Non-Resonant Terms in Higher-Order Averaging

Note that in evaluating second- and higher order terms, it has been discussed in literature [34, 42–44] that there exists an extra term that is comprised of the commutator between the resonant and non-resonant term. The origin of this term can be derived and seen by inspecting the lower limit of the time integration (Eq. (2.22)), which is 0 (or perhaps the initial condition, which can be substituted by any other variable). The effect of this extra term is not clear and sometimes deemed an artefact and therefore disregarded in literature.

## 2.5.4 Characteristic Frequencies

The nuclear spins can be manipulated by the rf irradiations, and the pulse sequences are tailored to reintroduce desired spin interactions to the system (recoupling), or to average undesired spin interactions (decoupling). In order to analyze the effect of the pulse sequences using Floquet theory, it is important to determine the resonance conditions (Eq. (2.35) and (2.40)) of the pulses sequences. Here, we make a hypothesis that all periodic pulse sequences can have a maximum of two characteristic frequencies per channel, these are the modulation frequencies  $\omega_m$  and the effective nutation frequency  $\omega_{\text{eff}}$ . The modulation frequency  $\omega_m = 2\pi/\tau_m$  is dictated by the time period spanned by a basic repeating unit in a pulse sequence. The notion of a basic repeating unit also includes the supercycle implementation, i.e. all four pulses are considered in the supercycle version of XiX<sup>cw</sup> [45]. The effective nutation frequency  $\omega_{\text{eff}} = \beta/\tau_m$  is quantified by the net flip angle  $0 \leq \beta < \pi$  acquired over a basic cycle  $\tau_m$ . The net flip angle  $\beta$  can be determined easily in the case of amplitude-modulated pulse sequences. However, it is non-trivial if the pulse sequence is phase-modulated, for e.g. TPPM [46], in which  $\beta$  can be determined analytically with quaternions or Euler rotations. The modulation frequencies  $\omega_m = 2\pi/\tau_m$  and the effective nutation frequencies  $\omega_{\text{eff}} = 2\pi/\tau_m$  for various pulse sequences are tabulated in Table 2.1, along with some instances of pulse sequence illustrated in Fig. 2.5.

Sequence	$\nu_m$	$\nu_{\text{eff}}$
CW	-	$\nu_{1\text{cw}}$
Lee-Goldburg [47]	-	$\sqrt{\nu_{1\text{cw}}^2 + \nu_{\text{offset}}^2}$
PMLG- $n$ [48]	$1/(n\tau_p)$	-
Symmetry-based $CN_n^V$ , $RN_n^V$ [49]	$1/(N\tau_p)$	-
XiX [50]	$1/(2\tau_p)$	-
XiX <sup>cw</sup> [45, 51]	$1/(2\tau_p)$	$\nu_{1\text{cw}}$
TPPM [46, 52]	$1/(2\tau_p)$	$2\nu_m \cos^{-1}(\cos^2 \phi \cos^2(\nu_1 \tau_p) + \sin^2 \phi)$

**Table 2.1** Characteristic frequencies of pulse sequences. The entry is marked with - if the characteristic frequency is not relevant.

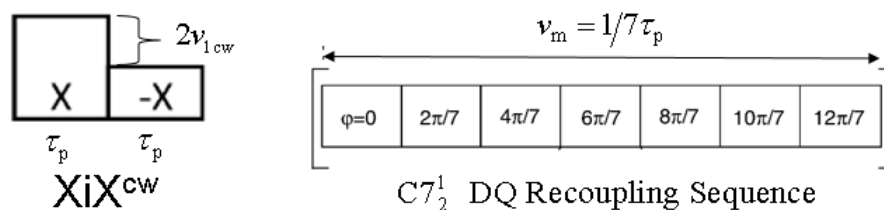


**Figure 2.5** Schematic drawing of the XiX<sup>cw</sup> and the symmetry-based C7<sub>2</sub><sup>1</sup> sequences. The XiX<sup>cw</sup> sequence has a modulation frequency of  $\nu_m = 1/(2\tau_p)$  and effective field of  $\nu_{\text{eff}} = \nu_{1\text{cw}}$ , while the C7 sequence has  $\nu_m = 1/(7\tau_p)$  and no effective field  $\nu_{\text{eff}}$ .

## 2.6 Recoupling and Decoupling Sequences

In a recoupling experiment, the spin interactions are partially reintroduced during the mixing period to correlate nuclei or transfer polarization. On the other hand, the decoupling sequences are employed for better averaging of the anisotropic interactions, leading to higher resolution spectra. In principle, both AHT and Floquet theory can be used to design recoupling or decoupling sequences, and the results are equivalent. In general, it is easier to use AHT on simple recoupling sequences as they are usually all rotor-synchronized, and AHT provides more physical insight. While Floquet theory is able to treat complicated scenarios like decoupling during mixing (Chapter 3), non-rotor synchronized recoupling sequences under MAS (Chapter 4), amplitude-modulated recoupling sequences (Chapter 5). At last, a general theory that describes any arbitrary decoupling sequences (simultaneously amplitude- and phase-modulated) will be presented in Chapter 6.





## Chapter 3

# Symmetry-Based Sequences for Scalar $J$ -Coupling Experiments

In solid-state NMR spectroscopy under magic-angle spinning (MAS), polarization-transfer processes can be mediated by the scalar  $J$  coupling or by dipolar coupling. The latter is averaged out by the MAS, while the  $J$  coupling is always present but the coupling strength is relatively small. One way to use the isotropic  $J$  couplings for polarization transfer in solids is the generation of an effective Hamiltonian that contains only the  $J$ -coupling interaction. This is exploited in the through-bond correlation spectroscopy or TOBSY experiment [53–55] (Fig. 3.6) which is a viable alternative to dipolar-coupling based polarization transfer schemes in particular when moderate to fast MAS (>25 kHz) is applied. Since the transfer mechanism is based on an isotropic interaction, 100 % transfer efficiency is theoretically possible in a given spin pair. Additionally, a  $J$ -coupling based experiment does not experience dipolar truncation [56], i.e. the polarization can be transferred to weakly coupled nuclei in the presence of a strongly coupled third spin. In order to generate such an effective Hamiltonian, the much larger anisotropic interactions (dipolar coupling and chemical-shielding anisotropy) have to be suppressed to a high degree while simultaneously the isotropic chemical shift has to be averaged out in full analogy to the liquid-state TOCSY experiment [57, 58]. These objectives are often achieved by using a symmetry-based pulse sequence [49].

### Declaration

Part of the chapter is based on the published manuscript:

K. O. Tan, I. Scholz, J. D. van Beek, B. H. Meier, M. Ernst, *Improved decoupling during symmetry-based C9-TOBSY sequences*, J. Magn. Reson. 239, 61, **2014**.

### 3.1 Introduction to $CN_n^v$ and $RN_n^v$ Sequences

Symmetry-based  $CN_n^v$  or  $RN_n^v$  pulse sequences are a family of pulse sequences that can be used for decoupling or recoupling during selected time periods in magic-angle spinning (MAS) solid-state NMR experiments [49, 59, 60]. Symmetry-based sequences have been used in homonuclear recoupling [61, 62], homonuclear decoupling [63], scalar  $J$ -coupling [54, 55, 64], heteronuclear dipolar recoupling [65, 66] and heteronuclear decoupling [67] experiments. The sequences are comprised of a series of  $N$  phase-modulated basic pulse elements with a net flip angle of either a  $\pi$  (R) or  $2\pi$  (C) fitted into  $n$  rotor periods. The experimental details of the C or R sequences are given as follows

- A basic cycle of the  $CN_n^v$  sequence consists of  $N$  basic net  $2\pi$  rotation elements (Fig. 3.2) with incrementing phase of  $\Delta\phi = \frac{2\pi v}{N}$  in  $n$  rotor periods (Fig. 3.1).
- A basic cycle of the  $RN_n^v$  sequence consists of  $N/2$  pair of basic net  $\pi$  rotation elements (Fig. 3.2) with phases of  $\phi = \pm\frac{\pi v}{N}$  in  $n$  rotor periods (Fig. 3.1). The R sequence is essentially similar to a TPPM sequence that is repeated by  $N/2$  times.

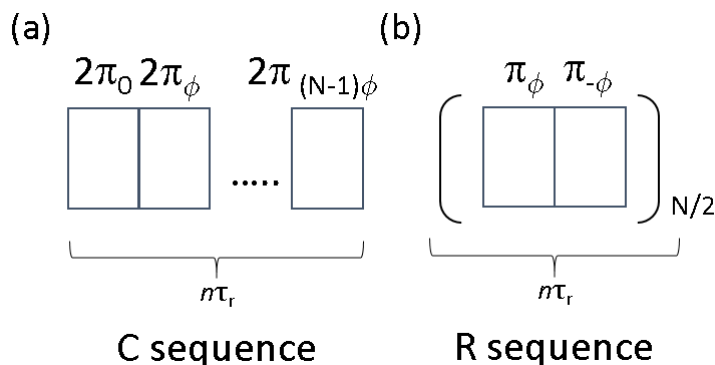


**Figure 3.1** Schematic diagrams of  $CN_n^v$  and  $RN_n^v$  Sequences.

The choice of the numbers  $N$ ,  $n$ , and  $v$  allows the selection of terms in the time-dependent Hamiltonian which become time independent under the combined rotations by MAS and rf irradiation. Such sequences can be analyzed either using average Hamiltonian (AHT) [16, 68] or Floquet theory [33, 35]. Using these theories, space-spin selection rules can be derived to aid the selection of the variables  $N$ ,  $n$ , and  $v$ .

#### Basic C Elements (POST) and R Elements (Composite $\pi$ )

The POST element  $((\pi/2)_x(2\pi)_{-x}(3\pi/2)_x)$  is an amplitude-modulated composite pulse that generates a net  $2\pi$  flip angle (Fig. 3.2a). The composite pulse fulfils the requirement of being a C element, and it is shown to be robust with respect to offset [61]. Similarly, the

composite  $\pi$  pulse  $((\pi/2)_x(3\pi/2)_{-x})$  (Fig. 3.2b) is used because it is more broad banded compared to a simple  $\pi$  pulse [60].

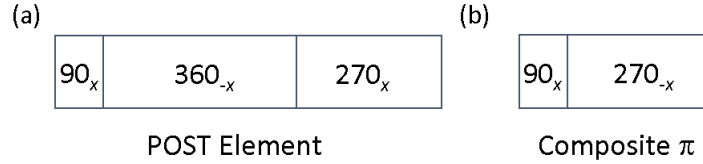


**Figure 3.2** Schematic drawings of (a) POST element and (b) a composite  $\pi$  pulse.

### 3.1.1 Space-Spin Selection Rules

The symmetry-based C and R sequences are essentially phase-modulated sequences, i.e. the spin interactions are rotated around the z-axis. It could be shown from the effective Hamiltonian derived from AHT or Floquet theory that a spin interaction of rank component  $s = [-\ell, -\ell + 1, \dots, \ell]$  with  $m$  spatial component is recoupled if the following selection rules are satisfied:

- For a  $CN_n^V$  sequence with  $z$  being any integer number

$$mn - sV = zN, \quad (3.1)$$

- and for a  $RN_n^V$  sequence with  $z_\lambda$  which has the same parity as the spin rank tensor  $\ell$ , i.e. homonuclear dipolar coupling has a rank of  $\ell = 2$  and hence  $z_\lambda = 0, \pm 2, \pm 4, \dots$ . Similarly, the possible  $z_\lambda$  for CSA tensor is  $z_{\lambda=1} = \pm 1, \pm 3, \dots$

$$mn - sV = \frac{z_\lambda N}{2} \quad (3.2)$$

A space-spin selection diagram (Fig. 3.3) is presented to illustrate the selection rules (Eq. (3.1)) for a homonuclear DQ recoupling  $C7_2^1$ , which recouples a tensor component of  $m = 1$  and  $s = 2$ . Similarly, another DQ recoupling  $R26_4^{11}$  with tensor components  $m = 1$  and  $s = -2$  fulfilling the selection rules (Eq. (3.2)) is shown in Fig. 3.3b. Note that, an opening in the grey vertical bar on the right hand side exists only if the selection rules are fulfilled. Otherwise, the first-order effective Hamiltonian will be devoid of these terms. Moreover, only the first-order selection rules are presented here, and they can be extended to second or higher order selection rules, which might play a crucial role in decoupling experiment [67]. In principle, isotropic chemical shift with  $m = s = 0$  is always allowed in any C sequence since it obeys the selection rule (Eq. (3.1)). Although it is allowed by the selection rules, the scaling factor is usually 0 in the ideal case if the basic element is a net  $2\pi$  pulse for

C sequence, or net  $\pi$  pulse for the R sequence. Further discussion of the scaling factor is presented in the next section.

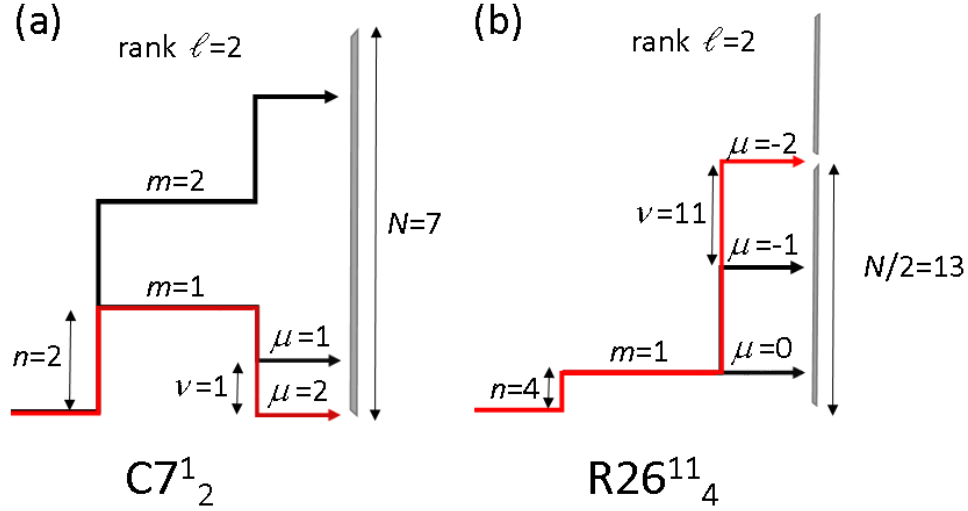


Figure 3.3 Space-spin selection diagrams for (a)  $C7_2^1$  and (b)  $R26_4^{11}$ .

### Scaling Factors

The selection rules only provide a qualitative analysis of the allowed and forbidden spin interactions. While a full analysis of the effective Hamiltonian including the size of the scaling factors would require a detailed knowledge of the basic C or R element. In general, the recoupling sequences are more efficient if the selected time-independent term has a high scaling factor while the undesired terms have zero scaling factor. The calculation of the scaling factors can be performed using AHT [65] or Floquet theory [48].

### 3.1.2 Resonance Conditions and Effective Hamiltonians

We consider a general heteronuclear spin system with a single  $I$  spin and two  $S$  spins that is, in the usual Zeeman rotating frame and using spherical-tensor notation [68], characterized by a full time-dependent Hamiltonian of the form

$$\begin{aligned}
 \hat{\mathcal{H}}(t) = & \sum_{p=1}^2 \sum_{n=-2}^2 \omega_p^{(n)} e^{in\omega t} T_{1,0}^{(p)} + \sum_{n=-2}^2 \omega_I^{(n)} e^{in\omega t} T_{1,0}^{(I)} + \sum_{p=1}^2 \sum_{\substack{n=-2 \\ n \neq 0}}^2 \omega_{Ip}^{(n)} e^{in\omega t} \frac{2}{\sqrt{6}} T_{1,0}^{(p)} T_{1,0}^{(I)} \\
 & + \sum_{p=1}^2 \omega_{Ip}^{(0)} \frac{-1}{\sqrt{3}} T_{1,0}^{(p)} T_{1,0}^{(I)} + \sum_{\substack{n=-2 \\ n \neq 0}}^2 \omega_{1,2}^{(n)} e^{in\omega t} T_{2,0}^{(1,2)} + \omega_{1,2}^{(0)} T_{0,0}^{(1,2)} \\
 & + \omega_{IS} \sum_{p=1}^2 (S_{px} \cos(\phi(t)) + S_{py} \sin(\phi(t))) + \omega_{II}(t) I_x
 \end{aligned} \tag{3.3}$$

where the  $\omega_p^{(n)} = \frac{2}{\sqrt{6}} d_{n,0}^2(-\theta_m) e^{-in\gamma} \sum_{m=-2}^2 d_{m,n}^2(\beta) e^{-im\alpha} \rho_{2,m}^{(p)}$  represents the Fourier components of the chemical shift of the  $S$  spins and  $\omega_1^{(n)}$  for the  $I$  spins, respectively. While  $\omega_{1,2}^{(n)} = d_{n,0}^2(-\theta_m) e^{-in\gamma} d_{0,n}^2(\beta) \rho_{2,0}^{(1,2)}$  symbolizes the Fourier components of the homonuclear dipolar couplings and  $\omega_{1p}^{(n)} = d_{n,0}^2(-\theta_m) e^{-in\gamma} d_{0,n}^2(\beta) \rho_{2,0}^{(Ip)}$  represents the heteronuclear dipolar coupling. These Fourier components can be derived from (Eq. (2.14)) with  $\rho_{2,m}$  being the spin tensor defined in the PAS. Lastly, the isotropic  $J$  coupling term is given by  $\omega_{1,2}^{(0)} = -2\sqrt{3}\pi J$ . The irradiation of the  $S$  spins by the C-sequence has a constant rf-field amplitude  $\omega_{1S}$  but a time-dependent phase  $\phi(t)$ , while the simultaneous decoupling of the  $I$  spins has a time-dependent amplitude  $\omega_{1I}(t)$  but constant phase if amplitude-modulated decoupling sequences are used. For a Floquet treatment [33, 34], we have to perform an interaction-frame transformation of the time-dependent Hamiltonian of Eq. (3.3) into an interaction frame with the rf-field Hamiltonians of both  $I$  and  $S$  channels. The effective Hamiltonian can be derived or adapted to the case without or with decoupling (see Sec. 3.2.1) on the  $I$  spins.

### C Sequence without Decoupling

In the case of no  $I$ -spin irradiation, i.e.,  $\omega_{1I}(t) = 0$ , this leads to a time-dependent interaction-frame Hamiltonian with only two basic frequencies,  $\omega_r$  and  $\omega_m^{(S)}$ . The interaction-frame Hamiltonian can be expressed in the form of a Fourier series as

$$\hat{\mathcal{H}}(t) = \sum_{n=-2}^2 \sum_{k=-\infty}^{\infty} \hat{\mathcal{H}}^{(n,k)} e^{in\omega_r t} e^{ik\omega_m^{(S)} t} \quad (3.4)$$

with the Fourier components [35] given by

$$\begin{aligned} \hat{\mathcal{H}}^{(0,k)} &= \left\{ \omega_{1,2}^{(0)} T_{0,0}^{(1,2)} + \omega_1^{(0)} T_{1,0}^{(I)} \right\} \delta_{k,0} + \sum_{p=1}^2 \omega_p^{(0)} \sum_{s=-1}^1 a_{1,s}^{(k)} T_{1,s}^{(p)} \\ &\quad + \sum_{p=1}^2 \omega_{1p}^{(0)} \frac{-1}{\sqrt{3}} T_{1,0}^{(I)} \sum_{s=-1}^1 a_{1,s}^{(k)} T_{1,s}^{(p)} \\ \hat{\mathcal{H}}^{(n,k)} &= \left\{ \omega_1^{(n)} T_{1,0}^{(I)} \right\} \delta_{k,0} + \sum_{p=1}^2 \omega_p^{(n)} \sum_{s=-1}^1 a_{1,s}^{(k)} T_{1,s}^{(p)} \\ &\quad + \sum_{p=1}^2 \omega_{1p}^{(n)} \frac{2}{\sqrt{6}} T_{1,0}^{(I)} \sum_{s=-1}^1 a_{1,s}^{(k)} T_{1,s}^{(p)} + \omega_{1,2}^{(n)} \sum_{s=-2}^2 a_{2,s}^{(k)} T_{2,s}^{(1,2)} \end{aligned} \quad (3.5)$$

Here the  $a_{\ell,s}^{(k)}$  are the Fourier coefficients resulting from the interaction-frame transformation of the  $T_{\ell,0}$  spherical-tensor operators and are defined as

$$\tilde{T}_{\ell,0}(t) = \sum_{s=-\ell}^{\ell} a_{\ell,s}(t) T_{\ell,s} = \sum_{s=-\ell}^{\ell} \sum_{k=-\infty}^{\infty} a_{\ell,s}^{(k)} e^{ik\omega_m^{(S)}t} T_{\ell,s} \quad (3.6)$$

Figure 3.4 shows a plot of the  $a_{\ell,s}^{(k)}$  Fourier coefficients for an example,  $C9_6^1$  sequence using POST as a basic C element [61] as a function of the index  $k$  for the three first-rank ( $\ell = 1$ ) and the five second-rank ( $\ell = 2$ ) tensor components. They can either be calculated analytically [35] or numerically by simulating the interaction-frame trajectory of the  $T_{\ell,0}$  spherical-tensor components under the  $C9_n^1$  sequence. If the resonance condition

$$n_0\omega_r + k_0\omega_m^{(S)} = 0 \quad (3.7)$$

is fulfilled, this leads to a recoupling with an effective first-order Hamiltonian of the form

$$\hat{\mathcal{H}}^{(1)} = \hat{\mathcal{H}}^{(0,0)} + \hat{\mathcal{H}}^{(n_0,k_0)} + \hat{\mathcal{H}}^{(-n_0,-k_0)} \quad (3.8)$$

The resonance conditions (Eq. (3.7)) can be simplified to  $k_0 = -nn_0$  by substituting  $\omega_r = n\omega_m^{(S)}$ . This would then further simplify Eq. (3.8) into the form

$$\hat{\mathcal{H}}^{(1)} = \hat{\mathcal{H}}^{(0,0)} + \hat{\mathcal{H}}^{(n_0,-nn_0)} + \hat{\mathcal{H}}^{(-n_0,nn_0)} \quad (3.9)$$

Moreover, following the treatment by Vinogradov et al. [35], the Fourier coefficients  $a_{\ell,s}^{(k)}$  for a  $CN_n^V$  sequence are only non zero if the condition

$$k = zN - sV \quad (3.10)$$

is fulfilled where  $z$  is an integer. Equation (3.10) is equivalent to the symmetry-based selection rules derived from the average Hamiltonian description (Eq. (3.1)). The sparse but regular non-zero values of the Fourier coefficients are the reason for the high recoupling selectivity of the symmetry-based recoupling sequences. The selection rules together with the first-order effective Hamiltonian (Eqs. 3.9 and 3.5) shown here, is in general applicable to all types of  $CN_n^V$  sequences. The recoupling or decoupling information of a particular  $CN_n^V$  sequence is encoded in the Fourier coefficients  $a_{\ell,s}^{(k)}$  in Eq. (3.5).

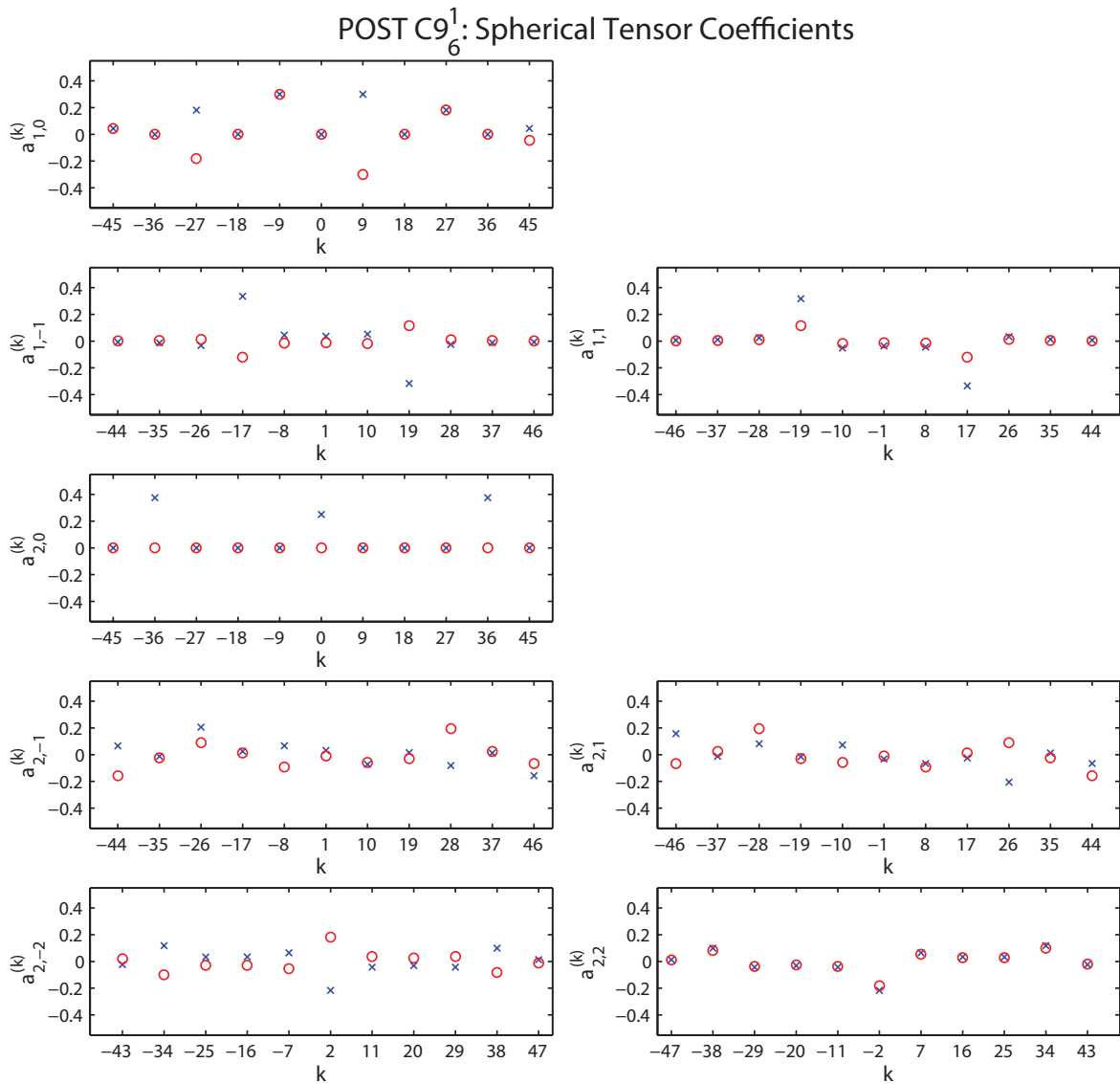


**Figure 3.4** Plot of the spherical Fourier coefficients  $a_{\ell,s}^{(k)}$  (real part blue 'x', imaginary part red 'o') as a function of  $k$  for the  $C9_6^1$  pulse sequence using POST as a basic C element. All values not shown in the plots are zero due to the symmetry of the pulse sequence.

### 3.2 Interference between TOBSY C9 and Decoupling

A number of TOBSY sequences have been published using such symmetry-based C- or R-type sequences with either hard pulses [54, 69] or adiabatic inversion pulses [55, 70, 71]. In principle, the symmetry-based pulse sequences do not need additional decoupling if the averaging of the heteronuclear dipolar couplings by the symmetry-based pulse sequence itself works sufficiently well [72, 73]. Such an approach works best at high spinning and high nutation frequencies. However, in the regime of moderate spinning frequencies (25-50 kHz), proton decoupling during the mixing time is essential to achieve efficient polarization transfer. Proton decoupling during symmetry-based sequences on the X channel is usually achieved using cw irradiation on the protons. As a rule of thumb, it was postulated that the rf field on the protons should be at least three times the rf field on the X nucleus to achieve good decoupling performance [74, 75]. This demand on the proton rf-field amplitude has led to the development of pulse sequences with lower rf-field requirements on the X nuclei [76]. An added complication is the fact, that the polarization-transfer efficiency does not increase steadily with increasing decoupling rf field but shows strong modulations which make an experimental optimization of the decoupling field strength more demanding (see Fig. 3.5).

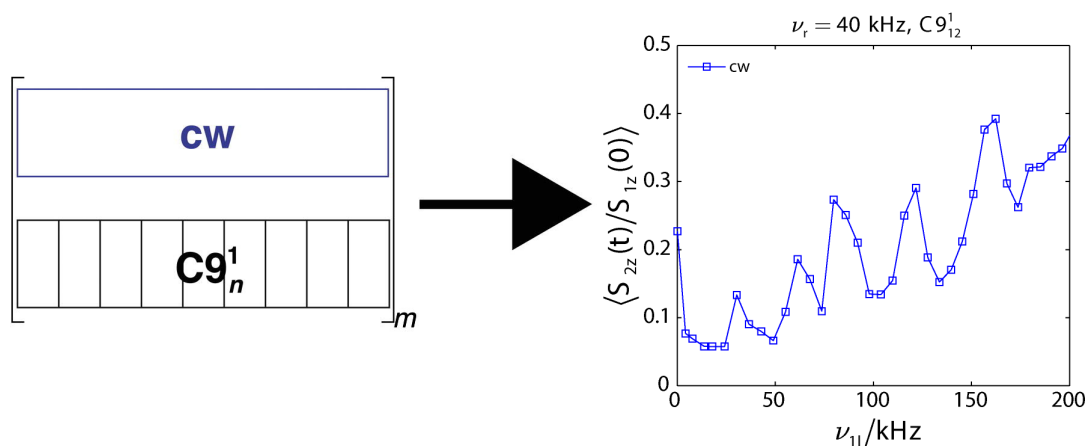


**Figure 3.5** The interference effect between decoupling and C sequence.

The strong dependence of the transfer efficiency on the decoupling is a result of heteronuclear recoupling through matching of the decoupling rf-field amplitude to multiples of the modulation frequency of the symmetry-based pulse sequence and to the MAS frequency [72]. Good decoupling can only be achieved by using either very high rf-field amplitudes or at intermediate rf-field amplitudes where the recoupling conditions are avoided. There are pulsed recoupling schemes where more complex decoupling schemes like TPPM [52] have



been used during the recoupling sequence [77, 78], but such an approach has, to the best of our knowledge, not yet been reported during windowless pulse sequences on the X channel. Here, we analyze the heteronuclear recoupling interference between symmetry-based C sequences and CW decoupling (Fig. 3.6) in more detail using operator-based Floquet theory [33, 34] and then generalize it to amplitude-modulated decoupling sequences like XiX (Fig. 3.6) [50, 79].

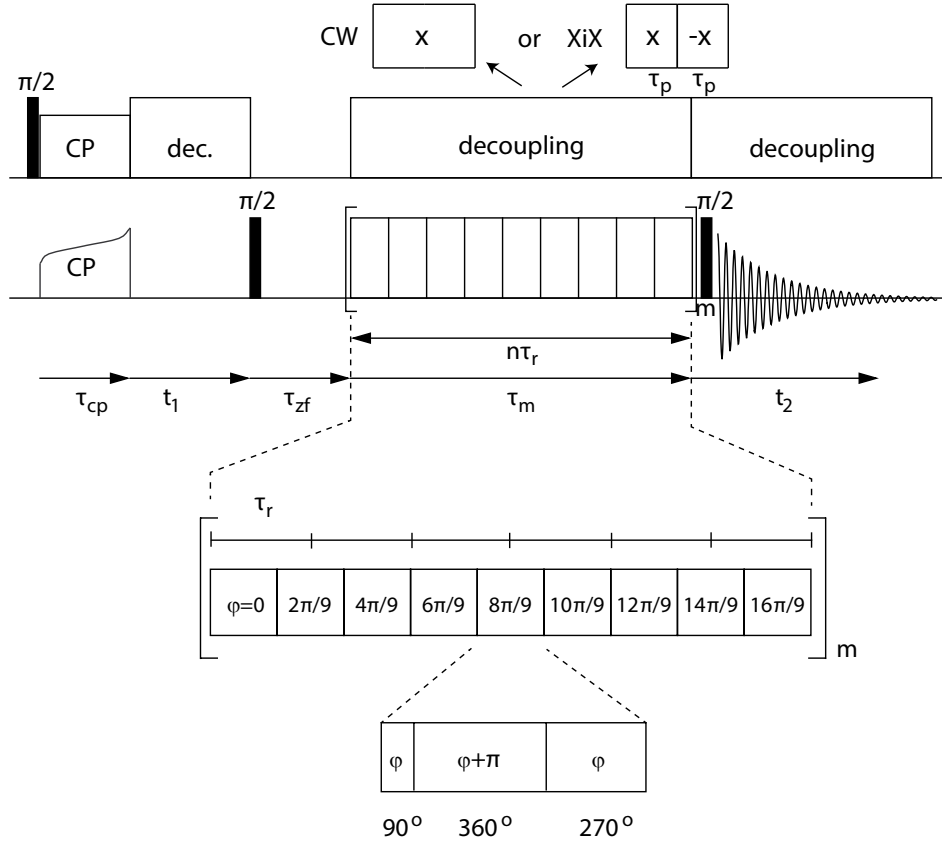


**Figure 3.6** Pulse sequence for a two-dimensional homonuclear TOBSY correlation experiment using a  $C9_6^1$  sequence for the polarization transfer and cw or XiX decoupling during the mixing time.

### 3.2.1 Floquet Theory and Effective Hamiltonian

The general first-order effective Hamiltonian and the selection rules were shown explicitly in Sec. 3.1.2. If we inspect the selection rules (Eq. 3.10) of a  $C9_n^1$  TOBSY sequence, one can see that the non-zero values of  $a_{\ell,s}^{(k)}$  are found for  $k = 9z$  for  $s=0$ ,  $k = 9z \pm 1$  for  $s = \mp 1$ , and  $k = 9z \pm 2$  for  $s = \mp 2$  (see Fig. 3.4). Following from Eq. (3.9) and the fact that  $n_0$  is restricted to the values of  $\pm 1$  and  $\pm 2$  in the first-order Hamiltonian, all  $C9_n^1$  sequences with  $n = 9p \pm 3$  where  $p$  is an integer can be used as TOBSY sequences since they do not recouple any resonant terms in Eq. (3.5) except  $\hat{\mathcal{H}}^{(0,0)}$ , which is scalar or isotropic in

nature. Therefore, the effective first-order TOBSY Hamiltonian is given by

$$\hat{\mathcal{H}}^{(1)} = \omega_{1,2}^{(0)} T_{0,0}^{(1,2)} + \sum_{p=1}^2 \omega_p^{(0)} a_{1,0}^{(0)} T_{1,0}^{(p)} + \sum_{p=1}^2 \omega_{1p}^{(0)} \frac{-1}{\sqrt{3}} T_{1,0}^{(I)} a_{1,0}^{(0)} T_{1,0}^{(p)} + \omega_1^{(0)} T_{1,0}^{(I)} \quad (3.11)$$

which can be simplified to

$$\hat{\mathcal{H}}^{(1)} = \omega_{1,2}^{(0)} T_{0,0}^{(1,2)} + \omega_1^{(0)} T_{1,0}^{(I)} \quad (3.12)$$

since the  $a_{1,0}^{(0)}$  Fourier coefficient is zero if the flip angle of the basic C element is an integer multiple of  $2\pi$ . In principle, the  $C9_n^1$  sequences can be used without any additional decoupling on the  $I$  spins since the sequence itself decouples the  $S$  spins from the  $I$  spins. In practice, however, additional proton irradiation is almost always required in order to increase the transfer efficiency if the MAS frequency is not fast enough to suppress the higher order terms. We will now inspect the situation when CW decoupling is applied during the C9 mixing sequence.

### C9 with CW or XiX Decoupling

The description of the  $C9_n^1$  sequences becomes more complex when there is simultaneous rf irradiation on the protons. In this situation, the resulting interaction-frame Hamiltonian has three basic frequencies  $\omega_r$ ,  $\omega_m^{(S)}$ , and the rf-field amplitude  $\omega_{1I}$  in the case of cw irradiation or the modulation frequency  $\omega_m^{(I)}$  in the case of an amplitude modulated sequences like the XiX sequence [50, 79]. Again, the Hamiltonian can be expressed in the form of Fourier series as

$$\hat{\mathcal{H}}(t) = \sum_{n=-2}^2 \sum_{k=-\infty}^{\infty} \sum_{\ell=-\infty}^{\infty} \hat{\mathcal{H}}^{(n,k,\ell)} e^{in\omega_r t} e^{ik\omega_m^{(S)} t} e^{i\ell\omega_m^{(I)} t} \quad (3.13)$$

in which the Fourier components of the Hamiltonian are given by

$$\begin{aligned} \hat{\mathcal{H}}^{(0,k,\ell)} &= \left\{ \omega_{1,2}^{(0)} T_{0,0}^{(1,2)} \right\} \delta_{k,0} \delta_{\ell,0} + \left\{ \sum_{p=1}^2 \omega_p^{(0)} \sum_{s=-1}^1 a_{1,s}^{(k)} T_{1,s}^{(p)} \right\} \delta_{\ell,0} + \left\{ \omega_1^{(0)} \sum_{s=-1}^1 a_{1,s}^{(\ell)} T_{1,s}^{(I)} \right\} \delta_{k,0} \\ &\quad + \sum_{p=1}^2 \omega_{1p}^{(0)} \frac{-1}{\sqrt{3}} \sum_{s=-1}^1 a_{1,s}^{(\ell)} T_{1,s}^{(I)} \sum_{s=-1}^1 a_{1,s}^{(k)} T_{1,s}^{(p)} \\ \hat{\mathcal{H}}^{(n,k,\ell)} &= \left\{ \omega_1^{(n)} \sum_{s=-1}^1 a_{1,s}^{(\ell)} T_{1,s}^{(I)} \right\} \delta_{k,0} + \left\{ \omega_{1,2}^{(n)} \sum_{s=-2}^2 a_{2,s}^{(k)} T_{2,s}^{(1,2)} + \sum_{p=1}^2 \omega_p^{(n)} \sum_{s=-1}^1 a_{1,s}^{(k)} T_{1,s}^{(p)} \right\} \delta_{\ell,0} \\ &\quad + \sum_{p=1}^2 \omega_{1p}^{(n)} \frac{2}{\sqrt{6}} \sum_{\chi=-1}^1 a_{1,\chi}^{(\ell)} T_{1,\chi}^{(I)} \sum_{s=-1}^1 a_{1,s}^{(k)} T_{1,s}^{(p)} \end{aligned} \quad (3.14)$$

In this representation, the differences between cw irradiation and amplitude-modulated decoupling schemes on the protons are encoded in the values of the Fourier coefficients  $a_{1,s}^{(\ell)}$  and  $a_{2,s}^{(\ell)}$ . The values of these coefficients can be determined as described above. Analytical expressions for the Fourier coefficients of the XiX sequences as well as graphical plots can be found in the literature [50]. To achieve efficient heteronuclear decoupling, first-order resonance conditions that reintroduce parts of the heteronuclear dipolar couplings have to be avoided. Such resonance conditions are defined by

$$n_0\omega_r + k_0\omega_m^{(S)} + \ell_0\omega_m^{(I)} = 0 \quad (3.15)$$

and the resulting effective Hamiltonian is given by

$$\hat{\mathcal{H}}^{(1)} = \hat{\mathcal{H}}^{(0,0,0)} + \sum_{n_0,k_0,\ell_0} \hat{\mathcal{H}}^{(n_0,k_0,\ell_0)} \quad (3.16)$$

where

$$\hat{\mathcal{H}}^{(n_0,k_0,\ell_0)} = \sum_{p=1}^2 \omega_{1p}^{(n_0)} \frac{2}{\sqrt{6}} \sum_{\chi=-1}^1 a_{1,\chi}^{(\ell_0)} T_{1,\chi}^{(I)} \sum_{s=-1}^1 a_{1,s}^{(k_0)} T_{1,s}^{(p)} \quad (3.17)$$

and the second term in Eq. (3.16) sums over all sets of  $(n_0, k_0, \text{ and } \ell_0)$  that fulfil the resonance condition (Eq. (3.15)). Note that Eq. (3.17) contains undesirable heteronuclear dipolar components that lead to a decay of magnetization during TOBSY and hence lower transfer. The magnitude of this contribution can be expressed as a function of  $\omega_m^{(I)}/\omega_r$  by summing over all contributions of Eq. (3.17) and simplifying the expression to

$$I_{\text{IS}} \left( \frac{\omega_m^{(I)}}{\omega_r} \right) \leq \sum_{n_0=-2, \neq 0}^2 \sum_{\ell_0=-\infty}^{\infty} \sum_{s=-1}^1 \sum_{\chi=-1}^1 \left| a_{1,s}^{-(\ell_0\omega_m^{(I)}/\omega_m^{(S)} + n n_0)} \right| \left| a_{1,\chi}^{(\ell_0)} \right| \quad (3.18)$$

where again in the case of cw decoupling the term  $\omega_m^{(I)}/\omega_r$  has to be replaced by  $\omega_{\text{II}}/\omega_r$ .

Figure 3.7 shows a plot of Eq. (3.18) which represents the upper limit of the magnitude of the recoupled heteronuclear dipolar coupling for the case of cw irradiation on the protons for the  $\text{C9}_6^1$  (Fig. 3.7a) and the  $\text{C9}_{12}^1$  (Fig. 3.7b) TOBSY sequences using POST as a basic C element. One can clearly see that there are windows with minimal decoupling interference around  $\omega_{\text{II}}/\omega_r = 3z/2$  for the  $\text{C9}_6^1$  sequence and around  $\omega_{\text{II}}/\omega_r = 3z/4$  for the  $\text{C9}_{12}^1$  sequence where  $z$  is an integer. Moreover, the plot shows that at higher decoupling field strength as well as in the case of no decoupling, the magnitude of the interference terms is reduced, which agrees with experimental observations. The strong modulation of the transfer efficiency as a function of the decoupling rf-field strength observed experimentally

can, indeed, be explained by the interference profile. Therefore, optimizing the decoupling rf-field amplitude is very important for an efficient polarization transfer in the cw case, and using the highest available rf-field amplitude does not necessarily give the best result.

For decoupling using the XiX sequence, we have two free parameters, namely the modulation frequency  $\omega_m^{(1)}$  and the rf-field amplitude  $\omega_{11}$ . Figures 3.7c and d show a plot of the magnitude of the decoupling interference as a function of  $\omega_m^{(1)}/\omega_r$  and  $\omega_{11}/\omega_m^{(1)}$ . The plot shows that for certain XiX modulation frequencies there are no first-order interference terms for all rf-field amplitudes. Decoupling at these XiX modulation frequencies has an

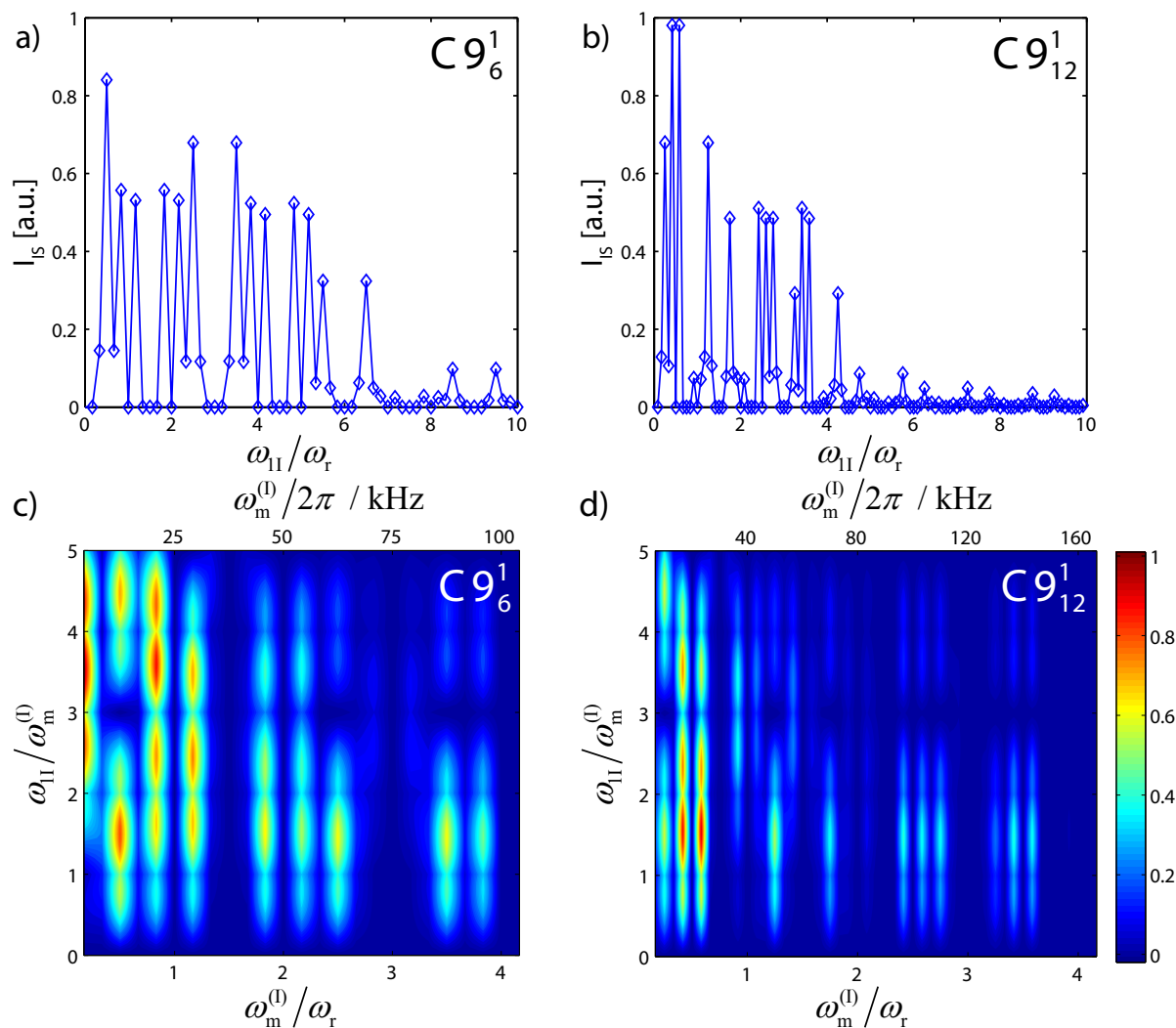


**Figure 3.7** Plot of the magnitude of the undesired first-order heteronuclear recoupling for cw irradiation as a function of the ratio  $\omega_{11}/\omega_r$  for a) the  $C9_6^1$  and b) the  $C9_{12}^1$  TOBSY sequences. The lines connecting the data points are a guide to the eye. Plot of the magnitude of the analytical first-order heteronuclear recoupling under decoupling using XiX irradiation as a function of  $\omega_m^{(1)}/\omega_r$  and  $\omega_{11}/\omega_m^{(1)}$  for c) the  $C9_6^1$  sequence and d) the  $C9_{12}^1$  TOBSY sequences. Good decoupling is achieved in areas where the heteronuclear recoupling terms are small.

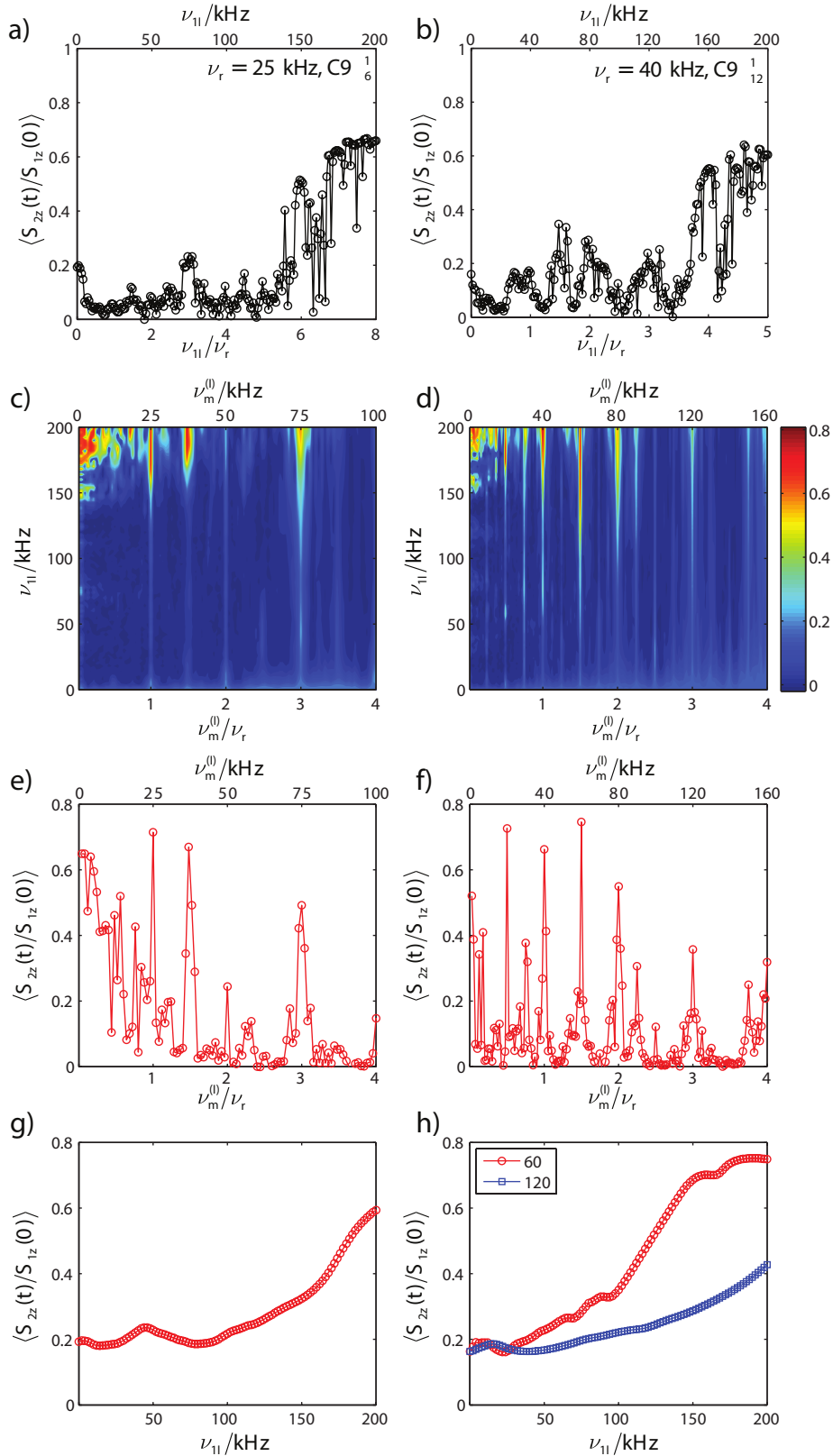
advantage that the rf-field amplitude can be chosen freely without the danger of accidentally fulfilling a heteronuclear dipolar recoupling condition.

### 3.2.2 Simulations and Experimental Results

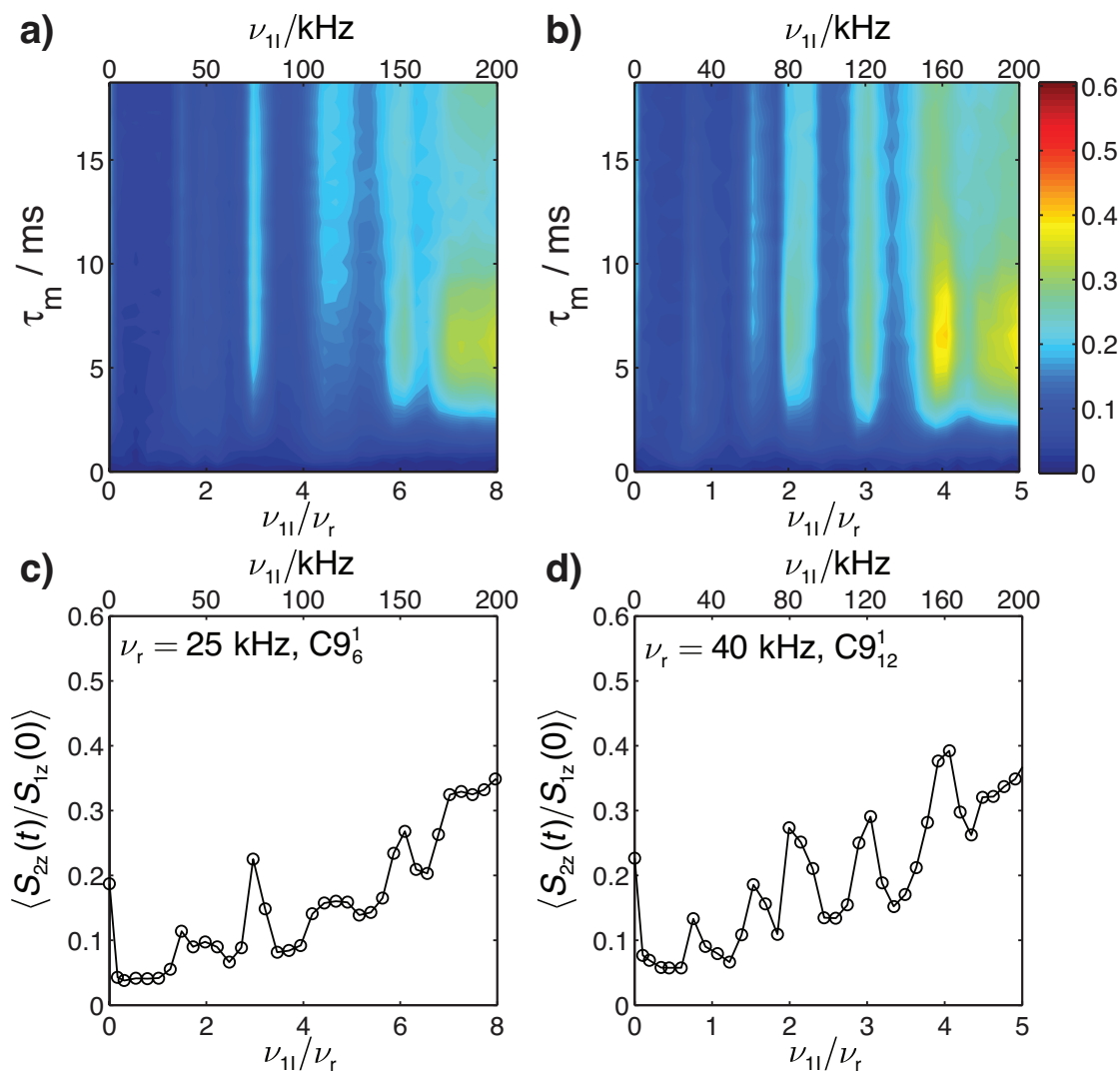
To further characterize the expected decoupling behaviour predicted by the analytical calculations, numerical simulations were carried out on a model four-spin CH<sub>2</sub>-C spin system using the spin-simulation environment GAMMA [80] with the spin parameters of crystalline glycine. Figure 3.8 shows a plot of the transfer efficiency from the CH<sub>2</sub> group to the quaternary carbon atom as a function of the proton rf-field amplitude for 25 kHz MAS using the C9<sub>6</sub><sup>1</sup> sequence (Fig. 3.8a) and 40 kHz MAS using the C9<sub>12</sub><sup>1</sup> sequence (Fig. 3.8b). Details of the simulation parameters can be found in the caption of Fig. 3.8. The regions of high polarization transfer can be correlated with the region of low magnitude of recoupled heteronuclear dipolar coupling in Fig. 3.7. For the C9<sub>6</sub><sup>1</sup> sequence, we see a local maximum of the polarization transfer at the ratio of  $\omega_{11}/\omega_r = 1.5$  and 3 which correspond to areas where the first-order recoupling Hamiltonian is minimum (Fig. 3.7a). The same type of patterns can be observed for the C9<sub>12</sub><sup>1</sup> sequence where polarization transfer is increased in areas of low first-order dipolar recoupling (Fig. 3.7b).

Figure 3.8 show the same type of transfer-efficiency simulations for XiX decoupling as a function of the XiX modulation frequency and the rf-field amplitude again for 25 kHz MAS using the C9<sub>6</sub><sup>1</sup> sequence (Fig. 3.8c) and 40 kHz MAS using the C9<sub>12</sub><sup>1</sup> sequence (Fig. 3.8d). There is again high polarization transfer for values of  $\omega_m^{(1)}/\omega_r$  where we observe no heteronuclear recoupling terms (Fig. 3.7c and d). Such areas can be found for  $\omega_m^{(1)}/\omega_r = 1, 1.5, 2,$  and 3 at both 25 and 40 kHz MAS (Figs. 3.8c and d). Figures 3.8e and f show slices through the 2D plots of Fig. 3.8c and d for  $\nu_{11} = 180$  kHz. Although the conditions for good decoupling are quite narrow in the  $\omega_m^{(1)}/\omega_r$  dimension, the pulse length of the decoupling sequence can be adjusted accurately, hence preserving the experimental robustness of the decoupling sequence. The dependence on the rf-field amplitude  $\nu_{11}$  is, as expected, more linear which is illustrated in slices through  $\nu_m^{(1)}/\nu_r = 3$  (Fig. 3.8g) for 25 kHz MAS and  $\nu_m^{(1)}/\nu_r = 1.5$  and 3 (Fig. 3.8h) for 40 kHz MAS. In contrast to cw decoupling, the transfer efficiency increases steadily with increasing rf-field amplitudes since the first-order resonance conditions depend only on  $\nu_m^{(1)}$  but not on  $\nu_{11}$ . Nevertheless, the increasing transfer efficiency can only be understood if one considers higher-order contributions to the effective Hamiltonians, which have an implicit dependence on  $\nu_{11}$ .

To verify the results of the theoretical calculations and spin-dynamics simulations, measurements on 1,2-<sup>13</sup>C glycine ethylester were performed as one-dimensional experiments where an initial state was prepared with polarization on the CH<sub>2</sub> group only. The transfer



**Figure 3.8** Simulated transfer efficiency of TOBSY C9 with CW ((a) & (b)) and XiX ((c) & (d)) decoupling.  $C9_6^1$  sequence with  $\nu_r = 25$  kHz and  $\tau_m = 7.2$  ms is used in (a) & (c) while  $C9_{12}^1$  sequence with  $\nu_r = 40$  kHz and  $\tau_m = 6.24$  ms is used in (b) & (d) respectively. e) A slice through (c) at the rf-field amplitude  $\nu_{11} = 180$  kHz, f) a slice through (d) at the rf-field amplitude  $\nu_{11} = 180$  kHz. g) A slice through (c) at the modulation frequency  $\nu_m^{(1)} = 75$  kHz, h) a slice through (d) at  $\nu_m^{(1)} = 60$  and 120 kHz. Efficient polarization transfer is achieved in areas where the decoupling interference (Fig. 3.7) is minimal.



**Figure 3.9** Experimental polarization-transfer efficiencies in 1,2-<sup>13</sup>C-glycine ethylester as a function of the mixing time and the rf-field amplitude of the cw decoupling on protons. a)  $\nu_r = 25$  kHz using the C9<sub>6</sub><sup>1</sup> sequence b)  $\nu_r = 40$  kHz using the C9<sub>12</sub><sup>1</sup> sequence. c) A slice through a) at the mixing time  $\tau_m = 6.24$  ms, d) a slice through b) at the mixing time  $\tau_m = 7.2$  ms.

of polarization to the carbonyl group was then measured as a function of various parameters. All experiments were carried out on a Varian Infinity+ 500 MHz spectrometer using a home-built 1.8 mm double-resonance MAS probe [81]. Figure 3.9 shows the experimental polarization-transfer efficiency as a function of the mixing time and the decoupling rf-field amplitude for spinning frequencies of 25 kHz (Fig. 3.9a) and 40 kHz (Fig. 3.9b). Slices through the maximum of the polarization transfer at mixing times of  $\tau_m = 6.24$  and 7.2 ms, respectively, are shown in Figs. 3.9c and 3.9d. The experimental polarization-transfer profile as a function of the cw decoupling rf-field amplitude shows the same features as the numerical simulations (Figs. 3.8a and 3.8b). The main difference is that the lines are broadened significantly due to rf-field inhomogeneities present only in the experimental data and,

therefore, the sharp features visible in Fig. 3.8 are smeared out. The overall line shapes, however, are very similar and show maxima and minima at the same positions.

The experimental dependence of the polarization-transfer efficiency under XiX decoupling has also been measured as a function of the XiX modulation frequency and the proton rf-field amplitude for selected areas where good decoupling was expected from the simulations. Figure 3.10 shows experimental polarization-transfer efficiencies for MAS frequencies of 25 kHz (Fig. 3.10a) and 40 kHz (Figs. 3.10b and c) for modulation frequencies of  $\omega_m^{(1)} = 1.5\omega_r$  (Fig. 3.10b) and  $\omega_m^{(1)} = 3\omega_r$  (Figs. 3.10a and c). As expected, best polarization transfer is obtained when the correct modulation frequency is used, as can be seen from Figs. 3.10d-f, which show slices through Figs. 3.10a-c at an rf-field amplitude of 200 kHz. There is an almost steady increase of the polarization-transfer efficiency with increasing rf-field strength as can be seen from Figs. 3.10g-i which show a slice through the ideal modulation frequencies of Figs. 3.10a-c.

### 3.2.3 Conclusions

The simulations and measurement shown in the previous sections clearly show that XiX decoupling is a viable alternative to cw decoupling during TOBSY transfer mediated by  $C9_n^1$  sequences. The advantage of the XiX decoupling during the  $C9_n^1$  sequence is best illustrated in Fig. 3.11 where the polarization-transfer efficiency under cw and XiX decoupling is compared as a function of the rf-field amplitude. At almost all rf-field amplitudes, XiX decoupling leads to an improved polarization transfer. In addition, optimization of the XiX sequences in terms of the rf-field amplitude is straightforward. Typically, the hypothesis that the highest rf-field amplitude possible will give the best polarization transfer is clearly invalid for the cw decoupling during the  $C9_n^1$  TOBSY sequence. To achieve the same level of polarization transfer, much lower decoupling fields can be used. This is shown in Fig. 3.12 which shows TOBSY spectra of the tripeptide MLF at a MAS frequency of 40 kHz using the  $C9_{12}^1$  sequence and cw decoupling (Fig. 3.12a) with a decoupling rf-field amplitude of  $\nu_{11} = 195$  kHz and for comparison one using XiX decoupling (Fig. 3.12b) with a modulation frequency of  $\nu_m^{(1)} = 1.5\nu_r = 60$  kHz and a decoupling field strength of  $\nu_{11} = 130$  kHz. Two slices through the resonances of Leu-C $\alpha$  and Met-C $\beta$  (Figs. 3.12c and d) show that the polarization-transfer efficiency of the two spectra is very similar with slightly higher efficiencies in the XiX decoupled spectrum while the decoupling power has been reduced by roughly a factor of two.



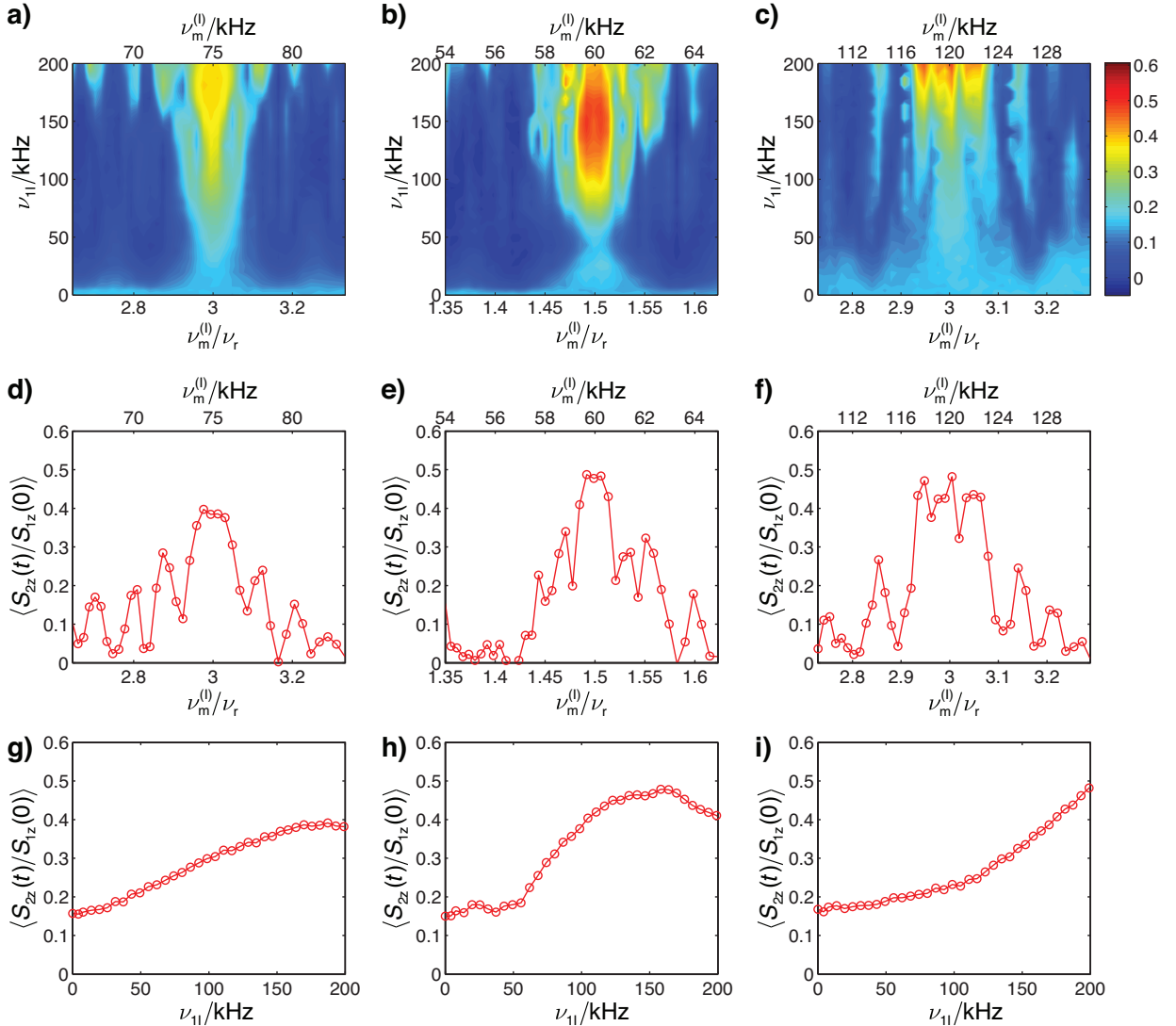


**Figure 3.10** Experimental polarization-transfer efficiency under proton XiX decoupling in 1,2- $^{13}\text{C}$ -glycine ethyl ester as a function of the rf-field amplitude  $\nu_{\text{II}}$  and the modulation frequency  $\nu_{\text{m}}^{(1)}$ . a)  $\nu_{\text{r}} = 25$  kHz using the  $\text{C9}_6^1$  sequence around the condition  $\omega_{\text{II}}/\omega_{\text{r}} = 3$  at a mixing time of 6.24 ms. b)  $\nu_{\text{r}} = 40$  kHz using the  $\text{C9}_{12}^1$  sequence around the condition  $\omega_{\text{II}}/\omega_{\text{r}} = 1.5$  at a mixing time of 6.6 ms. c)  $\nu_{\text{r}} = 40$  kHz using the  $\text{C9}_{12}^1$  sequence around the condition  $\omega_{\text{II}}/\omega_{\text{r}} = 3$  at a mixing time of 6.6 ms. d) A slice through a) at the rf-field amplitude  $\nu_{\text{II}} = 181$  kHz, e) a slice through b) at the rf-field amplitude  $\nu_{\text{II}} = 164$  kHz, and f) a slice through c) at the rf-field amplitude  $\nu_{\text{II}} = 200$  kHz. g) A slice through a) at the modulation frequency  $\nu_{\text{m}}^{(1)} = 75.3$  kHz, h) a slice through b) at the modulation frequency  $\nu_{\text{m}}^{(1)} = 60$  kHz, and i) a slice through c) at the modulation frequency  $\nu_{\text{m}}^{(1)} = 120$  kHz.

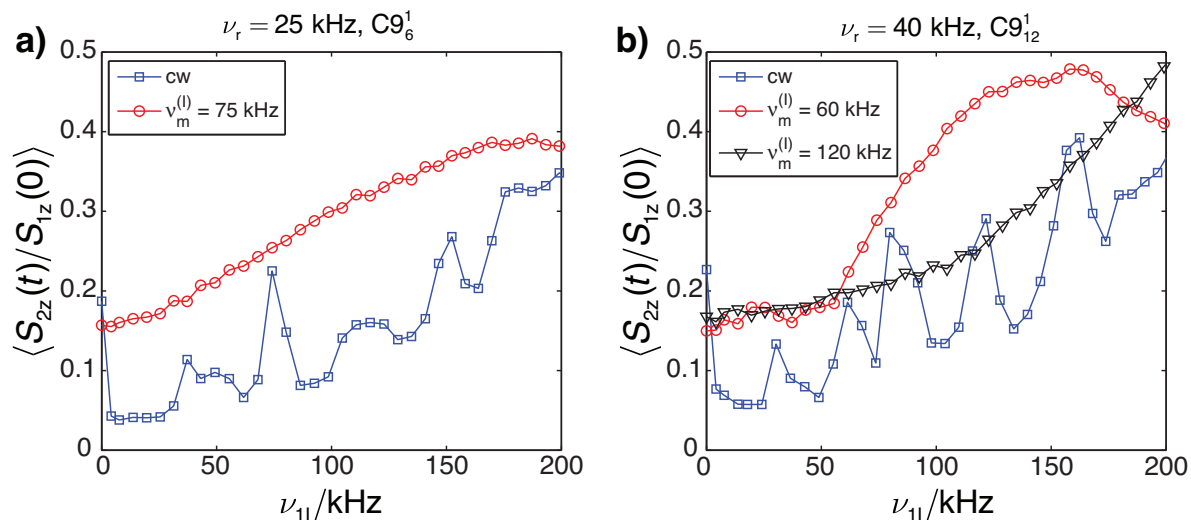


**Figure 3.11** Comparison of the experimental polarization-transfer efficiencies in 1,2- $^{13}\text{C}$  glycine ethyl ester as a function of the rf-field amplitude of XiX decoupling. a)  $\nu_r = 25 \text{ kHz}$  using the  $\text{C9}_6^1$  sequence using cw decoupling (blue squares) and XiX decoupling with a modulation frequency of 75 kHz (red circles) at a mixing time of 6.24 ms. b)  $\nu_r = 40 \text{ kHz}$  using the  $\text{C9}_{12}^1$  sequence using cw decoupling (blue squares) at 7.2 ms and XiX decoupling with a modulation frequency of 60 kHz (red circles) and 120 kHz (black triangles) at a mixing time of 6.6 ms.

### 3.2.4 Further Discussions

It was discussed in the literature [82, 83] that the symmetry-based pulse sequences can be supercycled (SC) to compensate unwanted higher-order cross-terms and experimental errors like misset of rf values. The transfer efficiency of supercycled TOBSY, along with the interference analysis will be investigated. In addition, the heteronuclear scalar coupling  $J_{IS}$  was neglected in the interference analysis because the size of the coupling is much smaller than the dipolar coupling. The justification of this assumption will also be discussed briefly here. Apart from the interference analysis, it was observed that the transfer efficiency of TOBSY is influenced by the spin diffusion. The impact of spin diffusion will be studied in this section.

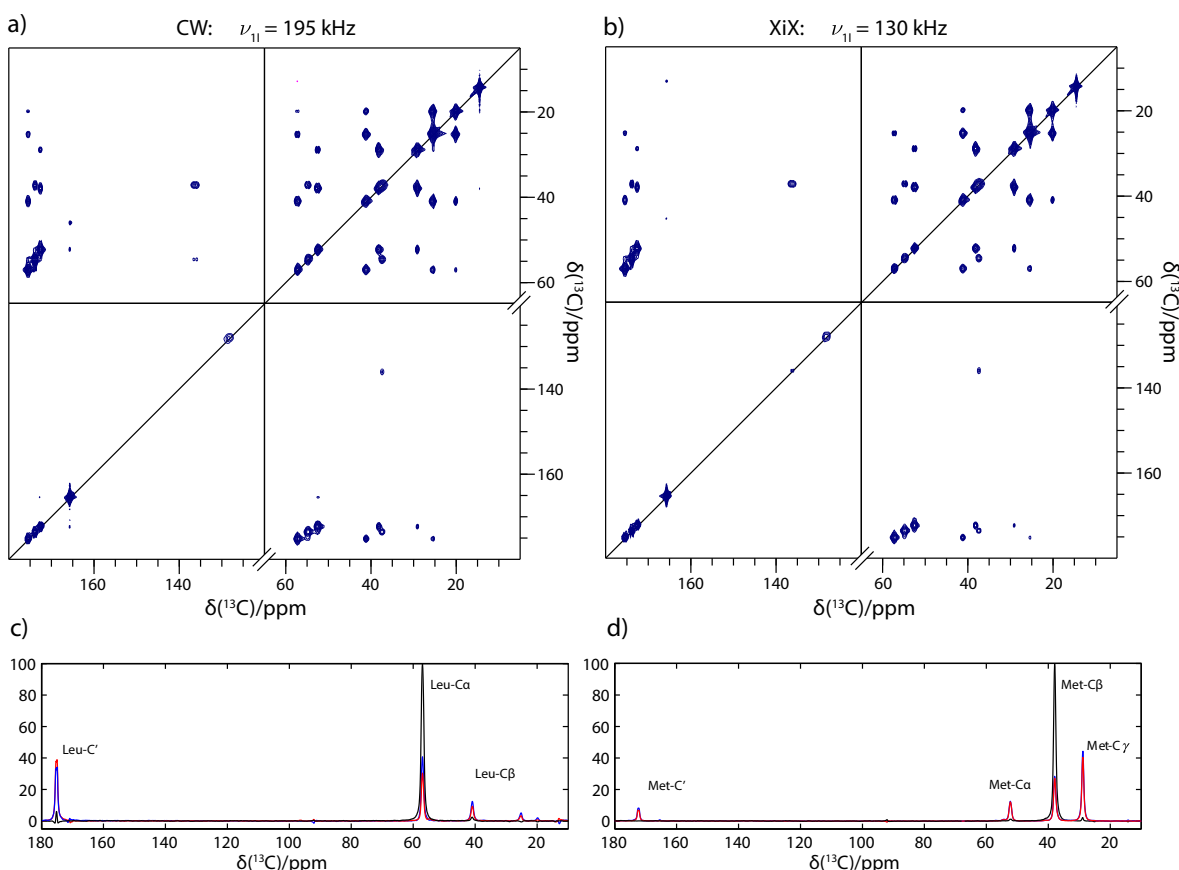


**Figure 3.12** Experimental TOBSY spectra recorded with the pulse sequence shown in Fig. 3.6 on the tripeptide MLF at a MAS frequency of 40 kHz using the  $C9_{12}^1$  sequence with a mixing time of 7.8 ms. The spectrum in a) was recorded using cw decoupling during the mixing time with an rf-field amplitude of  $\nu_{11} = 195$  kHz while the spectrum in b) was recorded using XiX decoupling during the mixing time with a modulation frequency of  $\nu_m^{(1)} = 1.5\nu_r = 60$  kHz and a rf-field amplitude of  $\nu_{11} = 130$  kHz. The slices in c) and d) through two selected resonances show that the polarization-transfer efficiency under XiX decoupling (red) is even slightly better than the polarization-transfer efficiency under cw decoupling (blue) despite the much lower rf-field amplitude. The spectrum in black is the reference spectrum for a vanishing mixing time.

### Supercycle Symmetry-Based C Sequences

We explore one of the supercycled implementations called phase-inverted  $C9_n^V C9_n^{-V}$  [82, 84], in which the phases of all pulses in every second C9 cycle are inverted. It was observed that the phase-inverted SC-C9 (Fig. 3.13b) has a similar profile than the non-supercycled version (Fig. 3.13a) during CW decoupling, and a significant improvement was obtained in the high power region ( $\sim 180$  kHz). An interference analysis was performed for the SC regime to correlate theoretical predictions with the experimental results. In general, the interference profiles for both normal and supercycled TOBSY are indeed similar (Fig. 3.14a), i.e. little interference at  $\omega_{11}/\omega_r = 1.5, 3, \text{ and } 4$ . These theoretical results corroborate well with the experimental results where good TOBSY transfers are observed at decoupling

power of  $\nu_{\text{H}} = 60, 120, \text{ and } 160$  kHz. However, some differences are seen around  $\omega_{\text{H}}/\omega_{\text{r}} = 1.5$  and 3, where three consecutive points with zero scaling factors are no longer observed in the SC regime. This implies that the TOBSY transfer becomes more narrow-banded with respect to the rf field, and this is reflected in the experimental data (Fig. 3.13a and b). As the interference profiles at high decoupling power  $\nu_{\text{H}} = 180$  kHz (Fig. 3.13b) are similar for both TOBSY sequences, there is limited information to support the superior performance of supercycled C9 in the region of high power decoupling at  $\sim 180$  kHz (Fig. 3.13b). We foresee that a determination of second-order Hamiltonians might be needed to provide further insight. On the other hand, the performance of SC-C9 TOBSY with XiX decoupling was also examined and the improvement was marginal (See Sec. A.3.2).

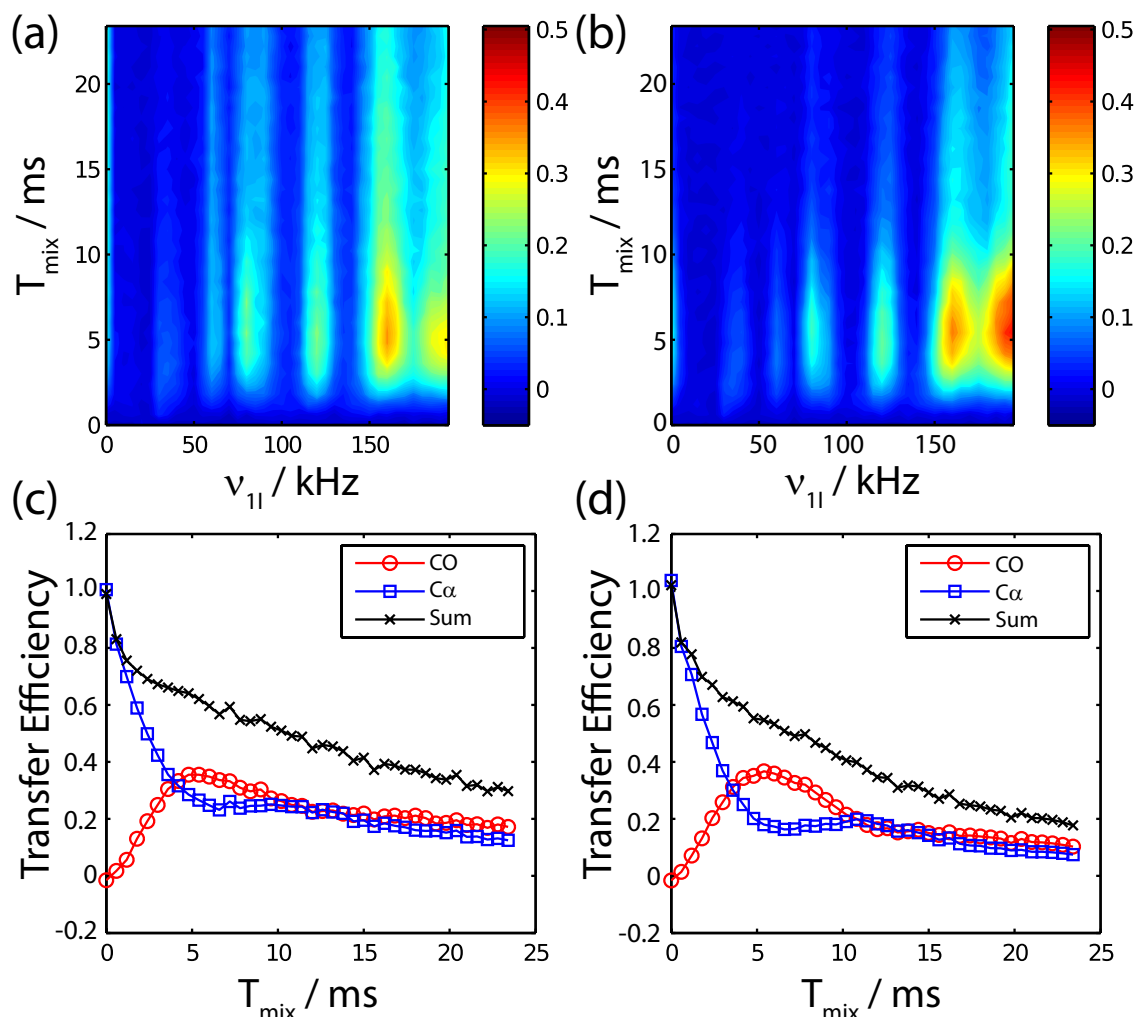


**Figure 3.13** Experimental transfer efficiency of (a,c) TOBSY  $\text{C9}_{12}^1$  (b,d) Supercycle TOBSY  $\text{C9}_{12}^1 \text{C9}_{12}^{-1}$  for 1,2- $^{13}\text{C}$  glycine ethyl ester at  $\nu_{\text{r}} = 40$  kHz. (c,d) show the 1D slice of (a,b) at proton decoupling power of  $\nu_{\text{H}} = 160$  kHz.

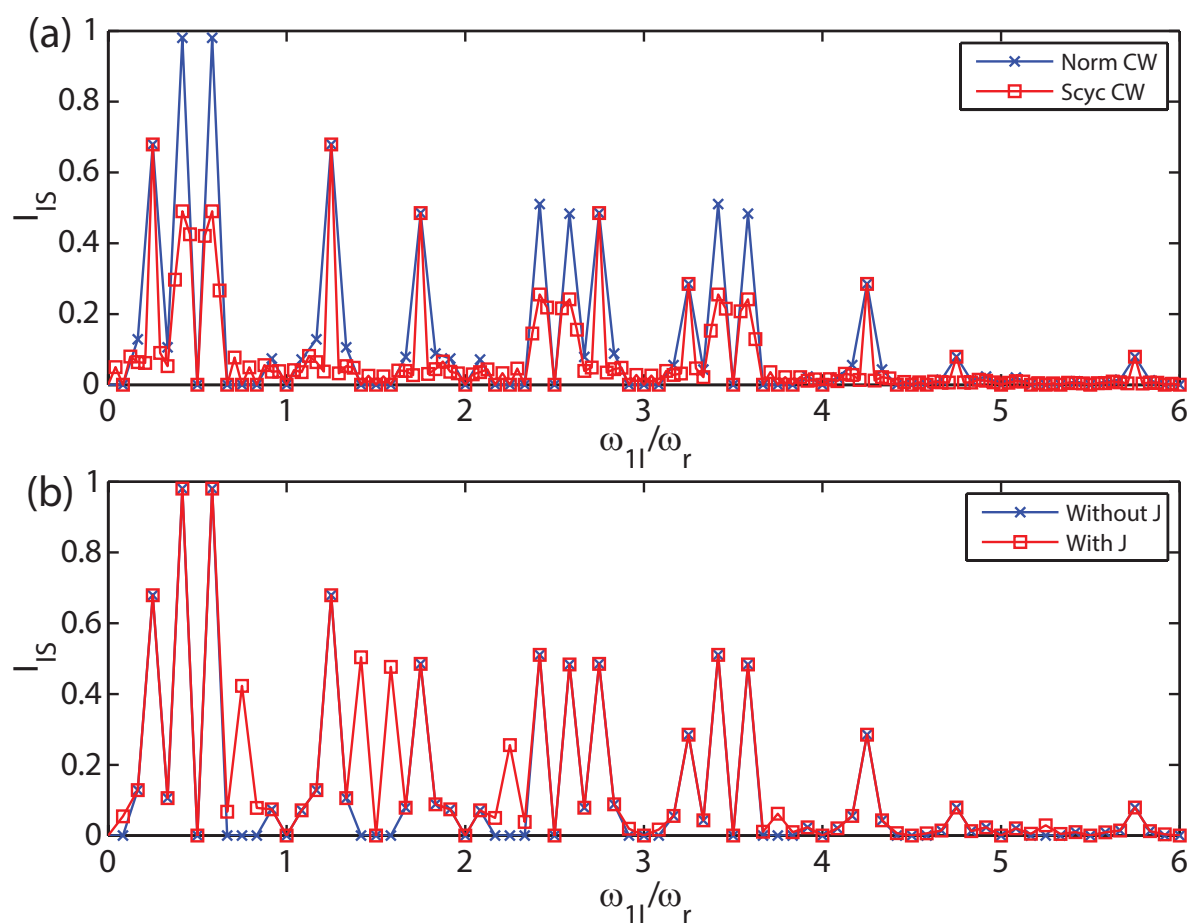


**Figure 3.14** (a) Interference analysis of normal (blue) and supercycled (red) TOBSY C9 sequence during CW decoupling. (b) Interference analysis of normal TOBSY C9<sub>12</sub> sequence with heteronuclear  $J$  coupling included (red) and excluded (blue).

### Inclusion of Heteronuclear $J$ Couplings into the Interference Analysis

In principle, the heteronuclear  $J_{IS}$  coupling can be included easily by considering the  $n_0 = 0$  term in Eq. (3.18), and the remaining part of the interference analysis remains the same. One can see that the inclusion of  $J_{IS}$  in the interference analysis introduces large interferences at  $\omega_{11}/\omega_r \sim 0.8, 1.5$ , and  $2.3$  (Fig. 3.14b). The region at  $\omega_{11}/\omega_r = 1.5$  was originally deemed as a decoupling-free region (Fig. 3.14a) prior to the inclusion of heteronuclear  $J_{IS}$  coupling. As the size of the scaling factor is large, the effective interference strength is approximately  $0.5 \cdot 150 = 75$  Hz, which is large enough to quench the transfer mediated by the homonuclear  $J$  coupling of 55 Hz. While the window at  $\omega_{11}/\omega_r = 3$  remain relatively free and therefore expected to be a better decoupling condition than  $\omega_{11}/\omega_r = 1.5$ . This is in good agreement with experimental results (Fig. 3.9d) where the transfer efficiency is  $\sim 30\%$  at  $\omega_{11}/\omega_r = 3$  and  $\sim 20\%$  at  $\omega_{11}/\omega_r = 1.5$ . Nevertheless, the higher transfer can also be attributed to better second-order cross-term compensation at higher decoupling power.

### Contribution of Spin Diffusion During TOBSY

It was discovered that dipolar-based spin diffusion contributes significantly in the TOBSY sequence. This effect is examined by simulating TOBSY (Fig. 3.15) with the homonuclear  $J$  coupling included (red) or excluded (blue) for various decoupling regimes. The simulation results show that the amount of spin diffusion depends crucially on the parameters chosen for proton decoupling. For instance, the dipolar-based spin diffusion has contributed in between 2 – 30% (blue) to the total transfer of 65 – 75% (red) at a mixing time  $\tau_{\text{mix}}$  of 7–8 ms. The spin diffusion is more significant for XiX decoupling with modulation frequency of  $\nu_{\text{m}}^{(1)} = 75$  kHz (blue cross) than  $\nu_{\text{m}}^{(1)} = 10$  kHz (blue square). This implies that the matched resonance condition of  $\nu_{\text{m}}^{(1)} = 3\nu_{\text{r}}$  (75 kHz) might be a second-order resonant recoupling condition which recouples three-spin flip-flop terms that give rise to spin-diffusion, i.e. like RESORT [86]. While the TOBSY sequence with CW decoupling (blue circle) might be just a non-resonant second-order transfer experiment, i.e. PAR [85] type of experiment.

The effect of spin diffusion can be either advantageous or disadvantageous depending on the context of the experiment. A possible disadvantage is that the experiment is not a strictly through-bond experiment, and this might cause complications or ambiguity in resonance assignment. On the other hand, since both Hamiltonians are ZQ, the presence of dipolar-based spin diffusion could speed up the rate of polarization-transfer, which is evident by inspecting the initial build-up polarization of CW decoupling (red circle) and resonant XiX decoupling (red cross) at  $\tau_{\text{mix}} \leq 7$  ms (Fig. 3.15). This is certainly beneficial if the transfer is hampered by short relaxation time. However, the amount of spin diffusion is inversely related to the maximum attainable transfer efficiency, because the effective transfer is no longer isotropic. This is shown in the case of non-resonant XiX decoupling, which has highest transfer (red square) due to least spin diffusion (blue square).

## 3.3 Low-Power TOBSY Sequences at Fast MAS

In the advent of fast MAS, i.e. up to  $\sim 100$  kHz [87–90], low-power pulse sequences [45, 91] are widely used in biological applications in solid-state NMR because they cause less rf heating on the biological samples. It is our interest to design an efficient low-power TOBSY sequence that employs an rf field that is smaller than the spinning frequency  $\omega_{\text{r}}$ . In order to design an efficient TOBSY sequence, many factors have to be considered, for e.g. the magnitude of the higher order cross terms, offset effect and rf inhomogeneity. In the regime of fast MAS, higher-order cross terms are usually small and they can be neglected, while rf errors and offset issues are more critical. A brute-force scan of symmetry-based pulse sequences combined with cross-term analysis (Sec. 4.2.2) has suggested several

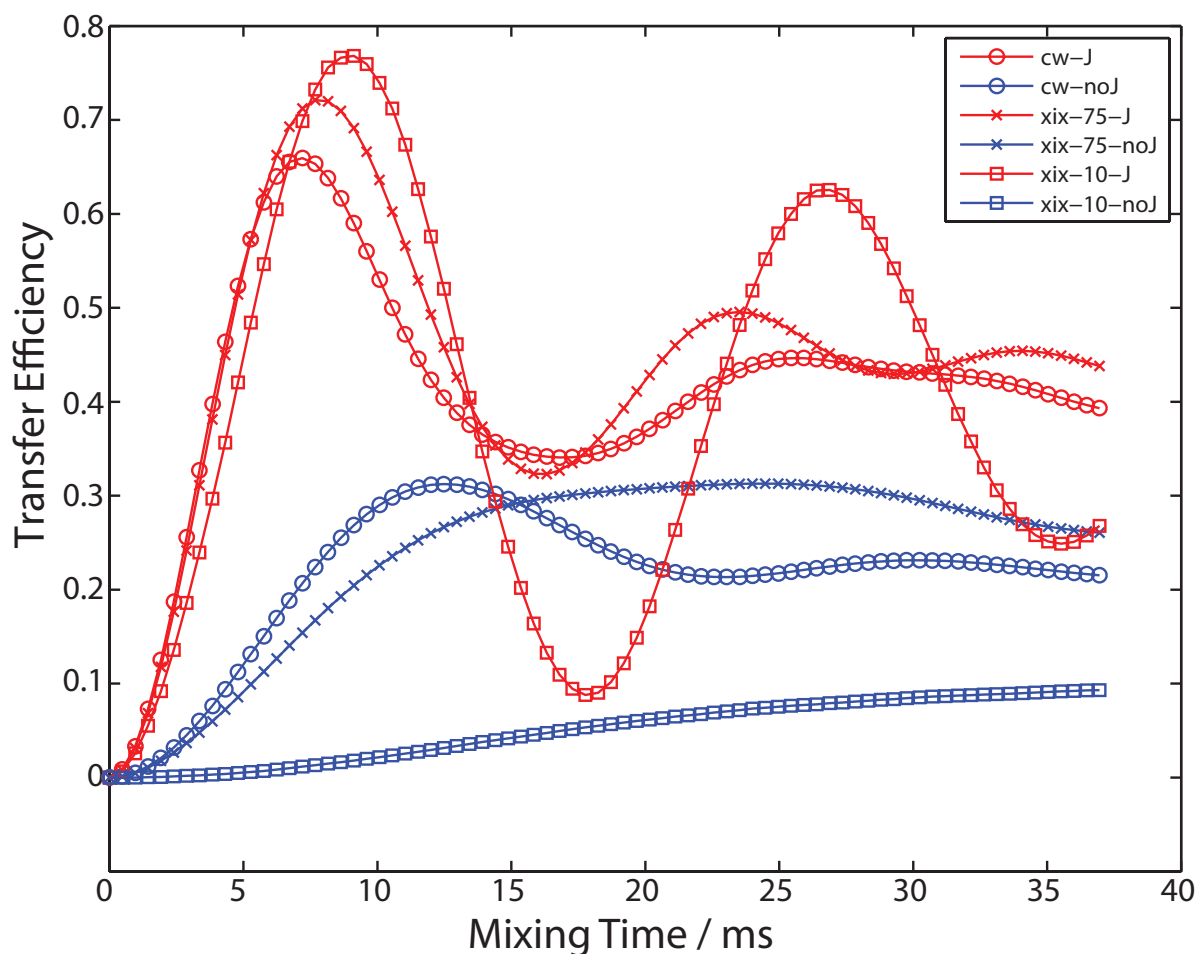


**Figure 3.15** The contribution of spin diffusion during TOBSY is examined by simulating TOBSY  $C9_6^1$  with  $J$  coupling included (red) and excluded (blue) at  $\nu_r = 25$  kHz for a glycine four-spin CCHH system and proton Larmor frequency of 500 MHz. Proton decoupling power of  $\nu_{11} = 180$  kHz using CW (circle), XiX with  $\nu_m^{(1)} = 10$  kHz (square), or  $\nu_m^{(1)} = 75$  kHz (cross).

good candidates<sup>1</sup> with a different range of rf requirements that can be chosen depending on bandwidth of the resonances of interest. We will focus on the conventional  $C9_{39}^1$  and  $C9_{48}^1$  sequence, because the cross-term analysis has indicated that the  $C9_n^1$  family of sequence does not generate any destructive  $\hat{S}^\pm$  term in the second-order Hamiltonian [145]. The rf requirements are  $0.375\nu_r$  for  $C9_{48}^1$  and  $\sim 0.462\nu_r$  for  $C9_{39}^1$ . The performances of these two TOBSY sequences will be examined at two fast MAS regimes, namely at  $\nu_r = 55.5$  kHz and  $\nu_r = 111.1$  kHz, which is suitable for a 1.3 and 0.7 mm probe respectively. The experiments were performed on a simple molecule glycine ethyl ester as a proof of principle, and then extended to ubiquitin to show that it is a practical sequence for biological applications.

<sup>1</sup>They are  $C9_{39}^1$ ,  $C9_{48}^1$ ,  $C15_{50}^1$ ,  $C25_{167}^{10}$ ,  $C25_{167}^5$ ,  $C25_{180}^{12}$ , and  $C23_{240}^{11}$ . Preliminary simulation shows that  $C25_{167}^5$  compensates offset and rf inhomogeneity rather well.

### 3.3.1 Experimental Results on Glycine

The transfer efficiency of TOBSY  $C9_{39}^1$  was measured experimentally on fully protonated glycine ethyl ester at  $\nu_r = 55.5$  kHz (Fig. 3.16). One can see that the rf power employed is only a fraction of the spinning frequency  $\nu_{13C} \sim 0.45\nu_r$ . Moreover, one can see from the build-up curve (Fig. 3.16b) that the oscillations are pronounced and follow a sinusoidal relation ( $\sim \sin(t/2J)$ ) with the peak mixing time at  $\sim 11$  ms, close to the theoretical value of 9.1 ms. A spectrum at the optimum TOBSY transfer (Fig. 3.17) is extracted and it shows that a high transfer of 80% was obtained. One of the factors that contribute to the high transfer is the small rf inhomogeneity due to rf filter after successive CP steps. This effect [92] is discussed explicitly in Sec. A.3.3.

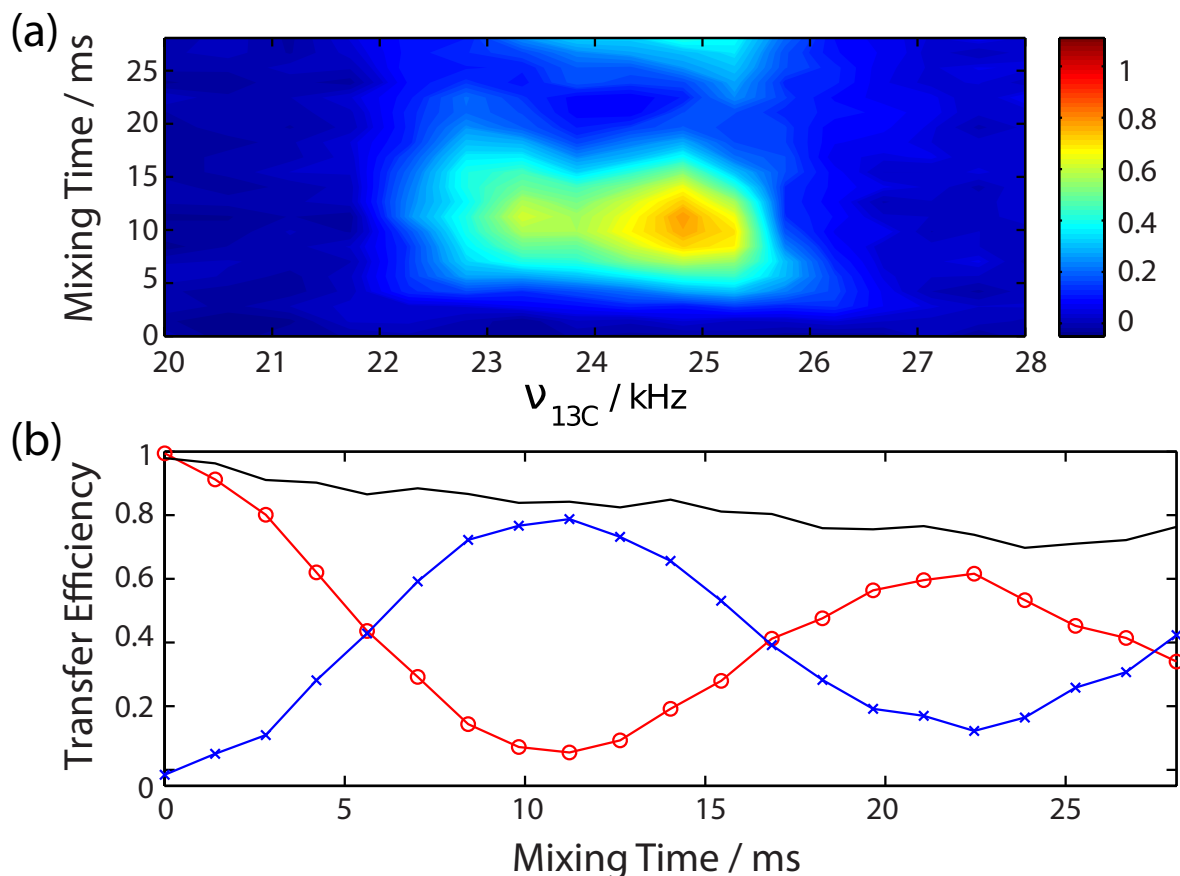


**Figure 3.16** Experimental TOBSY  $C9_{39}^1$  on glycine at 400 MHz with  $\nu_r = 55.5$  kHz. A 1D slice at  $\nu_{13C} = 24.8$  kHz is shown here with Ca (red), Co (blue) and sum (black).



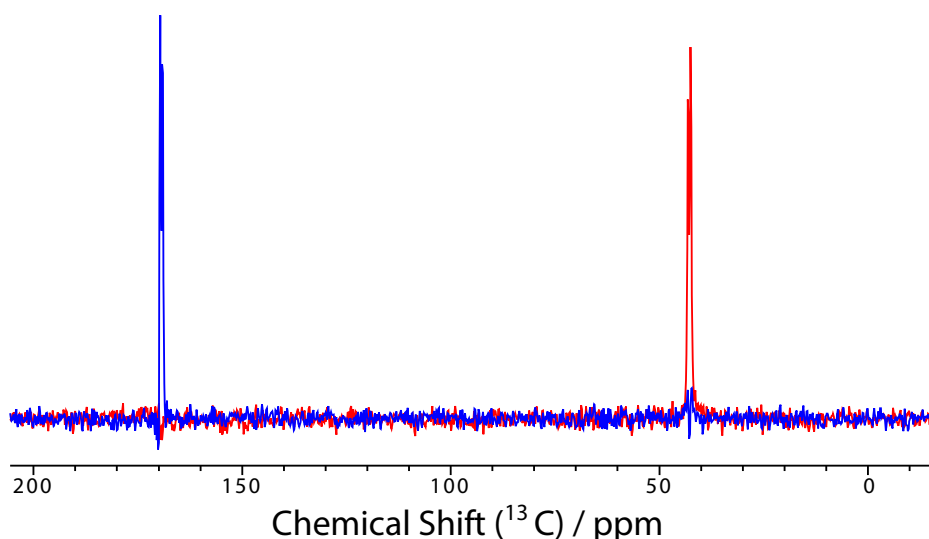


**Figure 3.17** 1D Spectra of low-power TOBSY  $C9_{39}^1$  on glycine ethyl ester from Ca (red) to CO (blue) at 400 MHz with  $\nu_r = 55.5$  kHz and  $\nu_{1S} \sim 25$  kHz. The transfer efficiency is  $\sim 80\%$ . Note that the CO line width is narrower than Ca, thereby having higher peak intensity than the intensity of the source (Ca).

### 3.3.2 Comparing DREAM and TOBSY on Ubiquitin

A comparison of performance between TOBSY and DREAM, an efficient dipolar-based recoupling sequence, will be studied on ubiquitin. We expect that TOBSY is able to spread the polarization further down the side chain compared to the DREAM sequence, for a number of reasons. Firstly, TOBSY is a ZQ sequence and the transferred polarizations have positive sign. On the other hand, DREAM is a DQ sequence and the transferred polarization have opposite sign, this might lead to an effectively lower transfer along the side chains due to the competition between the relay transfer (positive intensity) and the direct transfer (negative intensity). In addition, the TOBSY sequence is isotropic in nature and it does not experience dipolar truncation [56], which is inevitable for the DREAM sequence. Although it can be argued that the circumstance in DREAM can be avoided by strategic optimization of the rf sweeping parameters such that the matching conditions are fulfilled sequentially, the experimental optimization can be laborious. The optimization becomes more difficult as the MAS frequency increases, because the rf field requirement also increases proportionally, thereby causing the offset-dependent effective field to be harder to be manipulated. This is not an issue for the TOBSY sequence, which is essentially not a recoupling sequence. Nevertheless, the TOBSY sequence might suffer from short relaxation time or be susceptible to higher-order cross terms like heteronuclear dipolar coupling. Both factors discussed here, are expected to be less important as MAS frequency increases. Therefore, we ex-

pect TOBSY to be better<sup>2</sup> at higher MAS frequency. The advantage of TOBSY over the DREAM sequence is that the rf field requirement or resonance selectivity can be tailored by choosing different  $CN_n^V$  sequence, while the DREAM sequence has a fixed  $\nu_{rf} = \nu_r/2$  relation<sup>3</sup>. Lastly, in the case of biological macromolecules with flexible parts or motions that greatly averaged dipolar coupling, scalar-based TOBSY remains the only viable option for correlating nuclei. The performances of TOBSY C9 and DREAM were examined by experiments on fully protonated ubiquitin at  $\nu_r = 55.5$  kHz, and deuterated ubiquitin with 100 % back-exchanged with H<sub>2</sub>O at  $\nu_r = 111.1$  kHz.

### Experimental data of TOBSY C9<sub>39</sub><sup>1</sup> at MAS frequency of 55.5 kHz

Figure 3.18 shows the 2D spectrum of protonated ubiquitin at 850 MHz. It was observed that the cross-peak correlating Ca (Fig. 3.18d) in TOBSY is less intense than that of the DREAM sequence. This is expected as the heteronuclear dipolar coupling is still significant to affect the TOBSY transfer. Interestingly, the cross-peaks at around the 20-30 ppm regions (Fig. 3.18d) are much more intense for TOBSY, perhaps due to motion-averaged or smaller heteronuclear dipolar coupling in DREAM. This could also account for the less efficient dipolar-based DREAM sequence due to smaller homonuclear dipolar coupling.

### Experimental data of TOBSY C9<sub>48</sub><sup>1</sup> at MAS frequency of 111.1 kHz

Figure 3.19 shows the 2D spectra of deuterated ubiquitin at 850 MHz. It is evident that more cross peaks are observed in TOBSY than DREAM, implying that TOBSY is more offset-compensating. Furthermore, Fig. 3.19c shows that TOBSY is able to transfer polarization across multiple resonances (for e.g. side chain of Isoleucine) more efficiently than DREAM. Moreover, the total polarization survives longer in TOBSY than DREAM<sup>4</sup>, and therefore relative longer mixing time could be used to spread the polarization further. Nevertheless, DREAM is still feasible for one-bond transfer (Fig. 3.19d).

### 3.3.3 Conclusions

It was demonstrated that low-power TOBSY C9 sequences with  $\nu_{rf} < \nu_r/2$  are efficient sequences for polarization transfer across multiple resonances at MAS frequencies faster than  $\nu_r = 55.5$  kHz, for both protonated or deuterated sample. We intend to apply the TOBSY sequence for proton-detected side-chain assignment [3] at MAS frequencies of  $\nu_r \geq 100$  kHz.

<sup>2</sup> The only remaining problems are the offset effect and rf inhomogeneity.

<sup>3</sup> One can in principle design a low-power DQ recoupling sequence using symmetry-based C sequences

<sup>4</sup> The short  $T_{1\rho}$  in DREAM is perhaps due to Deuterium-induced relaxation, which has to be verified experimentally.

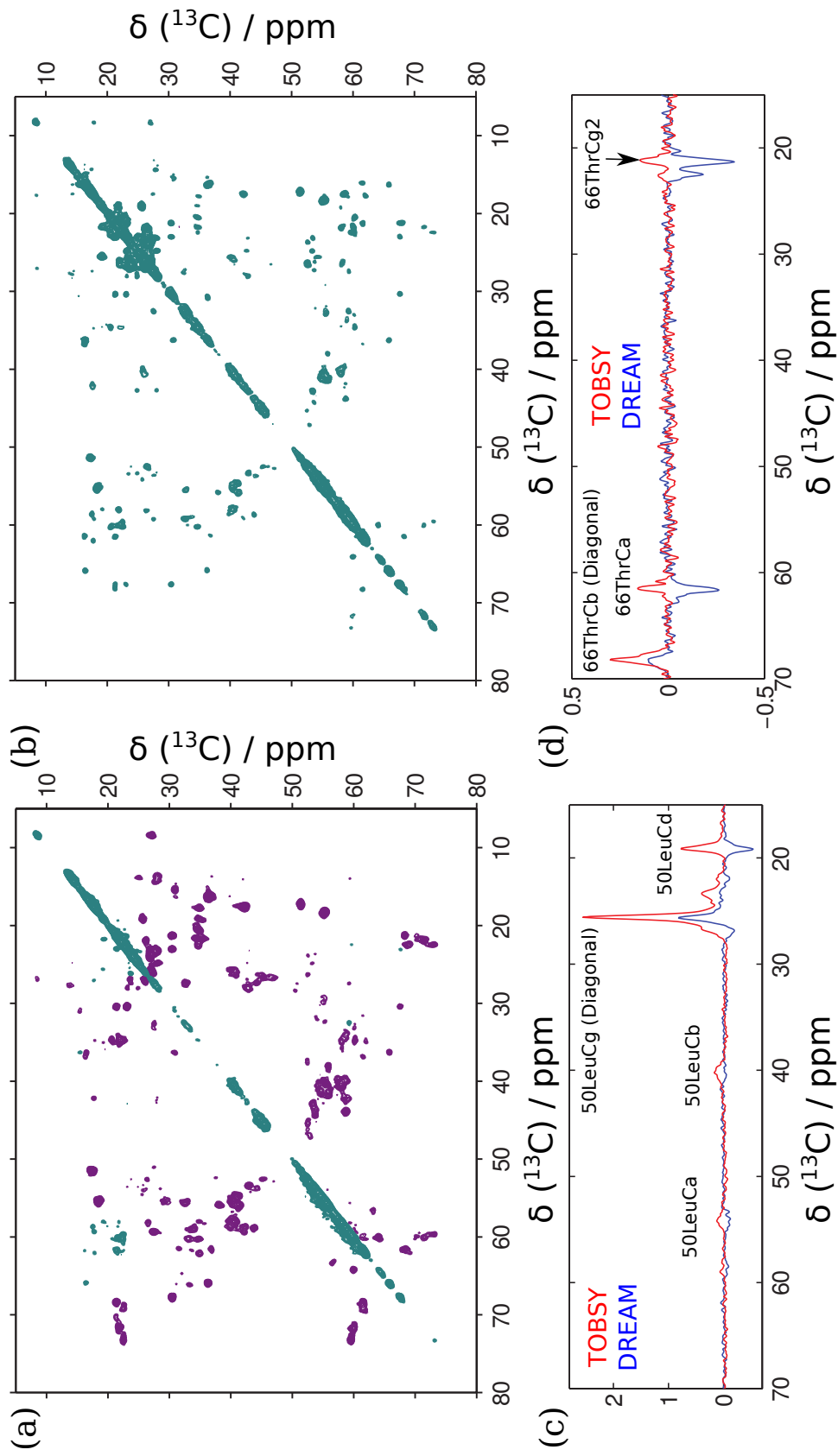


**Figure 3.18** 2D spectra of protonated ubiquitin at  $\nu_r = 55.5$  kHz at 850 MHz without proton decoupling and the measurement time is 7 hours. The mixing sequence used is of (a) DREAM with  $\nu_{\text{IS}} = 29$  kHz with  $\tau_{\text{mix}} \sim 5$  ms or (b) TOBSY C9<sub>48</sub> with  $\nu_{\text{IS}} \sim 21$  kHz with  $\tau_{\text{mix}} \sim 18$  ms, and the carrier frequency of both sequences is at 35 ppm. 1D slice across the resonances of (c) 50LeuCa and (d) 66ThrCb are shown here.

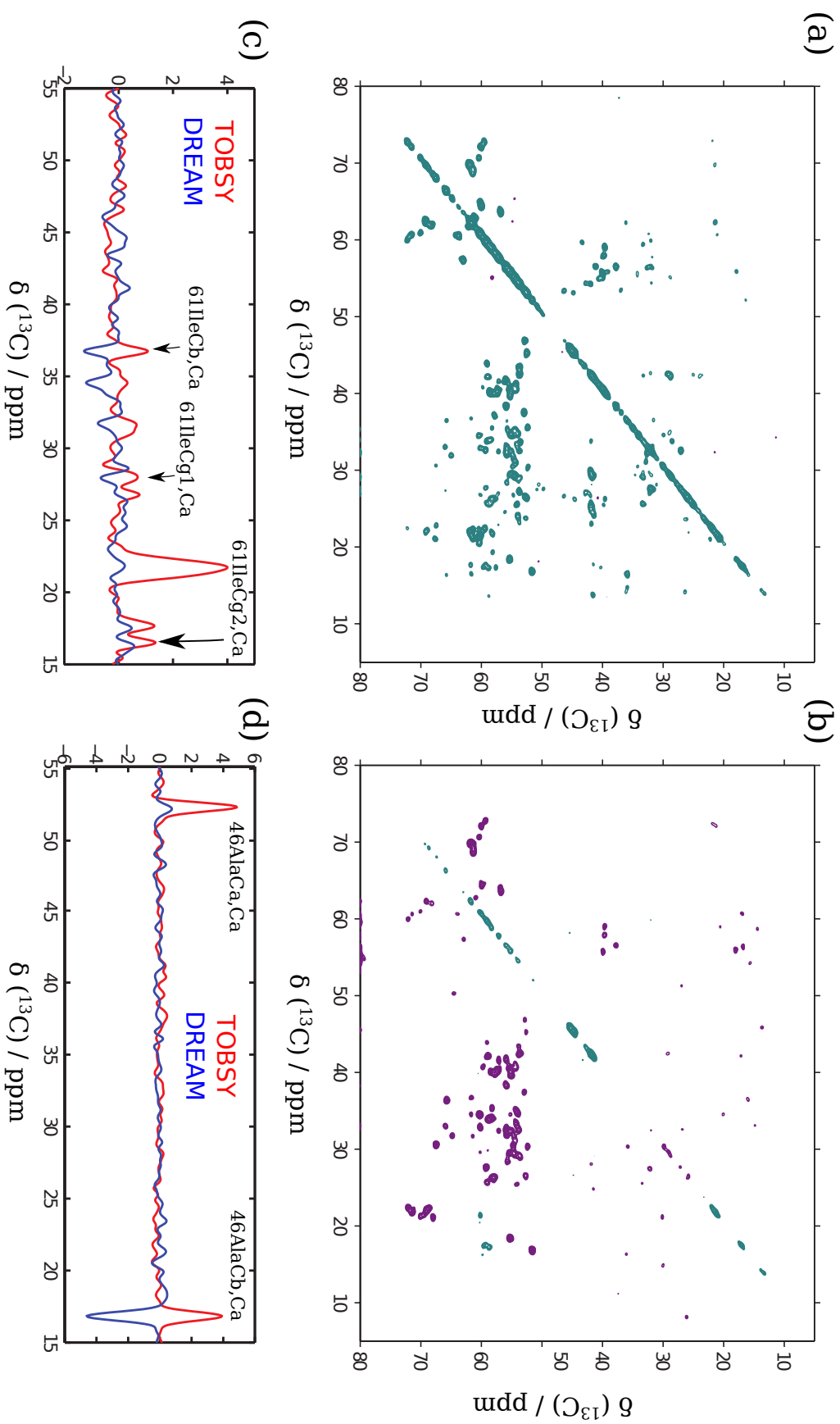


**Figure 3.19** 2D spectra of deuterated ubiquitin at  $\nu_r = 111.1$  kHz at 850 MHz without proton decoupling and the measurement time is 14 hours. The mixing sequence used is of (a) DREAM with  $\nu_{1S} = 52$  kHz with  $\tau_{\text{mix}} \sim 7$  ms or (b) TOBSY C9<sub>48</sub><sup>1</sup> with  $\nu_{1S} \sim 38$  kHz with  $\tau_{\text{mix}} \sim 13$  ms, and the carrier frequency of both sequences is at 37.5 ppm. 1D slice across the resonances of (c) 611IleCa and (d) 46AlaCa are shown here.

## Chapter 4

# Asynchronous Symmetry-Based Homonuclear Dipolar Recoupling Sequence

Polarization-transfer experiments in solid-state NMR can be mediated via either  $J$  or dipolar coupling, depending on the choice of the symmetry-based sequences. The pulses in symmetry-based sequences were originally designed to be rotor-synchronized. It was discovered recently [93] that the asynchronous regime can be employed and it outperforms the synchronous regime when the destructive interactions are significant. A theoretical explanation for the recoupling in the asynchronous regime will be presented in this chapter.

### Declaration

Part of the chapter is based on the published manuscript:

K. O. Tan, M. Rajeswari, P. K. Madhu, M. Ernst. *Asynchronous symmetry-based sequences for homonuclear dipolar recoupling in solid-state nuclear magnetic resonance*, J. Chem. Phys. 142, 065101, 2015.

## 4.1 Introduction

As discussed in Sec. 3.1, symmetry-based  $CN_n^v$  pulse sequences [59] can be used to generate effective Hamiltonians during selected time periods in solid-state NMR experiments. The choice of the numbers  $N$ ,  $n$ , and  $v$  allows the selection or removal of terms in the time-dependent Hamiltonian which become time independent under the combined rotations by MAS and rf irradiation. Nevertheless, these sequences are only efficient if the following two conditions are fulfilled: (i) the desired time-independent term has a sufficiently high scaling

factor, and (ii) all undesired terms are suppressed efficiently. Although the two requirements can be achieved easily in a first-order AHT picture, second-order cross terms often lead to undesired contributions to the effective Hamiltonian that reduce the transfer efficiency significantly. Second-order terms can be calculated based on AHT [67, 94, 95] but are often easier to calculate using Floquet theory [33, 35].

Here, a novel solution for the suppression of undesired higher-order cross terms is presented. This is crucial for situations where the desired first-order time-independent term is small compared to the undesired higher-order cross terms, which leads to a truncation of the first-order dipolar Hamiltonian. An example for such a situation was shown recently by Bechmann and coworkers [93], who showed that the widely used  $C7_{\frac{1}{2}}$  sequence [96] is not able to generate double-quantum coherences efficiently in 1,4- $^{13}\text{C}_2$ -mono-ammonium maleate. The spin system has a relatively weak dipolar coupling  $\delta_{\text{D}}/2\pi = 432$  Hz [97] compared to the anisotropy of the CSA tensor  $\delta_{\text{CSA}} = -67.7$  ppm, corresponding to a value of approximately 12 kHz on a 700 MHz spectrometer. In this situation, the rotor-synchronized C7 sequence (using a standard C element of the form  $2\pi_{\phi}2\pi_{\phi+\pi}$ ) leads to very poor double-quantum (DQ) efficiency. However, the efficiency could be improved significantly by breaking the rotor synchronization of the C7 sequence, for example by lengthening the duration of the first  $2\pi$  pulse in all C elements [93]. There are two surprising facts in this experimental observation: (i) The asynchronous  $C7_{\frac{1}{2}}$  sequence still generates an effective DQ Hamiltonian, and (ii) the compensation of the CSA tensors is better for the non-rotor-synchronized sequence. To the best of our knowledge, there has not yet been any theoretical explanation to account for these two unexpected effects.

Here, a theoretical framework based on multi-mode operator-based Floquet theory [33, 34] that can explain the recoupling conditions observed in such non-rotor synchronized sequences, is derived. The theoretical description is based on the idea that by lengthening one of the  $2\pi$  pulses in the C element, an effective field is introduced in the C7 sequence that needs to be taken into account when discussing the resonance condition. We also propose a variant of the experiment which is based on superimposing a cw rf-field on the basic C element [45, 51] while sharing the additional pulse duration  $\Delta\tau_{\text{c}}$  proportionally throughout the C element. The first scheme will be called pulse-width variation (PWV) (Fig. 4.1a) and the later scheme pulse-amplitude variation (PAV) (Fig. 4.1b). In addition, we show that the performance of the C7 sequence based on the POST [61] element can also be improved by making the sequence asynchronous in an analogous way (Figs. 4.1c and d).

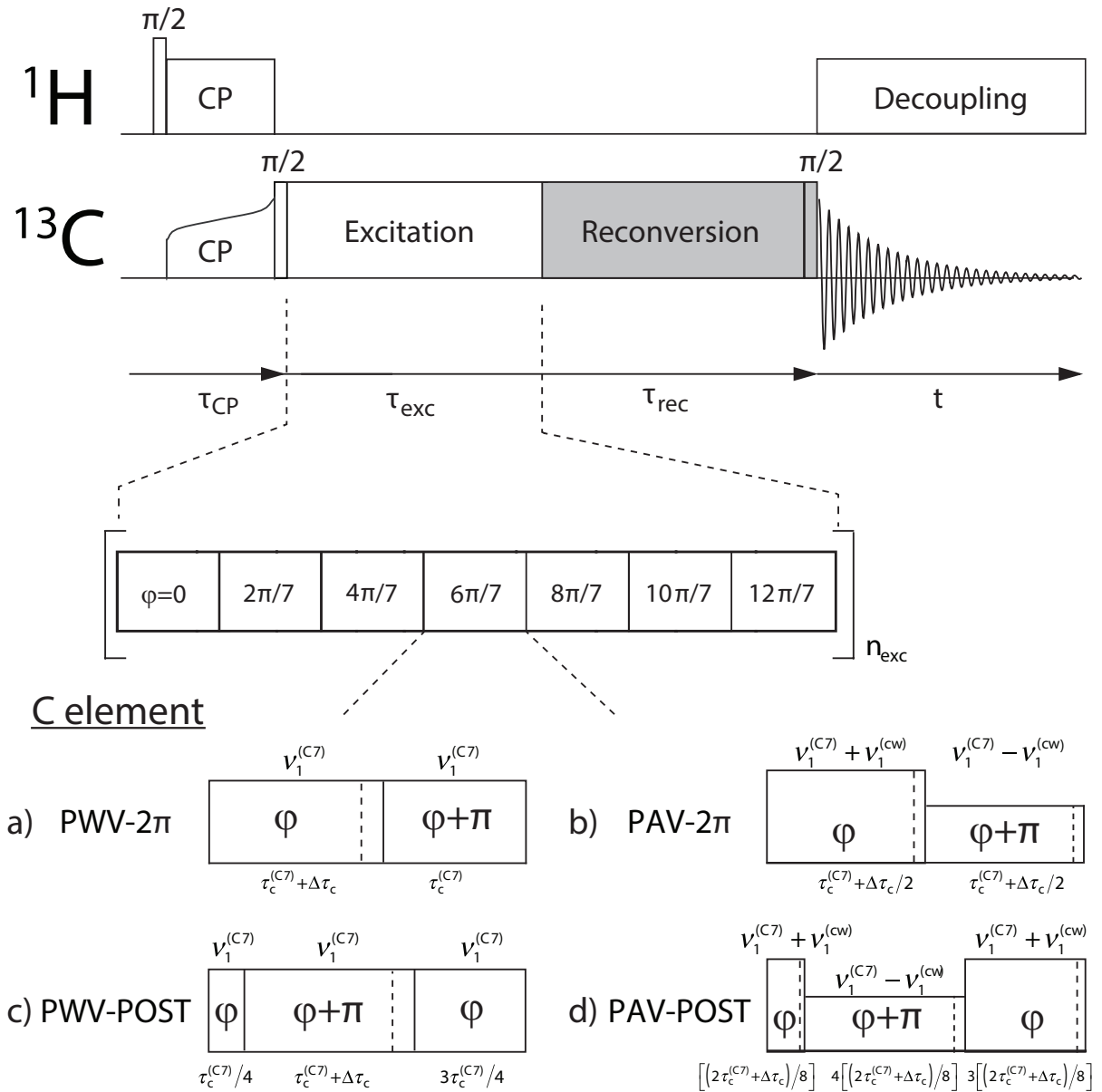


**Figure 4.1** Pulse sequence for double-quantum filtered  $C7_2^1$  experiments using (a) PWV- $2\pi$  (b) PAV- $2\pi$  (c) PWV-POST (d) PAV-POST as a choice of the basic C element. The shaded reconversion block and the following pulse are phase-shifted in each scan to select only the double-quantum coherences [98]. The details of the C elements are listed inside the bracket, i.e.  $v_1^{(C7)}$  and  $v_1^{(CW)}$  symbolize the rf amplitude as required by the original C7 sequence and the continuous-wave component respectively, while the duration of the pulse is shown in the lower horizontal brace. The pulses within the C element are separated by commas. In the ideal rotor-synchronized case,  $\tau_c^{(C7)}$  is defined such that  $v_1^{(C7)}\tau_c^{(C7)} = 1$  and the additional pulse duration  $\Delta\tau_c$  would be zero.

## 4.2 Resonance Conditions and Effective Hamiltonians

We consider a spin system with two homonuclear-coupled  $S$  spins. The full time-dependent Hamiltonian under MAS with a time-dependent rf irradiation can be adapted from Eq. (3.3):

$$\begin{aligned} \hat{\mathcal{H}}(t) = & \sum_{p=1}^2 \sum_{n=-2}^2 \omega_p^{(n)} e^{in\omega_r t} T_{1,0}^{(p)} + \sum_{\substack{n=-2 \\ n \neq 0}}^2 \omega_{1,2}^{(n)} e^{in\omega_r t} T_{2,0}^{(1,2)} \\ & + \omega_{1S}(t) \sum_{p=1}^2 (S_{px} \cos(\phi(t)) + S_{py} \sin(\phi(t))) \end{aligned} \quad (4.1)$$

where the last term represents a general rf Hamiltonian with a time-dependent amplitude  $\omega_{1S}(t)$  and phase  $\phi(t)$ . If the sequence is periodic in time, it will in general have a characteristic cycle time  $\tau_m = 2\pi/\omega_m$  and an effective field  $\omega_{\text{eff}}$ . If the pulse sequence has a total propagator that is not an identity propagator, then the net flip angle  $\beta_{\text{eff}}$  of the sequence is not an interger multiple of  $2\pi$  and this gives rise to an effective field  $\omega_{\text{eff}} = \beta_{\text{eff}}/\tau_m$  [46, 99]. Note that the rotor-synchronized versions of the  $\text{CN}_n^V$  sequences have a vanishing effective field  $\omega_{\text{eff}}$  since each C element is an integer multiple of a  $2\pi$  rotation. In order to determine possible resonance conditions, an interaction-frame transformation is performed with respect to the full rf Hamiltonian (Eq. (4.2)) with the propagator (Eq. (4.3)).

$$\hat{\mathcal{H}}(t) = \hat{U}_{\text{rf}}^{-1}(t) \hat{\mathcal{H}}(t) \hat{U}_{\text{rf}}(t) \quad (4.2)$$

$$\hat{U}_{\text{rf}}(t) = \hat{T} \exp \left( -i \int_0^t dt_1 \hat{\mathcal{H}}_{\text{rf}}(t_1) \right) \quad (4.3)$$

The resulting time-dependent interaction-frame Hamiltonian can then be expressed as a Fourier series with three basic frequencies, namely  $\omega_r$ ,  $\omega_m$  and  $\omega_{\text{eff}}$ :

$$\hat{\mathcal{H}}(t) = \sum_{n=-2}^2 \sum_{k=-\infty}^{\infty} \sum_{\ell=-2}^2 \hat{\mathcal{H}}^{(n,k,\ell)} e^{in\omega_r t} e^{ik\omega_m t} e^{i\ell\omega_{\text{eff}} t} \quad (4.4)$$

where the Fourier components are given by

$$\hat{\mathcal{H}}^{(0,k,\ell)} = \sum_{p=1}^2 \omega_p^{(0)} \sum_{s=-1}^1 a_{1,s}^{(k,\ell)} T_{1,s}^{(p)} \quad (4.5)$$

$$\hat{\mathcal{H}}^{(n,k,\ell)} = \sum_{p=1}^2 \omega_p^{(n)} \sum_{s=-1}^1 a_{1,s}^{(k,\ell)} T_{1,s}^{(p)} + \omega_{1,2}^{(n)} \sum_{s=-2}^2 a_{2,s}^{(k,\ell)} T_{2,s}^{(1,2)} \quad (4.6)$$



where the terms  $a_{r,s}^{(k,\ell)}$  are the Fourier coefficients (Figs. 4.2 and 4.3) calculated from the interaction-frame transformation of the spherical-tensor operators and are defined as

$$\tilde{T}_{r,0}(t) = \sum_{s=-r}^r a_{r,s}(t) T_{r,s} = \sum_{s=-r}^r \sum_{k=-\infty}^{\infty} \sum_{\ell=-\infty}^{\infty} a_{r,s}^{(k,\ell)} e^{ik\omega_m t} e^{i\ell\omega_{\text{eff}} t} T_{r,s} \quad (4.7)$$

Note that the values of  $n$  and  $\ell$  (Eq. (4.4)) can only be an integer ranging from -2 to +2, whereas  $k$  can be any integer value. Moreover, the resonance conditions are defined in general by any set of values  $(n_0, k_0, \ell_0)$  that fulfill the condition

$$n_0\omega_r + k_0\omega_m + \ell_0\omega_{\text{eff}} = 0 \quad (4.8)$$

with a first-order effective Hamiltonian of the form

$$\hat{\mathcal{H}}^{\hat{a}(1)} = \hat{\mathcal{H}}^{\hat{a}(0,0,0)} + \sum_{(n_0,k_0,\ell_0)} \hat{\mathcal{H}}^{\hat{a}(n_0,k_0,\ell_0)} \quad (4.9)$$

Equations (4.8) and (4.9) generalize the resonance conditions for the original symmetry-based sequences to sequences with a non-vanishing effective field  $\omega_{\text{eff}}$  (Eq. (4.15)) [46]. The effective nutation frequency  $\omega_{\text{eff}}$  for the case of asynchronous  $C7_2^1$  can be determined via a quaternion description [100].

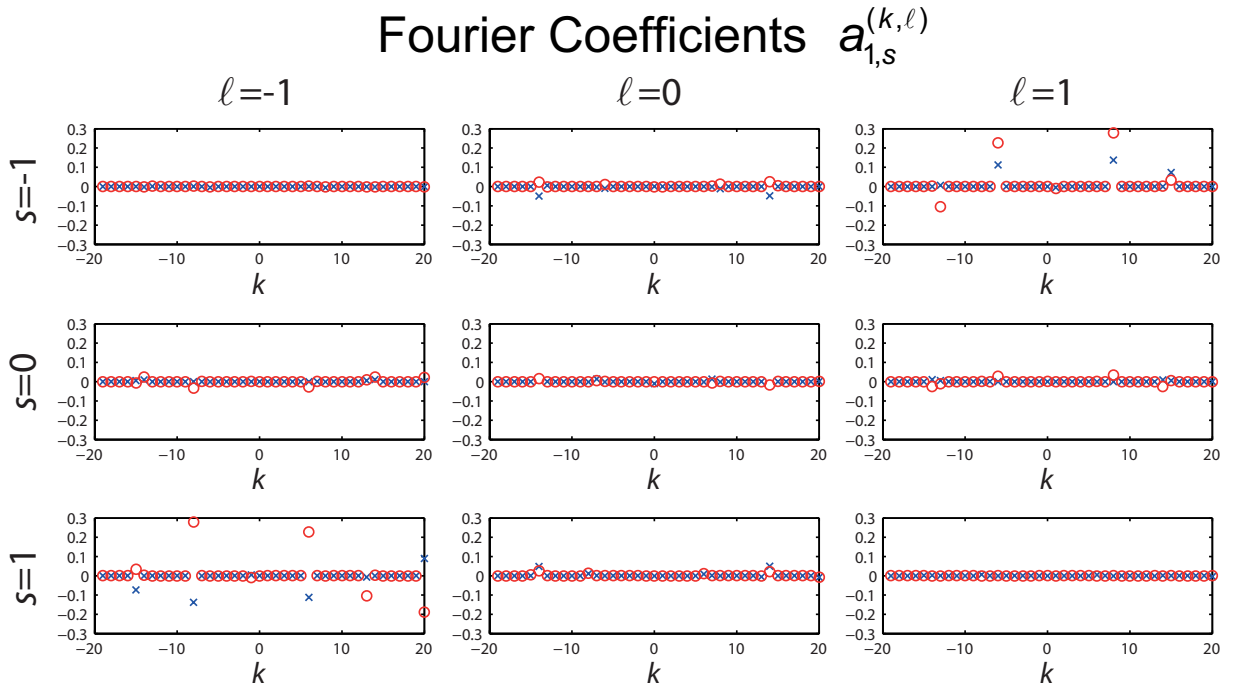


**Figure 4.2** Plot of the spherical Fourier coefficients  $a_{1,s}^{(k,\ell)}$  (real part blue 'x', imaginary part red 'o') for the asynchronous ( $\Delta\tau_c=0.31\ \mu\text{s}$ )  $C7_2^1$  pulse sequence with POST element.

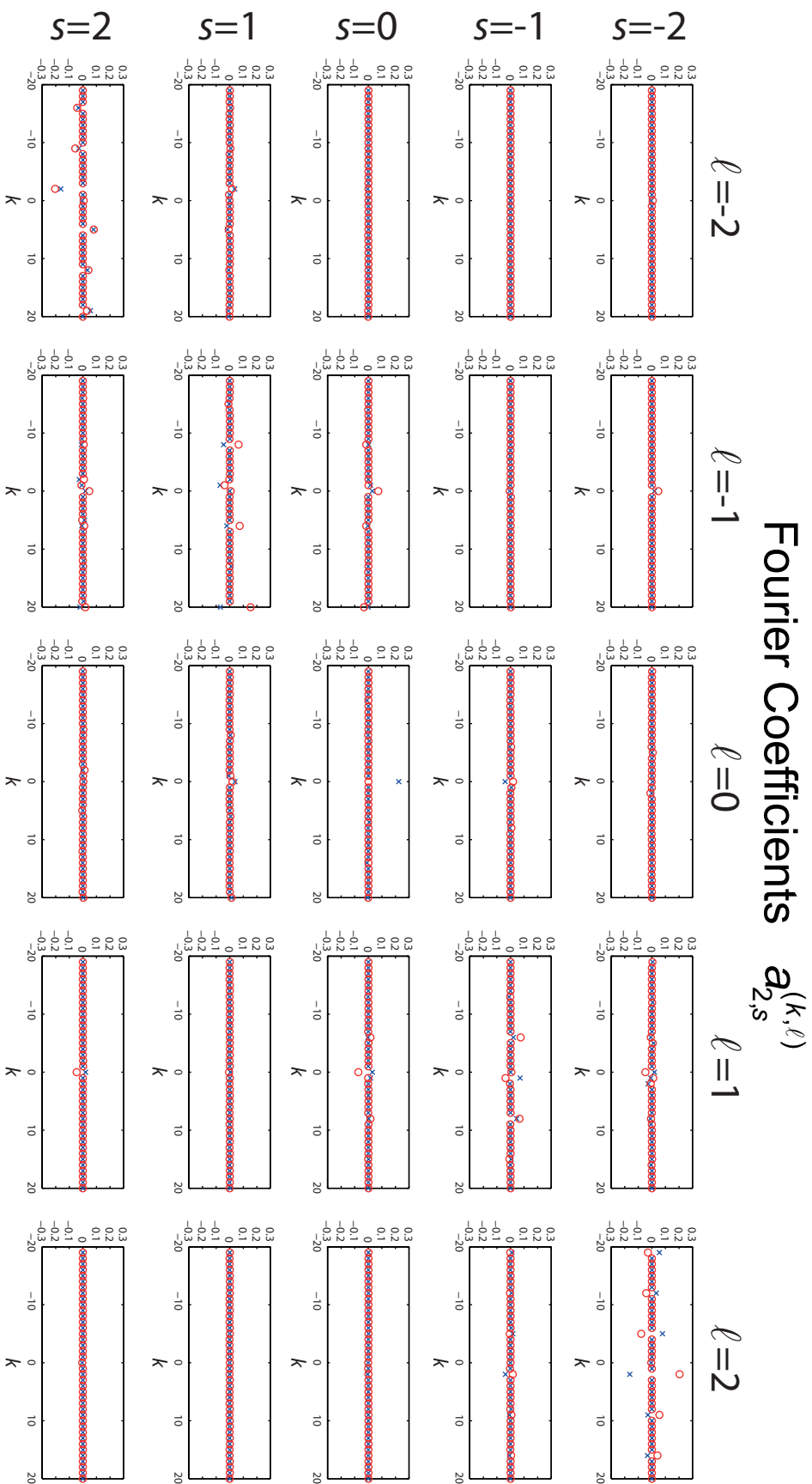


**Figure 4.3** Plot of the spherical Fourier coefficients  $a_{2,s}^{(k,\ell)}$  (real part blue 'x', imaginary part red 'o') for the asynchronous ( $\Delta\tau_c = 0.31 \mu\text{s}$ )  $C7_2^1$  pulse sequence using POST as a basic C element. The only interesting Fourier coefficients that scale the double-quantum terms are  $a_{2,s}^{(k,\ell = \pm 2, \ell = \pm 2)}$ .

**Determination of the Effective Field  $\omega_{\text{eff}}$** 

The quaternions for the  $C7_2^1$  sequence with an effective nutation per C element  $\beta_c$  can be defined (see Eqs. A.9 and A.9 in Sec. A.2):

$$Q_k \left( \cos \left[ \frac{2\pi\nu}{N} (k-1) \right], \sin \left[ \frac{2\pi\nu}{N} (k-1) \right], 0, \beta_c \right) \quad (4.10)$$

The overall net rotation of the entire C7 cycle can be determined by calculating

$$Q_{\text{eff}}(I_{xx}, I_{yy}, I_{zz}, \beta_c) = \begin{bmatrix} I_{xx}^{(\text{eff})} \sin \left( \frac{\beta_{\text{eff}}}{2} \right) \\ I_{yy}^{(\text{eff})} \sin \left( \frac{\beta_{\text{eff}}}{2} \right) \\ I_{zz}^{(\text{eff})} \sin \left( \frac{\beta_{\text{eff}}}{2} \right) \\ \cos \left( \frac{\beta_{\text{eff}}}{2} \right) \end{bmatrix} = Q_7 Q_6 \cdots Q_2 Q_1 \quad (4.11)$$

Following this, the effective flip angle  $\beta_{\text{eff}}$  can then be derived using

$$\begin{aligned} \cos \left( \frac{\beta_{\text{eff}}}{2} \right) = & \cos^7(x) + \frac{7}{16} \sin^2(x) \left\{ 6 \cos \left( \frac{\pi}{7} \right) \cos(x) + 5 \cos \left( \frac{\pi}{7} \right) (\cos(3x) + \cos(5x)) \right. \\ & \left. + 8 \sin \left( \frac{\pi}{14} \right) \cos^3(x) (3 \cos(2x) - 1) - 16 \cos^5(x) \sin \left( \frac{3\pi}{14} \right) \right\} \end{aligned} \quad (4.12)$$

where  $x = \beta_c/2$ . Since only a small additional flip angle  $x$  is considered, one can perform a Taylor series expansion up to the fourth order

$$\cos \left( \frac{\beta_{\text{eff}}}{2} \right) = 1 - \frac{7}{24} \left( -19 + 140 \cos \left( \frac{\pi}{7} \right) + 116 \sin \left( \frac{\pi}{14} \right) - 68 \sin \left( \frac{3\pi}{14} \right) \right) x^4 + \mathcal{O}(x^5) \quad (4.13)$$

Hence, one obtains the approximated numerical result

$$\beta_{\text{eff}} = 2 \arccos \left[ 1 - 1.65066 \beta_c^4 \right] \quad (4.14)$$

$$\omega_{\text{eff}} = \frac{\beta_{\text{eff}}}{\tau_m} = \frac{\arccos \left[ 1 - 1.65066 \beta_c^4 \right] \omega_m}{\pi} \quad (4.15)$$

Eq. (4.14) is a good approximation for small flip angles  $\beta_c$  up to  $\pi/5$  with an error of less than 10 %. Additionally, the effective axis of direction ( $I_{xx}^{(\text{eff})}$ ,  $I_{yy}^{(\text{eff})}$ , and  $I_{zz}^{(\text{eff})}$ ) can also be determined (Eq. (4.11)). While  $\tau_m = N(2\tau_c^{(C7)} + \Delta\tau_c)$  (Fig. 4.1) is the length of the entire asynchronous C7 cycle, and  $\beta_c$  is the effective nutation angle of a single C element. The case of rotor-synchronized sequences with a zero effective field  $\omega_{\text{eff}} = 0$  is just a special case of this general description which reduces to bimodal Floquet theory (see Sec. 3.2.1).

Using the resonance conditions of the original C7<sub>2</sub><sup>1</sup> sequence, the DQ terms are found in the Hamiltonian with the Fourier component  $(n_0, k_0) = (\pm 1, \mp 2)$ . For the non-rotor synchronized cases, the timing of the sequences considered here is close to that of the original rotor-synchronized sequences so that the high double-quantum scaling factor can still be exploited. Therefore, it is still desirable to keep the Fourier number  $(n_0, k_0) = (\pm 1, \mp 2)$  in the non-rotor synchronized sequence. In addition,  $\ell_0 = \pm 2$  is required because the relevant double-quantum term has also a coherence order of  $\pm 2$  under the action of the effective field. Hence, one expects the double-quantum recoupling condition of the non-rotor synchronized sequence to be  $(n_0, k_0, \ell_0) = \pm(-1, 2, 2)$ .

### 4.2.1 First-Order Effective Hamiltonian

The first-order effective Hamiltonian with a set of Fourier number  $(n_0, k_0, \ell_0) = \pm(-1, 2, 2)$ , is given by

$$\begin{aligned} \hat{\mathcal{H}}^{(1)} &= \hat{\mathcal{H}}^{(0,0,0)} + \hat{\mathcal{H}}^{(1,-2,-2)} + \hat{\mathcal{H}}^{(-1,2,2)} \\ &= \sum_{p=1}^2 \sum_{s=-1}^1 \omega_p^{(0)} a_{1,s}^{(0,0)} T_{1,s}^{(p)} + \sum_{p=1}^2 \sum_{s=-1}^1 \left( \omega_p^{(1)} a_{1,s}^{(-2,-2)} + \omega_p^{(-1)} a_{1,s}^{(2,2)} \right) T_{1,s}^{(p)} \\ &\quad + \sum_{s=-2}^2 \left( \omega_{1,2}^{(1)} a_{2,s}^{(-2,-2)} + \omega_{1,2}^{(-1)} a_{2,s}^{(2,2)} \right) T_{2,s}^{(1,2)} \end{aligned} \quad (4.16)$$

$$= \sum_{p=1}^2 \sum_{s=-1}^1 \omega_p^{(0)} a_{1,s}^{(0,0)} T_{1,s}^{(p)} + \omega_{1,2}^{(1)} a_{2,2}^{(-2,-2)} T_{2,2}^{(1,2)} + \omega_{1,2}^{(-1)} a_{2,-2}^{(2,2)} T_{2,-2}^{(1,2)} \quad (4.17)$$

The Fourier coefficients for the rank-one tensors  $a_{1,s}^{(\pm 2, \pm 2)}$  are zero because the Fourier coefficients of any rank- $r$  tensor  $a_{r,s}^{(k_0, \ell_0)}$  are zero for any integer  $\ell_0$  that fulfils the inequality  $|\ell_0| > r$ . The effective Hamiltonian of Eq. (4.17) consists of two types of terms: (i) chemical-shift terms represented by the first-rank spherical tensor operators  $T_{1,s}$  and the dipolar-coupling terms represented by the second-rank spherical-tensor operators  $T_{2,\pm 2}$ .

In order to compare the performance of the sequences, the effective magnitude of the chemical-shift term  $a_{1,\text{eff}}^{(0,0)}$  (Eq. (4.18)) and the double-quantum scaling factor  $|a_{2,-2}^{(2,2)}|$  (see Fig. 4.2) are calculated and shown in Fig. 4.4 as a function of the rf-field amplitude and the additional length of the C element  $\Delta \tau_c$ .

$$a_{1,\text{eff}}^{(0,0)} = \sqrt{\sum_{s=-1}^1 |a_{1,s}^{(0,0)}|^2} \quad (4.18)$$

The magnitude of  $a_{1,\text{eff}}^{(0,0)}$  depends on the choice of the basic C element and the rf amplitude of the sequence  $v_1^{(C7)}$ . It is evident from Fig. 4.4 that there is hardly any compromise in the offset compensation for the case of the basic C element  $2\pi_\phi 2\pi_{\phi+\pi}$  (Fig. 4.4a) if the sequence is made asynchronous ( $\Delta\tau_c \neq 0$ ) compared to the synchronous sequence ( $\Delta\tau_c = 0$ ). For the POST (Fig. 4.4c) element, there is a 1.1% increase in the scaling factor for the chemical-shift term.

The double-quantum scaling factor  $|a_{2,-2}^{(2,2)}|$  which characterizes the recoupling efficiency is also shown for the basic  $2\pi_\phi 2\pi_{\phi+\pi}$  (Fig. 4.4b) and the POST (Fig. 4.4d) element. The magnitude of the double-quantum scaling factor for both C elements at the asynchronous condition ( $\Delta\tau_c \neq 0$ ) is slightly smaller (less than 5%) than for the synchronous sequence ( $\Delta\tau_c = 0$ ). This implies that the build-up rate of the double-quantum term will be slightly slower under asynchronous recoupling conditions. From these results, it is not obvious why the asynchronous sequence outperforms the synchronous one. For an explanation, a closer inspection of the terms originating from the second-order effective Hamiltonian is required.

## 4.2.2 Second-Order Effective Hamiltonian

### Synchronous Case

Since the CSA tensor is by far the largest term in the Hamiltonian, we will restrict our calculations of the second-order effective Hamiltonians to CSA-CSA cross terms. Such cross terms will result in three rank-one tensors, namely  $T_{1,0}$  and  $T_{1,\pm 1}$ . The bimodal second-order effective Hamiltonian  $\hat{\mathcal{H}}^{(2)}$  for the synchronous C7 sequence [60, 67] is given by the sum of the non-resonant and the resonant parts

$$\hat{\mathcal{H}}^{(2)} = \hat{\mathcal{H}}^{(0,0)} + \sum_{n_0, k_0} \hat{\mathcal{H}}^{(n_0, k_0)}_{(2)} \quad (4.19)$$

with

$$\hat{\mathcal{H}}^{(n_0, k_0)}_{(2)} = \sum_{v, \kappa} -\frac{1}{2} \left[ \frac{\hat{\mathcal{H}}^{(n_0-v, k_0-\kappa)}}{v\omega_r + \kappa\omega_m}, \hat{\mathcal{H}}^{(v, \kappa)} \right] = \sum_{v, \kappa} -\frac{1}{2} \frac{\omega_S^{(n_0-v)} \omega_S^{(v)}}{v\omega_r + \kappa\omega_m} \times A_\kappa(k_0) \quad (4.20)$$

where the spin parts  $A_\kappa(k_0)$  are given by

$$\begin{aligned} A_\kappa(k_0) = & \left( a_{1,-1}^{(k_0-\kappa)} a_{1,0}^{(\kappa)} - a_{1,0}^{(k_0-\kappa)} a_{1,-1}^{(\kappa)} \right) T_{1,-1} + \left( a_{1,-1}^{(k_0-\kappa)} a_{1,1}^{(\kappa)} - a_{1,1}^{(k_0-\kappa)} a_{1,-1}^{(\kappa)} \right) T_{1,0} \\ & + \left( a_{1,0}^{(k_0-\kappa)} a_{1,1}^{(\kappa)} - a_{1,1}^{(k_0-\kappa)} a_{1,0}^{(\kappa)} \right) T_{1,1} \end{aligned} \quad (4.21)$$

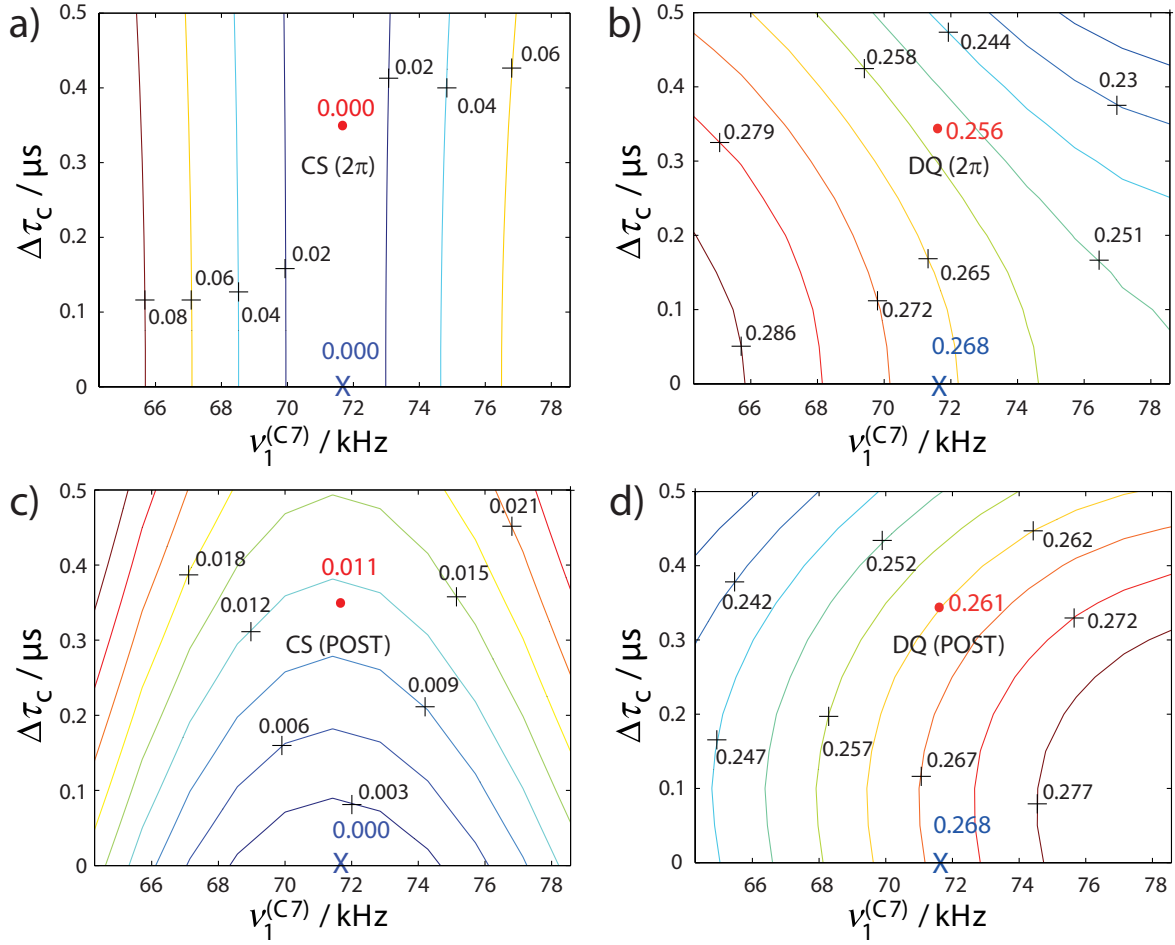


**Figure 4.4** Contour plots showing the magnitude of Fourier coefficients for the chemical-shift  $a_{1,\text{eff}}^{(0,0)}$  (a,c) and double-quantum term  $|a_{2,-2}^{(2,2)}|$  (b,d) for C7 sequence using (a,b)  $2\pi\phi 2\pi\phi + \pi$  (c,d) POST as C element. The position of the synchronous  $\Delta\tau_c = 0$  and asynchronous condition  $\Delta\tau_c = 0.35 \mu\text{s}$  is marked with a blue cross and red dot respectively.

### Asynchronous Case

For the case of asynchronous C7, the trimodal second-order effective Hamiltonian is given by

$$\hat{\mathcal{H}}^{(2)} = \hat{\mathcal{H}}_{(2)}^{(0,0,0)} + \sum_{n_0, k_0, \ell_0} \hat{\mathcal{H}}_{(2)}^{(n_0, k_0, \ell_0)} \quad (4.22)$$

with

$$\begin{aligned} \hat{\mathcal{H}}_{(2)}^{(n_0, k_0, \ell_0)} &= \sum_{\nu, \kappa, \lambda} -\frac{1}{2} \left[ \frac{\hat{\mathcal{H}}^{(n_0 - \nu, k_0 - \kappa, \ell_0 - \lambda)} \hat{\mathcal{H}}^{(\nu, \kappa, \lambda)}}{\nu\omega_r + \kappa\omega_m + \lambda\omega_{\text{eff}}} \right] \\ &= \sum_{\nu, \kappa, \lambda} -\frac{1}{2} \frac{\omega_S^{(n_0 - \nu)} \omega_S^{(\nu)}}{\nu\omega_r + \kappa\omega_m + \lambda\omega_{\text{eff}}} \times A_{\kappa, \lambda}(k_0, \ell_0) \end{aligned} \quad (4.23)$$

and the spin parts  $A_{\kappa,\lambda}(k_0, \ell_0)$  are given by

$$\begin{aligned} A_{\kappa,\lambda}(k_0, \ell_0) = & \left( a_{1,-1}^{(k_0-\kappa, \ell_0-\lambda)} a_{1,0}^{(\kappa,\lambda)} - a_{1,0}^{(k_0-\kappa, \ell_0-\lambda)} a_{1,-1}^{(\kappa,\lambda)} \right) T_{1,-1} \\ & + \left( a_{1,0}^{(k_0-\kappa, \ell_0-\lambda)} a_{1,1}^{(\kappa,\lambda)} - a_{1,1}^{(k_0-\kappa, \ell_0-\lambda)} a_{1,0}^{(\kappa,\lambda)} \right) T_{1,1} \\ & + \left( a_{1,-1}^{(k_0-\kappa, \ell_0-\lambda)} a_{1,1}^{(\kappa,\lambda)} - a_{1,1}^{(k_0-\kappa, \ell_0-\lambda)} a_{1,-1}^{(\kappa,\lambda)} \right) T_{1,0} \end{aligned} \quad (4.24)$$

Note that the full resonant contribution in Eqs. (4.19) and (4.22) has to sum over all values of  $n_0$ ,  $k_0$ , and  $\ell_0$  that fulfil the resonance conditions  $n_0\omega_r + k_0\omega_m = 0$  and  $n_0\omega_r + k_0\omega_m + \ell_0\omega_{\text{eff}} = 0$ , respectively. Since this is a second-order resonance condition, the values  $n_0 = \pm 3$  and  $n_0 = \pm 4$  are also allowed. The effective Hamiltonian describing the double-quantum recoupling up to second order can be summarized as

$$\hat{\mathcal{H}} \approx \hat{\mathcal{H}}^{(1)} + \hat{\mathcal{H}}^{(2)} = \omega_{\text{DQ}}^{(+2)} T_{2,+2} + \omega_{\text{DQ}}^{(-2)} T_{2,-2} + \omega_{\text{CSA}}^{(0)} T_{1,0} + \omega_{\text{CSA}}^{(+1)} T_{1,+1} + \omega_{\text{CSA}}^{(-1)} T_{1,-1} \quad (4.25)$$

where the first two coefficients  $\omega_{\text{DQ}}^{(\pm 2)}$  describe the strength of the first-order double-quantum terms, while the last three coefficients,  $\omega_{\text{CSA}}^{(0)}$  and  $\omega_{\text{CSA}}^{(\pm 1)}$ , describe the strength of the second-order CSA contributions. Following this, we define an effective magnitude of the undesired rank-one terms  $\omega_{\text{CSA}}^{(\text{eff})}$ , which is defined as

$$\omega_{\text{CSA}}^{(\text{eff})} = \sqrt{\sum_{s=-1}^1 |\omega_{\text{CSA}}^{(s)}|^2} \quad (4.26)$$

for simpler analysis (similar to Eq. (4.18)). Based on Eqs. (4.22)-(4.24), the magnitude of the second-order CSA-CSA cross term ( $\omega_{\text{CSA}}^{(0)}$ ,  $\omega_{\text{CSA}}^{(\pm 1)}$ , and  $\omega_{\text{CSA}}^{(\text{eff})}$ ) for the synchronous and asynchronous case can be calculated analytically as a function of the Euler angle  $\beta$  as shown in Fig. 4.5a and Fig. 4.5b, respectively.

For simplicity, the CSA tensor with  $\delta_{\text{CSA}}/2\pi = 11847.5$  Hz was assumed to be axially symmetric ( $\eta = 0$ ), and the Euler angles were chosen at  $\alpha = \gamma = 0$  for all  $\beta$  values. In addition, the effective double-quantum coupling strength  $\omega_{\text{DQ}}^{(\pm 2)}$  for  $\delta_{\text{D}}/2\pi = -432$  Hz is also plotted in Fig. 4.5 for comparison. Note that the magnitude of the  $\omega_{\text{CSA}}^{(\pm 1)}$  terms is the same because they form a complex conjugate pair, and similarly for the  $T_{2,\pm 2}$  terms. Moreover, the CSA tensors for the two spins are assumed to be identical and the cross-terms for only one of them are shown here.

One can clearly see that in the synchronous case (Fig. 4.5a), the magnitude of the unwanted CSA cross-terms, specifically the  $T_{1,\pm 1}$  terms, are comparable or even larger than

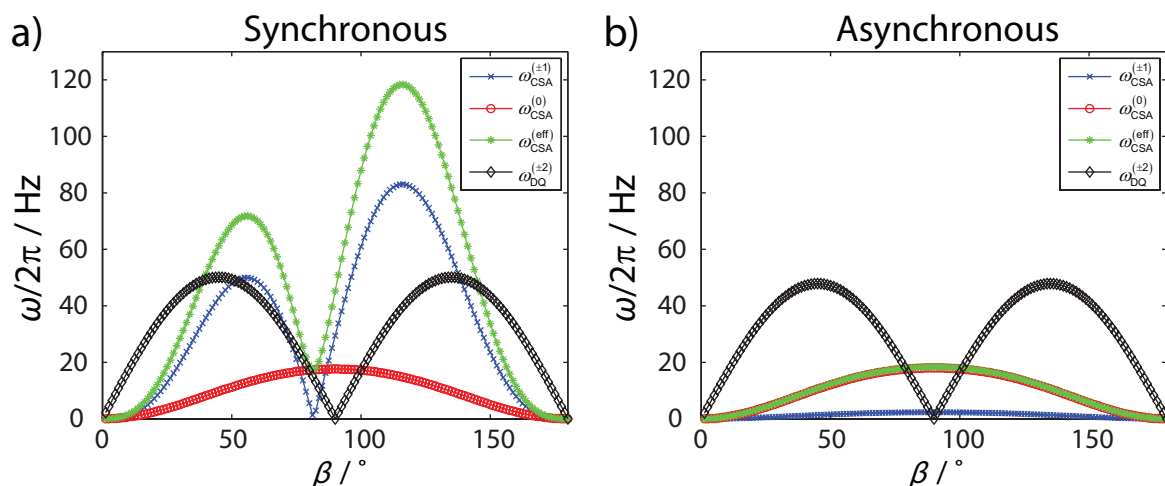


**Figure 4.5** The dependence of the interaction strength on the  $\beta$  Euler angle calculated for the synchronous (a) and asynchronous (b) cases. The desired effective double-quantum term is  $\omega_{\text{DQ}}^{(\pm 2)}$  (black diamond), while the unwanted second-order CSA-CSA cross terms are  $\omega_{\text{CSA}}^{(\pm 1)}$  (blue crosses),  $\omega_{\text{CSA}}^{(0)}$  (red circles), and  $\omega_{\text{CSA}}^{(\text{eff})}$  (green asterisks). The calculations were performed based on the  $2\pi\phi 2\pi\phi + \pi$  basic element, at a MAS frequency of 10.204 kHz.

the magnitude of the desired double-quantum term  $T_{2,\pm 2}$ . Since the second-order CSA cross terms do not commute with the double-quantum term  $T_{2,\pm 2}$  in the Hamiltonian, they will have detrimental effect on the double-quantum efficiency by truncating the double-quantum Hamiltonian. In the case of asynchronous C7 (Fig. 4.5b), the magnitude of the  $T_{1,\pm 1}$  terms is reduced by roughly a factor of 10. The main reason for this efficient CSA suppression is due to a smaller number of possible second-order resonant terms  $\hat{\mathcal{H}}_{(2)}^{(n_0, k_0, \ell_0)}$  in the asynchronous case, i.e. the  $n_0 = \pm 3$  and  $\pm 4$  terms are absent because of the introduction of the effective nutation frequency  $\omega_{\text{eff}}$ . However, the  $T_{1,0}$  terms originating from the non-resonant  $\hat{\mathcal{H}}_{(2)}^{(0,0,0)}$  terms are unchanged and the amplitude is the same in both cases. For most crystallite orientations, the magnitude of the  $T_{1,0}$  terms is smaller than the double-quantum term  $T_{2,\pm 2}$ . The analytical results are in good agreement with the numerical simulations (vide infra) and experimental observations that the asynchronous condition has a much higher double-quantum efficiency in 1,4- $^{13}\text{C}_2$ -mono-ammonium maleate.

To support the results of the analytical calculations that the improvement in double-quantum recoupling efficiency is mainly due to better CSA compensation in the second-order effective Hamiltonian, numerical simulations [80] on a one-spin system were performed. The anisotropy of the CSA tensor was set to  $\delta_{\text{CSA}}/2\pi = 11847.5$  Hz and the time evolution of the one-spin system under the synchronous and asynchronous C7 sequence was simulated. Figure 4.6a shows that the dephasing of the initial magnetization due to



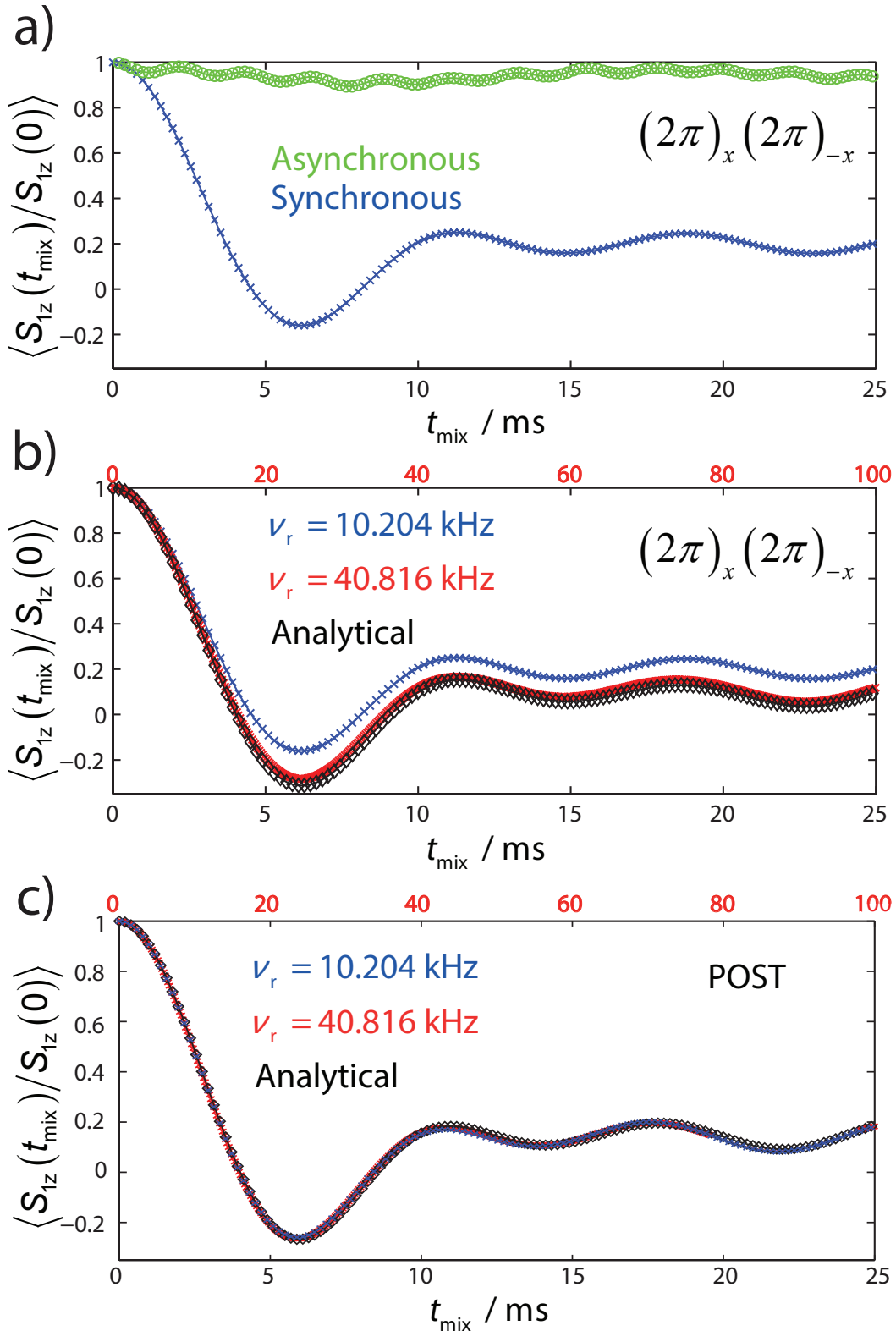


**Figure 4.6** (a) shows the numerical simulation of a single spin with an anisotropy of the CSA  $\delta_{\text{CSA}}/2\pi = 11847.5 \text{ Hz}$  under the synchronous (blue crosses) and asynchronous sequence (green circles) with the basic element of (a,b)  $2\pi_\phi 2\pi_{\phi+\pi}$  and (c) POST at a MAS frequency of 10.204 kHz. (b,c) shows an overlay of the same single spin simulation under synchronous condition repeated at a MAS frequency of 40.816 kHz (red crosses) with its respective x-axis (red). Evolution (black diamond) using the analytical second-order Hamiltonian (Eqs. (4.22)-(4.24)) is also shown in (b,c).

the second-order contributions of the CSA tensor is more severe for the synchronous sequence compared to the asynchronous sequence. This is due to the much larger magnitude of the  $T_{1,\pm 1}$  terms in the synchronous C7 sequence as discussed above. In order to verify that indeed the second-order effective Hamiltonian is the main contribution to the observed dephasing, the simulation was repeated with a four times larger MAS frequency. The MAS frequency dependence is shown in Fig. 4.6b where the dephasing profiles at two different frequencies have very similar shape except for the scaling of the time axis by a factor of four, thus supporting the argument that the spin dephasing is due to the second-order CSA-CSA cross term. This is valid because the second-order effective Hamiltonian of such a symmetry-based  $\text{CN}_n^V$  sequence scales inversely proportional to the  $\omega_r$  or  $\omega_m$  (Eq. (4.27)), if the first order effective Hamiltonian  $\hat{\mathcal{H}}^{(1)}$  is 0.

$$\begin{aligned}
\hat{\mathcal{H}} &= \hat{\mathcal{H}}^{(1)} + \hat{\mathcal{H}}^{(2)} \\
&= \hat{\mathcal{H}}_{(2)}^{(0,0)} + \sum_{n_0, k_0} \hat{\mathcal{H}}_{(2)}^{(n_0, k_0)} \\
&= \sum_{n_0, k_0} \sum_{\nu, \kappa} -\frac{1}{2} \left[ \frac{\hat{\mathcal{H}}^{(n_0-\nu, k_0-\kappa)}, \hat{\mathcal{H}}^{(\nu, \kappa)}}{\nu \omega_r + \kappa \omega_m} \right] \\
&= \sum_{n_0, k_0} \sum_{\nu, \kappa} -\frac{1}{2} \left[ \frac{\hat{\mathcal{H}}^{(n_0-\nu, k_0-\kappa)}, \hat{\mathcal{H}}^{(\nu, \kappa)}}{(n\nu + \kappa) \omega_m} \right] \tag{4.27}
\end{aligned}$$

Hence, the dephasing profile should be similar, differing only by the time scale, if third and higher-order contributions are negligible. The small discrepancies are due to higher-order terms that have a non-linear dependency on the inverse MAS frequency, as verified by the good agreement between the analytically calculated time evolution based on Eqs. (4.22)-(4.24) and the numerical simulation at the higher MAS frequency.

### 4.2.3 Higher-Order Space-Spin Selection Rules

It was discussed in Sec. 3.1.1 that space-spin selection diagrams can be drawn to provide a qualitative analysis of the allowed and forbidden spin interactions in the first-order Hamiltonian, during the mixing time of the symmetry-based  $\text{CN}_n^V / \text{RN}_n^V$  sequences. The selection rules can be easily extended to higher orders to analyze the higher-order Hamiltonians. The second-order selection rules [49, 67, 94, 95] for the allowed interactions are given by

$$(m_1 + m_2)n - (s_1 + s_2)\nu = zN \tag{4.28}$$

where  $m$  and  $s$  are the sub-rank tensor component of the spatial and spin part of an interaction, respectively, and the subscript (1 or 2) labels the type of interaction involved, and  $z$  is any integer number. The formulation of the second-order selection rules is not surprising, as one can infer a similar formalism from the second-order effective Hamiltonian  $\hat{\mathcal{H}}_{(2)}$  derived using Floquet theory (Eq. (4.29)).

$$\hat{\mathcal{H}}_{(2)}^{(n_0, k_0)} = -\frac{1}{2} \sum_{\nu, \kappa} \frac{[\hat{\mathcal{H}}^{(n_0-\nu, k_0-\kappa)}, \hat{\mathcal{H}}^{(\nu, \kappa)}]}{\nu \omega_r + \kappa \omega_m} \quad (4.29)$$

For instance, for the spatial component  $m$  ( $n_0$ ) that satisfies the resonance condition  $n_0 \omega_r + k_0 \omega_m = 0$ , one can also deduce the Fourier components  $\hat{\mathcal{H}}^{(m_1=n_0-\nu, k_1=k_0-\kappa)}$  and  $\hat{\mathcal{H}}^{(m_2=\nu, k_2=\kappa)}$  that appear in the second-order effective Hamiltonian (Eq. (4.29)), as the sum of the Fourier numbers also constitutes the resonance conditions, i.e.

$$\begin{aligned} (m_1 + m_2) \omega_r + (k_1 + k_2) \omega_m &= 0 \\ (m_1 + m_2) \omega_r / \omega_m + (k_1 + k_2) &= 0 \\ (m_1 + m_2)n + (k_1 + k_2) &= 0 \end{aligned} \quad (4.30)$$

In principle, there are infinite combinations of  $k_1$  and  $k_2$  that satisfy the condition  $k_1 + k_2 = 0$ , but we are interested only in the values of  $k_1$  such that the corresponding Fourier coefficients  $a_{r,s}^{(k_1)} \neq 0$ , which happens when

$$k_1 = z_1 N - s_1 \nu, \quad (4.31)$$

which is analogous to Eq. (3.10). Hence, by substituting Eq. (4.31) into Eq. (4.30) :

$$\begin{aligned} (m_1 + m_2)n + (z_1 N - s_1 \nu + z_2 N - s_2 \nu) &= 0 \\ (m_1 + m_2)n - (s_1 + s_2) \nu &= -(z_1 + z_2)N \\ (m_1 + m_2)n - (s_1 + s_2) \nu &= zN \end{aligned} \quad (4.32)$$

where  $z = -(z_1 + z_2)$  is still an integer. One can clearly see that the higher-order selection rules are indeed derivable from Floquet theory (see Eq. (4.32) and Eq. (4.28)). Following the treatment of the second-order selection rules, one can deduce the number of allowed CSA $\otimes$ CSA cross terms, and hence the size of second-order Hamiltonians qualitatively by counting the number of allowed terms [69, 95], which are tabulated in Fig. 4.7. Apart from knowing that there are in total 20 allowed CSA $\otimes$ CSA cross terms in the case of rotor-synchronized C7<sub>1</sub><sup>2</sup>, one can deduce that 8 of them originated from the non-resonant term  $\hat{\mathcal{H}}_{(2)}^{(0,0)}$  that is comprised of the  $\hat{S}_z$  terms, 8 terms from the  $n_0 = 3$  resonant term  $\hat{\mathcal{H}}_{(2)}^{(\pm 3, \mp 6)}$

and the remaining 4 terms from the  $n_0 = 4$  resonant term  $\hat{\mathcal{H}}_{(2)}^{(\pm 4, \mp 8)}$ . Out of the 12 contributions from the resonant terms, half of them (6) is  $\hat{S}^+$  and the other half is  $\hat{S}^-$ , which is not surprising as the total Hamiltonian must be Hermitian. These results are obtained based on the fact that the Fourier integers of the second-order effective Hamiltonian  $\hat{\mathcal{H}}_{(2)}^{(n_0, k_0)}$  satisfy the relation  $n_0 = m_1 + m_2$  (see third column in Fig. 4.7), and the commutator relations :

$$[\hat{T}_{1,0}, \hat{T}_{1,\pm 1}] = \pm \hat{T}_{1,\pm 1} \quad (4.33)$$

$$[\hat{T}_{1,-1}, \hat{T}_{1,1}] = \hat{T}_{1,0} \quad (4.34)$$

Following that, one can exploit the commutator relations and derive the following relation:

$$[\hat{T}_{1,s_1}, \hat{T}_{1,s_2}] = c \hat{T}_{1,s_1+s_2} \quad \text{where } c = \begin{cases} 1 & \text{if } s_1 < s_2 \\ -1 & \text{if } s_1 > s_2 \end{cases} \quad (4.35)$$

$m_1$	$m_2$	$m_1+m_2$	$s_1$	$s_2$	$s_1+s_2$
-2	2	0	-1	1	0
-2	2	0	1	-1	0
-1	1	0	-1	1	0
-1	1	0	1	-1	0
1	-1	0	-1	1	0
1	-1	0	1	-1	0
2	-2	0	-1	1	0
2	-2	0	1	-1	0
-2	-2	-4	0	-1	-1
-2	-2	-4	-1	0	-1
1	2	3	-1	0	-1
1	2	3	0	-1	-1
2	1	3	-1	0	-1
2	1	3	0	-1	-1
2	2	4	0	1	1
2	2	4	1	0	1
-1	-2	-3	0	1	1
-1	-2	-3	1	0	1
-2	-1	-3	1	0	1
-2	-1	-3	0	1	1

}

$S_Z$

}

$S^-$

}

$S^+$

**Figure 4.7** All allowed CSA $\otimes$ CSA cross-terms based on second-order selection rules (Eq. (4.28)).

and this is valid<sup>1</sup> for rank-one tensors. Therefore, one can deduce the spin part of the cross-term simply by computing  $s_1 + s_2$  (see last column in Fig. 4.7). The final results are summarized as follows:

$$\begin{aligned}\hat{\mathcal{H}}_{(2)}^{(0,0)} &= f(\hat{S}_z) \\ \hat{\mathcal{H}}_{(2)}^{(\pm 3, \mp 6)} &= g(\hat{S}^+, \hat{S}^-)\end{aligned}\quad (4.36)$$

$$\hat{\mathcal{H}}_{(2)}^{(\pm 4, \mp 8)} = h(\hat{S}^+, \hat{S}^-) \quad (4.37)$$

where  $f$ ,  $g$ , and  $h$  are just numerical functions that depends on the details of the spatial part of the Hamiltonian, and the details of the C element, i.e. the Fourier coefficients  $a_{r,s}^{(k)}$ . Another important results to note from here is that it is actually the resonant terms (Eqs. 4.36 and 4.37) that get compensated (Fig. 4.5) in the asynchronous  $C7_2^1$  regime that renders the higher transfer efficiency. While the non-resonant term  $\hat{\mathcal{H}}_{(2)}^{(0,0)}$  still persists in the asynchronous regime, and they can possibly be eliminated by sophisticated<sup>2</sup> supercycle regime [95]. This feature was exploited by *Edén et al* [94, 95, 102] to design efficient second-order triple-quantum recoupling experiments.

## 4.3 Details of Numerical Simulations and Experiments

### Numerical Simulations

The numerical simulations were performed in the spin-simulation environment GAMMA [80], using a two-spin C-C system with parameters similar to that of 1,4-<sup>13</sup>C<sub>2</sub>-mono-ammonium maleate. The anisotropy of the homonuclear dipolar coupling is  $\delta_D/(2\pi) = -432$  Hz and the isotropic chemical-shift difference between the <sup>13</sup>C resonances is zero. The CSA tensor parameters are  $\delta_{\text{CSA}} = -67.7$  ppm,  $\eta = 1.0$ , and  $(\alpha_{\text{CSA}}, \beta_{\text{CSA}}, \gamma_{\text{CSA}}) = (90^\circ, 67^\circ, 10^\circ)$  [97], relative to the principal-axes system of the dipolar-coupling tensor. The CSA tensors of the two <sup>13</sup>C resonances are related by the mirror-plane symmetry  $\sigma_v$ . A total of 144 powder orientations using the ZCW scheme [104] were used for the simulations, which were performed using the same pulse sequence as the one implemented experimentally (see Fig. 4.1), i.e., with a four-step phase cycle to select only double-quantum coherences. The simulations were carried out at a MAS frequency of  $\nu_r = 10.204$  kHz, with on-resonance rf irradiation on the two chemically-equivalent <sup>13</sup>C spins.

<sup>1</sup>It becomes more complicated for commutator relation involving any rank-2 spin interactions, but can be worked out from Eq. 22 of [101].

<sup>2</sup>It was shown that a nested and MQ phase cycling  $(SS')3^{\pm 1}$  [95] could remove the ZQ terms.

## Experiments

All experiments were carried out on a sample 1,4- $^{13}\text{C}_2$ -mono-ammonium maleate diluted 1:7 in natural abundance material. A Bruker Avance III 700 MHz spectrometer was used with a 2.5 mm TriGamma triple-resonance MAS probe at a MAS frequency of  $\nu_r = 10.204$  kHz. A total of 32 scans with the basic phase-cycling block of  $\phi_{\text{C7}}^{(\text{Excitation})} = (x, x, x, x)$ ,  $\phi_{\text{C7}}^{(\text{Reconversion})} = (y, -x, -y, x)$ , and  $\phi^{(\text{Detection})} = (x, -x, x, -x)$  was used to perform the double-quantum filtered experiment. A recycle delay of 20 s was used in all experiments, and the double-quantum efficiency was normalized with respect to the cross-polarization intensity under the same experimental conditions.

## 4.4 Results and Discussions

Figure 4.8 shows the results of numerical simulations and experiments for the double-quantum filtered  $\text{C7}_2^1$  sequence using  $2\pi_\phi 2\pi_{\phi+\pi}$  (Figs. 4.8a, c, e, and g) and POST (Figs. 4.8b, d, f, and h) as the basic C element. The plots show the DQF efficiency as a function of the additional pulse duration  $\Delta\tau_c$  and the C7 rf-field amplitude  $\nu_1^{(\text{C7})}$  for the pulse-width variation (PWV) (Figs. 4.8a, b, e, and f), or as a function of the cw rf amplitude  $\nu_1^{(\text{CW})}$  for the pulse-amplitude variation (PAV) (Figs. 4.8c, d, g, and h) (see also Fig. 4.1). The agreement between simulations and experiments is very good for all the discussed cases. Both experimental and numerical results confirm that the asynchronous sequence suppresses the CSA tensor much more efficiently as expected from the calculated scaling factor of the CSA-CSA cross terms (Fig. 4.5). In addition, the DQF efficiencies are in general higher using the POST element (Figs. 4.8b, d, f, and h) than the  $2\pi_\phi 2\pi_{\phi+\pi}$  element (Figs. 4.8a, c, e, and g). Such a result is expected as the POST [61] element is known to be more robust against chemical-shift offsets and rf inhomogeneity. In addition, numerical simulations show (see Fig. 4.6) that the POST element suppresses third- and higher-order CSA cross-terms more efficiently than the  $2\pi_\phi 2\pi_{\phi+\pi}$  element. This is implied from the good agreement between the analytical result and numerical simulations at  $\nu_r = 10.204$  kHz (Fig. 4.6).

The theoretical resonance conditions predicted using Floquet theory are also shown in the plots of the simulated efficiencies (Figs. 4.8a-d) for the synchronous ( $\Delta\tau_c = 0$ ) and the asynchronous case ( $\Delta\tau_c \neq 0$ ) as black crosses and dashed black lines. There is a small deviation between the experimentally observed and predicted resonance conditions (Fig. 4.8a-d). This is caused by the CSA-CSA cross terms which shifts the resonance condition, as confirmed by the numerical simulation without a CSA tensor. The value of the optimum incremented pulse duration  $\Delta\tau_c = 0.31 \mu\text{s}$  found in Fig. 4.8a and e matches the value used in the literature [93], and it agrees well with the value of  $\Delta\tau_c = 0.31 \mu\text{s}$  predicted from the

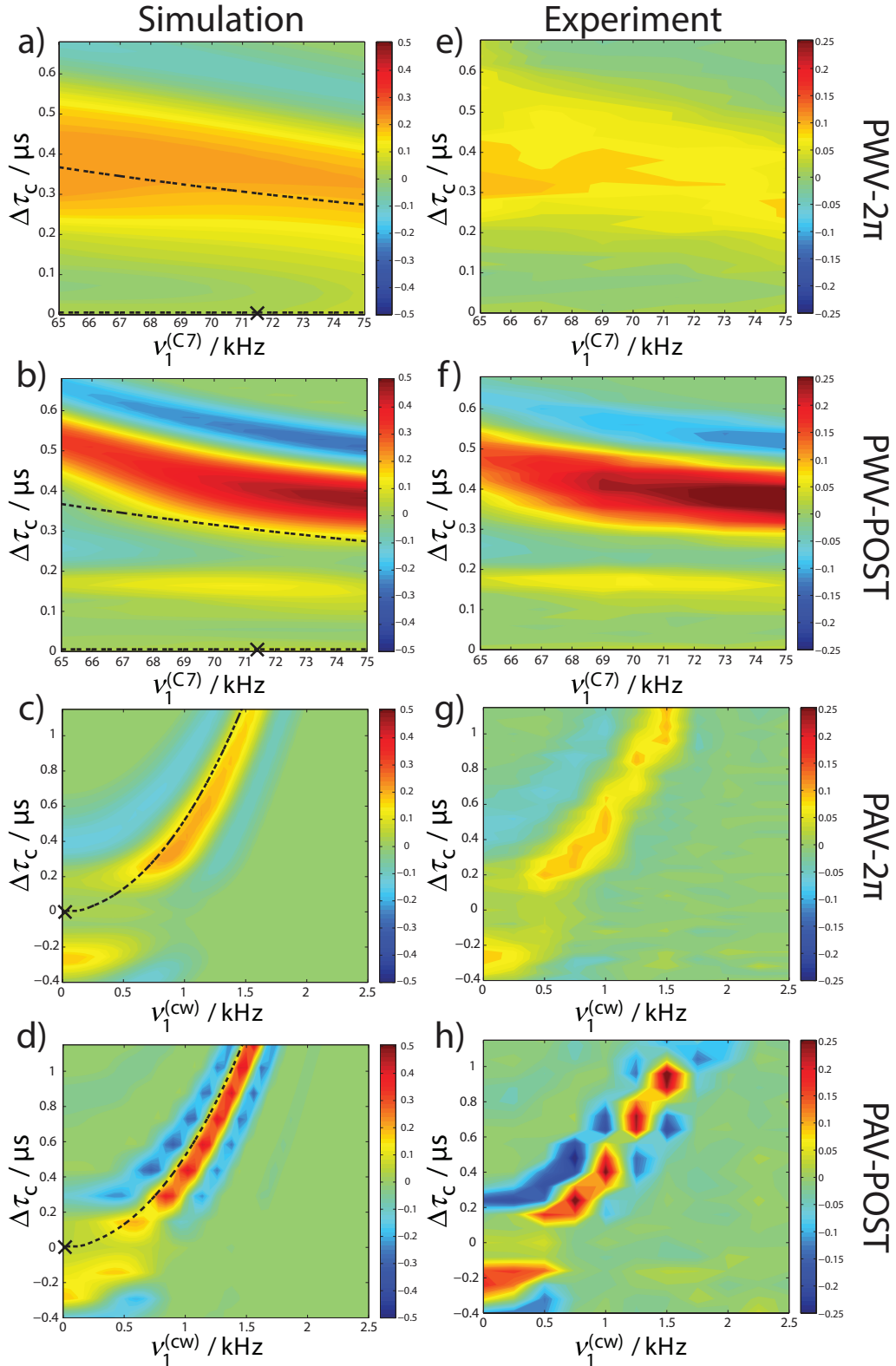


**Figure 4.8** DQ efficiencies obtained by (a-d) simulations and (e-h) experiments, as a function of the pulse duration  $\Delta\tau_c$  and rf field  $v_1^{(C7)}$  (a,b,e,f) or  $v_1^{(cw)}$  (c,d,g,h). The first-order resonance conditions are plotted using dashed line (–) and the ideal synchronous version is marked with a cross (X) in Fig. (a-d). The choice of the C elements are (a,e) PWV- $2\pi$ , (b,f) PWV-POST, (c,g) PAV- $2\pi$ , and (d,h) PAV-POST. The contour plots were obtained for a fixed excitation blocks  $n_{exc}=13$  for Fig. (a,c,e, and g) and  $n_{exc}=22$  for Fig. (b,d,f, and h). The time increments are 18.2 (20) ns, the step size in the rf-field amplitudes is 1 (2) kHz for the PWV plots and 60 (250) Hz in the PAV plots in the simulations (experiment).

resonance condition using Eqs. (4.8) and (4.15).

An experimental build-up curve of the DQF efficiency is shown in Fig. 4.9 for the sequence using the basic C element PWV- $2\pi$  and also PWV-POST. The plot shows that the synchronized conditions ( $\Delta\tau_c=0$ ) have lower DQF efficiencies than the optimized condition ( $\Delta\tau_c = 0.31 \mu\text{s}$ ). It shows that regardless of the choice of the basic C element, the asynchronous sequence has higher DQF efficiencies than the synchronized sequence for spin systems with large CSA tensors. Additionally, the POST element is indeed a more robust element in both synchronous and asynchronous case. The maximum efficiency reached (18%) in the asynchronous POST C7 sequences is about 1/4 of the maximum theoretical efficiency (73%). A factor of 6 is gained compared to the synchronized sequences which reach a maximum double-quantum efficiency of about 3%. The obtained efficiency is quite good under such unfavourable conditions of large CSA and small couplings.

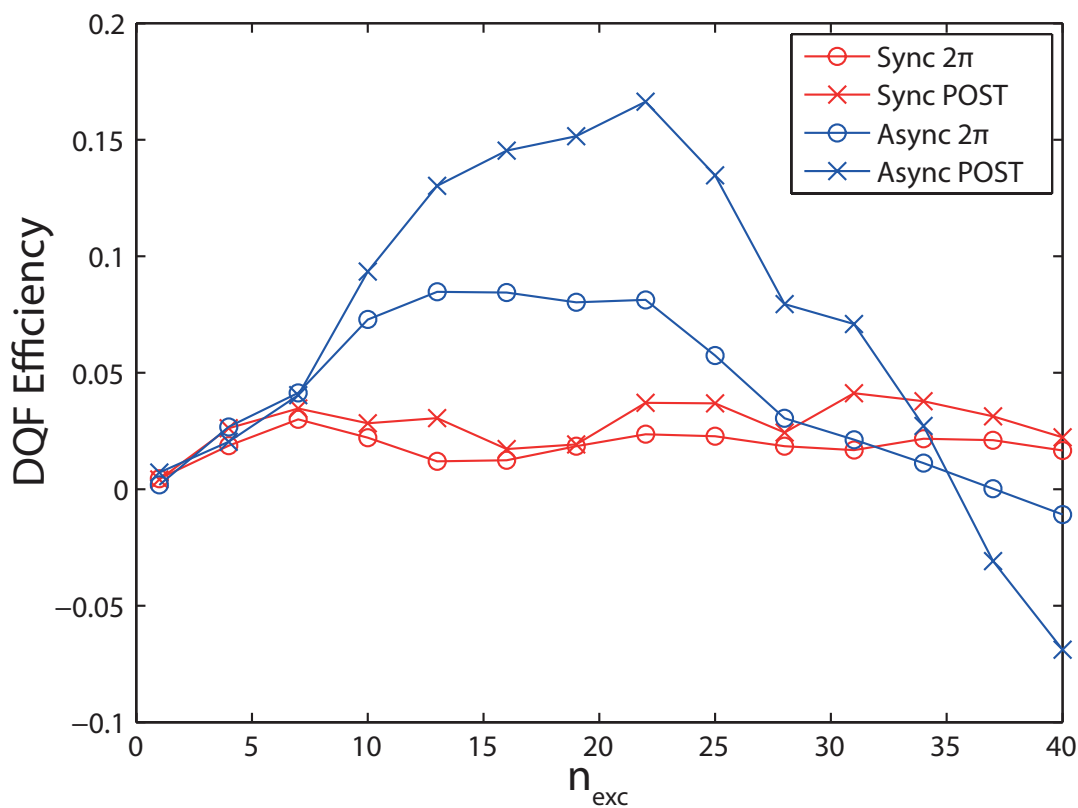


**Figure 4.9** Experimental build-up curve for double-quantum coherences of 1,4  $^{13}\text{C}_2$ -mono- ammonium maleate as a function of the number of excitation block  $n_{\text{exc}}$ , measured using the asynchronous ( $\Delta\tau_c = 0.35 \mu\text{s}$ ) (blue) and synchronous ( $\Delta\tau_c = 0 \mu\text{s}$ ) (red) conditions. The experimental results show that the PWV-POST (blue crosses) element gives higher DQF efficiency than the PWV- $2\pi$  (blue circles) element.



## 4.5 Conclusions for Asynchronous C7

In this work, we have extended the Floquet description of rotor-synchronized symmetry-based sequences to a more general framework that includes non-rotor synchronized sequences with an effective field. The possible resonance conditions are described using operator-based multi-mode Floquet theory. An example of such sequences, asynchronous  $C7_{\frac{1}{2}}$ , is discussed and shown to have a significantly higher double-quantum efficiency than the rotor-synchronized sequence in the presence of large CSA tensors. The better performance of the asynchronous sequence is due to the improved suppression of detrimental second-order CSA cross terms. This effect is shown using analytical Floquet calculations of second-order effective Hamiltonians and confirmed using numerical simulations as well as experimental measurements. Our description rationalizes the phenomenological observations by Bechmann and coworkers [93] who showed that the non-rotor-synchronized  $C7_{\frac{1}{2}}$  sequence, found using numerical optimization, outperforms the rotor-synchronized condition. The asynchronous  $C7_{\frac{1}{2}}$  would be an ideal sequence for spin systems with weak dipolar couplings and large CSA tensors, a typical situation encountered when using high-field spectrometers. In addition, a generalization of the concept of asynchronous sequences to R sequences is currently being investigated in our laboratory. We foresee possible applications in improved suppression of heteronuclear dipolar couplings during recoupling sequences without the need to irradiate the other spin. A second possible application is the use of such sequences in the presence of quadrupolar interaction.



# Chapter 5

## Broad-Band DREAM Recoupling Sequence

A homonuclear dipolar recoupling experiment was demonstrated in Sec. 4 using symmetry-based sequences. In this chapter, it will be shown that the dipolar coupling can also be recoupled via different spin-locking schemes, namely (i) only CW irradiation, i.e. HOR-ROR/DREAM [105–107], (ii) only phase-alternating sequence, i.e. XiX pulses, and (iii) combined CW and phase-alternating irradiation, i.e. XiX<sup>CW</sup> DREAM. Dipolar recoupling in case (iii) (XiX<sup>CW</sup> DREAM) will be the main section in this chapter and case (ii) (XiX DREAM) will be discussed in Sec. 5.5.

### Declaration

Part of the chapter is based on the published manuscript:

K. O. Tan, A. B. Nielsen, B. H. Meier, M. Ernst, *Broad-Band DREAM recoupling sequence*, J. Phys. Chem. Lett. 5, 3366, 2014.

## 5.1 Introduction

Homonuclear polarization-transfer schemes [108, 109] are an important building block in multi-dimensional NMR experiments because they allow the identification of pairs of nuclei coupled by spin-spin interactions. In solid-state NMR, the polarization transfer is often mediated via dipolar couplings which are distance dependent and hence allowing distance measurements and structure determination [110, 111]. Dipolar interactions are averaged out by magic-angle spinning (MAS) in a first-order average Hamiltonian (AHT) picture [68], but can be reintroduced via recoupling sequences. A large number of recoupling sequences have been developed over the years based on different concepts. The homonuclear

rotary-resonance (HORROR) [107] sequence is an example of such recoupling sequences where the rf-field amplitude of continuous wave (CW) irradiation is matched to half the MAS frequency in order to reintroduce the homonuclear dipolar coupling. The HORROR sequence is a simple sequence but it has limited practical importance due to its sensitivity to chemical-shift offsets and rf-field inhomogeneity. The sensitivity to the chemical-shift offsets is a consequence of the low rf-field amplitude, in particular at slower MAS frequencies. On the other hand, this feature makes it an attractive sequence for applications in biological samples at faster MAS spinning rates exceeding the carbon chemical-shift range. The adiabatic version of HORROR, called DREAM [105], mitigates the problems due to offset and rf-inhomogeneity and increases the theoretical transfer efficiency to 100%. These advantages have made the DREAM sequence a popular sequence in multi-dimensional correlation spectroscopy, which is used for resonance assignments in proteins [2, 3, 112–114]. However, the bandwidth of the DREAM polarization transfer is still limited to roughly the spinning frequency. In addition, the cross-peak intensities depend strongly on the position of the rf-carrier frequency. A detailed discussion is provided by *Westfeld et al.* [115].

Here, we propose a modified DREAM sequence that reduces the sensitivity to the carrier position to a greater extent by superimposing a phase alternating rf-irradiation scheme [39, 116, 117], i.e., XiX pulses [50] on top of the CW field. Figure 5.1a illustrates the basic idea of superimposing the two sequences where the individual rf-field amplitudes are added if the two sequences have the same phase or subtracted if they have opposite phase. The possible recoupling conditions of the new sequence are analyzed using a triple-mode Floquet framework [32]. In principle, these schemes allow us to considerably increase the rf amplitude while maintaining a HORROR-type recoupling. We will focus here on one specific resonance condition where the average rf power is still low and yet high transfer efficiency can be achieved.

## 5.2 Theory

We consider a system of two dipolar-coupled spins. The full time-dependent Hamiltonian of the system under MAS and rf irradiation in spherical-tensor notation [68] is given by

$$\begin{aligned} \hat{\mathcal{H}}(t) = & \sum_{p=1}^2 \sum_{n=-2}^2 \omega_p^{(n)} e^{in\omega_r t} T_{1,0}^{(p)} + \sum_{\substack{n=-2 \\ n \neq 0}}^2 \omega_{1,2}^{(n)} e^{in\omega_r t} T_{2,0}^{(1,2)} + \omega_{1,2}^{(0)} T_{0,0}^{(1,2)} \\ & + \omega_{1S}(t) \sum_{p=1}^2 S_{px} \end{aligned} \quad (5.1)$$

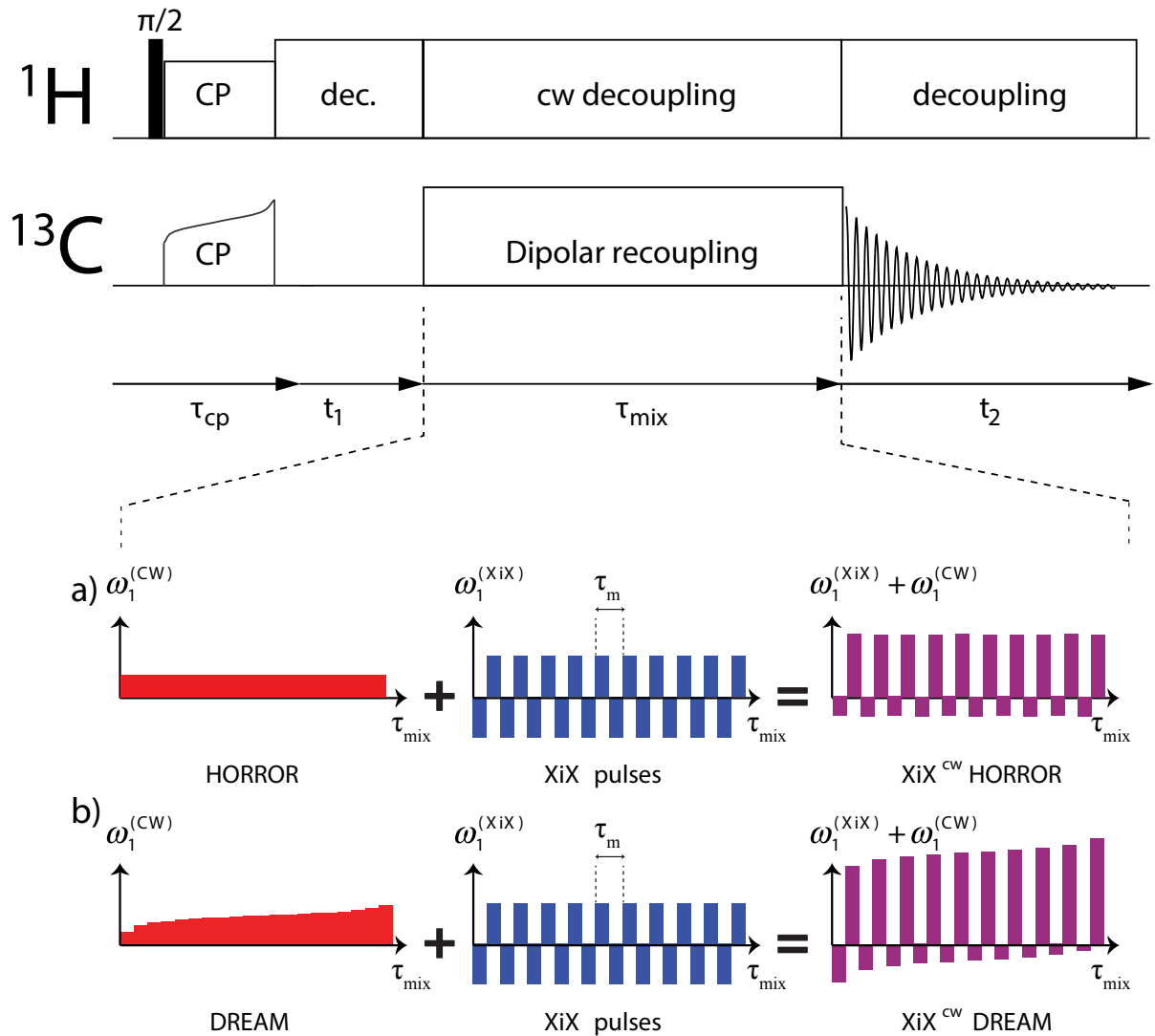


**Figure 5.1** Pulse sequence for a two-dimensional homonuclear  $^{13}\text{C}$ - $^{13}\text{C}$  correlation experiment using a) XiX<sup>cw</sup> HORROR or the adiabatic version b) XiX<sup>cw</sup> DREAM with CW decoupling on proton during the mixing time  $\tau_{\text{mix}}$ .  $\omega_1^{(\text{XiX})}$  and  $\omega_1^{(\text{cw})}$  represent the rf field strength of the phase-alternating and CW part respectively, and the cycle-time of the XiX pulses is given by  $\tau_{\text{mix}} = 2\pi/\omega_m$ .

where the last term  $\omega_{1S}(t) = \omega_1^{(\text{XiX})}(t) + \omega_1^{(\text{cw})}$  represents the time-dependent amplitude-modulated rf Hamiltonian, as depicted in Fig. 5.1. The pulse sequence is essentially an amplitude-modulated rf irradiation along the x-axis of the Zeeman interaction-frame. Hence, the interaction-frame transformation with the full rf Hamiltonian (Eq. (5.1)) can be done in a straightforward way since this Hamiltonian commutes with itself at all times. Prior to the interaction-frame transformation, we adopt a tilted-frame representation for the Hamiltonians by first rotating the Hamiltonians by a  $90^\circ$  rotation about the negative y-axis ( $\hat{S}_x \rightarrow \hat{S}_z$ ,  $\hat{S}_z \rightarrow -\hat{S}_x$ ). In the full rf interaction frame, we obtain a time-dependent Hamiltonian of the

form

$$\hat{\mathcal{H}}(t) = \sum_{n=-2}^2 \sum_{k=-\infty}^{\infty} \sum_{\ell=-2}^2 \hat{\mathcal{H}}^{(n,k,\ell)} e^{in\omega_r t} e^{ik\omega_m t} e^{i\ell\omega_1^{(\text{cw})} t} \quad (5.2)$$

with three basic frequencies, the MAS frequency  $\omega_r$ , the modulation frequency of the phase-alternating rf irradiation  $\omega_m$ , and the mean rf-field amplitude  $\omega_1^{(\text{cw})} = \omega_1(t)$ . The Fourier components of the Hamiltonian are given by

$$\hat{\mathcal{H}}^{(n,0,0)} = \left\{ \omega_{1,2}^{(0)} T_{0,0}^{(1,2)} \right\} \delta_{n,0} - \frac{1}{2} \omega_{1,2}^{(n)} T_{2,0}^{(1,2)} \quad (5.3)$$

$$\hat{\mathcal{H}}^{(n,k,\pm 1)} = \sum_{p=1}^2 \pm \frac{1}{\sqrt{2}} \omega_p^{(n)} T_{1,\pm 1}^{(p)} a_{1,\pm 1}^{(k)} \quad (5.4)$$

$$\hat{\mathcal{H}}^{(n,k,\pm 2)} = \frac{\sqrt{3}}{2\sqrt{2}} \omega_{1,2}^{(n)} T_{2,\pm 2}^{(1,2)} a_{2,\pm 2}^{(k)} \quad (5.5)$$

where  $a_{r,s}^{(k)}$  are the Fourier coefficients that characterize the interaction-frame transformation of the spherical-tensor operators in the tilted frame under the amplitude-modulated rf irradiation:

$$\tilde{T}_{r,0}(t) = \sum_{s=-r}^r a_{r,s}(t) T_{r,s} = \sum_{k=-\infty}^{\infty} \sum_{s=-r}^r a_{r,s}^{(k)} e^{ik\omega_m t} T_{r,s} \quad (5.6)$$

For a phase-alternating irradiation (XiX), the magnitude of the  $a_{r,s}^{(k)}$  coefficients depends only on the ratio  $\omega_1^{(\text{XiX})}/\omega_m$ . Note that the rf amplitude of the phase-alternating sequence  $\omega_1^{(\text{XiX})}$  has only an indirect effect on the effective Hamiltonian, i.e., it affects the magnitude of the effective Hamiltonian but does not shift the resonance conditions. The analytical expressions as well as graphical plots of the Fourier coefficients are provided by [50] *Ernst et al.* If the three basic frequencies  $\omega_r$ ,  $\omega_m$  and  $\omega_1^{(\text{cw})}$  fulfil the resonance condition  $n_0\omega_r + k_0\omega_m + \ell_0\omega_1^{(\text{cw})} = 0$ , one obtains an effective Hamiltonian of the form

$$\hat{\mathcal{H}}^{\hat{\Delta}(1)} = \hat{\mathcal{H}}^{\hat{\Delta}(0,0,0)} + \sum_{n_0,k_0,\ell_0} \hat{\mathcal{H}}^{\hat{\Delta}(n_0,k_0,\ell_0)} \quad (5.7)$$

where the values of  $n_0$  and  $\ell_0$  are restricted to the range from -2 to +2 and  $k_0$  can be any integer number. As we are interested in a double-quantum recoupling condition, the important terms are the double-quantum terms  $T_{2,\pm 2}$ . These terms are found in the Fourier components  $\hat{\mathcal{H}}^{\hat{\Delta}(n,k,\pm 2)}$ , which can be reintroduced via the double-quantum recoupling condition  $n_0\omega_r + k_0\omega_m \pm 2\ell_0\omega_1^{(\text{cw})} = 0$ . In principle, there are infinitely many possible combinations of setting the frequencies  $\omega_r$ ,  $\omega_m$ , and  $\omega_1^{(\text{cw})}$  to match the double-quantum recoupling con-

dition. In this paper, we focus on one specific resonance condition defined by

$$\omega_r = \omega_m = 2 \omega_1^{(\text{cw})} \quad (5.8)$$

Additionally, we impose the condition  $\omega_1^{(\text{XiX})} = \omega_m$  in order to maximize the transfer (*vide infra*). By fulfilling this condition, one obtains the first-order effective Hamiltonian

$$\begin{aligned} \hat{\mathcal{H}}^{(1)} &= \hat{\mathcal{H}}^{(0,0,0)} + \hat{\mathcal{H}}^{(1,0,-2)} + \hat{\mathcal{H}}^{(-1,0,2)} + \hat{\mathcal{H}}^{(1,-2,2)} + \hat{\mathcal{H}}^{(-1,2,-2)} \\ &+ \hat{\mathcal{H}}^{(2,-1,-2)} + \hat{\mathcal{H}}^{(-2,1,2)} + \hat{\mathcal{H}}^{(2,-3,2)} + \hat{\mathcal{H}}^{(-2,3,-2)} \\ &= \omega_{1,2}^{(0)} T_{0,0}^{(1,2)} + \left( \omega_{1,2}^{(\text{eff})} T_{2,2}^{(1,2)} + \omega_{1,2}^{(\text{eff})\dagger} T_{2,-2}^{(1,2)} \right) \end{aligned} \quad (5.9)$$

with the effective dipolar coupling strength  $\omega_{1,2}^{(\text{eff})}$  given by

$$\omega_{1,2}^{(\text{eff})} = \frac{\sqrt{3}}{2\sqrt{2}} \left( \omega_{1,2}^{(-1)} a_{2,2}^{(0)} + \omega_{1,2}^{(+1)} a_{2,2}^{(-2)} + \omega_{1,2}^{(-2)} a_{2,2}^{(+1)} + \omega_{1,2}^{(+2)} a_{2,2}^{(-3)} \right) \quad (5.10)$$

Note that the first term in Eq. (5.9) represents the homonuclear  $J$  coupling while the other terms are the desired double-quantum recoupling terms. In the following discussion, we will neglect the  $J$ -coupling Hamiltonian since the magnitude of the dipolar couplings is usually much larger than the scalar couplings. This sequence does not generate a  $\gamma$ -encoded effective Hamiltonian [107] because the mixing of the  $n = 1$  ( $\omega_{1,2}^{(\pm 1)}$ ) and  $n = 2$  ( $\omega_{1,2}^{(\pm 2)}$ ) (Eq. (5.10)) terms makes it impossible to express the  $\gamma$ -angle as an overall phase factor in the effective Hamiltonian (Eq. (5.9)). This is not necessarily a drawback and it has been shown recently that such a Hamiltonian can achieve a higher maximum transfer efficiency in the first transient [118] than one finds for  $\gamma$ -encoded sequences (73%), if the combination of the Fourier coefficients is chosen appropriately. In principle, for powdered solids, the rate of the polarization transfer can be determined by the first moment for the absolute value of effective dipolar coupling [119]

$$\left\langle \left| \omega_{1,2}^{(\text{eff})} \right| \right\rangle = \frac{\int_{\alpha, \beta, \gamma} \left| \omega_{1,2}^{(\text{eff})}(\alpha, \beta, \gamma) \right| \sin(\beta) d\alpha d\beta d\gamma}{\int_{\alpha, \beta, \gamma} \sin(\beta) d\alpha d\beta d\gamma} \quad (5.11)$$

which depends on the Fourier coefficients  $a_{2,2}^{(k)}$  and, therefore, on the ratio  $\omega_1^{(\text{XiX})}/\omega_m$ . Figure 5.2b (blue crosses) shows the first moment  $\langle |\omega_{1,2}^{(\text{eff})}| \rangle$  as a function of the ratio  $\omega_1^{(\text{XiX})}/\omega_m$  normalized by the value  $\langle |\omega_{1,2}^{(\text{eff})}(\omega_1^{(\text{XiX})}/\omega_m = 0)| \rangle$ , i.e., the HORROR condition. One can

clearly see that the value of  $\langle |\omega_{1,2}^{(\text{eff})}| \rangle$  decreases with increasing  $\omega_1^{(\text{XiX})}/\omega_m$ , in agreement with the observed slowdown of the polarization transfer from the numerical simulations shown in Fig. 5.2a. Besides that, the maxima of the polarization transfer extracted from Fig. 5.2a are plotted in Fig. 5.2b (red circles) and it shows an oscillatory behaviour as a function of the ratio  $\omega_1^{(\text{XiX})}/\omega_m$ . This behaviour can be correlated to the second moment [41] for the absolute value of effective dipolar coupling  $\langle \Delta |\omega_{1,2}^{(\text{eff})}|^2 \rangle$  (Eq. (5.13)).

$$\langle \Delta |\omega_{1,2}^{(\text{eff})}|^2 \rangle = \frac{\int_{\alpha,\beta,\gamma} \left( |\omega_{1,2}^{(\text{eff})}(\alpha, \beta, \gamma)| - \langle |\omega_{1,2}^{(\text{eff})}| \rangle \right)^2 \sin(\beta) d\alpha d\beta d\gamma}{\int_{\alpha,\beta,\gamma} \sin(\beta) d\alpha d\beta d\gamma} \quad (5.12)$$

$$N_{\text{eff}} = \frac{\langle \Delta |\omega_{1,2}^{(\text{eff})}|^2 \rangle}{\langle |\omega_{1,2}^{(\text{eff})}| \rangle} \quad (5.13)$$

Moreover, a dimensionless quantity  $N_{\text{eff}}$  (Eq. (5.13)) is defined here to characterise the maximum first transient efficiency (black diamond in Fig. 5.2b), and it is independent of the details on the spin system. The maximum of the polarization transfer is high when the quantity  $N_{\text{eff}}$  is low, and vice-versa. A good compromise between low values for  $N_{\text{eff}}$  (high maximum transfer efficiency) and high values for  $\langle |\omega_{1,2}^{(\text{eff})}| \rangle$  (fast transfer) is found when the ratio  $\omega_1^{(\text{XiX})}/\omega_m = 1$ , justifying the choice of the resonance condition selected in the theoretical discussion above. The reason that it is possible to achieve a higher polarization-transfer efficiency (or smaller  $N_{\text{eff}}$ ) in the non  $\gamma$ -encoded sequence compared to the  $\gamma$ -encoded HORROR sequence is that the effective Hamiltonian (Eq. (5.10)) recouples  $n = 1$  ( $\omega_{1,2}^{(\pm 1)}$ ) and  $n = 2$  ( $\omega_{1,2}^{(\pm 2)}$ ) terms simultaneously, hence providing an additional degree of freedom for the optimization of the orientation-dependent effective dipolar couplings. In the conventional HORROR condition, only the  $n = 1$  ( $\omega_{1,2}^{(\pm 1)}$ ) term is recoupled. The  $n = 2$  HORROR condition [120] is not often used, as it also reintroduces the undesirable CSA tensor, which is avoided in the case of XiX<sup>cw</sup>. The same reasoning allows us to ignore the heteronuclear dipolar couplings to first order in XiX<sup>cw</sup>. Nevertheless, the transfer efficiency could still be affected by higher-order terms involving the heteronuclear dipolar coupling. However, these terms can be assumed to be small if a suitable proton decoupling scheme is applied during the mixing time. The sequence can be further improved to compensate for rf inhomogeneity more efficiently and also to achieve a theoretical transfer efficiency approaching 100 % by performing an adiabatic experiment [106]. This can be implemented by sweeping the  $\omega_1^{\text{cw}}$  field through the on-resonance condition given in Eq. (5.8) (see also Fig. 5.1b).



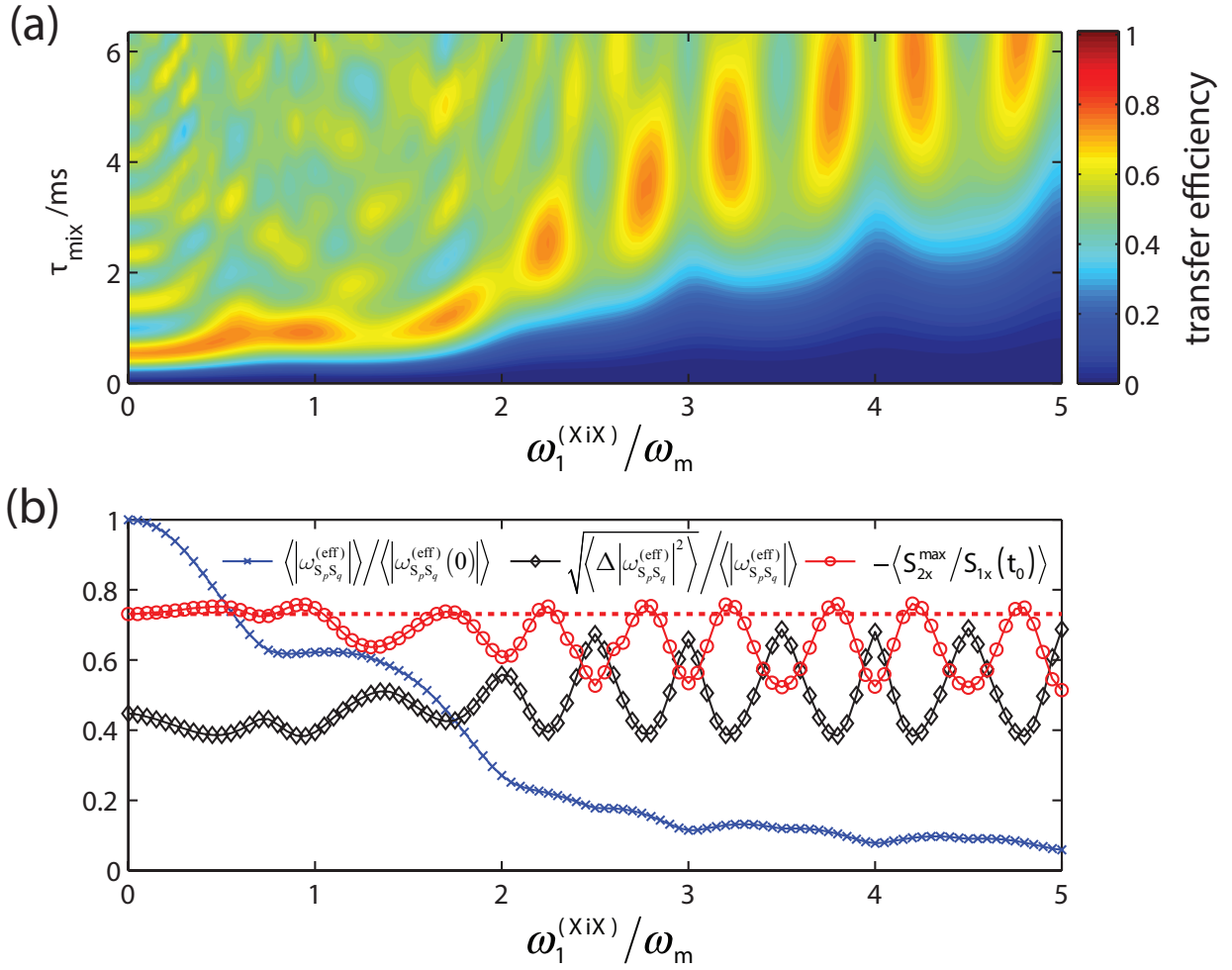


**Figure 5.2** (a) Simulated transfer efficiency  $-\langle S_{2x}(t)/S_{1x}(0) \rangle$  of an ideal dipolar-coupled two-spin system as a function of the mixing time  $\tau_{\text{mix}}$  and the ratio of the rf field amplitude of the XiX pulses to the modulation frequency  $\omega_1^{(\text{XiX})}/\omega_m$ . (b) The magnitude of the normalized first moment  $\langle |\omega_{S_p S_q}^{(\text{eff})}| \rangle / \langle |\omega_{S_p S_q}^{(\text{eff})}(\omega_1^{(\text{XiX})}/\omega_m = 0)| \rangle$  (blue cross) and the normalized second moment  $N_{\text{eff}}$  (black diamond) are calculated analytically using the effective Hamiltonian in Eq. (5.9). Also shown in the same plot is the maximum transfer  $-\langle S_{2x}^{\text{max}}/S_{1x}(t_0) \rangle$  (red circle) extracted from (a). The red dashed line indicates a value of 0.73 which is the maximum transfer efficiency obtained for a  $\gamma$ -encoded sequence.

### 5.3 Computational and Experimental Methods

First, we compare the performance of XiX<sup>cw</sup> DREAM with DREAM by means of numerical simulations for a four-spin CH<sub>2</sub>-C model system using the spin-simulation environment GAMMA [80]. The spin-system parameters were chosen such that they correspond to the parameters for crystalline glycine ethylester, with the isotropic chemical-shift difference of the two <sup>13</sup>C resonances set to 16 kHz corresponding to the values for a 500 MHz spectrometer. Figure 5.3a shows the simulated polarization-transfer efficiency from the carbonyl to

the aliphatic carbon as a function of the offset frequency  $\nu_{\text{off}}$ . The parameters for both simulations were first optimized at a MAS frequency of 20 kHz with the carrier frequency placed in the middle of the two  $^{13}\text{C}$  resonances. Then, the simulations were repeated at different carrier frequencies using the same parameters. The results show that the XiX<sup>cw</sup> DREAM sequence yields a maximum transfer efficiency of about 42% whereas the conventional DREAM experiment yields only a maximum of about 32%. Moreover, the transfer profile of XiX<sup>cw</sup> DREAM is broader and higher than that of DREAM for almost all values of the carrier frequency. Similar improvements are also observed in the experimental results (Fig. 5.3b) measured on a sample of 1,2- $^{13}\text{C}$ -glycine ethylester on a Varian Infinity+ 500 MHz spectrometer, using the same conditions as the numerical simulations shown in Fig. 5.3a. More details on the spin-system and the acquisition parameters can be found in Sec. A.3 and Table 5.1 respectively.

	Gly (XiX <sup>cw</sup> )	Gly (DREAM)	Ubi (XiX <sup>cw</sup> )	Ubi (DREAM)
$^{13}\text{C}$ rf $\nu_1^{(\text{cw})}$ / kHz	9.35	6.2	12.5	10.5
$^{13}\text{C}$ rf $\nu_1^{(\text{XiX})}$ / kHz	23.5	-	23.5	-
$^1\text{H}$ rf $\nu_{1\text{H}}^{(\text{cw})}$ / kHz	145	145	138	138
MAS frequency $\nu_r$ / kHz	20	20	25	25
XiX $\tau_m$ / $\mu\text{s}$	50	-	40	-
Mixing time $\tau_{\text{mix}}$ / ms	3.15	3.15	6	6
Carrier $^{13}\text{C}$	107	107	111	111
$d_{\text{est}}/2\pi$ / kHz	3.74	2.48	4.5	4.5
$\Delta/2\pi$ / kHz	1.48	1.23	-2.5	-2.5

**Table 5.1** Experimental details of DREAM and XiX<sup>cw</sup> DREAM on glycine and ubiquitin.

## 5.4 Results and Discussions for XiX<sup>cw</sup> DREAM

It is well known that the intensities of the cross peaks in a 2D DREAM spectrum are affected by the position of the carrier frequency [115], in particular if the chemical-shift range of the involved resonances is large compared to the spinning frequency. This effect was investigated for both DREAM and XiX<sup>cw</sup> DREAM sequences experimentally using the tripeptide MLF as a test sample on a 600 MHz spectrometer at a MAS frequency of 13 kHz. Figure 5.4 shows the DREAM spectra (Figs. 5.4a-c) and the XiX<sup>cw</sup> DREAM spectra (Figs. 5.4d-f) all obtained with a mixing time of 5.6 ms and CW decoupling of 100 kHz on protons. Both mixing sequences were first optimized on 1D spectra with the carrier frequency at 40 ppm

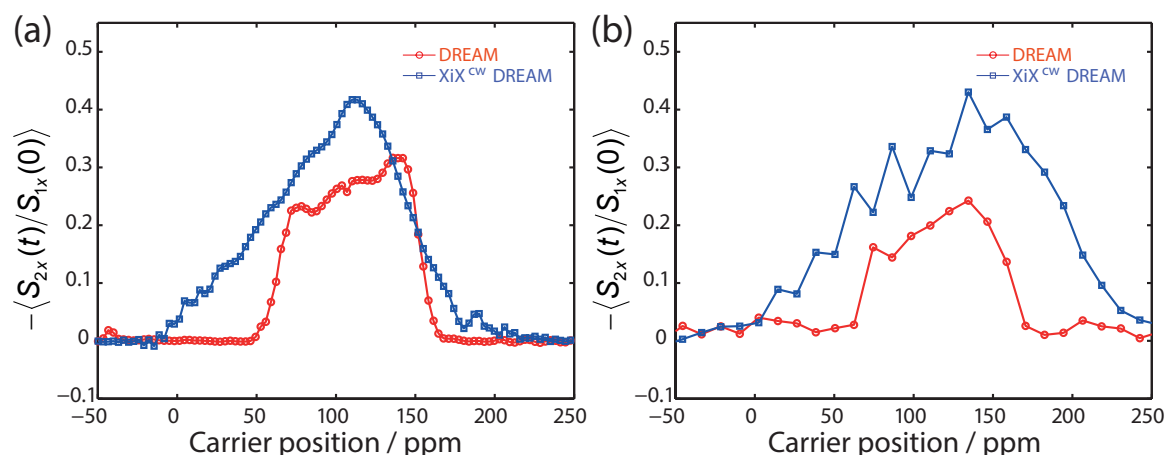


**Figure 5.3** Comparison of the dependence of the transfer efficiency on the position of the rf-carrier frequency between DREAM (red) and XiX<sup>CW</sup> DREAM (blue) for a) simulations of a four-spin CH<sub>2</sub>-C system b) experimental results measured on 1,2-<sup>13</sup>C-glycine ethyl ester on a 500 MHz spectrometer, for a mixing time  $\tau_{\text{mix}} = 3.15$  ms and  $\nu_r = 20$  kHz.

(Figs. 5.4b and e). Subsequently, two additional spectra were acquired with the same parameters but the carrier frequency placed at 0 ppm (Figs. 5.4a and d) and 80 ppm (Figs. 5.4c and f), respectively. All spectra shown in Fig. 5.4 were processed using the same parameters including the setting of the contour levels. It is clear from the DREAM spectra (Figs. 5.4a-c) that more than half of the cross peaks vanish when the carrier frequency is shifted by  $\pm 40$  ppm. The bandwidth of the recoupling condition becomes very limited under the strong offset conditions and only the <sup>13</sup>C resonances that are close to the anti-diagonal satisfy the double-quantum recoupling condition. In the XiX<sup>CW</sup> DREAM spectra (Figs. 5.4d-f), most of the cross peaks are still visible even when the carrier frequency is shifted and the cross-peak intensities are attenuated compared to the spectrum with the carrier frequency placed in the middle (Fig. 5.4e). It is evident from the spectra that XiX<sup>CW</sup> DREAM is less susceptible than DREAM to the exact placement of the carrier frequency, therefore, suggesting that it is a better offset-compensated sequence. Note that some of the cross peaks in Figs. 5.4d and f have positive intensities because they are either due to relay transfer or direct transfer mediated by a zero-quantum Hamiltonian if the rotational-resonance in a tilted rotating frame (R2TR) [121, 122] is satisfied.

In order to demonstrate that the new sequence is a practical choice for application in biomolecular solid-state NMR, full 2D <sup>13</sup>C homonuclear correlation spectra (Fig. 5.5) of U-<sup>13</sup>C-<sup>15</sup>N ubiquitin were acquired on a 600 MHz spectrometer at a spinning frequency of 25 kHz using both DREAM (Fig. 5.5a) and XiX<sup>CW</sup> DREAM (Fig. 5.5b). Both mixing sequences were optimized in 1D experiments with the carrier frequency positioned at 111 ppm

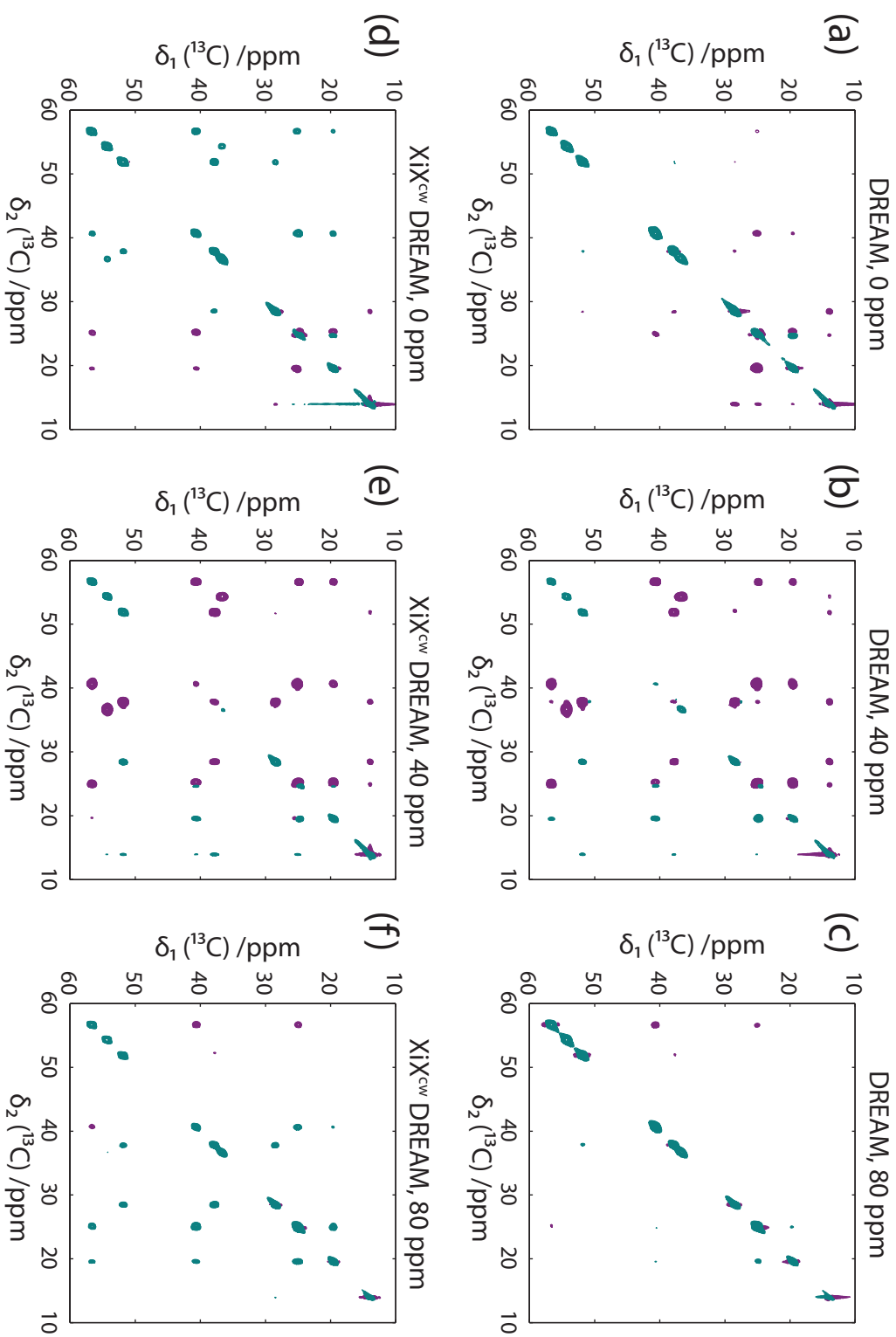


**Figure 5.4** Experimental two-dimensional homonuclear  $^{13}\text{C}$ - $^{13}\text{C}$  correlation spectra of the tripeptide MLF at MAS  $\nu_r = 13$  kHz on 600 MHz measured using (a, b, and c) DREAM and (d, e, and f) XIX $^{\text{cw}}$  DREAM respectively for a mixing time  $\tau_{\text{mix}}$  of 5.6 ms. Both sequences were optimized in 1D with the carrier frequency positioned at (b and e) 40 ppm. Additional spectra were acquired with the same optimized mixing sequence except that the carrier frequency is shifted to (a and d) 0 ppm and (c and f) 80 ppm respectively. Only the aliphatic carbon region is shown here with positive peaks in teal and negative peaks in magenta.

for the highest CO-CA transfer efficiency. The two spectra were processed with the same parameters and are plotted using identical contour levels. Both sequences show comparable performance for the CO-CA cross peaks, but it is evident that XiX<sup>cw</sup> DREAM outperforms DREAM in generating additional cross peaks in the aliphatic region. Two 1D slices through the resonances of 46Ala (Fig. 5.5c) and 22Thr (Fig. 5.5d) are shown to allow a better comparison of the two mixing sequences. Although the CA-CO cross-peak intensities of 46Ala (Fig. 5.5c) are comparable for both sequences, the relay transfer  $A46C\beta$  is much higher in the case of XiX<sup>cw</sup> DREAM. In Fig. 5.5d, one can clearly see that the  $C\gamma-C\beta$  cross peak under XiX<sup>cw</sup> DREAM regime is much higher than the one acquired using DREAM. More experimental details for the acquisition of the 2D spectra for ubiquitin are shown in Table 5.1.

We have proposed a new homonuclear dipolar recoupling sequence by superimposing a phase-alternating sequence onto the HORROR sequence. The recoupling conditions of such a sequence were generalized and studied analytically using Floquet theory. It can also be shown that the basic frequencies involved in the resonance conditions are similar to that of the <sup>RESPIRATION</sup>CP [118]. A specific recoupling condition (Eq. (5.8)) in which the original DREAM condition ( $\omega_1^{(cw)} = \omega_r/2$ ) is superimposed with XiX pulses, of which the cycle time  $\tau_m$  matches a rotor period  $\tau_r$ , is analyzed. This condition has the advantage that the theoretical maximum transfer efficiency can be higher than that of a  $\gamma$ -encoded sequence. The required average rf field strength applied in XiX<sup>cw</sup> is of the order of the spinning frequency  $\nu_r$ , which is twice as high as the one used in the HORROR condition. This increase is necessary to achieve the broader bandwidth and higher transfer efficiency as compared to HORROR. Still, the relatively low rf field power requirement (compared to POST-C7 [61] or PAMORE [117]) of XiX<sup>cw</sup> DREAM is also practical for applications in biological macromolecules, i.e. in obtaining a full 2D <sup>13</sup>C homonuclear correlation spectra of ubiquitin at intermediate spinning frequency. We believe that XiX<sup>cw</sup> DREAM, being a first-order recoupling sequence with efficient offset compensation, would be an ideal candidate as a dipolar recoupling sequence in such situation. Practical applications are mainly foreseen for assignment experiments in biological samples [2, 123].

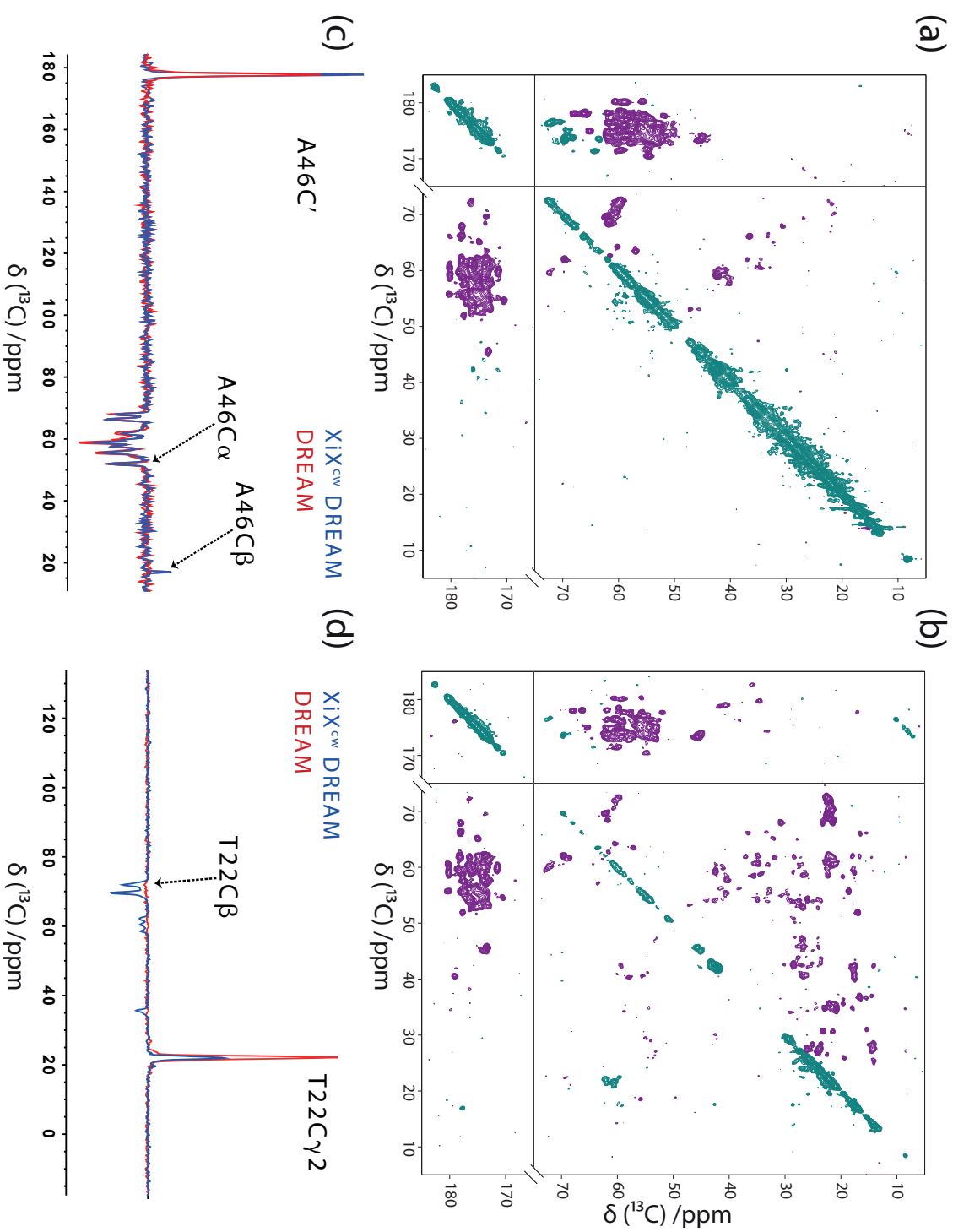


**Figure 5.5** Experimental 2D spectra measured on ubiquitin using a) DREAM b) XiX<sup>cw</sup> DREAM at MAS frequency of 25 kHz and the position of the carrier frequency at 111 ppm with a mixing time  $\tau_{\text{mix}}$  of 6 ms, on a 600 MHz spectrometer. Two 1D slices are taken from both spectra through the resonances (c) 46Ala, 177.9 ppm and (d) 22Thr, 22 ppm. Both slices show that XiX<sup>cw</sup> DREAM (blue) has higher transfer efficiency than DREAM (red) when the chemical shift offset is large.

### Prospects and Future Work

The main advantage of XiX<sup>cw</sup> DREAM is that the mean rf field ( $\overline{v_1} = 0.75v_r$ ) is higher than the normal DREAM sequence ( $\overline{v_1} = 0.5v_r$ ), for the specific chosen resonance condition (Eq. (5.8)) that uses the least rf field. There is in general many more possible resonance conditions to be exploited for DQ recoupling. Moreover, the XiX<sup>cw</sup> DREAM sequence might perform better at higher MAS where proton decoupling is not needed. At moderate MAS, the interference can be alleviated (perhaps not fully avoided) by using high power <sup>1</sup>H decoupling. In addition, a pulse sequence with large first moment (Eq. (5.11)) but smallest second moment (Eq. (5.12)) is desired because it gives fastest and highest theoretical transfer efficiency for the non-adiabatic regime. This can perhaps be optimized using optimal control, a genetic algorithm or any other numerical optimization scheme. The possible future works are summarized below:

1. Examine the XiX<sup>cw</sup> DREAM sequence at higher MAS without proton decoupling.
2. Explore other possible resonance conditions with higher rf fields at moderate MAS.
3. Numerically optimize the second moment to give highest transfer efficiency.
4. Incorporate the offset description into the resonance condition using the quaternions. Moreover, compare this method with the pulse version (RESPIRATION-CP [118]).

## 5.5 DQ Recoupling without CW field: XiX DREAM

In principle, the DQ term can be recoupled by employing only a phase-alternating sequence, i.e. XiX pulses. In this regime, the DQ terms are recoupled via a matching of the spinning frequency  $v_r$  with the modulation frequency  $v_m$  (Eq. (5.14)). In addition, novel adiabatic sequences will be demonstrated here in the absence of an effective CW field. A comparison with other different DQ recoupling schemes (DREAM and XiX<sup>cw</sup> DREAM) will be shown and discussed in the end.

### 5.5.1 Theory

The resonance conditions for such sequences can be described by bimodal Floquet theory:

$$n_0 v_r + k_0 v_m = 0 \quad (5.14)$$

where  $\nu_m$  is the modulation frequency of the XiX pulses. Following this, the Fourier components of the Hamiltonian have a general form of

$$\begin{aligned}\hat{\mathcal{H}}^{(n,k)} &= \omega_1^{(n)} (a_y^{(k)} S_{1y} - a_x^{(k)} S_{1x}) + \omega_2^{(n)} (a_y^{(k)} S_{2y} - a_x^{(k)} S_{2x}) \\ &\quad + \frac{3\omega_{1,2}^{(n)}}{2} \left( b_x^{(k)} (S_{1x}S_{2x} - S_{1y}S_{2y}) - b_y^{(k)} (S_{1x}S_{2y} + S_{1y}S_{2x}) \right) \\ &= \omega_1^{(n)} (a_y^{(k)} S_{1y} - a_x^{(k)} S_{1x}) + \omega_2^{(n)} (a_y^{(k)} S_{2y} - a_x^{(k)} S_{2x}) + \frac{3\omega_{1,2}^{(n)}}{2} \left( b_x^{(k)} S_x^\Sigma - b_y^{(k)} S_y^\Sigma \right)\end{aligned}\quad (5.15)$$

where the first two terms in Eq. (5.15) contain the CSA interaction and the last term contains homonuclear dipolar coupling with the double-quantum terms  $S_x^\Sigma$  and  $S_y^\Sigma$  (see Eq. (A.6)). The Fourier coefficients  $a_{x,y}^{(k)}$  and  $b_{x,y}^{(k)}$  are obtained after the interaction-frame transformation along the rf Hamiltonian ( $z$ -axis), and the size of the Fourier coefficients depend on the ratio of  $\omega_1^{(\text{XiX})}/\omega_m$  (Fig. 5.6). Note that the Cartesian instead of the spherical basis is chosen here, so that the description is consistent with the literature [50].

Following this, DQ recoupling experiments can be designed by setting correctly the Fourier coefficients so that high scaling factors are attributed for DQ term, and zero for other undesired interactions like CSA. There are two general methods to obtain pure DQ recoupling, namely setting (i)  $\nu_r = (2k+1)\nu_m/2$  and  $\nu_1^{(\text{XiX})} = (2k+1)\nu_m/2 = \nu_r$  or (ii)  $\nu_r = k\nu_m$  and  $\nu_1^{(\text{XiX})} = k/2\nu_m = \nu_r/2$ . The effective Hamiltonian of condition (i) is less interesting because it only recouples the  $n_0 = 2$  without the  $n_0 = 1$  term. While (ii) generates an effective Hamiltonian of the form

$$\begin{aligned}\hat{\mathcal{H}}^{(1)} &= \hat{\mathcal{H}}^{(0,0)} + \hat{\mathcal{H}}^{(1,-k)} + \hat{\mathcal{H}}^{(-1,k)} + \hat{\mathcal{H}}^{(2,-2k)} + \hat{\mathcal{H}}^{(-2,2k)} \\ &= \frac{3}{2} b_x^{(k=\pm 4)} \left( \omega_{1,2}^{(1)} + \omega_{1,2}^{(-1)} \right) S_x^\Sigma \\ &= \frac{3}{4} \left( \omega_{1,2}^{(1)} + \omega_{1,2}^{(-1)} \right) S_x^\Sigma\end{aligned}\quad (5.16)$$

where in the last line  $b_x^{(k=\pm 4)} = 1/2$  is substituted, and note that the Fourier coefficient is symmetric, i.e.  $b_x^{(k=4)} = b_x^{(k=-4)}$  (Fig. 5.6). This results in the equal contribution of the spatial components  $n_0 = \pm 1$  for the same spin term, thereby resulting in a cosine-modulated (non  $\gamma$ -encoded) sequence. The simulation shows that the XiX DQ recoupling scheme has the weakest transient at 52% (Fig. 5.7) due to the  $\cos \gamma$  dependence (Eq. (5.16)), and longer build-up curve compared to HORROR due to smaller DQ scaling factor. Nevertheless, one should compare the adiabatic versions next to conclude the practicability of the sequence.



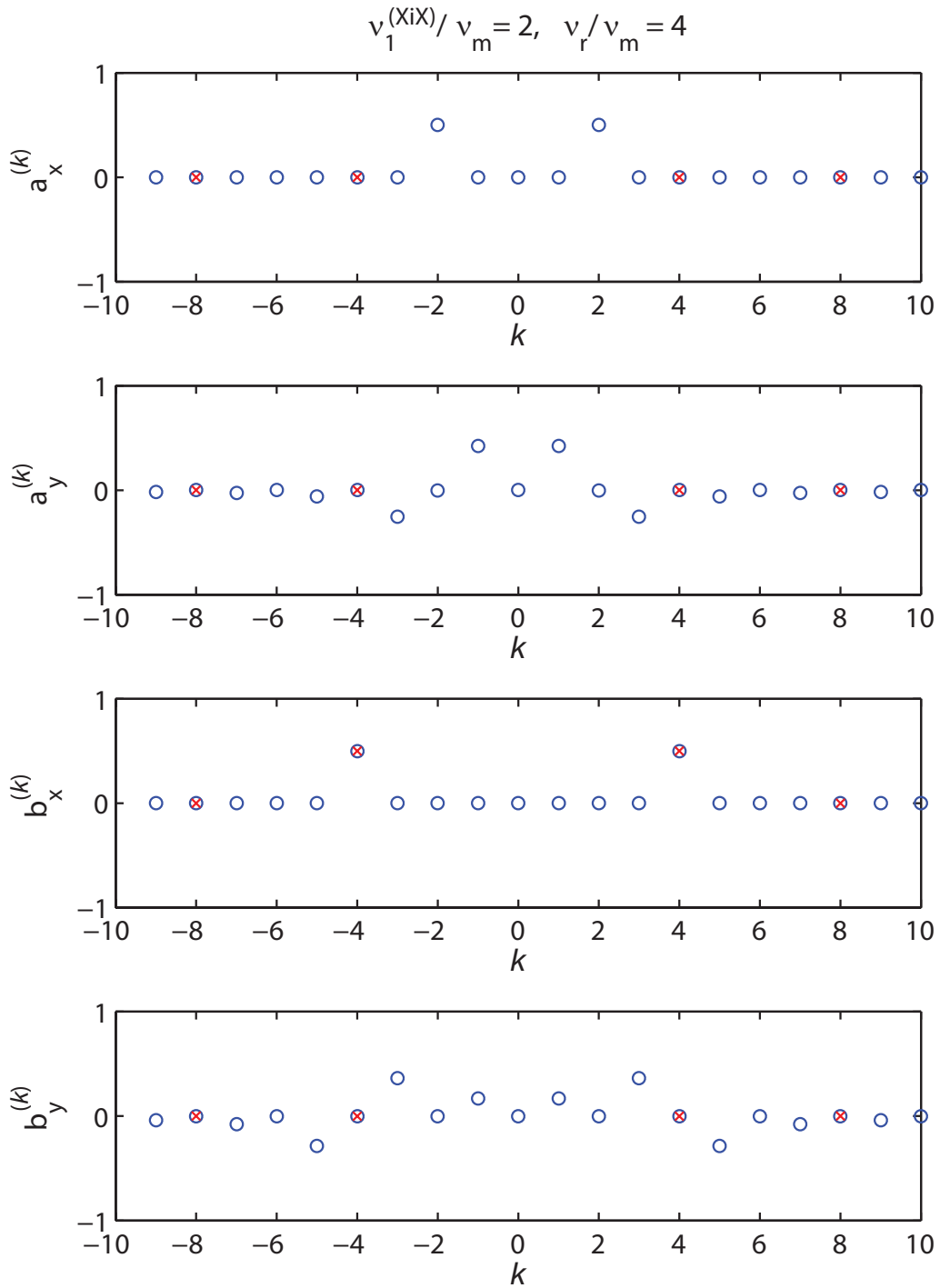


**Figure 5.6** Fourier coefficients of XiX pulses for  $v_1^{(\text{XiX})}/v_m = 2$ . Note that the coefficients are real, and symmetric with respect to  $\kappa$ . The coefficients for the recoupled term in the case of  $v_r/v_m = 4$ , are marked with red cross. This particular choice of  $v_1^{(\text{XiX})}/v_m$  and  $v_r/v_m$  allows the selection of purely DQ terms without CSA.

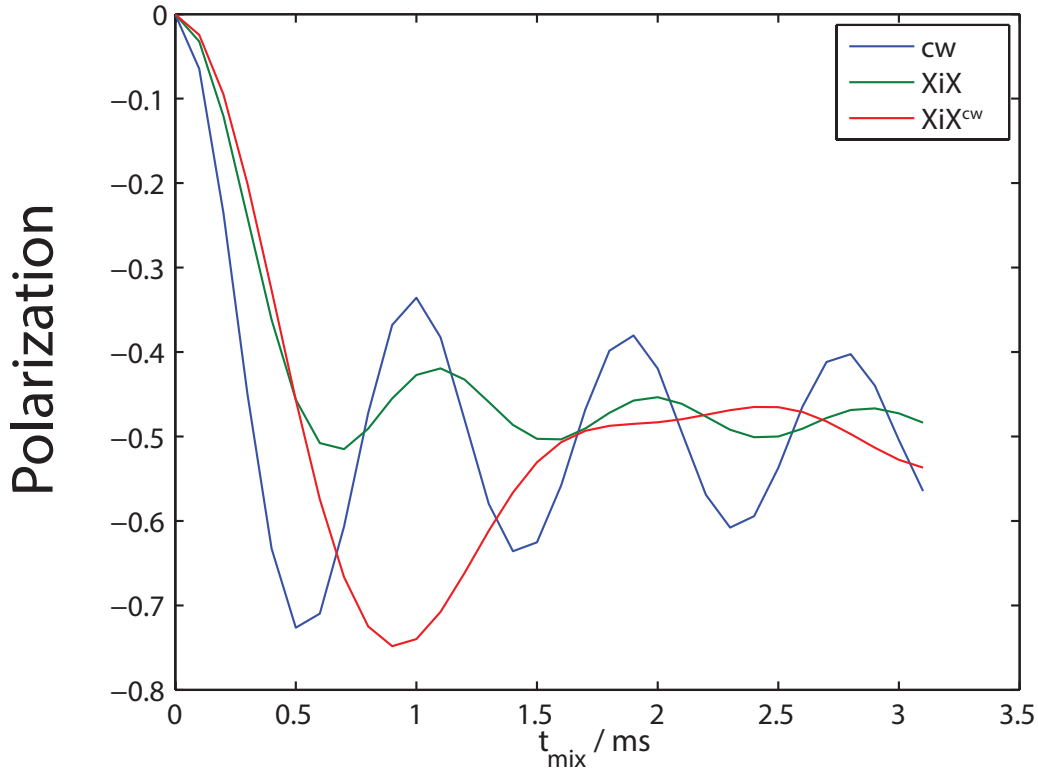


**Figure 5.7** Simulated two-spin ideal system with different DQ recoupling regimes. Only dipolar coupling  $\delta_D/(2\pi) = 4.2$  kHz is included in this simulation.

### 5.5.2 Adiabatic Sweep via $\nu_m$ and Pseudo CW Field

Adiabatic DQ experiments can be designed by introducing a large offset ( $S_Z^\Sigma$ ) in the beginning and in the end of the sequence (see Sec. 1.5). A complication arises in the case of XiX DQ recoupling as there is no effective field  $\nu_{\text{eff}} = 0$ . Nevertheless, a fictitious or pseudo CW field can be added to the XiX pulses in a way that the CW field at  $\tau_{\text{mix}}/2$ , and the accumulated flip angle throughout the entire mixing time  $\tau_{\text{mix}}$ , are both zero (Fig. 5.8c). The corresponding simulated intensity (Fig. 5.8d) shows a slowly increasing target polarization (up to 80%), a typical feature of an adiabatic experiment where the density operator is 'dragged' from  $S_Z^\Sigma$  to  $-S_Z^\Sigma$ . Whereas in the sudden experiment, the polarization transfer often exhibits strong oscillating transients.

Another possible way to perform an adiabatic experiment is to sweep through the modulation frequency  $\nu_m$  (Fig. 5.8a). Modulation of pulse length  $\tau_p$  is technically demanding and the mixing time  $\tau_{\text{mix}}$  has to be long to ensure that a sufficiently large number of steps are employed. Moreover, if the amplitude is kept constant while changing  $\tau_p$ , an offset  $S_Z^\Sigma$  is not necessarily introduced. Nevertheless, adiabatic modulation of  $\nu_m$  was examined by simulations and the result is shown in Fig. 5.8b. Although the polarization transfer builds up slowly, significant transients are still observed, implying that the experiment is not fully

adiabatic. Nonetheless, an increased transfer efficiency (60 %) is still obtained relative to the sudden experiment (52 %). It can be examined in a future experiment to sweep the phase-alternating rf field  $v_1^{(\text{XiX})}$  instead of  $v_m$ , but care has to be taken in order to avoid recoupling undesired terms like CSA.

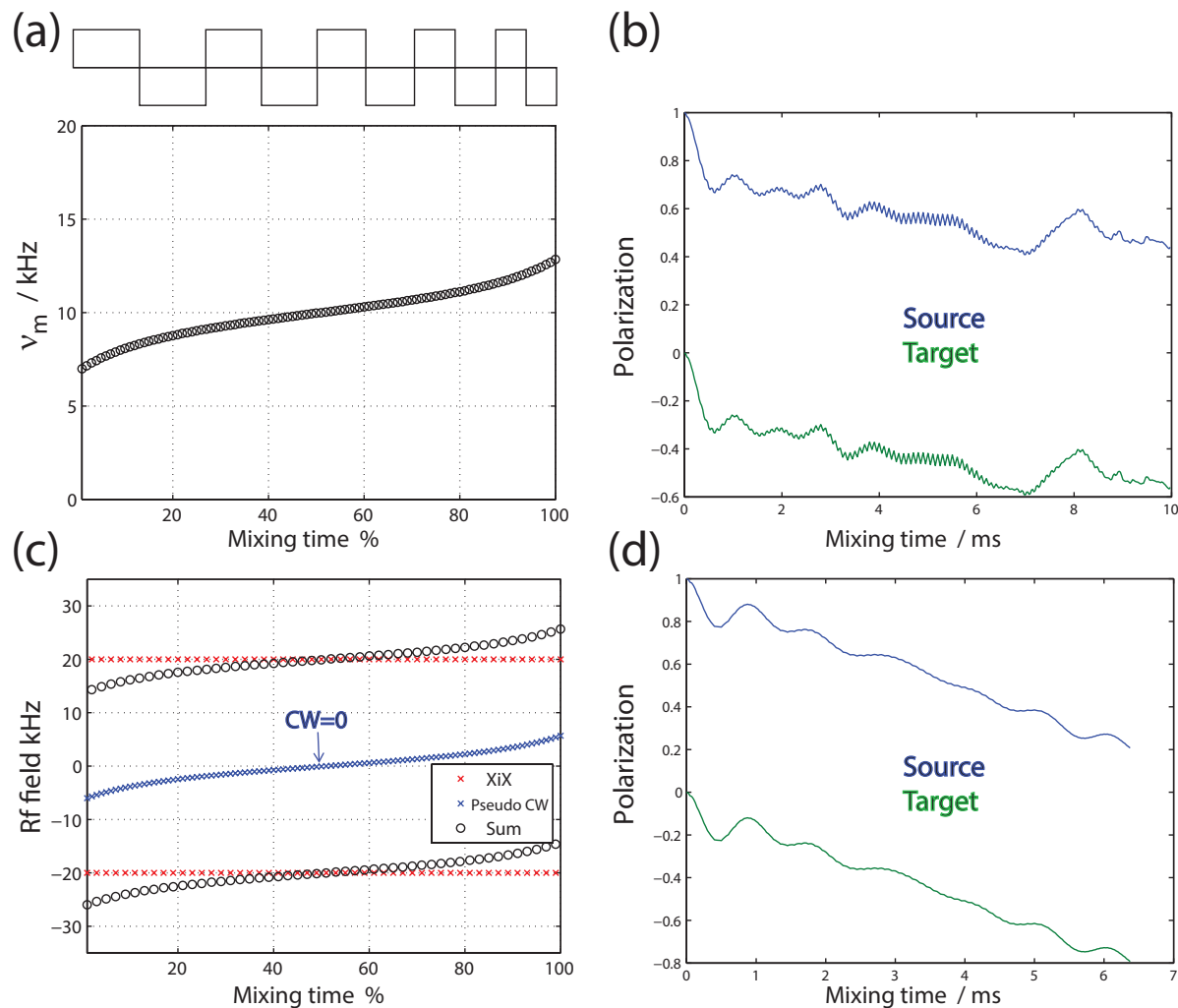


**Figure 5.8** Simulated two-spin ideal system with different adiabatic DQ recoupling regimes sweeping through  $v_m$  (a,b) or pseudo CW field (c,d). A schematic diagram of the adiabatic sweep of  $v_m$  is shown on top of (a). Only dipolar coupling  $\delta_D/(2\pi) = 4.2$  kHz is included in this simulation.

### 5.5.3 Conclusions

Finally, all three different adiabatic DQ recoupling experiments, CW DREAM, XiX with pseudo CW sweep, and XiX<sup>CW</sup> DREAM are compared experimentally. Fig. 5.9 shows that XiX<sup>CW</sup> DREAM is the most efficient sequence and XiX with pseudo CW sweep is least efficient with only 18% transfer and smallest recoupling bandwidth. Nevertheless, one can exploit this feature of narrow bandwidth to design a frequency-selective DQ experiment. This can be achieved by incorporating the offset effect into the effective field  $v_{\text{eff}}$  and resonance condition (see Sec. 6.3.4) using the quaternion description.

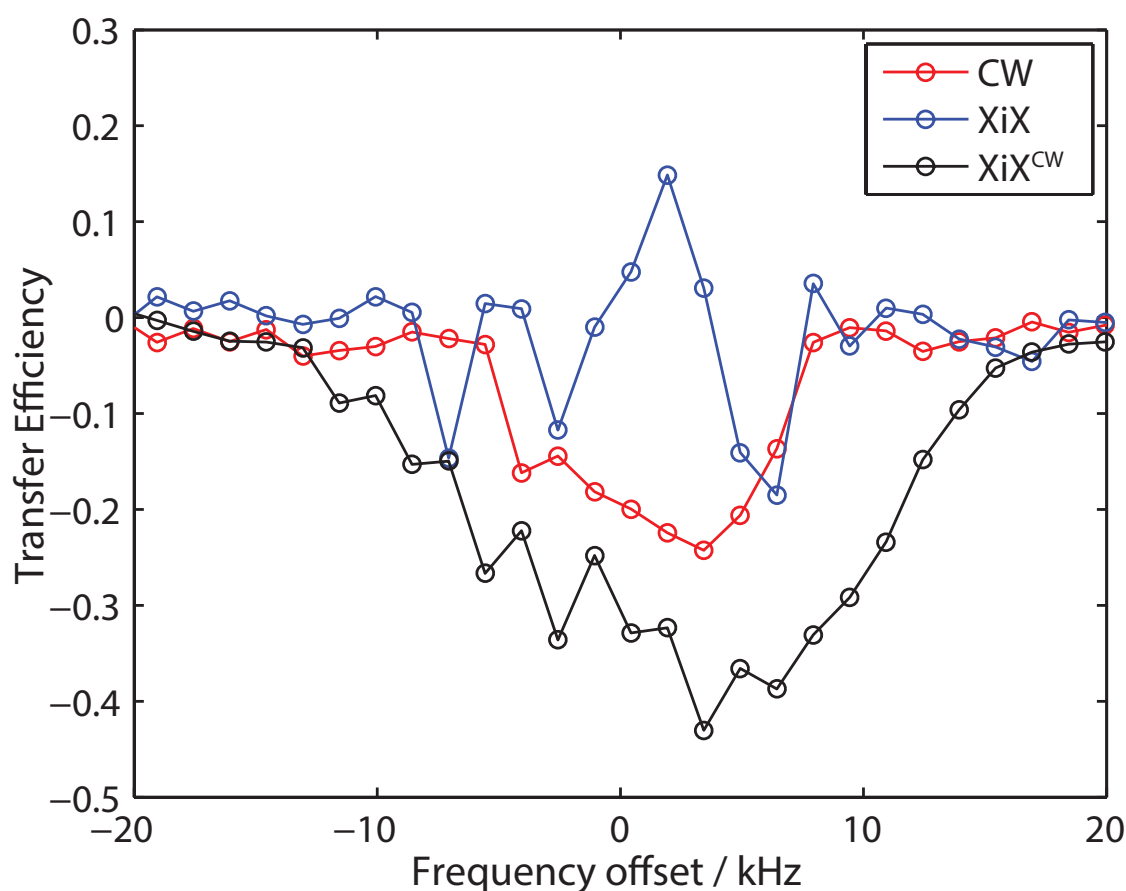


**Figure 5.9** Experimental 1D data of different adiabatic DQ recoupling sequences on glycine at 500 MHz and  $\nu_r = 40$  kHz. Note that a pseudo CW rf field sweep is implemented for the XiX regime.

# Chapter 6

## A Generalized Theoretical Framework for the Description of Spin Decoupling

A generalized theoretical framework that allows the analysis of arbitrary decoupling sequences in solid-state NMR under magic-angle spinning (MAS) conditions is presented in this chapter. It is based on the trimodal Floquet analysis of TPPM decoupling [46] where three characteristic frequencies are used to describe the pulse sequence. Such an approach can be used to describe arbitrary periodic decoupling sequences that differ only in the magnitude of the Fourier coefficients of the interaction-frame transformation. This generalized approach allows a much faster calculation of second-order residual line broadening as a function of pulse sequence parameters than numerical simulations, as the main calculations involved are one-spin trajectories under the radio-frequency Hamiltonian. We exemplify the usefulness of this framework by analyzing the performance of both low- and high- power decoupling sequences such as amplitude-modulated XiX (AM-XiX) [45], TPPM<sub>64</sub> [124], SPINAL-64 [125], frequency-swept SW<sub>f</sub>-TPPM [126], and others. In addition, the effect of chemical-shift offset, which can be significant in the regime of low-power decoupling will also be discussed.

### 6.1 Introduction

Heteronuclear spin decoupling under magic-angle spinning (MAS) [127–129] is an important aspect in obtaining high-resolution spectra in biological solids. Despite many contributions to improve heteronuclear spin decoupling during the past 25 years, there are still open questions and further improvements are desirable. A topic that has limited attention is the offset dependence of decoupling performance [128, 130–134]. While this seems to be of limited interest in the case of high-power decoupling [50, 52, 125–127, 135] where the nuta-

tion frequency is much larger than the MAS frequency ( $\nu_1 \gg \nu_r$ ), this issue is important for low-power decoupling [130, 136–139] where the nutation frequency of the decoupling field is smaller than the MAS frequency ( $\nu_1 \ll \nu_r$ ). With increasing maximum MAS frequencies over the past 20 years to nowadays 120 kHz and beyond [87, 140–142], low-power decoupling has become a competitive alternative to high-power decoupling for MAS beyond 50 kHz with no or only a small compromise on the achievable line width [127, 136, 143]. In biological samples, low-power decoupling sequences are often preferred since the corresponding rf duty cycle on a probe is much lower and the rf heating of samples is minimal compared to high-power decoupling schemes. However, the typical rf-field amplitude employed for the low-power decoupling sequence ( $\nu_1 < \nu_r/4$ ) is in the same order of magnitude as the range of proton chemical shifts on a high-field magnet. This situation might have detrimental effect on the performance of such decoupling sequences [127] because the optimum decoupling conditions can never be achieved simultaneously for all protons with different chemical shifts and, therefore, results in offset-dependent line broadening.

It is desired to understand how offset effects impact the performance of the decoupling sequences. Nonetheless, a theoretical treatment of offset effects in decoupling sequences is hindered by the complexity of the theory required to describe such sequences. Typically, one has to calculate the interaction-frame Hamiltonian in a tilted frame of reference that includes the time-dependent radio-frequency Hamiltonian as well as the offset term and physical rotations of the sample. The theoretical treatment of Hamiltonians under several time dependencies, which usually have non-commensurate frequencies in the case of decoupling is non-trivial in the framework of average Hamiltonian theory (AHT) [30]. Therefore, we resort to Floquet theory [34, 144], which does not require that the characteristic frequencies are commensurate. Floquet theory can be used to calculate effective Hamiltonians to different orders as a function of the offset frequency. During decoupling under MAS, non-resonant first- and second-order terms typically determine the size of the residual coupling. In addition, resonance conditions can lead to a partial recoupling of heteronuclear terms leading to deterioration of the decoupling performance.

The identification of characteristic frequencies for a pulse sequence is important because it constitutes a set of possible resonance conditions, which have to be avoided if they are destructive. The rf-irradiation part of all periodic pulse sequences can be characterized by a maximum of two characteristic frequencies [46, 145, 146], namely the modulation frequency ( $\nu_m = 1/\tau_m$ ) and the effective nutation frequency of the sequence ( $\nu_{\text{eff}}$ ) (see Sec. 2.5.4). While the physical spinning of the sample contributes only one frequency ( $\nu_r$ ) in the case of standard MAS condition, or two in the case of the double rotation technique (DOR) [147]. Based on this universal feature, we have developed a general Floquet frame-

work that allows the calculation of non-resonant second-order terms for arbitrary decoupling sequences without detailed knowledge of the decoupling sequence and the spin system involved (Fig. 6.1a). We obtain general effective Hamiltonians that characterize the residual couplings that either arise from cross terms between heteronuclear dipolar couplings and CSA tensors or from cross terms between heteronuclear and homonuclear dipolar couplings. The differences in the decoupling sequences (or in the offset) are not reflected in the general expressions but are encoded in the values of the Fourier coefficients indirectly. In order to evaluate the performance of a given decoupling sequence, the general expression based on Floquet theory have to be combined with the Fourier coefficients of the interaction-frame transformation that can be obtained numerically by calculating the interaction-frame trajectory (Fig. 6.1a).

## Low-Power Decoupling Sequences

An application of this general framework will be demonstrated in Sec. 6.3 to compare the performance of low-power amplitude-modulated XiX (AM-XiX) decoupling sequence and its super-cycled variant SC-AM-XiX [116], via the Fourier coefficients that characterize the size of the residual couplings. These theoretical analyses are then verified by comparison with numerical simulations. Then, the comparison between the two decoupling sequences is extended to the case where offset effect is included. Although resonance conditions are usually avoided for better decoupling performance in most scenarios, not all resonance conditions are destructive. It will be demonstrated in this work that recoupling of homonuclear dipolar couplings on the protons can improve the line width of the carbon resonances via the "self decoupling" [129, 148, 149] mechanism. This is particularly an important consideration due to the presence of a dense proton network in biological molecules. Following that, an optimization strategy for an efficient decoupling condition that exploits this self decoupling feature using the AM-XiX scheme will be presented in Sec. 6.3.3.

## High-Power Decoupling Sequences

In principle, the generalized framework can also be used to analyze high-power decoupling sequences including simple two-pulse TPPM [52], its supercycled version TPPM-64 [124] and adiabatic version  $SW_f$ -TPPM [132, 134]. Three different aspects will be discussed in this thesis. There are comparison between the basic and different variants of TPPM (Sec. 6.4.1), easier optimization strategy of SPINAL-64 (Sec. 6.4.2), and finite-pulse effect in adiabatic  $SW_f$ -TPPM (Sec. 6.4.3).

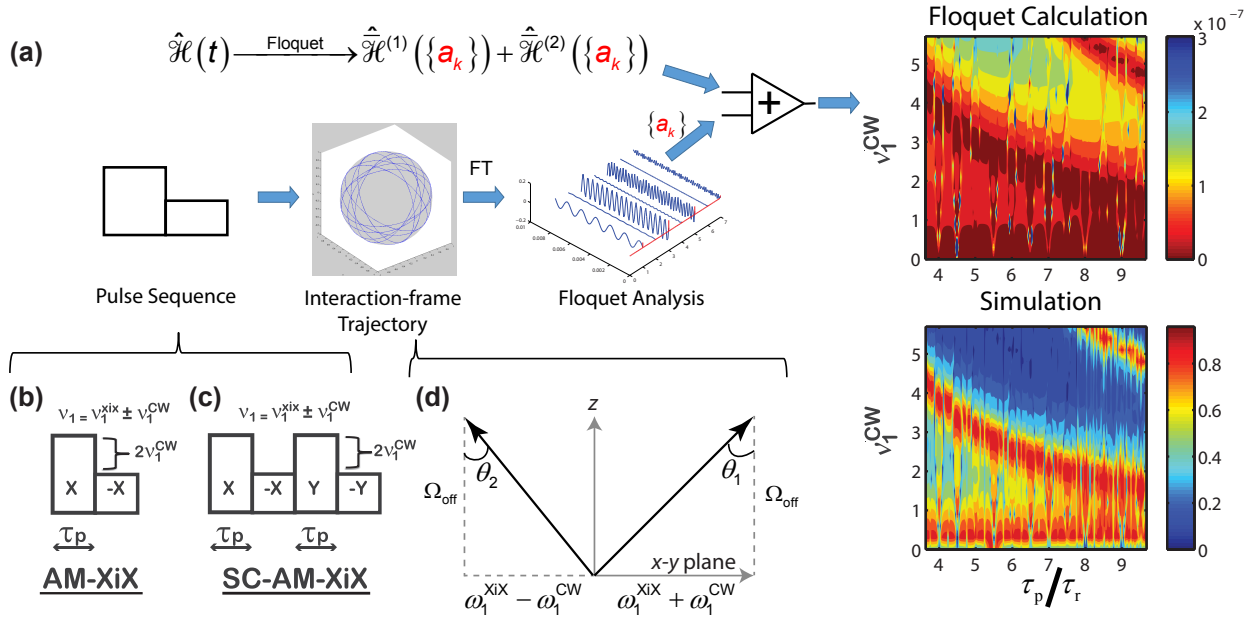


**Figure 6.1** Schematic diagram of a generalized theoretical framework for the description of heteronuclear spin decoupling. (a) shows the construction of general Hamiltonians for arbitrary decoupling sequences. The information of the decoupling sequences is encoded intrinsically in a set of Fourier coefficients  $\{a_k\}$ , which are calculated via interaction-frame trajectory, and then combined/substituted into the effective Hamiltonian in the later step. Two examples of low-power decoupling sequences: (b) AM-XiX and (c) SC-AM-XiX are shown here. The AM-XiX sequence has a modulation frequency of  $v_m = 1/(2\tau_p)$  and effective nutation frequency  $\omega_{\text{eff}} = \omega_1^{\text{CW}} \bmod \omega_m$  while SC-AM-XiX has  $v_m = 1/(4\tau_p)$  and  $\omega_{\text{eff}} = 2v_m \cos^{-1}(\cos^2(\pi\omega_1^{\text{CW}}/2\omega_m))/(2\pi)$ . (d) shows the effect of offset on the directions of the effective field for the first two pulses of AM-XiX and SC-AM-XiX.

## 6.2 Theory

### 6.2.1 General Floquet Description of Decoupling Sequences

Let us consider a general spin system that is comprised of  $N$   $I$  spins coupled to a single  $S$  spin. The Hamiltonian of the system is expressed in the usual rotating frame

$$\begin{aligned} \hat{\mathcal{H}}(t) = & \sum_{n=-2}^2 \omega_S^{(n)} e^{in\omega t} S_z + \sum_{k=1}^N \sum_{n=-2}^2 \omega_k^{(n)} e^{in\omega t} I_{kz} + \sum_{k=1}^N \sum_{n=-2}^2 \omega_{Sk}^{(n)} e^{in\omega t} 2S_z I_{kz} \\ & + \sum_{\substack{k < \ell \\ n \neq 0}} \sum_{n=-2}^2 \omega_{k\ell}^{(n)} e^{in\omega t} \left( 3I_{kz} I_{\ell z} - \vec{I}_k \cdot \vec{I}_\ell \right) + \hat{\mathcal{H}}_{\text{rf}}(t) \end{aligned} \quad (6.1)$$

where the symbols  $\omega_S^{(n)}$  and  $\omega_k^{(n)}$  represent the  $n$ -th spatial component of the chemical-shift tensors for the  $S$  and  $I$  spins respectively. Similarly,  $\omega_{Sk}^{(n)}$  and  $\omega_{k\ell}^{(n)}$  symbolize heteronuclear and homonuclear dipolar couplings accordingly. The rf Hamiltonian  $\hat{\mathcal{H}}_{\text{rf}}(t)$  in Eq. (6.1) has



a general form of

$$\hat{\mathcal{H}}_{\text{rf}}(t) = \omega_1(t) \sum_{k=1}^N (\cos(\phi(t)) I_{kx} + \sin(\phi(t)) I_{ky}) \quad (6.2)$$

for an arbitrary decoupling sequence. We transform the Hamiltonian of Eq. (6.1) into an interaction frame with the full rf-field Hamiltonian with the propagator:

$$\hat{\mathcal{H}}(t) = U_{\text{rf}}^{-1}(t) \hat{\mathcal{H}}(t) U_{\text{rf}}(t) \quad (6.3)$$

$$\hat{U}_{\text{rf}}(t) = \hat{T} \exp \left( -i \int_0^t \hat{\mathcal{H}}_{\text{rf}}(t_1) dt_1 \right) \quad (6.4)$$

Since only the  $I$  spins are involved in the rf Hamiltonian  $\hat{\mathcal{H}}_{\text{rf}}(t)$  (Eq. (6.2)), the  $I$ -spin terms in  $\hat{\mathcal{H}}(t)$  (Eq. (6.3)) will transform according to the following general equation

$$\tilde{I}_z(t) = \sum_{\chi=x,y,z} a_{\chi}(t) I_{\chi} = \sum_{k=-\infty}^{\infty} \sum_{\ell=-\infty}^{\infty} \sum_{\chi=x,y,z} a_{\chi}^{(k,\ell)} e^{ik\omega_m t} e^{i\ell\omega_{\text{eff}} t} I_{\chi} \quad (6.5)$$

where  $k$  and  $\ell$  are integer numbers,  $a_{\chi}^{(k,\ell)}$  represents the Fourier coefficient calculated from the interaction-frame transformation of the  $I_z$  operator,  $\omega_m = 2\pi/\tau_m$  is the modulation frequency that is present in all periodic pulse sequences and  $\omega_{\text{eff}}$  is the effective nutation frequency. The effective nutation frequency  $\omega_{\text{eff}}$  is defined as

$$\omega_{\text{eff}} = \beta_{\text{eff}}/\tau_m \quad (6.6)$$

i.e., the net flip angle [46, 145]  $\beta_{\text{eff}}$  over the period of a basic cycle  $\tau_m$ . The flip angle  $\beta_{\text{eff}}$  can be determined using Euler rotations or quaternions [100]. The modulation frequency  $\omega_m$ , the effective nutation frequency  $\omega_{\text{eff}}$ , and the MAS frequency  $\omega_r$  constitute the three basic frequencies that characterize the time-dependent Hamiltonian  $\hat{\mathcal{H}}(t)$  that is given by

$$\hat{\mathcal{H}}(t) = \sum_{n=-\infty}^{\infty} \sum_{k=-\infty}^{\infty} \sum_{\ell=-\infty}^{\infty} e^{in\omega_r t} e^{ik\omega_m t} e^{i\ell\omega_{\text{eff}} t} \hat{\mathcal{H}}^{(n,k,\ell)} \quad (6.7)$$

where the terms  $\hat{\mathcal{H}}^{(n,k,\ell)}$  are the Fourier coefficients of the time-dependent Hamiltonian in the interaction frame. Possible resonance conditions are characterized by

$$n_0 \omega_r + k_0 \omega_m + \ell_0 \omega_{\text{eff}} = 0 \quad (6.8)$$

where  $n_0$ ,  $k_0$ , and  $\ell_0$  are any set of integers that fulfill Eq. (6.8). The effective Hamiltonian on a resonance condition is then given by

$$\hat{\mathcal{H}} = \sum_{n_0, k_0, \ell_0} \hat{\mathcal{H}}^{(n_0, k_0, \ell_0)} + \sum_{n_0, k_0, \ell_0} \hat{\mathcal{H}}^{(2)}_{(n_0, k_0, \ell_0)} + \dots \quad (6.9)$$

where the first and second sum in Eq. (6.9) represents the first- and second-order effective Hamiltonian respectively [32, 34]. The full expressions for the Fourier components of the Hamiltonian  $\hat{\mathcal{H}}^{(n_0, k_0, \ell_0)}$  and  $\hat{\mathcal{H}}^{(2)}_{(n_0, k_0, \ell_0)}$  from Eq. (6.9) have already been derived in literature [46]. Since we are interested in the residual coupling under decoupling, we will focus now on the non-resonant terms

$$\begin{aligned} \hat{\mathcal{H}} &= \hat{\mathcal{H}}^{(0,0,0)} + \hat{\mathcal{H}}^{(2)}_{(0,0,0)} + \dots \\ &= \hat{\mathcal{H}}^{(0,0,0)} - \frac{1}{2} \sum_{\nu, \kappa, \lambda} \frac{\left[ \hat{\mathcal{H}}^{(-\nu, -\kappa, -\lambda)}, \hat{\mathcal{H}}^{(\nu, \kappa, \lambda)} \right]}{\nu \omega_r + \kappa \omega_m + \lambda \omega_{\text{eff}}} + \dots \end{aligned} \quad (6.10)$$

where the second-order term often dominates the performance of decoupling sequences. We can decompose the non-resonant second-order terms into six contributions

$$\begin{aligned} \hat{\mathcal{H}}^{(2)} &= -\frac{1}{2} \sum_{\nu, \kappa, \lambda} \frac{\left[ \hat{\mathcal{H}}^{(-\nu, -\kappa, -\lambda)}, \hat{\mathcal{H}}^{(\nu, \kappa, \lambda)} \right]}{\nu \omega_r + \kappa \omega_m + \lambda \omega_{\text{eff}}} \\ &= \hat{\mathcal{H}}_{\text{IS} \otimes \text{I}} + \hat{\mathcal{H}}_{\text{IS} \otimes \text{II}} + \hat{\mathcal{H}}_{\text{I} \otimes \text{II}} + \hat{\mathcal{H}}_{\text{II} \otimes \text{II}} + \hat{\mathcal{H}}_{\text{I} \otimes \text{I}} + \hat{\mathcal{H}}_{\text{IS} \otimes \text{IS}} \end{aligned} \quad (6.11)$$

The first two terms, namely the cross term between the heteronuclear dipolar coupling and the  $I$ -spin CSA tensor ( $\hat{\mathcal{H}}_{\text{IS} \otimes \text{I}}$ ) and the cross terms between heteronuclear and homonuclear dipolar couplings ( $\hat{\mathcal{H}}_{\text{IS} \otimes \text{II}}$ ) are the only<sup>1</sup> terms that lead to direct line broadening on the  $S$  spins. For simplicity, we will call the first term a CSA cross term and the second term a dipolar cross term. The other four cross terms yield effective Hamiltonians with purely  $I$  spin terms ( $\hat{\mathcal{H}}_{\text{I} \otimes \text{II}}$ ,  $\hat{\mathcal{H}}_{\text{II} \otimes \text{II}}$ ,  $\hat{\mathcal{H}}_{\text{I} \otimes \text{I}}$ , and  $\hat{\mathcal{H}}_{\text{IS} \otimes \text{IS}}$ ) do not impact the line width of the  $S$  spin directly but the first two terms can influence spin diffusion on the  $I$  spins since they contain two- and three-spin terms. The last two terms generate only fictitious fields. We will focus on the effects of the first two cross terms as they are the only ones that have a direct impact on the observed line widths of the  $S$  spins. Note that the expressions for these cross terms are written down here in a generalized form that is valid for any heteronuclear decoupling

<sup>1</sup>If multi  $S$  spins are considered, there exists also a cross term between two heteronuclear dipolar couplings, i.e.  $I_{k\chi} S_{1z} S_{2z}$  scaled by the same Fourier coefficients  $q_{\chi}^{(\nu)}$ .

sequence:

$$\bar{\mathcal{H}}_{\text{IS}\otimes\text{I}} = \sum_k \sum_{v=-2}^2 \sum_{\chi=x,y,z} iS_z I_{k\chi} q_\chi^{(v)} \left( \omega_{kS}^{(-v)} \omega_k^{(v)} + \omega_{kS}^{(v)} \omega_k^{(-v)} \right) \quad (6.12)$$

$$\bar{\mathcal{H}}_{\text{IS}\otimes\text{II}} = \sum_{k \neq \ell} \sum_{v=-2}^2 \sum_{\mu, \chi=x,y,z} -3iS_z I_{k\mu} I_{\ell\chi} \left( q_{\mu\chi}^{(v)} \omega_{kS}^{(-v)} \omega_{\ell}^{(v)} - \left( q_{\mu\chi}^{(v)} \right)^* \omega_{kS}^{(v)} \omega_{\ell}^{(-v)} \right) \quad (6.13)$$

In the complete description, there are four second-order  $I$ -spin terms that have indirect effect on the line width of the  $S$  spin:

$$\bar{\mathcal{H}}_{\text{I}\otimes\text{II}} = \sum_{k \neq \ell} \sum_{v=-2}^2 \sum_{\mu, \chi} -\frac{3i}{2} I_{k\mu} I_{\ell\chi} \left( q_{\mu\chi}^{(v)} \omega_k^{(-v)} \omega_{\ell}^{(v)} - \left( q_{\mu\chi}^{(v)} \right)^* \omega_k^{(v)} \omega_{\ell}^{(-v)} \right) \quad (6.14)$$

$$\begin{aligned} \bar{\mathcal{H}}_{\text{II}\otimes\text{II}} &= \sum_{k \neq \ell} \sum_{\chi} \sum_{v=-2}^2 \frac{9i}{8} \omega_{k\ell}^{(-v)} \omega_{k\ell}^{(v)} p_\chi^{(v)} I_{k\chi} \\ &+ \sum_{k \neq \ell \neq o} \sum_{v=-2}^2 \sum_{\mu, \chi, \xi} \frac{9i}{2} I_{k\mu} I_{\ell\chi} I_{o\xi} \left( p_{\mu\chi\xi}^{(v)} \omega_{k\ell}^{(-v)} \omega_{lo}^{(v)} - \left( p_{\mu\chi\xi}^{(v)} \right)^* \omega_{k\ell}^{(v)} \omega_{lo}^{(-v)} \right) \end{aligned} \quad (6.15)$$

$$\bar{\mathcal{H}}_{\text{I}\otimes\text{I}} = \sum_k \sum_{\chi} \sum_{v=-2}^2 \frac{i}{2} q_\chi^{(v)} I_{k\chi} \omega_k^{(-v)} \omega_k^{(v)} = \sum_k \sum_{\chi} \sum_{v=-2}^2 \frac{i}{2} q_\chi^{(v)} I_{k\chi} \left| \omega_k^{(v)} \right|^2 \quad (6.16)$$

$$\bar{\mathcal{H}}_{\text{IS}\otimes\text{IS}} = \sum_k \sum_{\chi} \sum_{v=-2}^2 \frac{i}{2} q_\chi^{(v)} I_{k\chi} \omega_{kS}^{(-v)} \omega_{kS}^{(v)} = \sum_k \sum_{\chi} \sum_{v=-2}^2 \frac{i}{2} q_\chi^{(v)} I_{k\chi} \left| \omega_{kS}^{(v)} \right|^2 \quad (6.17)$$

Here,  $q_\chi^{(v)}$ ,  $q_{\mu\chi}^{(v)}$ ,  $p_\chi^{(v)}$  and  $p_{\mu\chi\xi}^{(v)}$  are the scaling factors for the corresponding cross terms and they are defined as

$$q_\chi^{(v)} = \sum_{\kappa} \sum_{\lambda=-1}^1 \frac{\varepsilon_{\chi ij} a_j^{(-\kappa, -\lambda)} a_i^{(\kappa, \lambda)}}{v\omega_r + \kappa\omega_m + \lambda\omega_{\text{eff}}} \quad (6.18)$$

$$q_{\mu\chi}^{(v)} = \sum_{\kappa} \sum_{\lambda=-1}^1 \frac{\varepsilon_{\mu ij} a_j^{(-\kappa, -\lambda)} a_{\chi i}^{(\kappa, \lambda)}}{v\omega_r + \kappa\omega_m + \lambda\omega_{\text{eff}}} \quad (6.19)$$

$$p_\chi^{(v)} = \sum_{\mu} \sum_{\kappa} \sum_{\lambda=-2}^2 \frac{\varepsilon_{\chi ij} a_{\mu j}^{(-\kappa, -\lambda)} a_{\mu i}^{(\kappa, \lambda)}}{v\omega_r + \kappa\omega_m + \lambda\omega_{\text{eff}}} \quad (6.20)$$

$$p_{\mu\chi\xi}^{(v)} = \sum_{\kappa} \sum_{\lambda=-2}^2 \frac{\varepsilon_{\chi ij} a_{\mu j}^{(-\kappa, -\lambda)} a_{\xi}^{(\kappa, \lambda)}}{v\omega_r + \kappa\omega_m + \lambda\omega_{\text{eff}}} \quad (6.21)$$

where  $\varepsilon_{\chi ij}$  is the Levi-Civita symbol and  $a_{\mu\chi}^{(\kappa,\lambda)}$  are the Fourier coefficients for the rank-two spin tensors that can be defined as the convolution of the rank-one Fourier coefficients  $a_{\mu}^{(\kappa,\lambda)}$  (Eq. (6.5)):

$$a_{\mu\chi}^{(\kappa,\lambda)} = \sum_{k=-\infty}^{\infty} \sum_{\ell=-1}^1 a_{\mu}^{(k,\ell)} a_{\chi}^{(\kappa-k,\lambda-\ell)} \quad (6.22)$$

Note that the Fourier coefficients obey the relation  $a_{\chi}^{(k,\ell)} = (a_{\chi}^{(-k,-\ell)})^*$  and  $a_{\mu\chi}^{(k,\ell)} = (a_{\mu\chi}^{(-k,-\ell)})^*$ . It is also important to emphasize that the scaling factors for the cross terms ( $q_{\chi}^{(v)}$ ,  $q_{\mu\chi}^{(v)}$ ,  $p_{\chi}^{(v)}$  and  $p_{\mu\chi\xi}^{(v)}$ ) do not depend on the details of the spin system and the general expressions are the same for any decoupling sequence with non-zero values of the modulation frequency  $\omega_m$  and an effective nutation frequency  $\omega_{\text{eff}}$ . The details of the parameters of the decoupling sequences are encoded in the profile of the Fourier coefficients,  $a_{\chi}^{(k,\ell)}$ , which have to be calculated numerically in most cases.

### Probing Non-Refocussable Terms with Spin-Echo Sequence

In principle, the performance of a decoupling sequence can also be examined by measuring the  $T_2'$  using a spin echo sequence. It can be shown using a toggling frame that all terms with  $S_z$  including the CSA and dipolar cross terms (Eqs. (6.12)-(6.13)) will be refocussed during the spin echo sequence. In addition, there exist also some terms (Eqs. (6.14)-(6.17)) that are not refocussed by the  $\pi$  pulse. It would be interesting to probe the impact of these non-refocussable terms on the line width experimentally<sup>a</sup>, similar to Fig. 10 in [46].

<sup>a</sup>There has been an attempt recently to probe similar effects via numerical simulations[150], but it was realized that more proton spins have to be included to produce reliable results.

### Off-Resonant Irradiation

So far we have assumed on-resonance irradiation during decoupling and neglected the influence of offset effects. Such an approximation is not valid, especially for low-power decoupling, and therefore the offset effects are considered here. The simplest way of doing this is to include the offset of the radio frequency irradiation from the resonance frequency into the interaction-frame transformation (Fig. 6.1d). The inclusion of an offset term into the radio-frequency Hamiltonian modifies the propagator to

$$\hat{U}_{\text{rf}}^{(\Omega_{\text{off}})}(t) = \hat{T} \exp \left( -i \int_0^t \left( \hat{\mathcal{H}}_{\text{rf}}(t_1) + \Omega_{\text{off}} \sum_{k=1}^N I_{kz} \right) dt_1 \right) \quad (6.23)$$

in the interaction-frame transformation. Fortunately such a change in the Hamiltonian does not change the formal transformation of the  $I_z$  operator used to calculate the interaction-

frame Hamiltonian:

$$\tilde{I}_z(t) = \left( \hat{U}_{\text{rf}}^{(\Omega_{\text{off}})}(t) \right)^{-1} I_z \hat{U}_{\text{rf}}^{(\Omega_{\text{off}})}(t) = \sum_{\chi=x,y,z} a_{\chi}(t) I_{\chi} = \sum_{k=-\infty}^{\infty} \sum_{\ell=-\infty}^{\infty} \sum_{\chi=x,y,z} a_{\chi}^{(k,\ell)} e^{ik\omega_m t} e^{i\ell\omega_{\text{eff}}(\Omega_{\text{off}})t} I_{\chi} \quad (6.24)$$

The inclusion of the offset term into the interaction-frame transformation will only change the effective nutation frequency  $\omega_{\text{eff}}(\Omega_{\text{off}})$  and the Fourier coefficients  $a_{\chi}^{(k,\ell)}$  as a function of the offset. The general expressions obtained for the effective Hamiltonians (Eqs. (6.11)-(6.17)) as well as the ones for the scaling factors (Eqs. (6.18)-(6.21)) are unchanged (see Sec. 6.2.3 a proof of calculations of effective nutation frequency  $\omega_{\text{eff}}(\Omega_{\text{off}})$  and Fourier coefficients  $a_{\chi}^{(k,\ell)}(\Omega_{\text{off}})$ ).

The equations derived here are general and applicable to any decoupling sequence with or without chemical-shift offsets. The details of the decoupling sequence are contained in the interaction-frame transformation and are hidden in the Fourier coefficients  $a_{\chi}^{(k,\ell)}$  which can be obtained from a numerical calculation of the Fourier transform of the interaction-frame trajectory. For a given sequence and an offset frequency, the effective nutation frequency has to be calculated first and then the Fourier coefficients. The numerical values can then be used together with the general expressions for scaling factors (Eqs. (6.18)-(6.21)) to calculate the magnitude of the effective Hamiltonians as a function of parameters (Fig. 6.1a). In this way we can calculate the scaling factors of the various terms in the second-order effective Hamiltonian without the need to specify a spin-system topology and geometry since the scaling factors are independent of these values. The effects of offset on the decoupling performance are two-fold: (i) it deteriorates the decoupling efficiency if the chosen parameters move towards the offset-dependent resonance conditions due to  $\omega_{\text{eff}}(\Omega_{\text{off}})$  or (ii) it can affect both the resonant and non-resonant parts of the effective Hamiltonians through changes in the values of the Fourier coefficient  $a^{(k_0,\ell_0)}$ .

## 6.2.2 Low-Power Amplitude-Modulated XiX Sequences

The amplitude and phases for low-power AM-XIX and SC-AM-XIX sequences [45] are shown in Fig. 6.1, and their properties relevant for the Floquet calculations are summarized in Table 6.1. Analytical calculations of the effective nutation frequencies of these two decoupling sequences are straightforward in the case of on-resonance rf irradiation and given in Table 6.1. This can be achieved by either calculating the total propagator and then extracting the effective flip angle from it [46], or using Euler rotations or quaternions [100].

In the case of off-resonance irradiation, the calculation of the effective field becomes more complex as the nutation axis is different for each of the two pulses in AM-XIX with

the effective flip angles ( $\beta$ ) and polar angles ( $\theta$ ) of the two pulses (see Fig. 6.1d) given by:

$$\begin{aligned}\beta_1 &= \tau_p \sqrt{(\omega_1^{\text{XiX}} + \omega_1^{\text{CW}})^2 + \Omega_{\text{off}}^2} \\ \beta_2 &= \tau_p \sqrt{(\omega_1^{\text{XiX}} - \omega_1^{\text{CW}})^2 + \Omega_{\text{off}}^2} \\ \theta_1 &= \tan^{-1} \left( (\omega_1^{\text{XiX}} + \omega_1^{\text{CW}}) / \Omega_{\text{off}} \right) \\ \theta_2 &= \tan^{-1} \left( (\omega_1^{\text{XiX}} - \omega_1^{\text{CW}}) / \Omega_{\text{off}} \right)\end{aligned}\quad (6.25)$$

Using either Euler rotations or quaternions can be used to determine the effective nutation frequency  $\omega_{\text{eff}}$  of AM-XiX resulting in

$$\omega_{\text{eff}} = 2\omega_m \cos^{-1} (\cos(\beta_1/2) \cos(\beta_2/2) - \cos(\theta_1 + \theta_2) \sin(\beta_1/2) \sin(\beta_2/2)) / (2\pi) \quad (6.26)$$

The same approach can be applied to SC-AM-XiX sequence. The flip angle ( $\beta$ ) and the polar angle ( $\theta$ ) of the third and fourth pulse are the same as the ones of the first and second pulse  $\theta_3 = \theta_1$ ,  $\theta_4 = \theta_2$ ,  $\beta_3 = \beta_1$ , and  $\beta_4 = \beta_2$  but the azimuthal angle of the last two pulses changes from 0 to  $\pi/2$ . The effective nutation frequency  $\omega_{\text{eff}}$  for SC-AM-XiX is then given by (see Sec. 6.2.3):

$$\begin{aligned}\omega_{\text{eff}} &= 2\omega_m \cos^{-1} \left( \{ 2\cos^2(\beta_1/2) (\cos^2(\beta_2/2) - \cos^2(\theta_2) \sin^2(\beta_2/2)) \right. \\ &\quad + \sin(\beta_1) \sin(\beta_2) [\sin(\theta_1) \sin(\theta_2) - 2\cos(\theta_1) \cos(\theta_2)] \\ &\quad \left. - \sin^2(\beta_1/2) [\cos(\beta_2) + \cos^2(\beta_2/2) \cos(2\theta_1) - \cos(2(\theta_1 + \theta_2)) \sin^2(\beta_2/2)] \right\} / (4\pi) \end{aligned} \quad (6.27)$$

The analytical expressions of Eqs. (6.26)-(6.27) for the effective nutation frequencies of the two decoupling sequences allow an efficient calculation of the Fourier coefficients of the interaction-frame trajectories.

	AM-XiX		SC-AM-XiX	
$t$	$\omega_1(t)$	$\phi(t)$	$\omega_1(t)$	$\phi(t)$
$0 \leq t < \tau_p$	$\omega_1^{\text{XiX}} + \omega_1^{\text{CW}}$	0	$\omega_1^{\text{XiX}} + \omega_1^{\text{CW}}$	0
$\tau_p \leq t < 2\tau_p$	$\omega_1^{\text{XiX}} - \omega_1^{\text{CW}}$	$\pi$	$\omega_1^{\text{XiX}} - \omega_1^{\text{CW}}$	$\pi$
$2\tau_p \leq t < 3\tau_p$	$\omega_1^{\text{XiX}} + \omega_1^{\text{CW}}$	0	$\omega_1^{\text{XiX}} + \omega_1^{\text{CW}}$	$\pi/2$
$3\tau_p \leq t < 4\tau_p$	$\omega_1^{\text{XiX}} - \omega_1^{\text{CW}}$	$\pi$	$\omega_1^{\text{XiX}} - \omega_1^{\text{CW}}$	$3\pi/2$
$\omega_{\text{eff}}$	$\omega_1^{\text{CW}} \bmod \omega_m$		$2\omega_m \cos^{-1} (\cos^2(\pi\omega_1^{\text{CW}}/(2\omega_m))) / (2\pi)$	

**Table 6.1** Definition of parameters used for AM-XiX and SC-AM-XiX decoupling.

### Similarity between XiX with Offset and TPPM

When the offset effect is incorporated into the theoretical description of XiX decoupling, the analytical expression for the effective field is  $\omega_{\text{eff}} = 2\nu_m \cos^{-1} \left( \cos(\theta_1)^2 \cos(\beta_1) + \sin(\theta_1)^2 \right)$  (Eq. (6.26)), which has a similar expression as the effective field of the TPPM decoupling sequence without offset [46]. There is no surprise that both sequences have similar form as it can be inferred that the effective field directions of the XiX pulses with offset lie in the X-Z plane are similar to the effective fields of TPPM without offset that lie in the X-Y plane.

### 6.2.3 Verification of Offset-Dependent Effective Nutation Frequency and Fourier Coefficients

It was shown that the effective nutation frequency with the offset incorporated  $\nu_{\text{eff}}(\nu_{\text{off}})$  is given by Eq. (6.26) for AM-XiX and Eq. (6.27) for SC-AM-XiX. In order to prove that the approach and the analytical function is correct, the performance of the decoupling sequences is examined under a wide range of offset and rf values, so that the destructive resonance conditions are intentionally satisfied and traced. Figs. 6.2a–c show numerical simulations performed on a two-spin CH system with a small heteronuclear dipolar coupling of  $\delta_D/2\pi = 4$  kHz, at MAS frequency of 55.5 kHz, for the case of (a) CW (b) AM-XiX or (c) SC-AM-XIX decoupling. The effective field for the CW irradiation is trivial  $\nu_{\text{eff}} = \sqrt{(\nu_1^{\text{CW}})^2 + \nu_{\text{off}}^2}$ . One can see that the peak intensity drops significantly when the effective field matches the spinning frequency, i.e.  $\nu_r - \nu_{\text{eff}}(\nu_{\text{off}}) = 0$ , a heteronuclear recoupling condition plotted as black dotted line in Fig. 6.2a. Similar analyses are performed for the AM-XiX decoupling (Fig. 6.2b) with resonance conditions  $\nu_r - \nu_m - \nu_{\text{eff}}(\nu_{\text{off}}) = 0$  (black) and  $2\nu_r - 3\nu_m + \nu_{\text{eff}}(\nu_{\text{off}}) = 0$  (magenta); and for SC-AM-XiX (Fig. 6.2c) with resonance conditions  $\nu_r - 2\nu_m - \nu_{\text{eff}}(\nu_{\text{off}}) = 0$  (black),  $\nu_r - 3\nu_m + \nu_{\text{eff}}(\nu_{\text{off}}) = 0$  (magenta),  $2\nu_r - 5\nu_m - \nu_{\text{eff}}(\nu_{\text{off}}) = 0$  (cyan), and  $2\nu_r - 6\nu_m + \nu_{\text{eff}}(\nu_{\text{off}}) = 0$  (white). One can see that all destructive resonance conditions are predicted successfully analytically. It is proven that the analytical expressions (Eqs. (6.26)-(6.27)) of the resonance conditions with offset incorporated are correct. Next, the effect of offset on Fourier coefficients will be demonstrated.

The dephasing of FID at the recoupling condition is dictated by the effective Hamiltonian characterized by the offset incorporated Fourier coefficients  $a_{\chi}^{(k,\ell)}(\nu_{\text{off}})$ . For instance, the first-order effective Hamiltonian for the resonance condition  $\nu_r - 3\nu_m + \nu_{\text{eff}}(\nu_{\text{off}}) = 0$

(magenta) of SC-AM-XiX (Fig. 6.2c) is determined as follows:

$$\begin{aligned}\hat{\mathcal{H}}^{(1)} &= \hat{\mathcal{H}}^{(1,-3,1)} + \hat{\mathcal{H}}^{(-1,3,-1)} \\ &= 2S_z [(\omega_{\text{IS}}^{(1)} a_x^{(-3,1)} + \omega_{\text{IS}}^{(-1)} a_x^{(3,-1)}) I_x + (\omega_{\text{IS}}^{(1)} a_y^{(-3,1)} + \omega_{\text{IS}}^{(-1)} a_y^{(3,-1)}) I_y \\ &\quad + (\omega_{\text{IS}}^{(1)} a_z^{(-3,1)} + \omega_{\text{IS}}^{(-1)} a_z^{(3,-1)}) I_z]\end{aligned}\quad (6.28)$$

Where  $\omega_{\text{IS}}^{(1)}$  is the  $n=1$  spatial component of heteronuclear dipolar coupling. The Fourier coefficients  $a_{\chi}^{(k,\ell)}(\nu_{\text{off}})$  at offset frequency of  $\nu_{\text{off}} = 21$  kHz (marked black cross in Fig. 6.2c) are determined by using Eqs. (6.26)-(6.27). Finally, the values of the Fourier coefficients<sup>2</sup>  $a_{\chi=x,y,z}^{(k=\pm 3, \ell=\mp 1)}$  are substituted into the effective Hamiltonian (Eq. (6.28)), which is used then to dephase the signal (Fig. 6.2d). The analytical result (blue) shows an excellent agreement with the numerically simulated data (red), for at least 40 ms. This implies the effective Hamiltonian or the Fourier coefficients are precisely determined. It is proven that our approach to the offset effect is valid and accurate for any arbitrary decoupling sequence by verifying the analytical expressions of offset-dependent effective frequency  $\nu_{\text{eff}}(\nu_{\text{off}})$  and Fourier coefficients  $a_{\chi}^{(k,\ell)}(\nu_{\text{off}})$ .

## 6.3 Understanding Low-Power Decoupling Sequences

### 6.3.1 Materials and Methods

All numerical simulations shown in Sec. 6.3 were performed in the spin-simulation environment GAMMA [80] using 200 powder orientations chosen by the ZCW scheme [104]. The simulations were performed on either a CH<sub>2</sub> (Figs. 6.3 and 6.5) or C<sub>2</sub>H<sub>4</sub> (Fig. 6.4) spin system with parameters similar to that of glycine ethylester. All simulation data are normalized with respect to the ideal situation where everything is fully averaged. All experimental measurements were carried out on a sample of uniformly labeled <sup>13</sup>C, <sup>15</sup>N-glycine ethylester with a 1.3 mm triple-resonance MAS probe on a Bruker Avance-III 400 MHz spectrometer. All experimental data are normalized with respect to the maximum peak intensity obtained in the 2D AM-XiX plot in Fig. 6.4c except in Fig. 6.5 where the data are normalized with respect to the on-resonance condition.

---

<sup>2</sup>The values used are  $a_x^{(-3,1)} = (a_x^{(3,-1)})^* = -0.03055 - 0.142i$ ,  $a_y^{(-3,1)} = (a_y^{(3,-1)})^* = -0.1272 + 0.06974i$ , and  $a_z^{(-3,1)} = (a_z^{(3,-1)})^* = 0.0999 + 0.04531i$ .



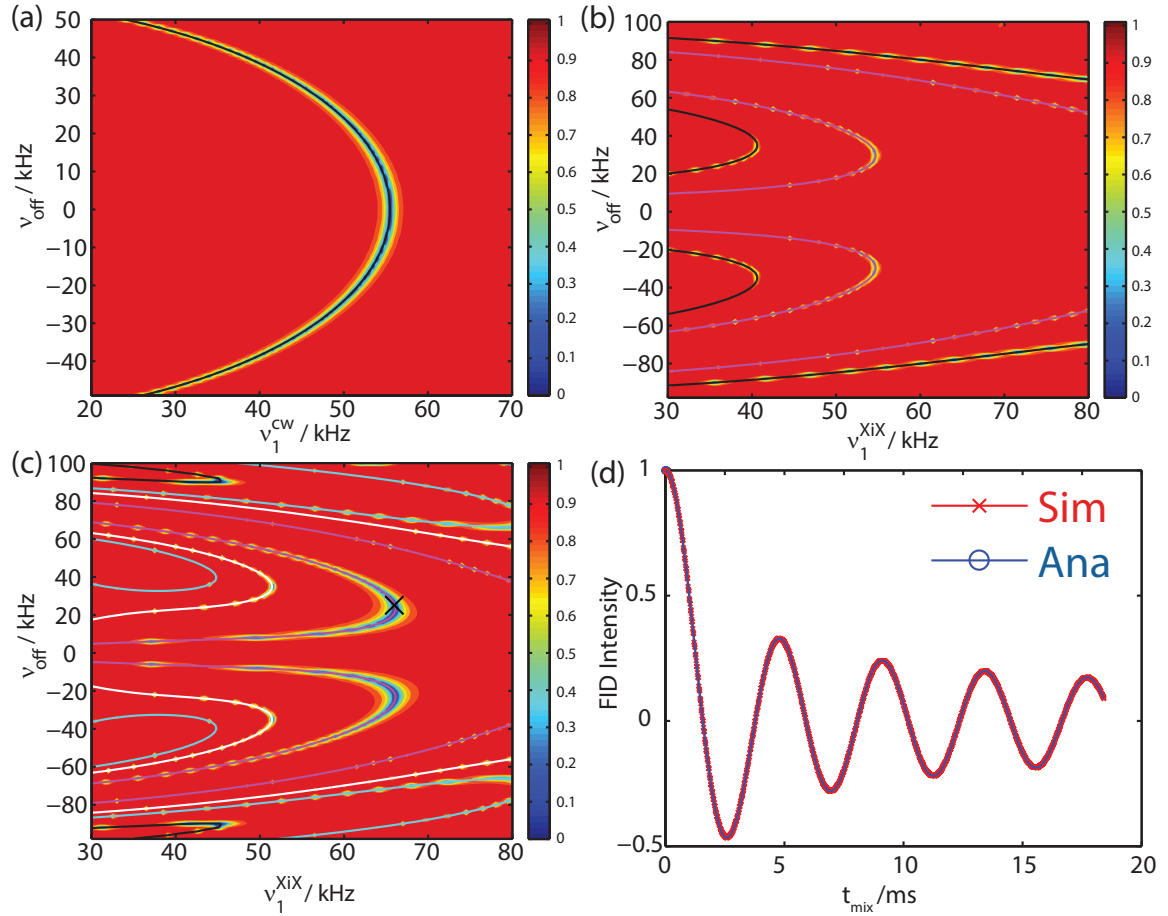


**Figure 6.2** Simulated peak intensity of a CH system under (a) CW (b) AM-XiX or (c) SC-AM-XiX decoupling. Same pulse width of  $\tau_p=12.5 \mu\text{s}$  and CW field of  $v_1^{\text{CW}}=5 \text{ kHz}$  are used in (b) and (c). Plot (d) shows the dephasing of FID intensity using analytical Hamiltonian (Eq. (6.28)) (blue) and numerical simulations (red) for SC-AM-XiX decoupling at  $v_{\text{off}}=21 \text{ kHz}$  and  $v_1^{\text{XiX}}=66 \text{ kHz}$ , a bad decoupling condition marked with black cross in (c).

### 6.3.2 Decoupling Efficiency of AM-XiX and SC-AM-XiX

The general criteria for good decoupling are: (i) The magnitude of the second-order heteronuclear cross terms that lead to line broadening are as small as possible. (ii) The condition is far away from any resonance conditions that lead to line broadening. (iii) Strong homonuclear interactions can help obtaining narrower lines [146]. The resonance conditions of the AM-XiX sequence ( $v_r + k_0 v_m \pm v_{\text{eff}} = 0$ ) were already discussed in the literature [45] and are shown in Fig. 6.3i and j as white lines. One can see that the line intensity drops significantly when the decoupling parameters match the resonance conditions. On the other hand, the line intensity is highest when it is far away from the V-shaped region (white lines in Fig. 6.3i) are chosen formed by two adjacent resonance conditions. The V-shaped form of the two adjacent resonance conditions is caused by the effective nutation frequency  $v_{\text{eff}} = v_1^{\text{CW}} \bmod v_m$  which increases linearly with the CW field for the AM-XiX sequence.

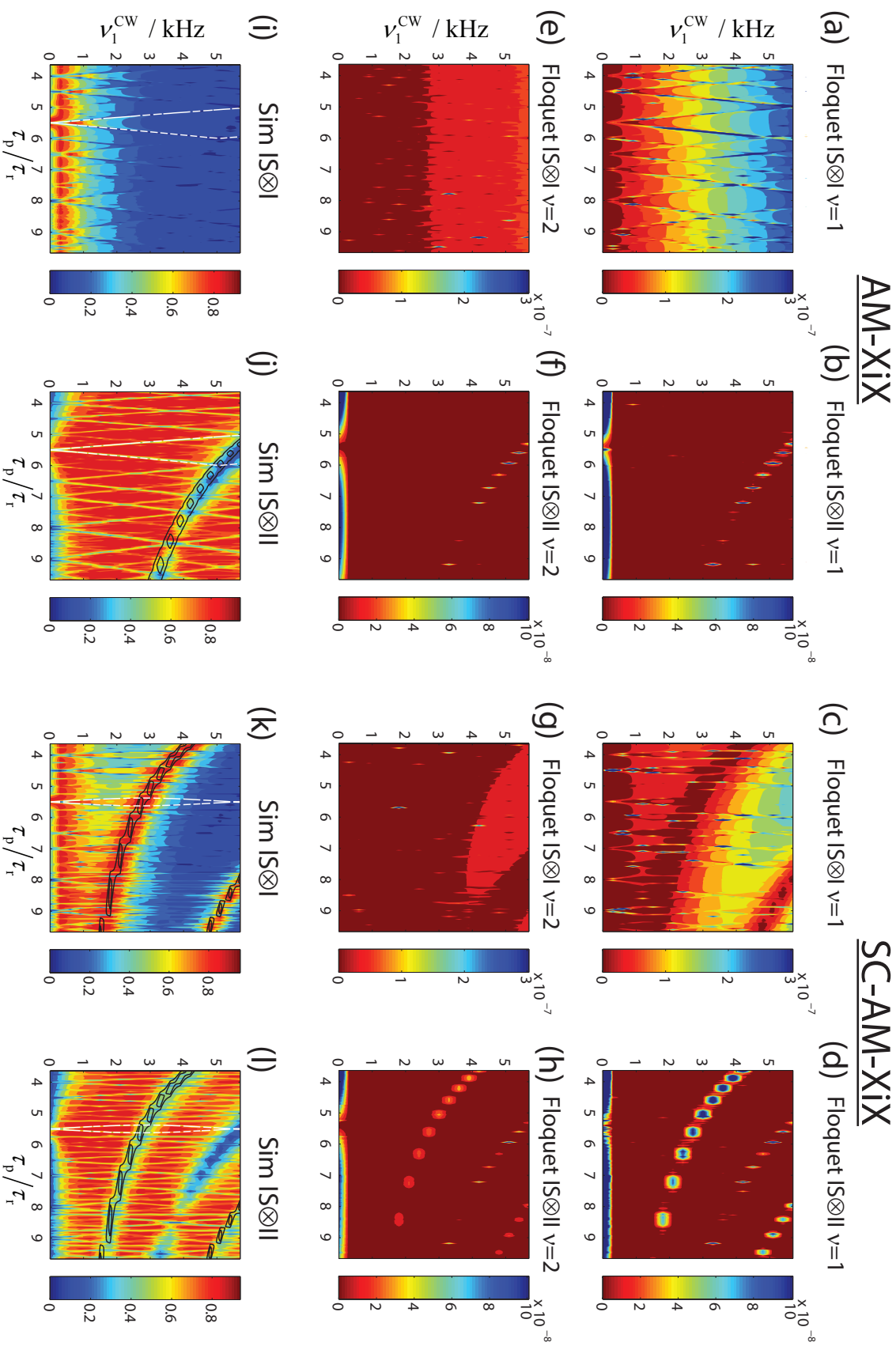


**Figure 6.3** Size of the cross-term scaling factors  $\hat{q}_{\text{CSA}}^{(v)}$  ((a), (c), (e) and (g)) and  $\hat{q}_{\text{DD}}^{(v)}$  ((b), (d), (f) and (h)) with spatial component  $v = 1$  (a)-(d) and  $v = 2$  (e)-(h) for the decoupling sequence AM-XiX ((a), (b), (e), (f), (i) and (j)) and SC-AM-XiX ((c), (d), (g), (h), (k) and (l)) respectively. Simulated intensity of a  $\text{CH}_2$  glycine with (i) and (k) only CSA and no homonuclear dipolar coupling ((j) and (l)) only homonuclear dipolar coupling and no CSA. All data (a)-(l) were obtained at  $\nu_1 = 60.6$  kHz,  $\nu_1^{\text{XiX}} = 11.2$  kHz and 400 MHz.

However, the effective field of the SC-AM-XiX sequences does not increase linearly with the CW field but it has an inverse cosine dependence with respect to the CW component (Table 6.1). The two adjacent resonance conditions of the SC-AM-XiX sequences form an oval shape as can be seen from the white lines in Fig. 6.3k and l. We would like to emphasize again that quantifying the characteristic frequency  $\nu_{\text{eff}}$  and the corresponding resonance conditions are important because of the criterion (ii), i.e., good decoupling conditions are typically far away from any destructive heteronuclear recoupling conditions.

To judge the residual line width of decoupling sequences as a function of the sequence parameters, the scaling factors for CSA cross term  $q_{\chi}^{(v)}$  (Eq. (6.18)) and for the dipolar cross term  $q_{\mu\chi}^{(v)}$  (Eq. (6.19)) can be used. We define the following expressions

$$\bar{q}_{\text{CSA}}^{(v)} = \sqrt{\sum_{\chi} |q_{\chi}^{(v)}|^2} \quad (6.29)$$

$$\bar{q}_{\text{DD}}^{(v)} = \sqrt{\sum_{\mu,\chi} |q_{\mu\chi}^{(v)}|^2} \quad (6.30)$$

where  $\bar{q}_{\text{CSA}}^{(v)}$  and  $\bar{q}_{\text{DD}}^{(v)}$  symbolize the norm [51] for the CSA and dipolar cross terms respectively. These norms are then used as simple measures for the strength of these contributions. These quantities are plotted in Figs. 6.3a-h for AM-XiX and SC-AM-XiX. The norms for the cross terms are calculated independently for the spatial rotating component  $\nu = 1$  (Figs. 6.3a-d) and  $\nu = 2$  (Figs. 6.3g-h) since they are weighted differently by the magnitude of the spatial components of the interactions in Eqs. (6.12)-(6.17). In principle, the two contributions could be combined if a detailed knowledge of the spin system is known, but the generality of the description would be lost. Additionally, the differences between the two components could perhaps grant more physical insights into the performance of decoupling sequences.

In general, we expect high peak intensity if the magnitude of the heteronuclear cross terms is small, and on the contrary, low peak intensity if the size of the cross terms is large. These correlations can be verified by comparing the magnitude of the cross terms (Figs. 6.3a-h) and the line intensities in the numerical simulations shown in Figs. 6.3i-l. For instance, the size of the CSA cross term for AM-XiX is zero at  $\nu_1^{\text{CW}}=0$  (Figs. 6.3a and e), a fact that is known from the XiX sequence [50]. As the magnitude of the cross term increases with higher field (Fig. 6.3a), the peak intensities fall (Fig. 6.3i). On the other hand, the size of the dipolar cross term is significant only at  $\nu_1^{\text{CW}} = 0$  (Figs. 6.3b and f) and at the resonance condition  $\nu_1^{\text{CW}} = \nu_m$ , which is indicated by black contours in Fig. 6.3j. The fact that the CSA cross term is smaller for lower  $\nu_1^{\text{CW}}$  fields while the dipolar cross term is smaller

at higher  $v_1^{\text{CW}}$  fields, limits the area of good decoupling for the AM-XiX sequence. Hence, a compromise on the magnitude of the  $v_1^{\text{CW}}$  field has to be chosen to minimize the total residual line broadening originating from both cross terms. The dipolar cross term can be neglected in all other regions because the symmetry of the Fourier coefficients originating from the CW part of the interaction-frame transformation imposes a cancellation of these terms except in areas close to the resonance conditions.

For the case of SC-AM-XiX, at  $v_1^{\text{CW}} = 0$  (Figs. 6.3c, d, g, and h) the two cross terms behave in a similar way compared to AM-XiX. However, for non-vanishing  $v_1^{\text{CW}}$  amplitudes, the CSA cross term does not increase uniformly and linearly with respect to the  $v_1^{\text{CW}}$  (Fig. 6.3i). It reaches a second minimum at  $v_1^{\text{CW}} \approx 2 - 5$  kHz (area marked with black contours in Fig. 6.3k) with a strong dependence on the modulation frequency (pulse length). In the same area, however, the dipolar cross terms are poorly averaged out (black contours at Figs. 6.3k and l) and, therefore, this area is not an overall good decoupling condition.

### 6.3.3 Using Homonuclear Recoupling Conditions for Better Decoupling

As discussed in the previous section, increasing homonuclear dipolar couplings can be beneficial for decoupling due to "self-decoupling" effects [129, 148, 149]. This can happen when the resonance conditions that recouple a homonuclear double-quantum (DQ) term are satisfied, i.e., resonance conditions with  $\ell_0 = 2$  [51]. For instance, it was observed that the DQ recoupling condition  $v_m = 2v_{\text{eff}}$  (black contours in Figs. 6.4a and c) coincides with regions of maximum peak intensity outside the destructive heteronuclear resonance conditions. This is due to the DQ term that leads to faster spin diffusion and, therefore, promotes a stronger "self decoupling" mechanism. The line-narrowing effect of homonuclear recoupling can also be exemplified by looking at another class of homonuclear resonance conditions  $v_r + k_0 v_m \pm 2v_{\text{eff}} = 0$ , where  $k_0$  can be any integer. It was shown that this form of resonance condition [51] is able to generate a DQ term, which has a scaling factor that can be amplified by fulfilling multiple DQ recoupling conditions simultaneously. One can obtain the equation  $v_m = 4v_{\text{eff}}$  (magenta) by solving the intersection of the two conditions characterized by  $v_r - 10v_m = 2v_{\text{eff}}$  and  $v_r - 11v_m = -2v_{\text{eff}}$  (white lines). Similarly, it can be seen that the magenta line coincides with another set of local maxima peak intensity. This effect is however not obvious in the experimental data (Fig. 6.4a), perhaps because the decoupling performance is smeared by the rf-inhomogeneity of the probe. For the case of SC-AM-XIX (Figs. 6.4b and d), the peak intensities at the equivalent DQ recoupling condition  $v_m = 2v_{\text{eff}}$  (black contours) are not better. This is because any benefits obtained by exploiting the self-decoupling mechanism are counterbalanced by the presence of large dipolar cross-term at the same region (see Figs. 6.3d and l) and the CSA terms are better

compensated along curve (Fig. 6.3c). This analysis shows that it could be beneficial to utilize the strong homonuclear coupling proton network for self-decoupling, especially for the case of AM-XiX. Thus, we suggest an optimization strategy for AM-XiX that exploits this self-decoupling effect into the good decoupling condition. Firstly, fix the pulse length  $\tau_p$  by fulfilling the condition where  $n$  is an integer  $\tau_p = n\tau_r/2$  [45], then fix  $\nu_1^{\text{XiX}}$  such that  $\nu_1^{\text{XiX}}\tau_p$  is a multiple of  $2\pi$  to average the CSA cross-term, and finally fix  $\nu_1^{\text{CW}}$  so that  $\nu_1^{\text{CW}} = 1/4\tau_p$  thereby fulfilling the DQ recoupling condition.

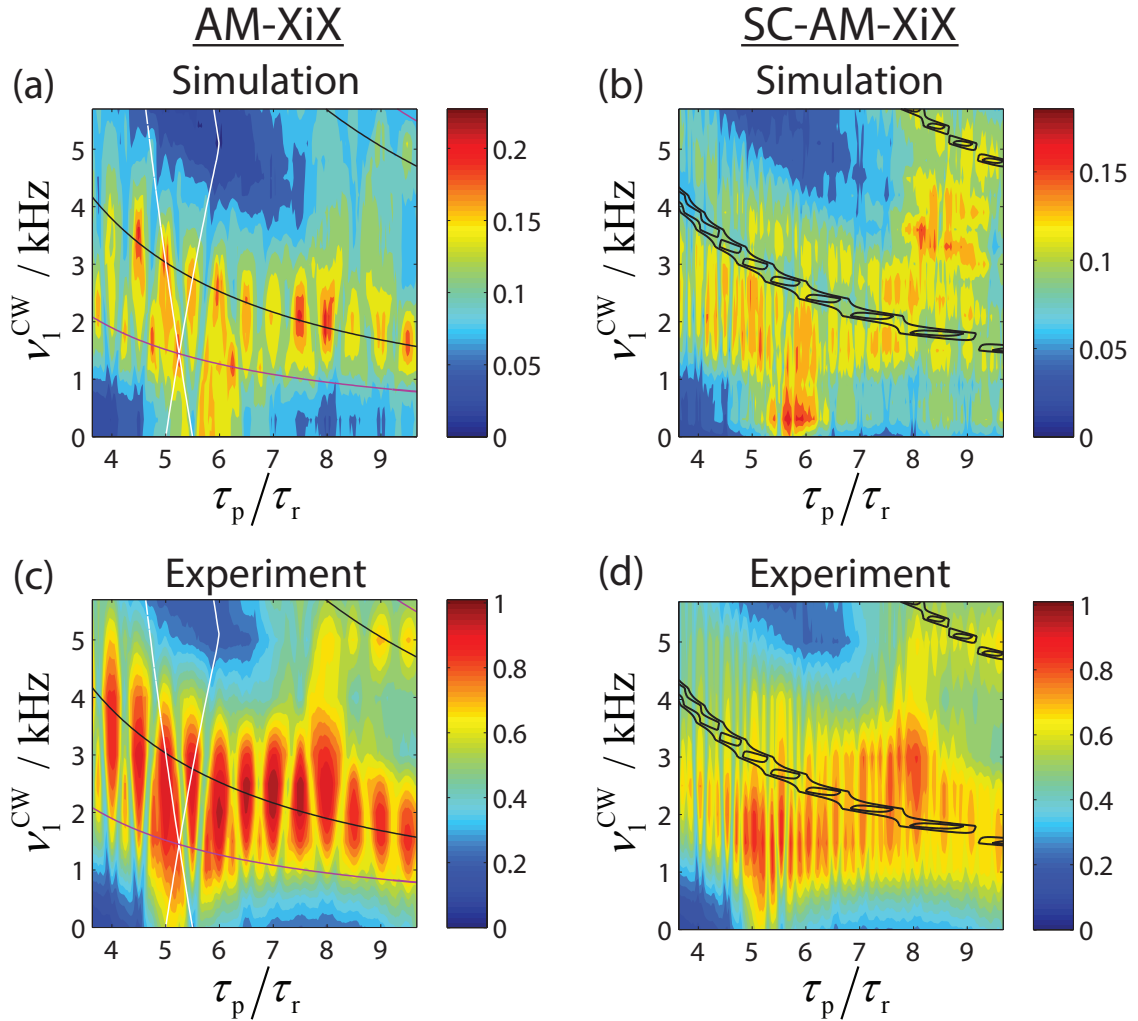


**Figure 6.4** Maximum line intensity of the  $C\alpha$  signal for AM-XiX ((a) and (c)) and SC-AM-XiX ((b) and (d)) at  $\nu = 60.6$  kHz and at 400 MHz magnet. The simulations ((a) and (b)) were performed on a  $C_2H_4$  glycine spin system with all spin interactions included and  $\nu_1^{\text{XiX}} = 11.2$  kHz. The experiments ((c) and (d)) were carried out using  $\nu_1^{\text{XiX}} = 11.8$  kHz. The first- and second-order double-quantum recoupling conditions are plotted in white ( $\nu_r - 10\nu_m = 2\nu_{\text{eff}}$  and  $\nu_r - 11\nu_m = -2\nu_{\text{eff}}$ ) ((a) and (c)) and black ( $\nu_m = 2\nu_{\text{eff}}$ ) ((a)-(d)) respectively. The line of intersections of the first-order recoupling is shown in magenta ( $\nu_m = 4\nu_{\text{eff}}$ ) ((a) and (c)).

### 6.3.4 Offset Effects on Decoupling Efficiency

To investigate the sensitivity of the two sequences to offset effects, a set of parameters was selected that resulted in good decoupling performance, i.e.,  $\tau_p = 91.5 \mu\text{s}$ ,  $\nu_1^{\text{XiX}} = 11.2 \text{ kHz}$ ,  $\nu_1^{\text{CW}} = 0.9 \text{ kHz}$  for AM-XiX and  $\nu_1^{\text{CW}} = 2.1 \text{ kHz}$  for SC-AM-XiX. The robustness of the selected decoupling condition with respect to the offset is shown in Fig. 6.5. The dependence of the magnitude of the second-order cross terms on the offset are shown in Figs. 6.5a-d for both AM-XiX (blue) and SC-AM-XiX (red). For on-resonance decoupling the CSA cross terms dominate the residual line width while the dipolar cross terms are almost negligible (Figs. 6.5a-d). However, the CSA cross-terms are relatively robust to  $\pm 2 \text{ kHz}$  variations in offset while the dipolar cross-terms scale significantly over the same range of offset. The dipolar cross-term of AM-XiX grows almost twice as fast as the SC-AM-XiX term. Based on this behaviour, one would expect that offset effects are mostly dependent on the dipolar cross term and that SC-AM-XiX shows better offset compensation.

To verify the predictions based on the scaling factors of the Floquet Hamiltonian (Figs. 6.5a-d), full numerical simulations on three-spin system were performed. To selectively investigate the influence of the CSA or dipolar cross terms, either the homonuclear dipolar coupling or the CSA tensor were set to zero. The dependence of the peak intensity on the CSA cross term is shown in Fig. 6.5e which shows a very good agreement with the scaling-factor plots (Figs. 6.5a and c). When only the dipolar cross term is considered (Fig. 6.5f), the maximum peak intensity dropped to 26% (SC-AM-XiX) and 10% (AM-XiX) of their original values when an offset of 1 kHz is introduced. It can be concluded that the dipolar cross-term is the dominant term that leads to line-broadening when an offset is introduced at this decoupling condition. Experimental data in Fig. 6.5g has demonstrated that the decoupling performance of SC-AM-XiX is less sensitive to that of AM-XiX, a finding that conforms to our theoretical predictions and simulations.

Note that the experimental data appears to be broader because it is normalized with respect to the best-obtained result whereas the simulation intensity is normalized with respect to perfect decoupling. Other reasons that account for the differences between experimental data and simulations include the adoption of a simpler three-spin  $\text{CH}_2$  system in the simulations to avoid complications arises from shifted resonance conditions due to fictitious-field terms and spin diffusion effect that are manifested in the cross terms involving only  $I$  spins (Eqs. (6.14)-(6.17)). Experimentally, we observe that SC-AM-XIX is more robust to proton offsets than AM-XIX decoupling (Fig. 6.5g). The explicit introduction of the offset terms in the Hamiltonian and variation in the magnitude of the residual cross-term as a function of offset can be used to understand the experimental behavior of decoupling sequence.

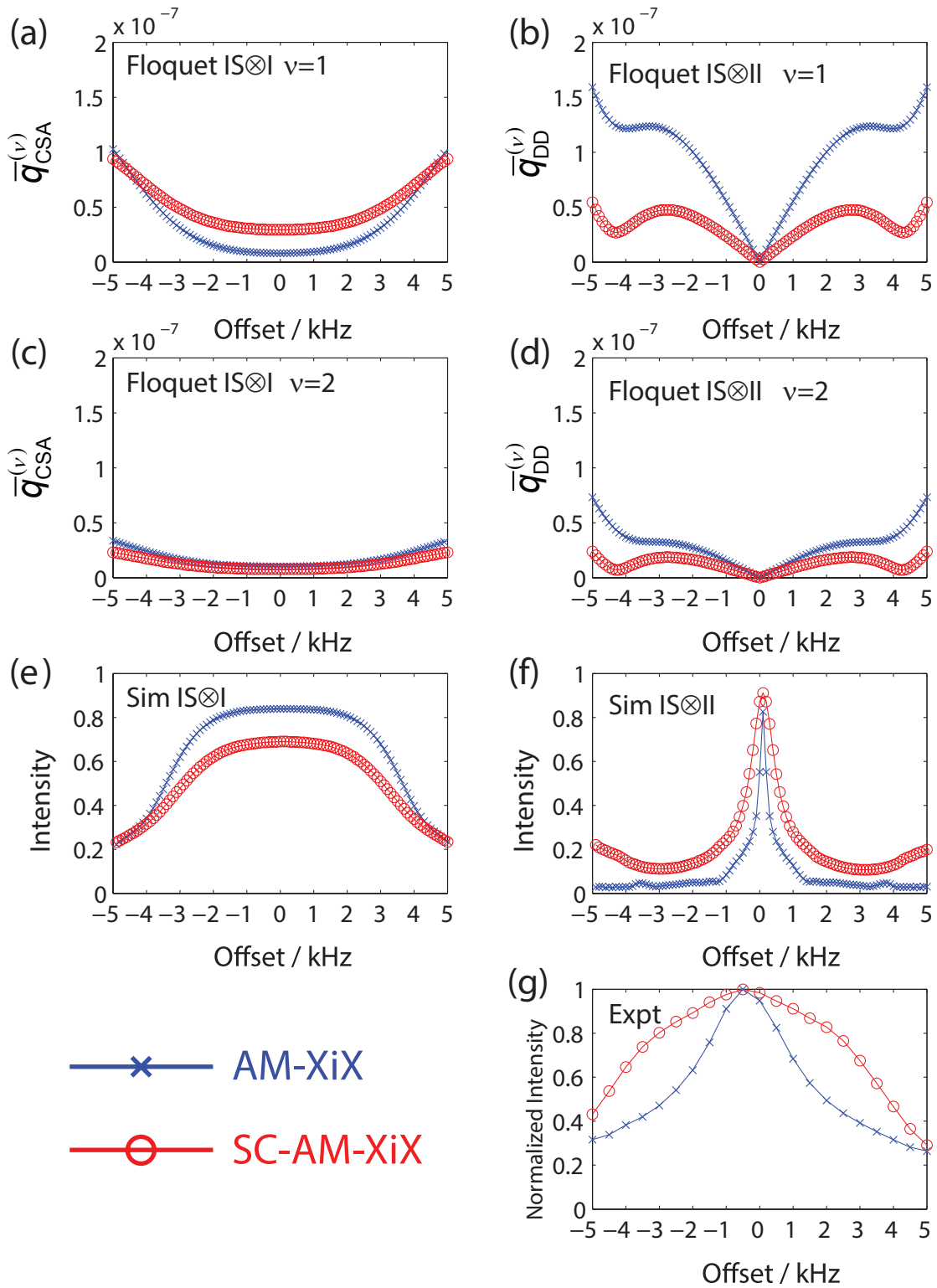


**Figure 6.5** The effect of offset on the optimized decoupling conditions of the respective sequences. The size of the cross-term scaling factors  $\bar{q}_{CSA}^{(\nu)}$  ((a) and (c)) and  $\bar{q}_{DD}^{(\nu)}$  ((b) and (d)) for the spatial component  $\nu = 1$  ((a) and (b)) and  $\nu = 2$  ((c) and (d)) are shown here. Simulated maximum line intensity of a CH<sub>2</sub> glycine spin system with (e) only CSA and no homonuclear dipolar coupling (f) only homonuclear dipolar coupling and no CSA. The calculations and simulations in (a)-(f) were performed using  $\tau_p = 91.5 \mu s$ ,  $\nu_1^{XiX} = 11.2 \text{ kHz}$ ,  $\nu_1^{CW} = 0.9 \text{ kHz}$  for AM-XiX (blue crosses) and  $\nu_1^{CW} = 2.1 \text{ kHz}$  for SC-AM-XiX (red circles). Experimental data from reference [45] is shown in (g) for comparison. All data (a)-(g) were obtained at  $\nu_r = 60.6 \text{ kHz}$  and 400 MHz.

### 6.3.5 Conclusions for AM-XiX and SC-AM-XiX

We have demonstrated that our generalized theoretical framework can be applied to understand low-power decoupling sequences like AM-XiX and SC-AM-XiX. The theoretical model reveals that the predicted region of good decoupling by calculating the size of the residual couplings like CSA and dipolar cross term. Moreover, it was discovered that the optimum-decoupling conditions are obtained by exploiting homonuclear dipolar recoupling conditions for AM-XiX. The research focus in the past has been devising methods to compensate the cross-terms, but we highlight here that perhaps exploiting self-decoupling mechanism by recoupling in the design of decoupling sequences could be valuable in future research. In addition, we have exemplified that our model can be extended to consider the off-resonance irradiations. It was shown that the degradation of decoupling efficiency due to dipolar terms is more dramatic for AM-XiX than SC-AM-XiX for a given experimental condition, i.e. rf field  $\nu_1$  and pulse length  $\tau_p$ . Hence, one can conclude that SC-AM-XiX is more robust to offset compared to AM-XiX, a theoretical prediction that is supported by experimental results and numerical simulations.

## 6.4 Understanding High-Power Decoupling Sequences

### 6.4.1 Comparing Basic, Supercycled and Adiabatic TPPM

It was known from the decoupling sequences used in liquid-state NMR that supercycling helps to reduce experimental artifacts like rf inhomogeneity and imprecise settings of rf carrier frequency. The situation is more complicated in solid-state NMR because the coherent effect of supercycling on the compensation of residual couplings is not well understood, i.e. it is possible that the higher order cross-terms are compensated less efficiently in supercycled sequences. Hence, we are interested in analyzing these effects theoretically using the generalized theoretical framework. Additionally, adiabatic variants are also examined here for comparison. We have chosen the two-pulse TPPM decoupling sequence (Fig. 6.6a) as the basic starting sequence. Then, the analysis will be extended to its variants like supercycled TPPM<sub>64</sub> (Fig. 6.6e) and adiabatic SW<sub>f</sub>-TPPM (Fig. 6.6b).

#### Basic TPPM

The CSA cross term<sup>3</sup> during basic TPPM is calculated theoretically, and the optimum decoupling performance (Fig. 6.7a and b) is observed near the expected  $\beta \cos \phi = \pi$  [46] relation (magenta dotted line in Fig. 6.7c), where  $\beta$  is the flip angle per pulse. The theoretic-

<sup>3</sup>The dipolar cross term is neglected here as the profile is not as pronounced as for the CSA cross term.





From these analyses, it can be concluded that the relation between the three variants of TPPM is not obvious, and each of them should be treated independently. Therefore, a basic decoupling sequence may not necessarily be made more robust by simply supercycling or swept adiabatically as the compensation of the residual couplings could either improve or deteriorate. However, the supercycled or adiabatic sweep might still be beneficial for experiments at higher MAS (above 100 kHz), as the rf-inhomogeneity and offset might have more impact than the residual couplings, i.e. similar situation as in solution-state NMR.

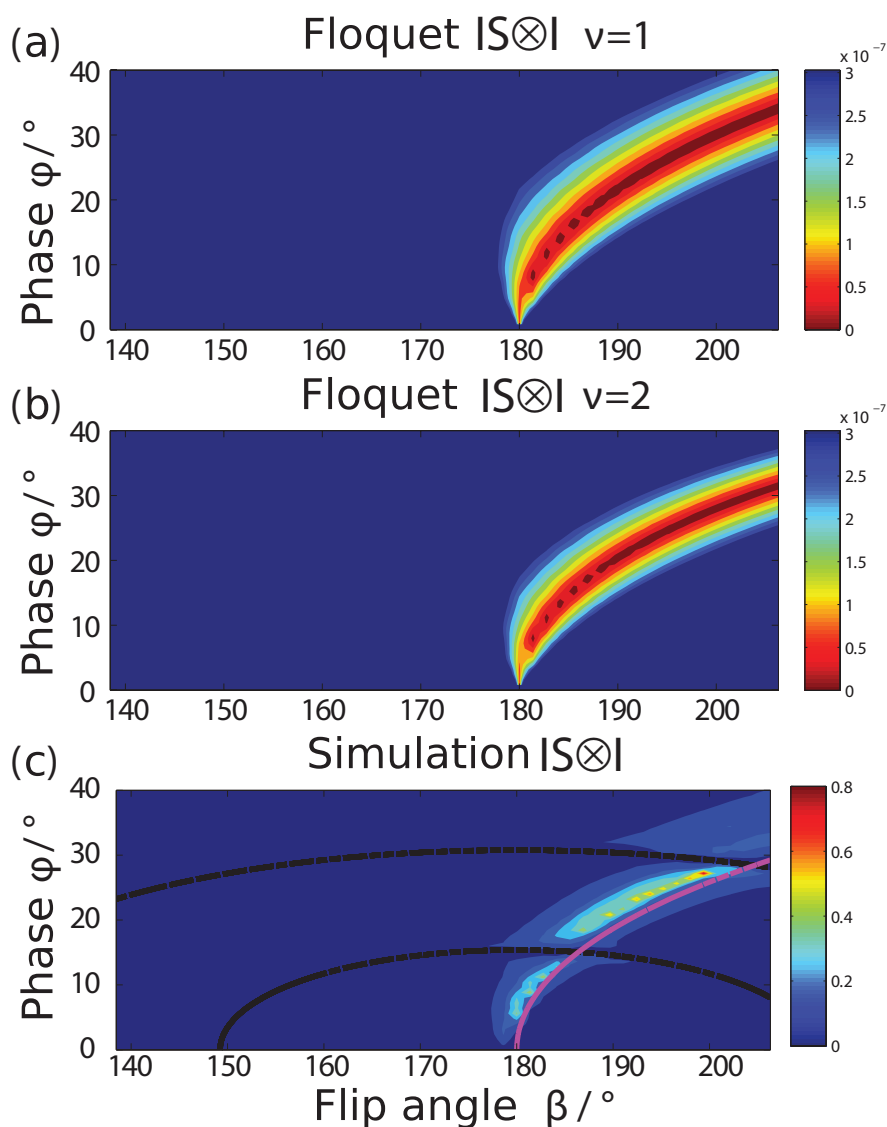


**Figure 6.7** Calculated CSA cross term for the spatial component (a)  $\nu = 1$  and (b)  $\nu = 2$  of basic TPPM. (c) Numerical simulations performed at three-spin  $\text{CH}_2$  on 850 MHz, no offset,  $\nu_r = 22.22$  kHz, fix  $\tau_p = 3.913 \mu\text{s}$  and  $\nu_{\text{IH}} = 130$  kHz, flip angle  $\beta = 183.12^\circ$ , are shown for comparison. The first-order resonance conditions plotted are  $\nu_r - \nu_m + \nu_{\text{eff}} = 0$  (dotted black at lower  $\phi$ ) and  $2\nu_r - \nu_m + \nu_{\text{eff}} = 0$  (dotted black at higher  $\phi$ ). The theoretical optimum decoupling  $\beta \cos \phi = \pi$  is also plotted (magenta).

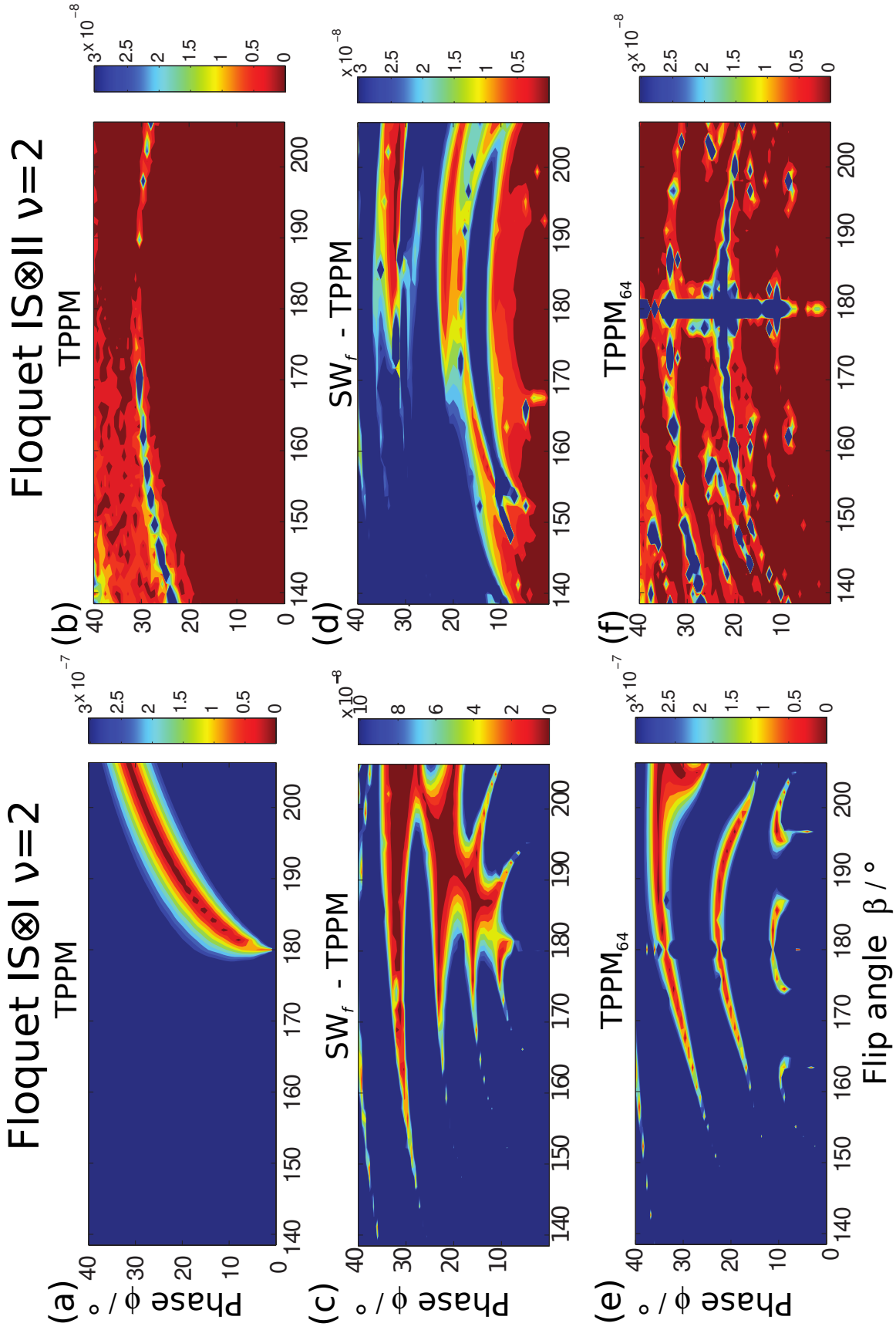


**Figure 6.8** Calculated (a, c, and e) CSA and (b, d, and f) dipolar cross term for  $v = 2$  spatial component of (a,b) basic TPPM (c,d) adiabatic  $SW_f$  - TPPM and (e,f) supercycled  $TPPM_{64}$  with nominal parameters of  $\nu_r = 22.22$  kHz, fix  $\tau_p = 3.913$  us and  $\nu_{IH} = 130$  kHz, flip angle  $\beta = 183.12^\circ$ .

### 6.4.2 Easier Optimization of SPINAL-64

It was postulated [124] that the optimization of the SPINAL-64 sequence (Fig. 6.6d) can be simplified by omitting the phase  $\alpha$ , as long as the following equation is satisfied:

$$\phi + \alpha = K \quad (6.31)$$

where  $K$  is a constant. It can be inferred from Fig. 6.9 [124] that the optimum decoupling performance of SPINAL is obtained for a fixed flip angle of  $\sim 185^\circ$  when  $K = 9$  (Eq. (6.31)). Therefore, it was hypothesized that the parameter phase  $\alpha$  is redundant and only  $\phi$  has to be optimized. Consequently, one can set<sup>4</sup>

$$\beta = 2\alpha = 0. \quad (6.32)$$

while  $\phi$  remains the only free parameter that has to be optimized. One can see that if Eq. (6.32) is satisfied, SPINAL-64 is essentially a supercycled TPPM (Fig. 6.6e).

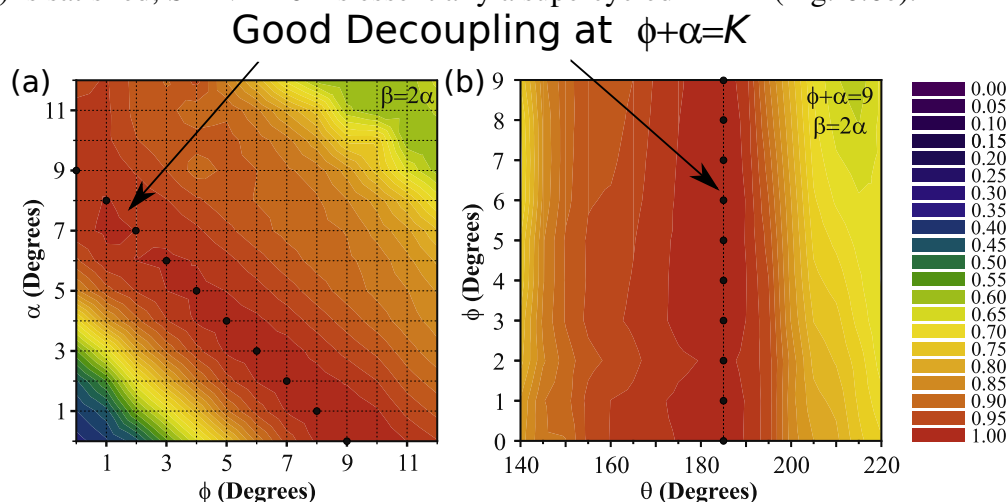


**Figure 6.9** Experimental data of SPINAL-64 with fixed phase  $\phi + \alpha = K = 9$ , at  $\nu_r = 22.2$  kHz and rf field of  $\nu_{1H} = 130$  kHz. The figure is extracted from *Mithu et al.* [124].

The hypothesis that the optimum SPINAL decoupling sequence depends only on the value  $K$  (Eq. (6.31)) is examined again here by numerical simulations. The result (Fig. 6.10a) indicates that the decoupling performance has relatively small variations along  $\phi + \alpha = K = 10$  (Eq. (6.32)), at least for small  $K$  values. It is evident that the condition is no longer applicable for large  $\phi, \alpha$  angle (Fig. 6.10c). Nevertheless, we will limit the discussion here to angles of  $\phi, \alpha \leq 15^\circ$ . In principle, both the dipolar and CSA cross terms have to be calculated to judge the decoupling performance. Prior to this, the effective field  $\nu_{\text{eff}}$  has to be determined, and interestingly, the result (Fig. 6.10b) shows that the magnitude

<sup>4</sup>The condition  $\beta = 2\alpha$  was already imposed in the original SPINAL sequence [125].

of  $v_{\text{eff}}$  is approximately constant<sup>5</sup> along the constant  $K$ . Note that this is only a qualitative result, and having the same  $v_{\text{eff}}$  does not strictly mean the same decoupling performance, otherwise optimum decoupling performance would also be expected at  $K=12$  and  $15$  (Fig. 6.10b), which are not observed (Fig. 6.10a).

The size of the CSA and dipolar cross terms are then calculated and verified by numerical simulations. The results show that the CSA cross term is small in most region except at  $K \sim 11$  and  $16$  (Fig. 6.11). Unfortunately, the dipolar cross term is small only at these same regions ( $K \sim 11, 16$ ). The actual performance of the decoupling sequence now depends heavily on the relative contribution between the two cross terms, i.e. the details of the spin system play an important role here. For the case of protonated samples, perhaps the dipolar cross term is more critical, and hence the full numerical simulation (Fig. 6.10a) is more similar to the dipolar cross term (Fig. 6.11f). Based on the theoretical and numerical cross term analysis, one can conclude that the optimization of parameter  $\alpha$  can indeed be omitted with  $\phi \leq 15^\circ$ , for the case of high-power decoupling regime.

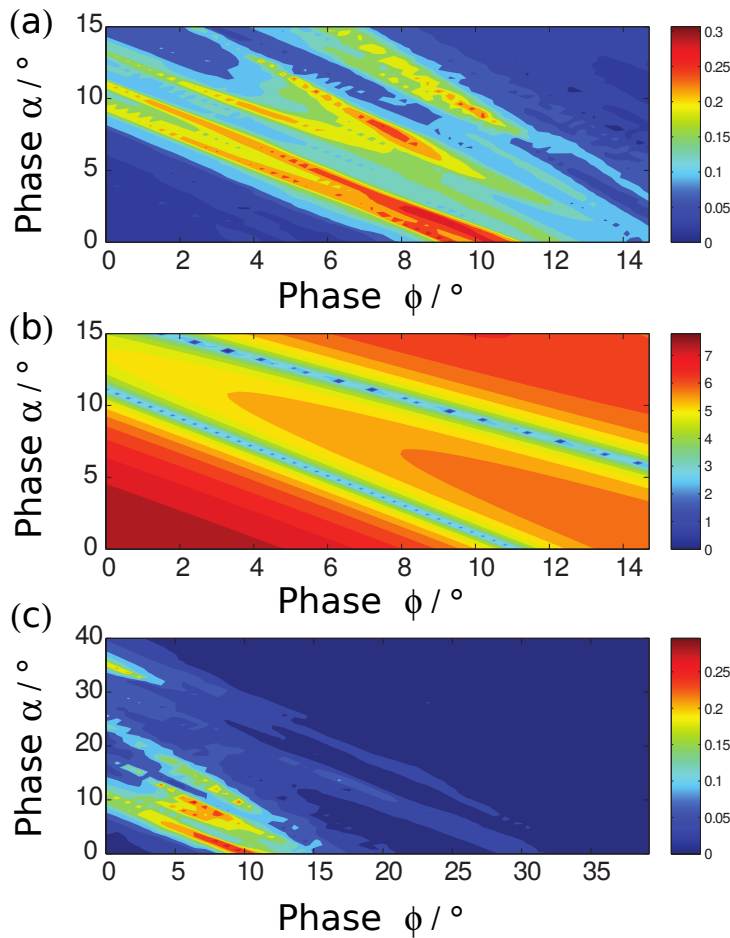


**Figure 6.10** (a,c) Simulated peak intensity for SPINAL on three-spin  $\text{CH}_2$  on 850 MHz, no offset,  $\nu_r = 22.22$  kHz, fix  $\tau_p = 3.913$   $\mu\text{s}$  and  $\nu_{1\text{H}} = 130$  kHz, flip angle  $\beta = 183.12^\circ$ . (b) shows the calculated logged effective field  $\log(v_{\text{eff}})$ , to increase the contrast. (c) Extension of (a) to a larger range.

<sup>5</sup>An analytical expression was derived and it is close but not strictly constant, i.e.  $\frac{\delta v_{\text{eff}}}{\delta \phi} \neq \frac{\delta v_{\text{eff}}}{\delta \alpha}$ .

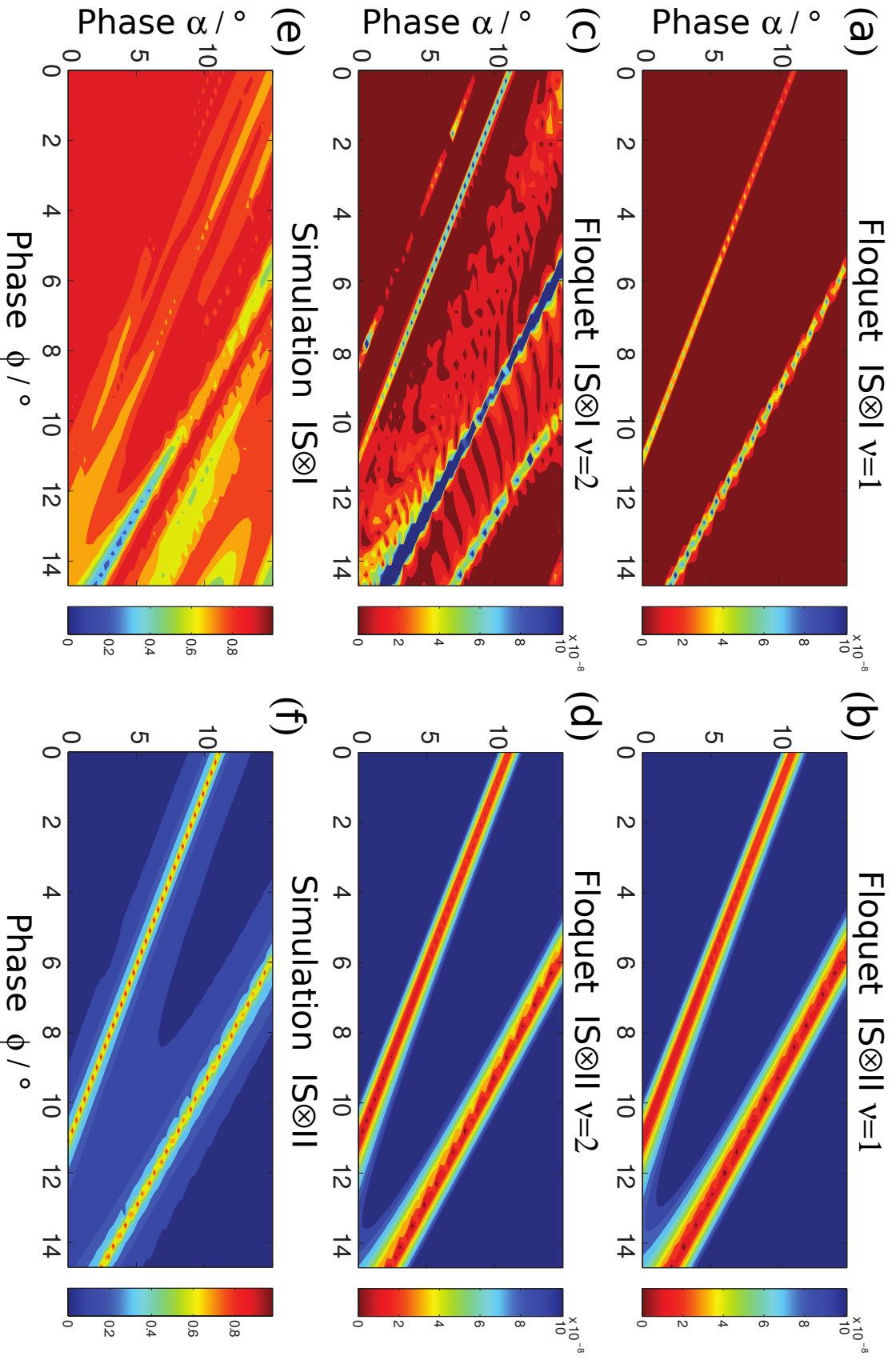


**Figure 6.11** Comparing the effect of (a, c, and e) CSA and (b, d, and f) dipolar cross terms using SPINAL using (a-d) Floquet calculations and (e and f) numerical calculations at  $\nu_1 = 22.22$  kHz and flip angle  $\beta = 183.12^\circ$ .

### 6.4.3 Elucidating Finite-Pulse Effect in Adiabatic SW-TPPM

The frequency-swept TPPM is comprised of 11 cycles of basic TPPM elements (Fig. 6.6b and c) with the nominal flip angle (1.0) being swept in the range of values listed here:

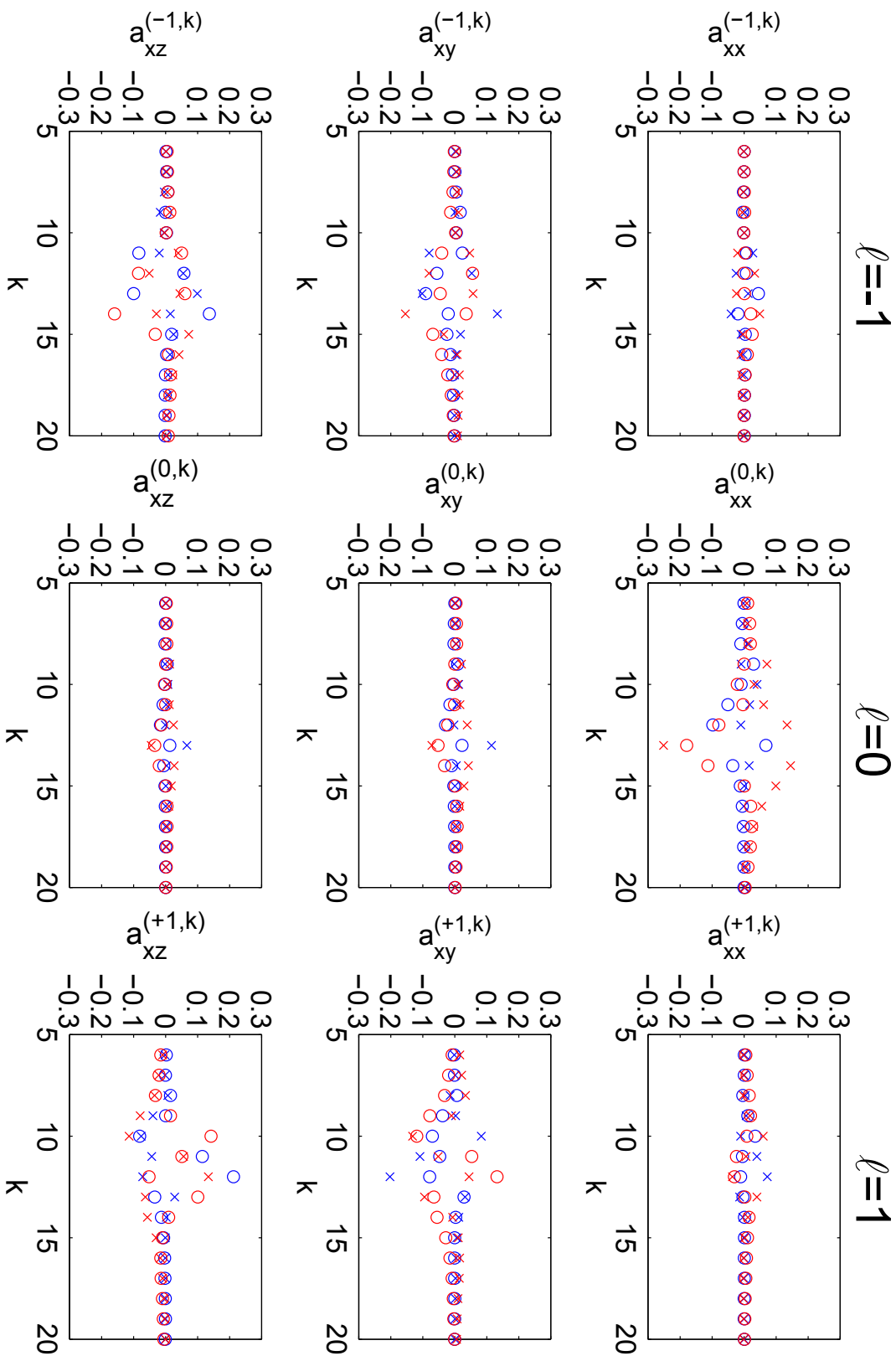
$$\text{Flip-angle } \beta = [0.78, 0.86, 0.94, 0.96, 0.98, 1.0, 1.02, 1.04, 1.06, 1.14, 1.22]. \quad (6.33)$$

The design of adiabatic swept-frequency TPPM [132, 134] was inspired originally by the adiabatic DREAM sequence [105, 106] (Sec. 5). In principle, the adiabatic condition can be implemented by either sweeping through the rf amplitude,  $SW_a$ -TPPM (Fig. 6.6c) or modulation frequency,  $SW_f$ -TPPM (Fig. 6.6b). Both methods are related in a way that the effective flip angles per element remain invariant in either scheme. In principle, one would expect both decoupling sequences to exhibit identical results, as the cycle time  $\tau_m$  (or  $\nu_m$ ) and effective field  $\nu_{\text{eff}}$  are essentially identical for both sequences. Surprisingly, it was reported [134] that there are some similarities and also significant differences, especially the deterioration of decoupling performance in the  $SW_a$ -TPPM case when homonuclear couplings are included. We believe that the difference arises because of the finite-pulse effect and we have studied it using the generalized theoretical framework.

Firstly, the Fourier coefficients of both sequences are determined prior to cross-term calculations. Interestingly, although both  $SW_a$ -TPPM and  $SW_f$ -TPPM have identical modulation frequency  $\nu_m$ , and the same magnitude and direction of effective field  $\vec{\nu}_{\text{eff}}$ , the Fourier coefficients cluster around similar values of  $k$  (Fig. 6.12) but not identical. This provides the first hint that the cross-term compensation might not be the same for both sequences.

Next, the CSA cross term are calculated and compared for both  $SW_a$ -TPPM and  $SW_f$ -TPPM. It is evident that the optimum decoupling conditions are obtained for  $\phi \geq 10^\circ$  (Fig. 6.13a-d) for both sequences. Both profiles have similar shapes but broader for  $SW_f$ -TPPM, as supported by simulations (Fig. 6.13e and f). It can be inferred that the  $SW_f$ -TPPM is better in compensating CSA cross term. Similar analyses were performed for the dipolar cross term, and the results indicate that both sequences in general favour decoupling at low  $\phi$  angle ( $\phi \leq 10^\circ$ ) (Fig. 6.14), with  $SW_a$ -TPPM performing significantly worse (Fig. 6.14a, c, and e). This finding is in agreement with the previous finding [134] that the experimental results of  $SW_a$ -TPPM degrades when the homonuclear dipolar couplings are added into simulations, and also in experimental data, where proton density is higher realistically.

A possible reason that accounts for these differences could be that only a single frequency  $\nu_{\text{eff}}$  is swept in  $SW_a$ -TPPM; whereas both  $\nu_{\text{eff}}$  and  $\nu_m$  are varied simultaneously in  $SW_f$ -TPPM. The details of the time-dependent characteristic frequencies  $\nu_{\text{eff}}(t)$  and  $\nu_m(t)$  for individual TPPM element should be scrutinized to gain more physical insights.





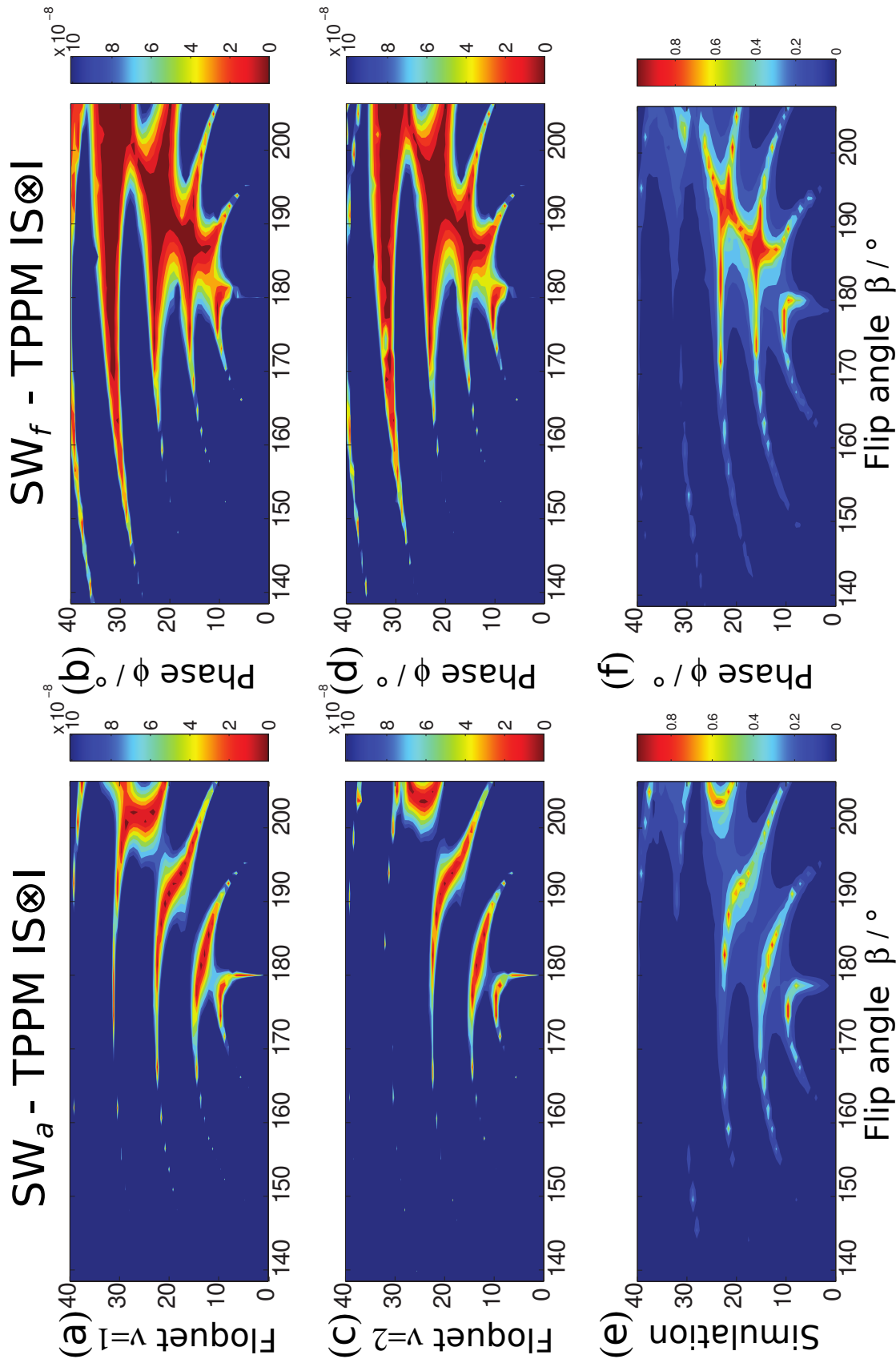


**Figure 6.13** Comparing (a, c, and e)  $SW_a$ -TPPM and (b, d, and f)  $SW_f$ -TPPM decoupling sequence in compensating CSA cross term using (a-d) Floquet calculations and (e and f) numerical calculations at  $\nu_r = 22.22$  kHz with  $\tau_p = 3.913$   $\mu$ s and  $\nu_{IH} = 130$  kHz, i.e. flip angle  $\beta = 183.12^\circ$  at  $\tau_m/2$ . Note that the colour bars in (a-d) are inverted for easier comparison by eye.

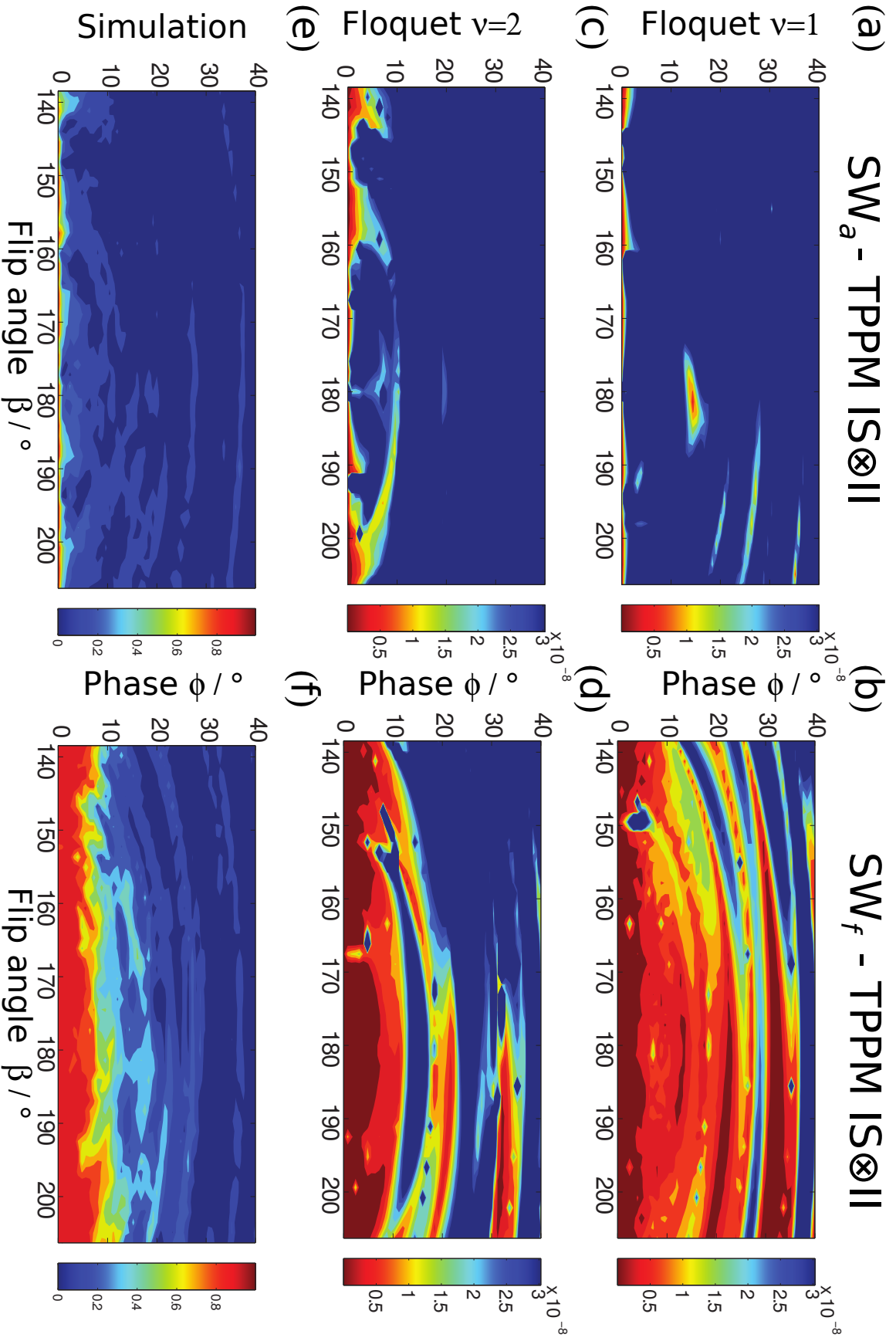


**Figure 6.14** Comparing (a, c, and e)  $SW_a$ -TPPM and (b, d, and f)  $SW_f$ -TPPM decoupling sequence in compensating dipolar cross term using (a-d) Floquet calculations and (e and f) numerical calculations at  $\nu_r = 22.22$  kHz with  $\tau_p = 3.913$   $\mu$ s and  $\nu_{1H} = 130$  kHz, i.e. flip angle  $\beta = 183.12^\circ$  at  $\tau_m/2$ . Note that the colour bars in (a-d) are inverted for easier comparison by eye.

**SW<sub>f</sub>-TPPM as an Efficient Decoupling Sequence**

Previous cross-term analyses showed that the optimum decoupling conditions that compensate the CSA ( $\phi \geq 10^\circ$ ) or dipolar ( $\phi \leq 10^\circ$ ) cross term almost never coincide, i.e. similar to the case in SPINAL-64 (Sec. 6.4.2). This is to say that robust decoupling, where both cross terms are compensated efficiently, is difficult to obtain. Full numerical simulations (both homonuclear dipolar couplings and CSA are included) are performed to examine the practicability of SW<sub>f</sub>-TPPM as an efficient decoupling sequence. The preliminary result (Fig. 6.15c) indicates that the optimum decoupling condition is rather narrow, and therefore sensitive to experimental variations such as rf inhomogeneity. The design of decoupling sequences in the future should focus more on the extent of overlapped region (correlation function) rather than just the magnitude of individual cross terms.

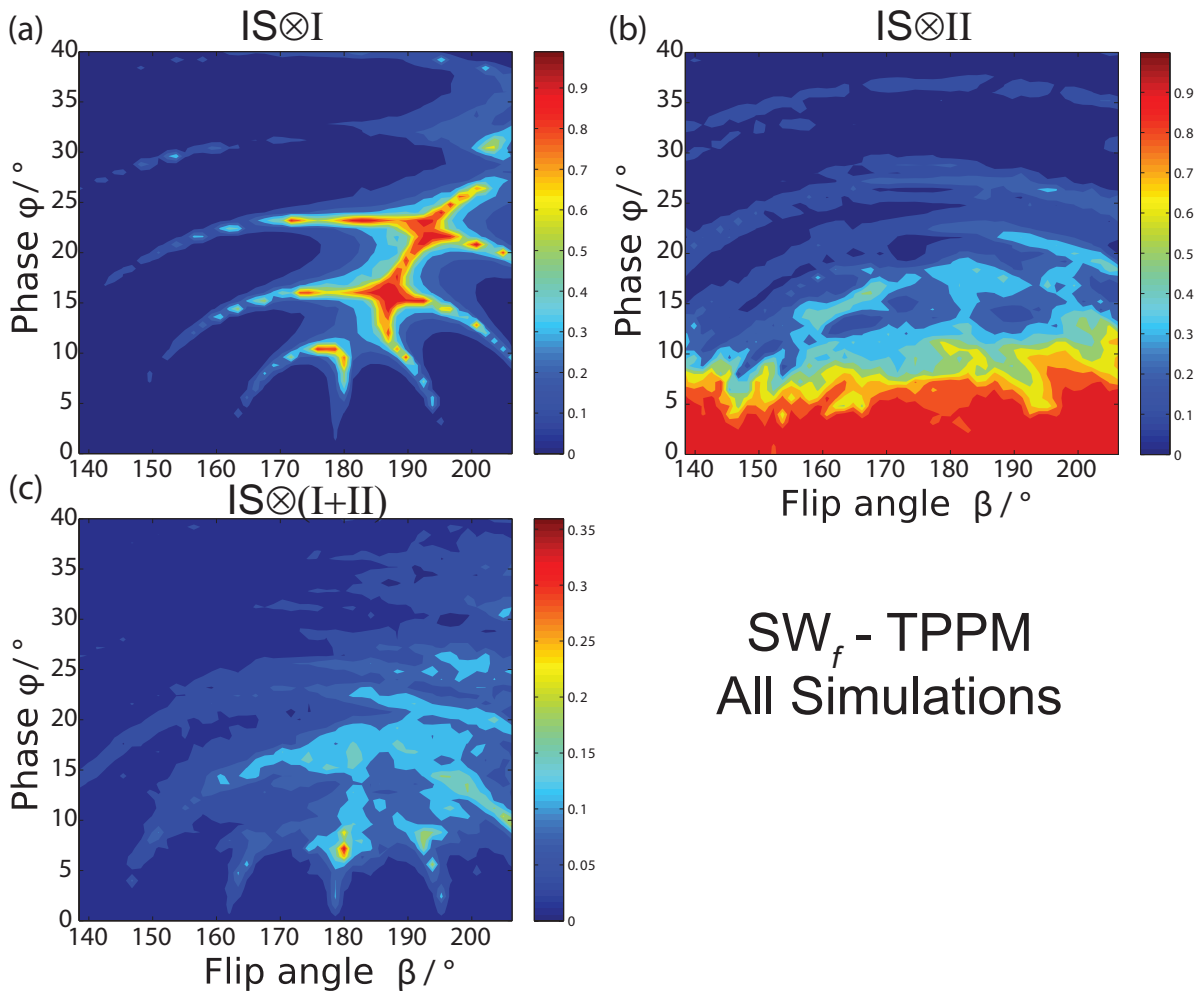


**Figure 6.15** Simulated peak intensity of SW<sub>f</sub>-TPPM decoupling on CH<sub>2</sub> on 850 MHz, no offset,  $\nu_r = 22.22$  kHz, and nominal flip angle of  $\beta = 183.12^\circ$ , for (a) homonuclear dipolar coupling included (b) CSA included and (c) both dipolar coupling and CSA included.

## 6.5 Conclusions

In this study, we have introduced a generalized triple-mode Floquet framework which can be used to describe the second-order effective Hamiltonians in arbitrary decoupling sequences under MAS. The derived equations for the effective Hamiltonians are independent of the details of the decoupling sequence which is manifest only through the values of the Fourier coefficients of the interaction-frame trajectory. These can be calculated numerically by evaluating the interaction-frame trajectory and enter through scaling factors into the effective Hamiltonians. Based on the scaling factors, a systematic comparison of different decoupling sequences can be performed without the need to perform full numerical simulations. In principle, the generalized framework can be applied to study homonuclear decoupling sequences too, with or without offset effect included. Moreover, it was shown <sup>6</sup> recently that the offset effect under high-power decoupling is not completely negligible. In addition, it was also demonstrated in Sec. 6.3.3 that self-decoupling driven by homonuclear recoupling can be significant to improve linewidth, even at high MAS frequency of 60.6 kHz. Homonuclear recoupling on protons should be emphasized in the future design of heteronuclear decoupling sequences. All these effects will be investigated in the future. In addition, such an analysis based on the Floquet treatment is computationally much more efficient than an analysis based on numerical simulations, whose performance depends on the details of the spin system and is therefore not generic to all molecules. Hence, this generalized theoretical framework can be exploited to design better decoupling sequences in the future.

---

<sup>6</sup>Unpublished work by Paul Hodgkinson.

# Chapter 7

## Outlook and Conclusions

The applications of operator-based Floquet theory have been demonstrated to be useful in analyzing pulse sequences in solid-state NMR. Particularly in situations where multiple incommensurate frequencies are involved, for instance, proton decoupling during TOBSY (Chapter 3), non-rotor synchronized DQ recoupling (Chapter 4), superposition of phase-alternating sequence in CW field (Chapter 5), and decoupling sequences which are usually non-rotor synchronized for optimum performances (Chapter 6).

In Chapter 3, it was demonstrated that the interference profile of proton decoupling during TOBSY can be predicted theoretically using trimodal Floquet theory. We realized that such interference free windows in  $C9_n^1$  might not be present in all symmetry-based C/R sequences (for e.g.  $C7_{1/2}^1$ ), and using decoupling during such sequences might even worsen the results. We are interested in investigating under what conditions these windows will appear, and try to generalize them to arbitrary symmetry-based C or R sequences.

In Chapter 4, a theoretical account for non-rotor synchronized symmetry-based C7 sequence was presented. It was shown that the asynchronous C7 regime is compensating CSA cross terms more efficiently than the synchronous regime. We foresee possible applications of the asynchronous implementation in improved suppression of other higher-order cross terms like heteronuclear dipolar couplings. This might have important implications in biological applications if heteronuclear decoupling during recoupling sequences can be neglected without a compromise on the performance. Similarly, the asynchronous regime can also be exploited in experiments that involve quadrupolar nuclei.

In Chapter 5, we have designed an offset-compensating sequence  $XiX^{CW}$  DREAM, whose transfer efficiency is less sensitive to the precise setting of the rf carrier frequency.

We have discussed only a specific recoupling condition that employs the least RF field. In principle, many other recoupling conditions can be used for DQ recoupling. The features and advantages of other DQ recoupling conditions will be explored in future work. A possible aspect is the performance in compensating higher-order cross terms in each recoupling scheme.

In Chapter 6, we have presented a generalized theoretical framework that is able to analyze arbitrary decoupling sequences. The performance of a decoupling sequence can be quantified by determining the scaling factors that scale the higher-order cross terms. The calculations of the scaling factors are at least a factor of 1000 times faster than numerical simulations since computationally expensive calculations like computing matrix exponentials for propagators are not required. Hence, we foresee an improved numerical optimization strategy, in which the scaling factors are set to be the target functions instead of the nominal intensity, will be a novel way of designing decoupling sequences. The output of such an improved strategy would yield results that are universal, i.e. independent of the spin system. There are a variety of numerical optimisation schemes like genetic algorithm [93] and optimal control theory [152, 153] that can be applied to search for optimum decoupling condition. Nevertheless, a grid-search approach, which is easy to be implemented, will be used as a proof of principle. This can be demonstrated with a simple two-pulse sequence with arbitrary rf field  $v_1$ , phase  $\phi$ , and pulse length  $\tau_p$ , that have to be optimized numerically at a particular MAS frequency.

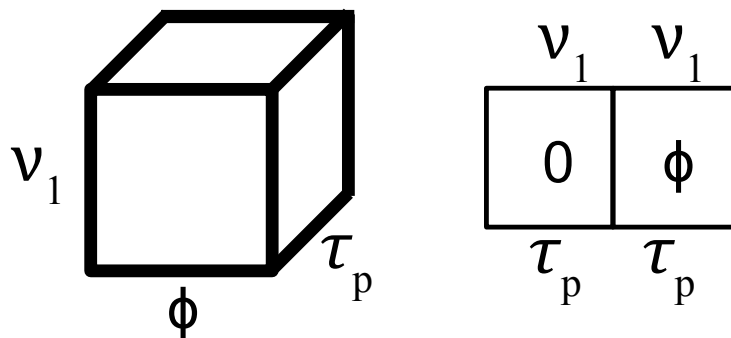


**Figure 7.1** 3D numerical optimizations of Fourier coefficients as functions of rf field  $v_1$ , phase  $\phi$ , and pulse length  $\tau_p$ .

# Appendix A

## A.1 Important Formulae

### A.1.1 Definition of Spin-Tensor Operators

Definition of rank-zero and rank-one tensors for a single spin using spherical tensor notation [68] are given as:

$$\begin{aligned}T_{00} &= E \\T_{10} &= I_z \\T_{11} &= \frac{-1}{\sqrt{2}}I^+ = \frac{-1}{\sqrt{2}}(I_x + iI_y) \\T_{1-1} &= \frac{-1}{\sqrt{2}}I^- = \frac{1}{\sqrt{2}}(I_x - iI_y)\end{aligned}\tag{A.1}$$

Definition of rank-zero, -one, and -two tensors for a two-spin system are

$$\begin{aligned}T_{00} &= \frac{-1}{\sqrt{3}}(\vec{I}_1 \cdot \vec{I}_2) \\T_{10} &= \frac{-1}{2\sqrt{2}}[I_1^+ I_2^- - I_1^- I_2^+] \\T_{1\pm 1} &= \frac{-1}{2}[I_1^\pm I_{2z} - I_{1z} I_2^\pm] \\T_{20} &= \frac{1}{\sqrt{6}}[3I_{1z} I_{2z} - (\vec{I}_1 \cdot \vec{I}_2)] \\T_{2\pm 1} &= \mp \frac{1}{2}[I_1^\pm I_{2z} + I_{1z} I_2^\pm] \\T_{2\pm 2} &= \frac{1}{2}[I_1^\pm \cdot I_2^\pm]\end{aligned}\tag{A.2}$$

In the case of a fictitious two-spin system, i.e. heteronuclear two-spin system or interaction between a spin and magnetic field, the non-secular parts of Eq. (A.2) vanish under high-field approximation and becomes

$$\begin{aligned} T_{00} &= \frac{-1}{\sqrt{3}} I_{1z} I_{2z} \\ T_{10} &= 0 \\ T_{20} &= \frac{2}{\sqrt{6}} I_{1z} I_{2z}. \end{aligned} \quad (\text{A.3})$$

### A.1.2 Definition of Zero- and Double-Quantum Hamiltonian

In a two-spin 1/2 coupled spin system without chemical-shift tensors, it is often convenient to describe the spin system using block diagonalized double- ( $S^\Sigma$ ) and zero- ( $S^\Delta$ ) quantum subspaces. It can be shown that the two subspaces do not interact with each other and they obey commutator relations

$$\begin{aligned} [S_i^\Sigma, S_j^\Sigma] &= i\varepsilon_{ijk} S_k^\Sigma \\ [S_i^\Delta, S_j^\Delta] &= i\varepsilon_{ijk} S_k^\Delta, \end{aligned} \quad (\text{A.4})$$

where  $\varepsilon_{ijk}$  is the Levi-Civita symbol. The zero-quantum Hamiltonians  $I^\Delta$  for a two-spin system are given by

$$\begin{aligned} I_x^\Delta &= \frac{1}{2} [I^+ S^- + I^- S^+] = I_x S_x + I_y S_y \\ I_y^\Delta &= \frac{-i}{2} [I^+ S^- - I^- S^+] = I_y S_x - I_x S_y \\ I_z^\Delta &= \frac{1}{2} [I_z - S_z] \end{aligned} \quad (\text{A.5})$$

whereas the double-quantum Hamiltonians  $I^\Sigma$  are given by

$$\begin{aligned} I_x^\Sigma &= \frac{1}{2} [I^+ S^+ + I^- S^-] = I_x S_x - I_y S_y \\ I_y^\Sigma &= \frac{-i}{2} [I^+ S^+ - I^- S^-] = I_y S_x + I_x S_y \\ I_z^\Sigma &= \frac{1}{2} [I_z + S_z]. \end{aligned} \quad (\text{A.6})$$



### A.1.3 Wigner Rotation Matrix Elements

Table A.1 shows the reduced rank-two Wigner rotation matrix elements  $d_{m',m}^\ell(\beta)$ . Note that the length or magnitude of a tensor is preserved, i.e.  $\sum_{m'=-\ell}^{\ell} d_{m',m}^\ell(\beta) = 1$ .

$m/m'$	+2	+1	0	-1	-2
2	$(\frac{1+\cos\beta}{2})^2$	$-\frac{1+\cos\beta}{2} \sin\beta$	$\sqrt{\frac{3}{8}} \sin^2\beta$	$-\frac{1-\cos\beta}{2} \sin\beta$	$(\frac{1-\cos\beta}{2})^2$
1	$\frac{1+\cos\beta}{2} \sin\beta$	$\cos^2\beta - \frac{1-\cos\beta}{2}$	$-\sqrt{\frac{3}{8}} \sin(2\beta)$	$\frac{1+\cos\beta}{2} - \cos^2\beta$	$-\frac{1-\cos\beta}{2} \sin\beta$
0	$\sqrt{\frac{3}{8}} \sin^2\beta$	$\sqrt{\frac{3}{8}} \sin(2\beta)$	$\frac{3\cos^2\beta-1}{2}$	$-\sqrt{\frac{3}{8}} \sin(2\beta)$	$\sqrt{\frac{3}{8}} \sin^2\beta$
-1	$\frac{1-\cos\beta}{2} \sin\beta$	$\frac{1+\cos\beta}{2} - \cos^2\beta$	$\sqrt{\frac{3}{8}} \sin(2\beta)$	$\cos^2\beta - \frac{1-\cos\beta}{2}$	$-\frac{1+\cos\beta}{2} \sin\beta$
-2	$(\frac{1-\cos\beta}{2})^2$	$\frac{1-\cos\beta}{2} \sin\beta$	$\sqrt{\frac{3}{8}} \sin^2\beta$	$\frac{1+\cos\beta}{2} \sin\beta$	$(\frac{1+\cos\beta}{2})^2$

**Table A.1** Rank  $\ell = 2$  reduced Wigner matrix elements.

## A.2 Determination of Effective Field Direction and Flip Angle using Quaternions

The magnitude and the axis of the effective nutation frequency  $\omega_{\text{eff}}$  can be determined analytically using a quaternion description [100]. The quaternion matrix is comprised of 4 variables, which are the net flip angle and the three components of the unit axis of direction for the pulse  $I_x$ ,  $I_y$  and  $I_z$ . For any basic cyclic element composed of  $N$  pulses, one can characterize the effective nutation angle  $\beta_{\text{eff}}$  and the axis of rotation by performing the following matrix multiplication

$$Q_{\text{eff}} = Q_N Q_{N-1} \cdots Q_2 Q_1, \quad (\text{A.7})$$

where the lower index represents the chronological order of the pulse, i.e.  $Q_1$  represents the first pulse. The matrix representation of the quaternions  $Q_k$  is given as

$$Q_1(I_x, I_y, I_z, \beta_c) = \begin{bmatrix} A \\ B \\ C \\ D \end{bmatrix} \quad (\text{A.8})$$

for the first quaternion, while the subsequent  $k \neq 1$  quaternions are defined as

$$Q_{k \neq 1}(I_x, I_y, I_z, \beta_c) = \begin{bmatrix} D & -C & B & A \\ C & D & -A & B \\ -B & A & D & C \\ -A & -B & -C & D \end{bmatrix} \quad (\text{A.9})$$

where the alphabets  $A$ ,  $B$ ,  $C$  and  $D$  represent

$$A = I_x \sin\left(\frac{\beta}{2}\right), B = I_y \sin\left(\frac{\beta}{2}\right), C = I_z \sin\left(\frac{\beta}{2}\right), D = \cos\left(\frac{\beta}{2}\right) \quad (\text{A.10})$$

where  $\beta$  symbolizes the net flip angle of the particular pulse. For instance, the TPPM [46] sequence which is comprised of two pulses having a phase difference of  $2\phi$  would have the quaternions given by

$$Q_k(\cos \phi, (-1)^{k+1} \sin \phi, 0, \omega_1 \tau_p). \quad (\text{A.11})$$

Now, one can determine the overall net rotation of the entire TPPM cycle ( $N=2$ ) by calculating

$$Q_{\text{eff}} = \begin{bmatrix} I_x^{(\text{eff})} \sin\left(\frac{\beta_{\text{eff}}}{2}\right) \\ I_y^{(\text{eff})} \sin\left(\frac{\beta_{\text{eff}}}{2}\right) \\ I_z^{(\text{eff})} \sin\left(\frac{\beta_{\text{eff}}}{2}\right) \\ \cos\left(\frac{\beta_{\text{eff}}}{2}\right) \end{bmatrix} = Q_2 Q_1, \quad (\text{A.12})$$

which then yields the analytic expression of  $\cos\left(\frac{\beta_{\text{eff}}}{2}\right)$  as

$$\cos\left(\frac{\beta_{\text{eff}}}{2}\right) = \cos^2(\phi) \cos(\beta) + \sin^2(\phi) \quad (\text{A.13})$$

and one obtains the analytical result

$$\beta_{\text{eff}} = 2 \arccos [\cos^2(\phi) \cos(\beta) + \sin^2(\phi)]. \quad (\text{A.14})$$

Following that, the effective nutation frequency  $\omega_{\text{eff}}$  can then be calculated

$$\omega_{\text{eff}} = \frac{\beta_{\text{eff}}}{\tau_m} = \frac{\arccos [\cos^2(\phi) \cos(\beta) + \sin^2(\phi)] \omega_m}{\pi} \quad (\text{A.15})$$

where  $\tau_m = 2\tau_p$  refers to the time period of a basic cycle. Additionally, the effective axis of direction can also be determined by solving the matrix in Eq. (A.12).

### A.3 Spin System Details of Glycine Ethylester

The details of the spin system<sup>1</sup> use for the numerical simulation (Fig. 5.3) is given here.

<b>CSA Tensor</b>	$S_1$ (C $\alpha$ )	$S_2$ (C')	$I_3$ (H $\alpha$ 1)	$I_4$ (H $\alpha$ 2)		
Shift (kHz)	-7.96	7.96	-0.2	-0.2		
anisotropy $\delta_{\text{CSA}}$ (ppm)	25.3	85.0	1.6	1.6		
asymmetry $\eta_{\text{CSA}}$ (ppm)	0.5	0.16	0	0		
Euler angle $\alpha_{\text{CSA}}$ (°)	90	0	0	0		
Euler angle $\beta_{\text{CSA}}$ (°)	30	90	109	109		
Euler angle $\gamma_{\text{CSA}}$ (°)	0	0	-29	-146		
<b>Dipolar / J Coupling</b>	$S_1S_2$	$S_1I_3$	$S_1I_4$	$S_2I_3$	$S_2I_4$	$I_3I_4$
Isotropic $J$ (Hz)	60	150	150	7	7	11
$\delta_{\text{Dipolar}} 2\pi$ (kHz)	-4.3	-46.6	-46.6	-6.1	-6.1	-44.0
Euler angle $\alpha_{\text{Dipolar}}$ (°)	0	0	0	0	0	0
Euler angle $\beta_{\text{Dipolar}}$ (°)	0	108	-29	-29	90	-146
Euler angle $\gamma_{\text{Dipolar}}$ (°)	0	108	-146	-146	90	-177

**Table A.2** Details of spin system in PAS of a four-spin glycine ethylester at 500 MHz.

<sup>1</sup>Note that the value of the CSA of H $\alpha$ , 1.6 ppm is just a rough estimate and the literature is limited due to difficulty in measurement. Nevertheless, the values of the CSA of amide H<sup>N</sup> are typically in the range of 3-15 ppm [154, 155].

### A.3.1 Additional Discussions for TOBSY

#### A.3.2 SC-C9 TOBSY with XiX

For the SC TOBSY during XiX decoupling, it was observed experimentally that both super-cycled and Normal TOBSY have maximum transfers at rf field of  $\sim 120$  kHz (Fig. A.1b). The SC-C9 has a slightly higher transfer ( $\sim 50\%$ ) than the normal sequence ( $\sim 45\%$ ), but it is narrow-banded with respect to the decoupling power. A 1D slice through the rf power at 130 kHz (Fig. A.1d) reveals that the transfer profile is more pronounced, i.e. more sinusoidal (Fig. A.1c). This implies that SC-C9 is a closer resemblance of the actual  $J$  experiment, which has a build-up curve following the  $\sin(\pi J \tau_{\text{mix}})$  relation, rather than dipolar-based experiment that leads to plateau after long mixing time. However, the total magnetization in SC-C9 (black in Fig. A.1d) decays faster than the normal C9 (black in Fig. A.1c). It could be that SC-C9 removed cross-terms that promote dipolar-based spin diffusion, while it reintroduces other destructive cross-terms that leads to faster dephasing of total magnetization.

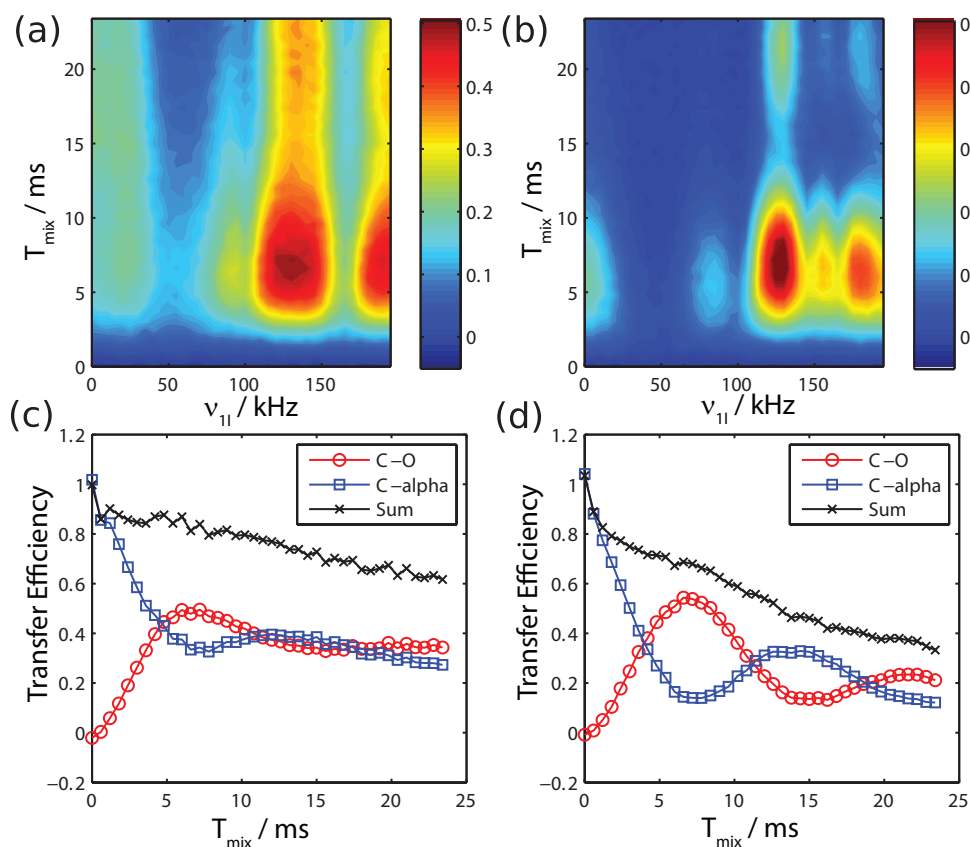


**Figure A.1** Experimental transfer efficiency of (a,c) TOBSY C9<sub>12</sub><sup>1</sup> (b,d) supercycle TOBSY C9<sub>12</sub><sup>1</sup>C9<sub>12</sub><sup>-1</sup> for 1,2-<sup>13</sup>C glycine ethylester at  $\nu_r = 40$  kHz. (c,d) show the 1D slice of (a,b) at proton XiX decoupling power of 130 kHz and  $\nu_m = 60$  kHz.

### A.3.3 Impacts of Crystallites Selection and RF Inhomogeneity

It was discussed in Sec. 3.3.1 that one of the factors that impact the TOBSY transfer efficiency is the rf inhomogeneity. This effect is probed by measuring the rf inhomogeneity using nutation experiments [92] after different CP steps. It is evident that the rf inhomogeneity is a factor of two worse ( $\sim 6\%$ ) in the single HC-CP (Fig. A.2) compare to two-step HN-NC-CP ( $\sim 3\%$ ). This simple analysis indicates that it is important to consider the effect of the preparation steps on the efficiency of a mixing sequence, which can be crucial particularly in multidimensional experiments.

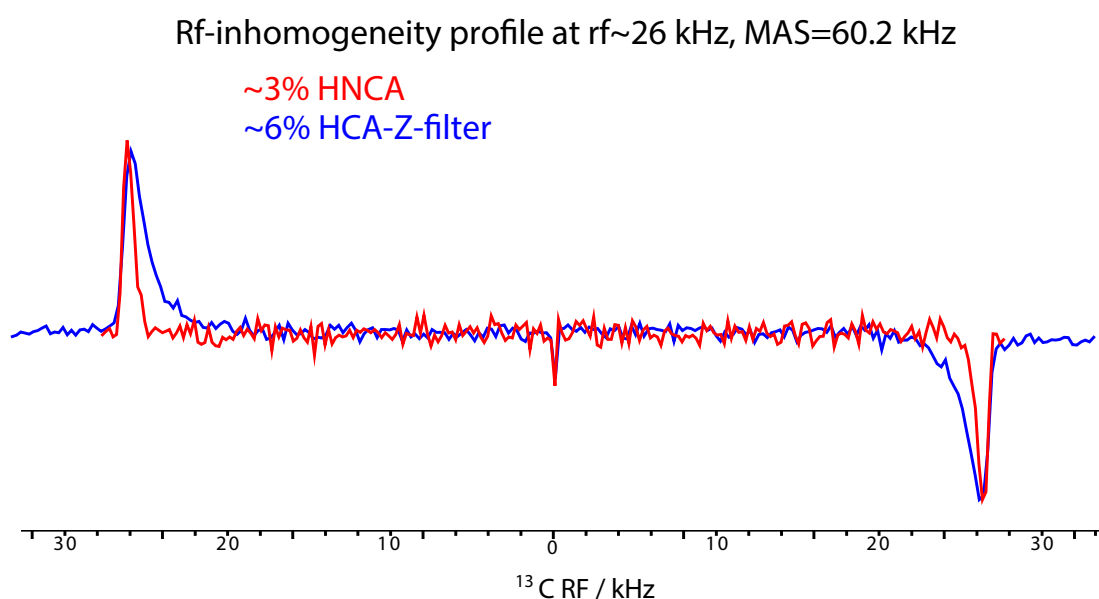


**Figure A.2** RF inhomogeneity of 1.3 mm probe after single HC CP (blue) or HNC two CP steps (red) on glycine at 400 MHz.

Another factor that explains a high transfer in TOBSY is because the crystallite with large CH dipolar coupling are filtered during the NC-CP step. The presence of large CH dipolar coupling reduces the TOBSY transfer significantly, even at MAS frequency of  $\nu_r = 55.5$  kHz. In order to exemplify this effect, the TOBSY transfer (Fig. A.3a) was simulated as a function of Euler angles of different crystallites. Since the dipolar coupling is orientation dependent, each crystallite has different magnitude of CH dipolar coupling (Fig. A.3b), and, therefore, different TOBSY transfer. It is evident that the TOBSY transfer (Fig. A.3c) is efficient when the dipolar coupling is small. The converse is true, the TOBSY transfer is small when the size of the CH dipolar coupling is large.

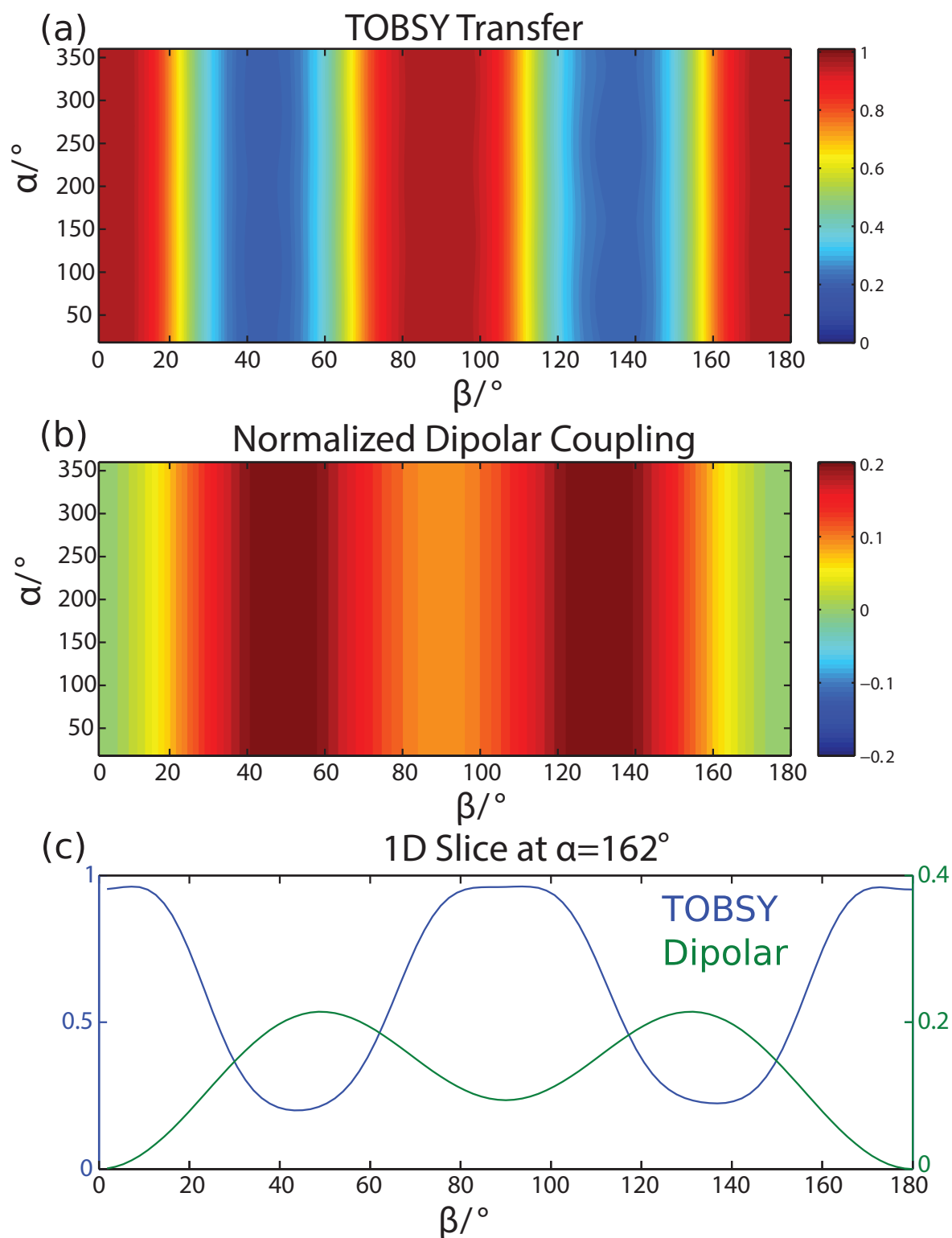


**Figure A.3** Plots of (a) TOBSY transfer efficiency (b) normalized CH dipolar coupling on CH dipolar coupling as functions of Euler angles of crystallites on glycine and  $\nu_r = 55.5$  kHz. A 1D slice across  $\alpha = 162^\circ$  is shown in (c).

# Bibliography

- [1] Anja Böckmann, Adam Lange, Anne Galinier, Sorin Luca, Nicolas Giraud, Michel Juy, Henrike Heise, Roland Montserret, François Penin, and Marc Baldus. Solid state NMR sequential resonance assignments and conformational analysis of the 2×10.4 kDa dimeric form of the *Bacillus subtilis* protein Crh. *Journal of Biomolecular NMR*, 27(4):323–339, 2003.
- [2] Anne Schuetz, Christian Wasmer, Birgit Habenstein, René Verel, Jason Greenwald, Roland Riek, Anja Böckmann, and Beat H. Meier. Protocols for the sequential solid-state NMR spectroscopic assignment of a uniformly labeled 25 kDa protein: HET-s(1-227). *Chembiochem*, 11(11):1543–51, 2010.
- [3] Jutta Pauli, Marc Baldus, B. van Rossum, H. de Groot, and Hartmut Oschkinat. Backbone and side-chain  $^{13}\text{C}$  and  $^{15}\text{N}$  signal assignments of the  $\alpha$ -spectrin SH3 domain by magic angle spinning solid-state NMR at 17.6 Tesla. *Chembiochem*, 2(4):272–81, 2001.
- [4] D. S. Wishart and B. D. Sykes. The  $^{13}\text{C}$  chemical-shift index: a simple method for the identification of protein secondary structure using  $^{13}\text{C}$  chemical-shift data. *Journal of Biomolecular NMR*, 4(2):171–80, 1994.
- [5] Haiyan Zhang, Stephen Neal, and David S. Wishart. RefDB: a database of uniformly referenced protein chemical shifts. *Journal of Biomolecular NMR*, 25(3):173–95, 2003.
- [6] Yang Shen, Frank Delaglio, Gabriel Cornilescu, and Ad Bax. TALOS+: a hybrid method for predicting protein backbone torsion angles from NMR chemical shifts. *Journal of Biomolecular NMR*, 44(4):213–23, 2009.
- [7] Charles D. Schwieters, John J. Kuszewski, Nico Tjandra, and G. Marius Clore. The Xplor-NIH NMR molecular structure determination package. *Journal of Magnetic Resonance*, 160(1):65–73, 2003.

- [8] P. Güntert, C. Mumenthaler, and K. Wüthrich. Torsion angle dynamics for NMR structure calculation with the new program DYANA. *Journal of Molecular Biology*, 273(1):283–98, 1997.
- [9] Hélène Van Melckebeke, Christian Wasmer, Adam Lange, Eiso AB, Antoine Loquet, Anja Böckmann, and Beat H. Meier. Atomic-resolution three-dimensional structure of HET-s(218-289) amyloid fibrils by solid-state NMR spectroscopy. *Journal of the American Chemical Society*, 132(39):13765–75, 2010.
- [10] Anne K Schütz, Toni Vagt, Matthias Huber, Oxana Y. Ovchinnikova, Riccardo Cadalbert, Joseph Wall, Peter Güntert, Anja Böckmann, Rudi Glockshuber, and Beat H. Meier. Atomic-resolution three-dimensional structure of amyloid  $\beta$  fibrils bearing the Osaka mutation. *Angewandte Chemie (International ed. in English)*, 54(1):331–5, 2015.
- [11] Jakob T. Nielsen, Morten Bjerring, Martin D. Jeppesen, Ronnie O. Pedersen, Jan M. Pedersen, Kim L. Hein, Thomas Vosegaard, Troels Skrydstrup, Daniel E. Otzen, and Niels C. Nielsen. Unique identification of supramolecular structures in amyloid fibrils by solid-state NMR spectroscopy. *Angewandte Chemie (International ed. in English)*, 48(12):2118–21, 2009.
- [12] Sang Ho Park, Bibhuti B. Das, Fabio Casagrande, Ye Tian, Henry J Nothnagel, Mignon Chu, Hans Kiefer, Klaus Maier, Anna A. De Angelis, Francesca M. Marassi, and Stanley J. Opella. Structure of the chemokine receptor CXCR1 in phospholipid bilayers. *Nature*, 491(7426):779–83, 2012.
- [13] Matthias Ernst and Beat H. Meier. Chapter 4 Spin diffusion in solids. In *Studies in Physical and Theoretical Chemistry*, volume 84 of *Studies in Physical and Theoretical Chemistry*, pages 83–121. Elsevier, 1998.
- [14] Shanmin Zhang, Beat H. Meier, and R. Ernst. Polarization echoes in NMR. *Physical Review Letters*, 69:2149–2151, 1992.
- [15] Heinz-Peter Breuer and Francesco Petruccione. *The Theory of Open Quantum Systems*. Oxford University Press, 2002.
- [16] Ulrich Haeberlen. *High resolution NMR in solids selective averaging*. Academic, New York, 1976.
- [17] Matthias Ernst and Beat H. Meier. *High-Resolution Solid-State NMR: Principles and Applications*. ETH-Zürich, 2014.



- [18] C. P. Jaroniec, B. A. Tounge, C. M. Rienstra, J. Herzfeld, and R. G. Griffin. Recoupling of heteronuclear dipolar interactions with rotational-echo double-resonance at high magic-angle spinning frequencies. *Journal of Magnetic Resonance*, 146(1):132–9, 2000.
- [19] Albert W. Overhauser. Polarization of nuclei in metals. *Physical Review*, 92(2):411–415, 1953.
- [20] F. Bloch and A. Siegert. Magnetic resonance for nonrotating fields. *Physical Review*, 57(6):522–527, 1940.
- [21] E. R. Andrew, A. Bradbury, and R. G. Eades. Nuclear Magnetic Resonance Spectra from a Crystal rotated at High Speed. *Nature*, 182(4650):1659–1659, 1958.
- [22] I. J. Lowe. Free Induction Decays of Rotating Solids. *Physical Review Letters*, 2(7):285–287, 1959.
- [23] M. Matti Maricq and J. S. Waugh. NMR in rotating solids. *The Journal of Chemical Physics*, 70(7):3300, 1979.
- [24] A. Pines, M. G. Gibby, and J. S. Waugh. Proton-enhanced NMR of dilute spins in solids. *The Journal of Chemical Physics*, 59(2):569, 1973.
- [25] S. Hediger, B.H. Meier, and R.R. Ernst. Adiabatic passage Hartmann-Hahn cross polarization in NMR under magic angle sample spinning. *Chemical Physics Letters*, 240(5-6):449–456, 1995.
- [26] Matthias Ernst and Beat H. Meier. Adiabatic Polarization-Transfer Methods in MAS Spectroscopy. *Encyclopedia of Magnetic Resonance*, 2010.
- [27] M. Garwood and L. DelaBarre. The return of the frequency sweep: designing adiabatic pulses for contemporary NMR. *Journal of Magnetic Resonance*, 153(2):155–77, 2001.
- [28] Dieter Suter, Gerard C. Chingas, Robert A. Harris, and Alexander Pines. Berry's phase in magnetic resonance. *Molecular Physics*, 61(6):1327–1340, 1987.
- [29] D. Suter, K. T. Mueller, and A. Pines. Study of the Aharonov-Anandan quantum phase by NMR interferometry. *Physical Review Letters*, 60(13):1218–1220, 1988.
- [30] U. Haeberlen and J. Waugh. Coherent Averaging Effects in Magnetic Resonance. *Physical Review*, 175(2):453–467, 1968.

- [31] M. Matti Maricq. Application of average Hamiltonian theory to the NMR of solids. *Physical Review B*, 25(11):6622–6632, 1982.
- [32] Ingo Scholz, Beat H. Meier, and Matthias Ernst. Operator-based triple-mode Floquet theory in solid-state NMR. *The Journal of Chemical Physics*, 127(20):204504, 2007.
- [33] Ingo Scholz, Jacco D. van Beek, and Matthias Ernst. Operator-based Floquet theory in solid-state NMR. *Solid State Nuclear Magnetic Resonance*, 37(3-4):39–59, 2010.
- [34] Michal Leskes, P. K. Madhu, and Shimon Vega. Floquet theory in solid-state nuclear magnetic resonance. *Progress in Nuclear Magnetic Resonance Spectroscopy*, 57(4):345–80, 2010.
- [35] Elena Vinogradov, P. K. Madhu, and Shimon Vega. Strategies for high-resolution proton spectroscopy in solid-state NMR. *Topics in Current Chemistry*, 246:33–90, 2005.
- [36] Matthias Ernst. Time-Dependent Hamiltonians: AHT and Floquet Theory. In *Third US-Canada Winterschool on Biomolecular NMR*, Stowe, 2013.
- [37] F. Dyson. The radiation theories of Tomonaga, Schwinger, and Feynman. *Physical Review*, 75(3):486–502, 1949.
- [38] Herbert Goldstein, Charles P. Poole, and John L. Safko. *Classical Mechanics*. Addison-Wesley, 2002.
- [39] Paul Schanda, Beat H. Meier, and Matthias Ernst. Accurate measurement of one-bond H-X heteronuclear dipolar couplings in MAS solid-state NMR. *Journal of Magnetic Resonance*, 210(2):246–259, 2011.
- [40] Jon H. Shirley. Solution of the Schrödinger Equation with a Hamiltonian Periodic in Time. *Physical Review*, 138(4B):B979–B987, 1965.
- [41] J. H. Van Vleck. The Dipolar Broadening of Magnetic Resonance Lines in Crystals. *Physical Review*, 74(9):1168–1183, 1948.
- [42] M. Goldman, P. J. Grandinetti, A. Llor, Z. Olejniczak, J. R. Sachleben, and J. W. Zwanziger. Theoretical aspects of higher-order truncations in solid-state nuclear magnetic resonance. *The Journal of Chemical Physics*, 97(12):8947, 1992.

- [43] A. Llor. Equivalence between dynamical averaging methods of the Schrödinger equation: average Hamiltonian, secular averaging, and Van Vleck transformation. *Chemical Physics Letters*, 199(3-4):383–390, 1992.
- [44] K. Takegoshi, Norihiro Miyazawa, Kshama Sharma, and P. K. Madhu. Comparison among Magnus/Floquet/Fer expansion schemes in solid-state NMR. *The Journal of Chemical Physics*, 142(13):134201, 2015.
- [45] Vipin Agarwal, Tiit Tuherm, Andres Reinhold, Jaan Past, Ago Samoson, Matthias Ernst, and Beat H. Meier. Amplitude-modulated low-power decoupling sequences for fast magic-angle spinning NMR. *Chemical Physics Letters*, 583:1–7, 2013.
- [46] Ingo Scholz, Paul Hodgkinson, Beat H. Meier, and Matthias Ernst. Understanding two-pulse phase-modulated decoupling in solid-state NMR. *The Journal of Chemical Physics*, 130(11):114510, 2009.
- [47] Moses Lee and Walter I. Goldburg. Nuclear-Magnetic-Resonance Line Narrowing by a Rotating rf Field. *Physical Review*, 140(4A):A1261–A1271, 1965.
- [48] Elena Vinogradov, P. K. Madhu, and Shimon Vega. Phase modulated Lee–Goldburg magic angle spinning proton nuclear magnetic resonance experiments in the solid state: A bimodal Floquet theoretical treatment. *The Journal of Chemical Physics*, 115(19):8983, 2001.
- [49] Malcolm H. Levitt. Symmetry-Based Pulse Sequences in Magic-Angle Spinning Solid-State NMR. *Encyclopedia of Nuclear Magnetic Resonance*, 9:165–196, 2007.
- [50] Matthias Ernst, Helen Geen, and Beat H. Meier. Amplitude-modulated decoupling in rotating solids: a bimodal Floquet approach. *Solid State Nuclear Magnetic Resonance*, 29(1-3):2–21, 2006.
- [51] Kong Ooi Tan, Anders B. Nielsen, Beat H. Meier, and Matthias Ernst. Broad-Band DREAM Recoupling Sequence. *J. Phys. Chem. Lett.*, 5:3366–3372, 2014.
- [52] Andrew E. Bennett, Chad M. Rienstra, Michèle Auger, K. V. Lakshmi, and Robert G. Griffin. Heteronuclear decoupling in rotating solids. *The Journal of Chemical Physics*, 103(16):6951, 1995.
- [53] M. Baldus and B.H. Meier. Total Correlation Spectroscopy in the Solid State. The Use of Scalar Couplings to Determine the Through-Bond Connectivity. *Journal of Magnetic Resonance, Series A*, 121(1):65–69, 1996.

- [54] Edme H. Hardy, R. Verel, and Beat H. Meier. Fast MAS total through-bond correlation spectroscopy. *Journal of Magnetic Resonance*, 148(2):459–64, 2001.
- [55] Edme H. Hardy, Andreas Detken, and Beat H. Meier. Fast-MAS total through-bond correlation spectroscopy using adiabatic pulses. *Journal of Magnetic Resonance*, 165(2):208–218, 2003.
- [56] Andreas Grommek, Beat H. Meier, and Matthias Ernst. Distance information from proton-driven spin diffusion under MAS. *Chemical Physics Letters*, 427(4-6):404–409, 2006.
- [57] L. Braunschweiler and R.R. Ernst. Coherence transfer by isotropic mixing: Application to proton correlation spectroscopy. *Journal of Magnetic Resonance (1969)*, 53(3):521–528, 1983.
- [58] John Cavanagh, Wayne J. Fairbrother, Arthur G. Palmer, Mark Rance, and Nicholas J. Skelton. *Protein NMR Spectroscopy*. Elsevier, 2007.
- [59] Y.K. Lee, Narayanan D. Kurur, M Helmle, O.G. Johannessen, Niels Chr. Nielsen, and M.H. Levitt. Efficient dipolar recoupling in the NMR of rotating solids. A sevenfold symmetric radiofrequency pulse sequence. *Chemical Physics Letters*, 242(3):304–309, 1995.
- [60] Marina Carravetta, Mattias Edén, Xin Zhao, Andreas Brinkmann, and Malcolm H. Levitt. Symmetry principles for the design of radiofrequency pulse sequences in the nuclear magnetic resonance of rotating solids. *Chemical Physics Letters*, 321(3-4):205–215, 2000.
- [61] M. Hohwy, H. J. Jakobsen, M. Edén, M. H. Levitt, and N. C. Nielsen. Broadband dipolar recoupling in the nuclear magnetic resonance of rotating solids: A compensated C7 pulse sequence. *The Journal of Chemical Physics*, 108(7):2686, 1998.
- [62] Giulia Mollica, P. K. Madhu, Fabio Ziarelli, André Thévand, Pierre Thureau, and Stéphane Viel. Towards measurement of homonuclear dipolar couplings in  $^1\text{H}$  solid-state NMR: recoupling with a rotor-synchronized decoupling scheme. *Physical Chemistry Chemical Physics : PCCP*, 14(13):4359–64, 2012.
- [63] P.K. Madhu, Xin Zhao, and Malcolm H Levitt. High-resolution  $^1\text{H}$  NMR in the solid state using symmetry-based pulse sequences. *Chemical Physics Letters*, 346(1-2):142–148, 2001.

- [64] Kong Ooi Tan, Ingo Scholz, Jacco D. van Beek, Beat H. Meier, and Matthias Ernst. Improved decoupling during symmetry-based C9-TOBSY sequences. *Journal of Magnetic Resonance*, 239:61–8, 2014.
- [65] Andreas Brinkmann and Malcolm H. Levitt. Symmetry principles in the nuclear magnetic resonance of spinning solids: Heteronuclear recoupling by generalized Hartmann–Hahn sequences. *The Journal of Chemical Physics*, 115(1):357, 2001.
- [66] Xin Zhao, Wilfried Hoffbauer, Jörn Schmedt auf der Günne, and M. H. Levitt. Heteronuclear polarization transfer by symmetry-based recoupling sequences in solid-state NMR. *Solid State Nuclear Magnetic Resonance*, 26(2):57–64, 2004.
- [67] Mattias Edén and Malcolm H. Levitt. Pulse sequence symmetries in the nuclear magnetic resonance of spinning solids: Application to heteronuclear decoupling. *The Journal of Chemical Physics*, 111(4):1511, 1999.
- [68] M. Mehring. *Principles of high resolution NMR in solids*. Springer, Berlin, 1983.
- [69] Jerry C.C Chan and Gunther Brunklaus. R sequences for the scalar-coupling mediated homonuclear correlation spectroscopy under fast magic-angle spinning. *Chemical Physics Letters*, 349(1-2):104–112, 2001.
- [70] Jörg Leppert, Oliver Ohlenschläger, Matthias Görlach, and Ramadurai Ramachandran. Adiabatic TOBSY in rotating solids. *Journal of Biomolecular NMR*, 29(2):167–73, 2004.
- [71] Ovidiu C. Andronesi, Dionyssios Mintzopoulos, Jochem Struppe, Peter M. Black, and A. Aria Tzika. Solid-state NMR adiabatic TOBSY sequences provide enhanced sensitivity for multidimensional high-resolution magic-angle-spinning <sup>1</sup>H MR spectroscopy. *Journal of Magnetic Resonance*, 193(2):251–8, 2008.
- [72] Ildelfonso Marin-Montesinos, Darren H. Brouwer, Giancarlo Antonioli, Wai Cheu Lai, Andreas Brinkmann, and Malcolm H. Levitt. Heteronuclear decoupling interference during symmetry-based homonuclear recoupling in solid-state NMR. *Journal of Magnetic Resonance*, 177(2):307–17, 2005.
- [73] Colan E. Hughes, Sorin Luca, and Marc Baldus. Radio-frequency driven polarization transfer without heteronuclear decoupling in rotating solids. *Chemical Physics Letters*, 385(5-6):435–440, 2004.

- [74] Yoshitaka Ishii, Jun Ashida, and Takehiko Terao.  $^{13}\text{C}$ - $^1\text{H}$  dipolar recoupling dynamics in  $^{13}\text{C}$  multiple-pulse solid-state NMR. *Chemical Physics Letters*, 246(4-5):439–445, 1995.
- [75] B.-Q. Sun, C. M. Rienstra, P. R. Costa, J. R. Williamson, and R. G. Griffin. 3D  $^{15}\text{N}$ - $^{13}\text{C}$ - $^{13}\text{C}$  chemical shift correlation spectroscopy in rotating solids. *Journal of the American Chemical Society*, 119(36):8540–8546, 1997.
- [76] M. Hohwy, C. M. Rienstra, C. P. Jaroniec, and R. G. Griffin. Fivefold symmetric homonuclear dipolar recoupling in rotating solids: Application to double quantum spectroscopy. *The Journal of Chemical Physics*, 110(16):7983, 1999.
- [77] Christopher P. Jaroniec, Brett A. Tounge, Judith Herzfeld, and Robert G. Griffin. Frequency Selective Heteronuclear Dipolar Recoupling in Rotating Solids: Accurate  $^{13}\text{C}$ - $^{15}\text{N}$  Distance Measurements in Uniformly  $^{13}\text{C}$ ,  $^{15}\text{N}$ -labeled Peptides. *Journal of the American Chemical Society*, 123(15):3507–3519, 2001.
- [78] Marvin J. Bayro, Ramesh Ramachandran, Marc A. Caporini, Matthew T. Eddy, and Robert G. Griffin. Radio frequency-driven recoupling at high magic-angle spinning frequencies: Homonuclear recoupling sans heteronuclear decoupling. *The Journal of Chemical Physics*, 128(5):052321, 2008.
- [79] Andreas Detken, Edme H. Hardy, Matthias Ernst, and Beat H. Meier. Simple and efficient decoupling in magic-angle spinning solid-state NMR: the XiX scheme. *Chemical Physics Letters*, 356(3-4):298–304, 2002.
- [80] S.A. Smith, T.O. Levante, B.H. Meier, and R. R. Ernst. Computer simulations in magnetic resonance. An object-oriented programming approach. *Journal of Magnetic Resonance, Series A*, 106(1):75–105, 1994.
- [81] A. Samoson, T. Tuherm, and J. Past. Ramped-speed cross polarization MAS NMR. *Journal of Magnetic Resonance*, 149(2):264–7, 2001.
- [82] A. Brinkmann, M. Edén, and Malcolm H. Levitt. Synchronous helical pulse sequences in magic-angle spinning nuclear magnetic resonance: Double quantum recoupling of multiple-spin systems. *J Chem Phys*, 112(19):8539–8554, 2000.
- [83] Per Eugen Kristiansen, Marina Carravetta, Jacco D. Van Beek, Wai Cheu Lai, and Malcolm H. Levitt. Theory and applications of supercycled symmetry-based recoupling sequences in solid-state nuclear magnetic resonance. *The Journal of Chemical Physics*, 124(23):234510, 2006.

- [84] Malcolm H. Levitt. Symmetry in the design of NMR multiple-pulse sequences. *The Journal of Chemical Physics*, 128(5):052205, 2008.
- [85] Gaël De Paëpe, Józef R. Lewandowski, Antoine Loquet, Anja Böckmann, and Robert G. Griffin. Proton assisted recoupling and protein structure determination. *The Journal of Chemical Physics*, 129(24):245101, 2008.
- [86] Ingo Scholz, Beat H. Meier, and Matthias Ernst. NMR polarization transfer by second-order resonant recoupling: RESORT. *Chemical Physics Letters*, 485(4-6):335–342, 2010.
- [87] Anja Böckmann, Matthias Ernst, and Beat H. Meier. Spinning proteins, the faster, the better? *Journal of Magnetic Resonance*, 253:71–9, 2015.
- [88] Vipin Agarwal, Susanne Penzel, Kathrin Szekely, Riccardo Cadalbert, Emilie Testori, Andres Oss, Jaan Past, Ago Samoson, Matthias Ernst, Anja Böckmann, and Beat H. Meier. De Novo 3D Structure Determination from Sub-milligram Protein Samples by Solid-State 100 kHz MAS NMR Spectroscopy. *Angewandte Chemie (International ed. in English)*, 53(45):12253–6, 2014.
- [89] Susanne Penzel, Albert A. Smith, Vipin Agarwal, Andreas Hunkeler, Mai-Liis Org, Ago Samoson, Anja Böckmann, Matthias Ernst, and Beat H. Meier. Protein resonance assignment at MAS frequencies approaching 100 kHz: a quantitative comparison of  $J$ -coupling and dipolar-coupling-based transfer methods. *Journal of Biomolecular NMR*, 2015.
- [90] Yusuke Nishiyama, Michal Malon, Yuji Ishii, and Ayyalusamy Ramamoorthy. 3D  $^{15}\text{N}/^{15}\text{N}/^1\text{H}$  chemical shift correlation experiment utilizing an RFDR-based  $^1\text{H}/^1\text{H}$  mixing period at 100 kHz MAS. *Journal of Magnetic Resonance*, 244:1–5, 2014.
- [91] Adam Lange, Ingo Scholz, Theofanis Manolikas, Matthias Ernst, and Beat H. Meier. Low-power cross polarization in fast magic-angle spinning NMR experiments. *Chemical Physics Letters*, 468(1-3):100–105, 2009.
- [92] Rupal Gupta, Guangjin Hou, Tatyana Polenova, and Alexander J. Vega. RF inhomogeneity and how it controls CPMAS. *Solid State Nuclear Magnetic Resonance*, 72:17–26, 2015.
- [93] Matthias Bechmann, John Clark, and Angelika Sebald. Genetic algorithms and solid state NMR pulse sequences. *Journal of Magnetic Resonance*, 228:66–75, 2013.

- [94] Mattias Edén and Andreas Brinkmann. Triple-quantum dynamics in multiple-spin systems undergoing magic-angle spinning: application to  $^{13}\text{C}$  homonuclear correlation spectroscopy. *Journal of Magnetic Resonance*, 173(2):259–79, 2005.
- [95] Andreas Brinkmann and Mattias Edén. Second order average Hamiltonian theory of symmetry-based pulse schemes in the nuclear magnetic resonance of rotating solids: application to triple-quantum dipolar recoupling. *The Journal of Chemical Physics*, 120(24):11726–45, 2004.
- [96] M. Hohwy and N. C. Nielsen. Systematic design and evaluation of multiple-pulse experiments in nuclear magnetic resonance spectroscopy using a semi-continuous Baker–Campbell–Hausdorff expansion. *The Journal of Chemical Physics*, 109(10):3780, 1998.
- [97] S. Dusold, H. Maisel, and A. Sebald. Magnitudes and orientations of interaction tensors determined from rotational resonance MAS NMR lineshapes of a four- $(^{13}\text{C})$ -spin system. *Journal of Magnetic Resonance*, 141(1):78–90, 1999.
- [98] A. Wokaun and R. R. Ernst. Selective excitation and detection in multilevel spin systems: Application of single transition operators. *The Journal of Chemical Physics*, 67(4):1752, 1977.
- [99] Johannes J. Wittmann, Valerie Mertens, Kazuyuki Takeda, Beat H. Meier, and Matthias Ernst. Quantification and compensation of the influence of pulse transients on symmetry-based recoupling sequences. *Journal of Magnetic Resonance*, 263:7–18, 2016.
- [100] B Blümich and H.W. Spiess. Quaternions as a practical tool for the evaluation of composite rotations. *Journal of Magnetic Resonance*, 61(2):356–362, 1985.
- [101] Robert D. Nielsen and Bruce H. Robinson. The spherical tensor formalism applied to relaxation in magnetic resonance. *Concepts in Magnetic Resonance Part A*, 28A(4):270–290, 2006.
- [102] Mattias Edén. Order-selective multiple-quantum excitation in magic-angle spinning NMR: creating triple-quantum coherences with a trilinear Hamiltonian. *Chemical Physics Letters*, 366(5-6):469–476, 2002.
- [103] M.E. Smith. Recent advances in experimental solid state NMR methodology for half-integer spin quadrupolar nuclei. *Progress in Nuclear Magnetic Resonance Spectroscopy*, 34(2):159–201, 1999.



- [104] Vera B. Cheng, Henry H. Suzukawa Jr., and Max Wolfsberg. Investigations of a non-random numerical method for multidimensional integration. *The Journal of Chemical Physics*, 59(8):3992, 1973.
- [105] René Verel, Marc Baldus, Matthias Ernst, and Beat H. Meier. A homonuclear spin-pair filter for solid-state NMR based on adiabatic-passage techniques. *Chemical Physics Letters*, 287(3-4):421–428, 1998.
- [106] R. Verel, M Ernst, and B H. Meier. Adiabatic dipolar recoupling in solid-state NMR: the DREAM scheme. *Journal of Magnetic Resonance*, 150(1):81–99, 2001.
- [107] N. C. Nielsen, H. Bildsøe, H. J. Jakobsen, and M. H. Levitt. Double-quantum homonuclear rotary resonance: Efficient dipolar recovery in magic-angle spinning nuclear magnetic resonance. *The Journal of Chemical Physics*, 101(3):1805, 1994.
- [108] Stephan Dusold and Angelika Sebald. Dipolar recoupling under magic-angle spinning conditions. *Annual Reports on NMR Spectroscopy*, 41:185–264, 2000.
- [109] Niels Chr Nielsen, Lasse A. Strassø, and Anders B. Nielsen. Dipolar recoupling. *Topics in Current Chemistry*, 306(April 2011):1–45, 2012.
- [110] Vladimir Ladizhansky. Homonuclear dipolar recoupling techniques for structure determination in uniformly  $^{13}\text{C}$ -labeled proteins. *Solid State Nuclear Magnetic Resonance*, 36(3):119–28, 2009.
- [111] R. G. Griffin. Dipolar recoupling in MAS spectra of biological solids. *Nature Structural Biology*, 5 Suppl:508–12, 1998.
- [112] Christiane Ritter, Marie-Lise Maddelein, Ansgar B. Siemer, Thorsten Lührs, Matthias Ernst, Beat H. Meier, Sven J. Saupe, and Roland Riek. Correlation of structural elements and infectivity of the HET-s prion. *Nature*, 435(7043):844–8, 2005.
- [113] Julia Gath, Birgit Habenstein, Luc Bousset, Ronald Melki, Beat H. Meier, and Anja Böckmann. Solid-state NMR sequential assignments of  $\alpha$ -synuclein. *Biomolecular NMR Assignments*, 6(1):51–5, 2012.
- [114] Birgit Habenstein, Christian Wasmer, Luc Bousset, Yannick Sourigues, Anne Schütz, Antoine Loquet, Beat H. Meier, Ronald Melki, and Anja Böckmann. Extensive de novo solid-state NMR assignments of the 33 kDa C-terminal domain of the Ure2 prion. *Journal of Biomolecular NMR*, 51(3):235–43, 2011.

- [115] Thomas Westfeld, René Verel, Matthias Ernst, Anja Böckmann, and Beat H. Meier. Properties of the DREAM scheme and its optimization for application to proteins. *Journal of Biomolecular NMR*, 53(2):103–12, 2012.
- [116] Vipin Agarwal, Mariana Sardo, Ingo Scholz, Anja Böckmann, Matthias Ernst, and Beat H. Meier. PAIN with and without PAR: variants for third-spin assisted heteronuclear polarization transfer. *Journal of Biomolecular NMR*, 56(4):365–77, 2013.
- [117] J. Lin, M. J. Bayro, R. G. Griffin, and N. Khaneja. Dipolar recoupling in solid state NMR by phase alternating pulse sequences. *Journal of Magnetic Resonance*, 197(2):145–52, 2009.
- [118] Sheetal Jain, Morten Bjerring, and Niels Chr. Nielsen. Efficient and Robust Heteronuclear Cross-Polarization for High-Speed-Spinning Biological Solid-State NMR Spectroscopy. *The Journal of Physical Chemistry Letters*, 3(6):703–708, 2012.
- [119] Charles P. Slichter. *Principles of Magnetic Resonance*, volume 1 of *Springer Series in Solid-State Sciences*. Springer Berlin Heidelberg, Berlin, Heidelberg, 1990.
- [120] T. G. Oas, R. G. Griffin, and M. H. Levitt. Rotary resonance recoupling of dipolar interactions in solid-state nuclear magnetic resonance spectroscopy. *The Journal of Chemical Physics*, 89(2):692, 1988.
- [121] K. Takegoshi, K. Nomura, and T. Terao. Selective homonuclear polarization transfer in the tilted rotating frame under magic angle spinning in solids. *Journal of Magnetic Resonance*, 127(2):206–16, 1997.
- [122] Phillip R. Costa, Boqin Sun, and Robert G. Griffin. Rotational resonance NMR: separation of dipolar coupling and zero quantum relaxation. *Journal of Magnetic Resonance*, 164(1):92–103, 2003.
- [123] Anne K Schütz, Birgit Habenstein, Nina Luckgei, Luc Bousset, Yannick Sourigues, Anders B. Nielsen, Ronald Melki, Anja Böckmann, and Beat H. Meier. Solid-state NMR sequential assignments of the amyloid core of full-length Sup35p. *Biomolecular NMR Assignments*, 2013.
- [124] Venus Singh Mithu and Perunthiruthy K. Madhu. Exploring connections between phase-modulated heteronuclear dipolar decoupling schemes in solid-state NMR. *Chemical Physics Letters*, 556:325–329, 2013.

- [125] B. M. Fung, A. K. Khitrin, and K. Ermolaev. An improved broadband decoupling sequence for liquid crystals and solids. *Journal of Magnetic Resonance*, 142(1):97–101, 2000.
- [126] Rajendra Singh Thakur, Narayanan D. Kurur, and P.K. Madhu. Swept-frequency two-pulse phase modulation for heteronuclear dipolar decoupling in solid-state NMR. *Chemical Physics Letters*, 426(4-6):459–463, 2006.
- [127] P. K. Madhu. Heteronuclear Spin Decoupling in Solid-State Nuclear Magnetic Resonance: Overview and Outlook. *Israel Journal of Chemistry*, 54(1-2):25–38, 2014.
- [128] Paul Hodgkinson. Heteronuclear decoupling in the NMR of solids. *Progress in Nuclear Magnetic Resonance Spectroscopy*, 46(4):197–222, 2005.
- [129] Matthias Ernst. Heteronuclear spin decoupling in solid-state NMR under magic-angle sample spinning. *Journal of Magnetic Resonance*, 162:1–34, 2003.
- [130] Venus Singh Mithu, Subhradip Paul, Narayanan D. Kurur, and P. K. Madhu. Heteronuclear dipolar decoupling in solid-state nuclear magnetic resonance under ultra-high magic-angle spinning. *Journal of Magnetic Resonance*, 209(2):359–63, 2011.
- [131] D.L. Vanderhart, William L. Earl, and A.N. Garroway. Resolution in  $^{13}\text{C}$  NMR of organic solids using high-power proton decoupling and magic-angle sample spinning. *Journal of Magnetic Resonance*, 44(2):361–401, 1981.
- [132] Rajendra Singh Thakur, Narayanan D. Kurur, and P. K. Madhu. An analysis of phase-modulated heteronuclear dipolar decoupling sequences in solid-state nuclear magnetic resonance. *Journal of Magnetic Resonance*, 193(1):77–88, 2008.
- [133] Asif Equbal, Subhradip Paul, Venus Singh Mithu, P.K. Madhu, and Niels Chr. Nielsen. Efficient heteronuclear decoupling in MAS solid-state NMR using non-rotor-synchronized rCW irradiation. *Journal of Magnetic Resonance*, 246:104–109, 2014.
- [134] Michal Leskes, Rajendra Singh Thakur, P. K. Madhu, Narayanan D. Kurur, and Shimon Vega. Bimodal Floquet description of heteronuclear dipolar decoupling in solid-state nuclear magnetic resonance. *The Journal of Chemical Physics*, 127(2):024501, 2007.
- [135] Markus Weingarth, Piotr Tekely, and Geoffrey Bodenhausen. Efficient heteronuclear decoupling by quenching rotary resonance in solid-state NMR. *Chemical Physics Letters*, 466(4-6):247–251, 2008.

- [136] Matthias Ernst, Ago Samoson, and Beat H. Meier. Low-power XiX decoupling in MAS NMR experiments. *Journal of Magnetic Resonance*, 163(2):332–339, 2003.
- [137] Mrignayani Kotecha, Nalinda P. Wickramasinghe, and Yoshitaka Ishii. Efficient low-power heteronuclear decoupling in  $^{13}\text{C}$  high-resolution solid-state NMR under fast magic angle spinning. *Magnetic Resonance in Chemistry*, 45(S1):S221–S230, 2007.
- [138] Markus Weingarth, Geoffrey Bodenhausen, and Piotr Tekely. Low-power decoupling at high spinning frequencies in high static fields. *Journal of Magnetic Resonance*, 199(2):238–41, 2009.
- [139] Markus Weingarth, Julien Trébosc, Jean-Paul Amoureux, Geoffrey Bodenhausen, and Piotr Tekely. Efficiency at high spinning frequencies of heteronuclear decoupling methods designed to quench rotary resonance. *Solid State Nuclear Magnetic Resonance*, 40(1):21–6, 2011.
- [140] Yusuke Nishiyama, Yuki Endo, Takahiro Nemoto, Hiroaki Utsumi, Kazuo Yamauchi, Katsuya Hioka, and Tetsuo Asakura. Very fast magic angle spinning ( $^1\text{H}$ - $^{14}\text{N}$ ) 2D solid-state NMR: sub-micro-liter sample data collection in a few minutes. *Journal of Magnetic Resonance*, 208(1):44–8, 2011.
- [141] Dirk Wilhelm, Armin Pürea, and Frank Engelke. Fluid flow dynamics in MAS systems. *Journal of Magnetic Resonance*, 257:51–63, 2015.
- [142] Ago Samoson, Tiit Tuhem, Jean Past, Andres Reinhold, Tiit Anupõld, and Ivo Heinmaa. New horizons for magic-angle spinning NMR. *Topics in Current Chemistry*, 246(2004):15–31, 2005.
- [143] Rudra N. Purusottam, Geoffrey Bodenhausen, and Piotr Tekely. Sensitivity improvement during heteronuclear spin decoupling in solid-state nuclear magnetic resonance experiments at high spinning frequencies and moderate radio-frequency amplitudes. *Chemical Physics Letters*, 614:220–225, 2014.
- [144] Ingo Scholz. *Operator-based floquet theory and its applications to solid-state NMR*. PhD thesis, 2010.
- [145] Kong Ooi Tan, M. Rajeswari, P. K. Madhu, and Matthias Ernst. Asynchronous symmetry-based sequences for homonuclear dipolar recoupling in solid-state nuclear magnetic resonance. *The Journal of Chemical Physics*, 142(6):065101, 2015.

- [146] Kazuyuki Takeda, Asato Wakisaka, and K. Takegoshi. Proton decoupling and recoupling under double-nutation irradiation in solid-state NMR. *The Journal of Chemical Physics*, 141(22):224202, 2014.
- [147] Boqin Sun, Jay H. Baltisberger, Y. Wu, Ago Samoson, and Alexander Pines. Sidebands in dynamic angle spinning (DAS) and double rotation (DOR) NMR. *Solid State Nuclear Magnetic Resonance*, 1(5):267–95, 1992.
- [148] G. Sinning, M. Mehring, and A. Pines. Dynamics of spin decoupling in carbon-13—proton NMR. *Chemical Physics Letters*, 43(2):382–386, 1976.
- [149] M. Mehring and G. Sinning. Dynamics of heteronuclear spin coupling and decoupling in solids. *Physical Review B*, 15(5):2519–2532, 1977.
- [150] Ilya Frantsuzov, Matthias Ernst, Steven P. Brown, and Paul Hodgkinson. Simulating spin dynamics in organic solids under heteronuclear decoupling. *Solid State Nuclear Magnetic Resonance*, 70:28–37, 2015.
- [151] A. E. Bennett, R. G. Griffin, and S. Vega. Recoupling of homo- and heteronuclear dipolar interactions in rotating solids. *Solid-State NMR IV Methods and Applications of Solid-State NMR*, 1994.
- [152] S. J. Glaser, T. Schulte-Herbrüggen, M. Sieveking, O. Schedletzky, N. C. Nielsen, O. W. Sørensen, and C. Griesinger. Unitary control in quantum ensembles: maximizing signal intensity in coherent spectroscopy. *Science (New York, N.Y.)*, 280(5362):421–4, 1998.
- [153] Navin Khaneja, Timo Reiss, Cindie Kehlet, Thomas Schulte-Herbrüggen, and Steffen J. Glaser. Optimal control of coupled spin dynamics: design of NMR pulse sequences by gradient ascent algorithms. *Journal of Magnetic Resonance*, 172(2):296–305, 2005.
- [154] K Pervushin, R Riek, G Wider, and K Wüthrich. Attenuated  $T_2$  relaxation by mutual cancellation of dipole-dipole coupling and chemical shift anisotropy indicates an avenue to NMR structures of very large biological macromolecules in solution. *Proceedings of the National Academy of Sciences of the United States of America*, 94(23):12366–71, 1997.
- [155] Gabriel Cornilescu and Ad Bax. Measurement of Proton, Nitrogen, and Carbonyl Chemical Shielding Anisotropies in a Protein Dissolved in a Dilute Liquid Crystalline Phase. *Journal of the American Chemical Society*, 122(41):10143–10154, 2000.



## Acknowledgements

First of all, I would like to thank my PhD supervisor Prof. Dr. Matthias Ernst for giving me an opportunity to work with him, even though I knew nothing about NMR (not even chemical-shift) when I came for an interview in ETH. Nevertheless, I am glad that I have learnt NMR theory from Matthias, who understands and treats theory like a theoretical physicist. I also appreciate the amount of freedom he has given me in roaming around ideas and gedanken experiments, while pulling me back to reality whenever it is necessary. The next person I would like to thank is Prof. Dr. Beat Meier, for letting me to join his group. I have learnt from him the importance of applying theoretical knowledge in useful applications. Other than that, he is an excellent teacher in conveying ideas and presenting scientific works. Apart from my supervisors, I would like to thank my collaborator, Prof. P. K. Madhu from TIFR, India. It was my pleasure to work with him in the past few years. He believes that all knowledge should be shared and there should be no secret in science. It was his attitude towards science that continues to inspire me to stay in this field. I would also like to thank my parents for giving me their full support even though they know little about what I do for living, and perhaps where I am living. I would not be where I am today if they had not funded my undergraduate study in Physics, which is obscure to the major society in Malaysia.

Life in ETH would be boring without the wonderful colleagues in the group. The colleagues are not just colleagues, they are more like close friends or buddies to me. I am indebted to Anders B. Nielsen for his generous time in teaching me basic NMR, also the collaborations on projects and teaching duties. I will also thank Vipin Agarwal for giving me the discussions in Floquet theory and collaborating projects; Francesco Ravotti for teaching me practical italians (especially counting number up to numero cinque) and showing me what kind of wine should be avoided ( if you could not afford French wine); Thomas Bauer and Johannes Wittmann for showing me what it takes to be a Bavarian, *Servus !*; Ivan Tomka for discussions in finance and fitness; Matthias Huber for waiting for me during ski; Julia Gath for teaching me chemistry/biology and generous dinner invitations; Andy Smith for enlightening me about DNP ; Susanne Penzel for wishing me merry christmas during summer time; Emilie for singing Formidable avec moi; Kathrin and Johannes Hellwagner

for sharing the 500 MHz duty with me; Chandra for her generous laughs in the coffee break room; Nils for triple-checking my experiments before acquisitions; Thomas Wiegand for various discussions relating to EPR; Fabian for discussing dDNP with me; Alons for showing me how to fill ubiquitin; Schnozzel for mimicking my laughter, and hope you still do that after i leave the group; Joeri for explaining amyloid fibrils and secondary chemical shift to me; Maarten for explaining x-ray crystallography; Vlastmil for entertaining us with the picture of his daughter. I would like to thank former group members Michael Batel, Andreas Grommek, Rosmarie Joss, Anne Schütz for all kind of assistance they offered. Last but not least, I would like to thank the technicians Riccardo, Alexander, and Andreas for various technical support; Gabriele Roder and Bella Giorgia for making my life in ETH simpler by taking care of the administrative matters. Moreover, I also feel obliged to thank Ms Debbi Käser as she promised to bring brownies if I acknowledge her in my thesis. Special thanks go to my friends in TIFR, Mumbai including Venus Singh Mithu, Rajeswari, Subhradip Paul, Bappaditya Chandra, and Kshama Sharma.

I am also grateful of the Malaysian community here in Switzerland for making me feel less home sick. In particular, I would like to thank Kim Siang Khaw for all the Assam Laksa and Roti Canai he had made; Chow Lih Yew for the Tiramisu and pineapple cookies; Jia En Low for Hainanese chicken rice; Zuo Yen Lee for making sure that no food is wasted in any gathering; Yi Cheng Ng for his bird nest; Yi Hao Ng for his entertainment via singing; Cheng Choon Ang for his ghost stories and roast pork; Cheng Scheidegger for her Nasi Lemak and Laksa; and Ah Fatt who runs the old town restaurant in Dietikon for blowing water with me in Cantonese. I am associating almost every Malaysian with food, and yes, we belong to a nation that prioritize food above other stuff.

I apologize if your name is not mentioned here. I can assure you that you are not forgotten and I do have a good memory to remember various things, especially useless stuff. That is to say please be nice to me and I will be nice to you. Well, although this sounds like a farewell or worst still an eulogy, but i will still say it: "*You all live in memory of Kong*".



# Curriculum Vitae

**Name:** Kong Ooi Tan  
**Date of birth:** 9th July 1987  
**Place of birth:** Ipoh  
**Nationality:** Malaysia

## Education

Aug 2011 - Apr 2016 Ph.D. under the supervision of Prof. Matthias Ernst at ETH Zürich

Sep 2007 - Jun 2011 Msci & ARCS in Physics at Imperial College London, UK

Sep 2006 - Jun 2007 First year undergraduate Physics at NTU, Singapore

Mar 2005 - Jun 2006 GCE A-level at Taylors' university College, Malaysia

Jan 2005 - Mar 2005 St Andrew's Junior College, Singapore

2001 - 2004 GCE O-Level at Poi Lam High School, Malaysia

## Work and Research Experience

- Aug 2011 - Apr 2016      Ph.D. project with Prof. Matthias Ernst, ETH Zürich.  
Teaching assistant for various physical chemistry courses.  
Chief of staff - Responsible for the management of the NMR spectrometers and equipments in the laboratory.
- Thesis Title: Pulse-Sequence Design in Solid-State NMR Using Floquet theory.
- Jan 2014 - Feb 2014      Student exchange program PEP-ISJRP with Prof. P. K. Madhu, Solid-state NMR Group, TIFR Mumbai, India.
- Nov 2012 - Dec 2012      Student exchange program PEP-ISJRP with Prof. P. K. Madhu, Solid-state NMR Group, TIFR Mumbai, India.
- Oct 2010 - Apr 2011      Master project with Prof. Sergey Lebedev, Plasma Physics Group, Imperial College London, UK.
- Thesis Title: Laboratory Experiments to model Astrophysical Phenomena: Supersonic Plasma Jets and Shocks.
- Aug 2010 - Oct 2010      DAAD-RISE Research internship with Prof. Stefano Sanvito, Computational Spintronics Group, Trinity College Dublin, Ireland.
- June 2010 - Aug 2010      SURE Research internship with Prof. Wolfgang Rhode, Astroparticle Physics Group, TU Dortmund, Germany.
- Summer 2008              Industrial apprenticeship at Inter-Excel, Malaysia.

## Publications

1. V. S. Mithu, K. O. Tan, P. K. Madhu, *Selective inversion of  $^1H$  resonances in solid-state nuclear magnetic resonance: Use of double-DANTE pulse sequence*, J. Magn. Reson. 237, 11, **2014**.
2. K. O. Tan, I. Scholz, J. D. van Beek, B. H. Meier, M. Ernst, *Improved decoupling during symmetry-based  $C^9$ -TOBSY sequences*, J. Magn. Reson. 239, 61, **2014**.
3. K. O. Tan, A. B. Nielsen, B. H. Meier, M. Ernst, *Broad-Band DREAM recoupling sequence*, J. Phys. Chem. Lett. 5, 3366, **2014**.
4. K. O. Tan, M. Rajeswari, P. K. Madhu, M. Ernst. *Asynchronous symmetry-based sequences for homonuclear dipolar recoupling in solid-state nuclear magnetic resonance*, J. Chem. Phys. 142, 065101, **2015**.
5. A. B. Nielsen, K. O. Tan, R. Shankar, S. Penzel, R. Cadalbert, A. Samoson, B. H. Meier, M. Ernst, *Theoretical description of RESPIRATION-CP*, Chem. Phys. Lett. 645, 11, **2016**.

*Front cover* : Various Pulse Sequences

*Back cover* :